The Dissertation Committee for Will Robert Grigsby Certifies that this is the approved version of the following dissertation:

Experimental Studies of High Energy Density Silicon Using Ultra-Fast Lasers

Committee:

Todd Ditmire, Supervisor

Michael Downer

Manfred Fink

Eric Taleff

Zhen Yao

Experimental Studies of High Energy Density Silicon Using Ultra-Fast Lasers

by

Will Robert Grigsby, B.S.

Dissertation

Presented to the Faculty of the Graduate School of
The University of Texas at Austin
in Partial Fulfillment
of the Requirements
for the Degree of

Doctor of Philosophy

The University of Texas at Austin
August, 2007

Acknowledgements

This work would not have been possible without the help of numerous people, some of which are included below. First and foremost, I want to thank my family, especially my parents, Bob and Paula Grigsby. They engendered in me an appreciation for nature, a curiosity for the world, and the drive to continue my education. Ever since I was a kid, I knew that I would get my PhD in chemistry, just like my dad. Luckily, my introduction to organic chemistry in high school steered me away and into physics; I have never looked back. My parents have shown me immense support and love for all of my life, and I would not be at this stage of my life if it were not for them. I thank my wonderful wife, Emily, for being the most caring, loving, and wonderful person I know. She too has been very supportive and uplifting during the difficult final years of my research. Plus, her smile and hugs have the power to melt away stress and ease my mind at the end of a day.

Next, I want to thank the many people in our research group who have helped me along my path. Professor Todd Ditmire has encouraged and challenged me throughout my graduate career. His enthusiasm, support, and insight are more than a student could ever ask for. He has given me the opportunity to learn and experience so much these past seven years, and I greatly appreciate it. I owe a debt of gratitude to my office mates, Gilliss Dyer, Aaron Edens, and Greg Hays for their camaraderie and support throughout

the years. These guys have been through thick and thin with me from our first days in Gleeson's class, to our last days of dissertation editing. Special thanks goes to Greg Hays for being a great friend and study partner throughout the process, but for also taking me under his wing in the lab once we started working together. He was kind enough to take the time to share his immense lab skills and knowledge with me, and he continues to be an excellent resource to this day. A also thank Allen Dalton for his hard work and perseverance through the many projects we worked on together. On several occasions he took control of the situation when I had extenuating circumstances arise. I greatly appreciate all of the hard work and help that Byoung-Ick Cho provided in producing my silicon wafer targets. He provided consulting services before and during target design, as well as manufacturing and quality control during and after production. Although not in our group, I also want to thank Ben Bowes for his help throughout the years. From many long hours in the lab working with me, to reading drafts of this dissertation, he has always been helpful and encouraging.

I want to thank the three post-docs that I have worked with throughout the years. Working in the lab, traveling to conferences, and drinking beer with Dan Symes was not only educational, but also immensely entertaining. My work and friendship with Aaron Bernstein has always been enriching, and I sill have more to learn from his immense knowledge and attention to detail. Lastly, I thank Hernan Quevedo for his friendship, motivation, and assistance in the lab. His help and encouragement have been a refreshing addition to this past year, and his help with ground loops and shielding helped make this work possible.

I want to thank my collaborators, both in the Physics Department, and also at the national labs. Mike Downer has provided excellent advice, insight, and assistance with this work. The ZBL group at SNL has been very supportive and helpful over the years, and I am thankful for the opportunity to work with them. I want to thank Jeff Colvin and others at LLNL for their support and assistance throughout the years with this project. Jeff has been involved since day one, and has proven to be a great resource. Finally, I want to thank the many others out there that have aided me in my journey. The trail has been rocky at times and smooth in others, but nearing the end, I can see that the view is excellent and all of the hard work has been worth it.

Experimental Studies of High Energy Density Silicon Using Ultra-Fast Lasers

Publication No._____________

Will Robert Grigsby, Ph.D.
The University of Texas at Austin, 2007

Supervisor: Todd Ditmire

Understanding material behavior under extreme conditions is an important area of research in physics and material science. One method to study the behavior of materials under these conditions is to drive a strong shock wave through a material and watch its response. In many cases the material response is complicated by phase transitions such as lattice restructuring (Barker 1975; Mabire and Hereil 2000; Swift, Tierney et al. 2005) and melting (Asay 1975; Elias, Chapron et al. 1988; Werdiger, Eliezer et al. 1999; Mabire and Hereil 2000; Swift, Tierney et al. 2005). To study these dynamics we are using lasers in high time resolution pump-probe experiments to develop a real time diagnostic on the phase of a shocked material. This technique enables probing of the entire phase history of a material as it shock compresses and releases.

In addition to linear reflectivity and ultra-fast 2D displacement interferometry, we developed a melting diagnostics based on the non-linear optical technique of third harmonic generation (THG) using a circularly polarized laser pulse. This diagnostic resolves the less than 300 fs melting transition of laser excited Si and GaAs, and it also detects a response in shock compressed silicon. Our results show that Si remains crystalline during compression of an elastic 100 kbar shock wave. Results from Si shocked to higher pressures (> 300 kbar) indicate a decrease in THG, suggesting some level of disordering or unexplained phase change.

Table of Contents

List of Tables xiii

List of Figures xiv

Chapter 1. Introduction 1

Chapter 2. Shock Wave Physics 5

2.1 Shock Waves 5
- 2.1.2 Jump Conditions and the Hugoniot 7
- 2.1.3 Equation of State 11
- 2.1.4 Shock Impedance 12

2.2 Shock Waves in Solids 16
- 2.2.1 Material Strength 16
- 2.2.2 Phase Transitions 18

2.3 Laser-Mater Interaction 20
- 2.3.1 Rocket Engine Blow-off Model of Shock Generation 21
- 2.3.2 Empirical Shock Pressure 23
- 2.3.3 Taylor-Sedov Self Similar Expansion 26
- 2.3.4 Absorption Mechanisms 29
- 2.3.5 Heat Conduction 30
- 2.3.6 Blackbody Radiation 36

Chapter 3. Optical Probing of Surfaces 39

3.1 Linear Reflectivity 39
- 3.1.1 Derivation of Snell's Law 40

3.2 Harmonic Generation in Reflection Geometry 42
- 3.2.1 Second Harmonic Generation at an Interface 42

3.2.2 Third Harmonic Generation at an Interface 49

3.3 Dielectric Constant 53
3.3.1 Drude Model 54
3.3.2 Skin Depth 58

3.4 Probing of Laser-Melted Semiconductors 59
3.4.1 Harmonic Generation 59
3.4.2 Reflectivity 60

Chapter 4. THOR Laser Description 64

4.1 Laser Background 64
4.1.1 Chirped Pulse Amplification 65
4.1.2 Ti:sapphire characteristics 68

4.2 THOR Specifics 69
4.2.1 Oscillator 69
4.2.2 Isolation 70
4.2.3 Stretcher 71
4.2.4 Regenerative Amplifier 73
4.2.5 4-pass Amplifier 74
4.2.6 5-pass Amplifier 74
4.2.7 Compressor 79
4.2.8 Timing System 80

4.3 Phase Modeling 83

4.4 Construction 95
4.4.1 Stretcher and Compressor Alignment 95
4.4.2 Regenerative Amplifier Alignment 98

4.5 Pre- & Post-Pulses 98
4.5.1 Spectrometer 98
4.5.2 2nd Order Autocorrelator 101

4.5.3 3^{rd} Order Autocorrelator 104

4.6 Future Improvements 105

Chapter 5. Experimental Description 107

5.1 General Experimental Layout 107
5.1.1 Shock Driving Laser Pulse 113
5.1.2 Probe Laser Pulse 113
5.1.3 Targets 115

5.2 Shock Wave Characterization 123
5.2.1 Simulations 123
5.2.2 Interferometry 128
5.2.3 Reflectivity 129
5.2.4 Third Harmonic Generation 130

Chapter 6. Results and Analysis 134

6.1 Shock Characterization 134
6.1.1 Interferometry Analysis 135
6.1.2 Interferometric Data – Tin/Soda Lime Glass 139
6.1.3 Interferometric Data – Tin/Lithium flouride 139
6.1.4 Matching of Simulations with Sn/LiF Data 145
6.1.5 Interferometric Data – Silicon 145
6.1.6 Hugoniot Measurements 151

6.2 Reflectivity 155

6.3 THG 161
6.3.1 Diagnostic development Using Femtosecond Laser Excitation of Silicon and Gallium Arsenide 161
6.3.2 THG Probing of Shock-Compressed Silicon 167

Chapter 7. Conclusions 174

7.1 Summary 174

7.2 Future Work 176

Appendicies 178

Appendix A. Experimental Procedures for Probing Shocked Silicon.. 178
A.1 Introduction 178
A.2 Laser Alignment into the Target Room 178
A.3 Single Shot Timing Setup 180
A.4 Aligning the shock beam to the chamber 184
A.5 Aligning the probe beam to the chamber 185
A.6 Adjusting the time delay between pump and probe 188
A.7 Setting the target zero position 190
A.8 Measuring spot sizes 192
A.9 3 ω alignment 193
A.10 Overlapping the spots 197
A.11 Setting the correct probe intensities 199
A.12 Setup checklist 200
A.13 Taking data 201

Appendix B. Various useful quantities 203

Appendix C. Gaussian Beam Profile 205

Appendix D. Depth of Field 208

Appendix E. Phase to Expansion Conversion 210

Appendix F. HYADES Source file “AlSi08.inf” 213

Appendix G. HYADES Source file “SnLif9.inf” 215

References 217

Vita 226

List of Tables

Table 1. Scaling laws for a blast wave in different geometries. 27

Table 2. Index of refraction data used in this dissertation for gallium arsenide, silicon, and amorphous silicon. The cold data comes from Palik while the Drude model parameters are discussed in the text. 56

Table 3. Various Drude model parameters for GaAs, with the increase in reflectivity upon melting factor listed for two different angles. The parameters come from Temnov 2006 and Huang 1998. 63

Table 4. Amplification data from the 5-pass amplifier (taken 10/6/2006). PRO 1 energy = 1.14 J, PRO 2 energy = 1.22 J, as measured at the crystal 76

Table 5. List of various orders of dispersion caused by passing through 112 cm BK7 glass 85

Table 6. List of material for the THOR laser. All units are in millimeters, and all materials are broken down by type and description. Depending on the current state of the laser, some of these values might be different. For example, if a different fiber length is used, or if the number of regen trips is changes, then the values in this chart will need to be changed 88

Table 7. Phase coefficients for two different configuration of the laser system. The top half describes the configuration when there is no additional material installed in the laser chain. The parameters have been optimized for compression down to ~ 45 fs. The bottom half describes the configuration when there is 450 cm of extra fused silica added to the laser chain. The parameters have been re-optimized for compression down to ~ 33.6 fs. The adjustable laser parameters are the angle of incidence on the stretcher grating and the spherical mirror spacing from the center of the diffraction grating. 93

Table 8. Experimental Results Combined with Simulation Parameters 143

Table 9. Table of parameters from the curve fits to the Sn/LiF data plotted in Figure 65. 144

Table 10. Table listing the calculated linear and non-linear Fresnel factors, which depend on the dielectric constant, along with the relative intensity of the harmonics generated in reflection from cold and melted Si or GaAs. 162

Table 11. Gaussian pulse widths and relationships for various Gaussian definitions 204

List of Figures

Figure 2. A high pressure disturbance can turn into a shock wave in a material a positive curvature to the P-V curve. 7

Figure 4. Plot of the theoretical Hugoniot curves and data for D_2, N_2, and O_2 at very high pressures. The peak compression of the materials all approach the theoretical limit of 4 for a monatomic gas. (The figure is adapted from Knudsen (Knudsen 2005)) 11

Figure 5. Plot of the various Hugoniot curves for several materials used in my research. (a) Plot of shock velocity vs. particle velocity. (b) Plot of Pressure vs. particle velocity. (c) Plot of pressure vs. specific volume. The curves are produced from the least-squares fits to EOS data, both of which are from Trunin (Trunin 2001). 13

Figure 6. Diagram illustrating an incoming shock wave striking an interface between two materials, which creates a reflected and transmitted wave. 14

Figure 7. Hugoniot for a material with strength or a phase transition. 16

Figure 8. Phase diagram for tin. The melt curve, Hugoniot, and various release isentropes are shown. The image is adapted from Werdiger 1999. 19

Figure 9. Inequality plot showing the region where silicon should melt upon shock loading. The temperature limits are from Ng 1995, while the pressure limits are due to the uncertainty in the slope of the melt region from Voronin 2003. 20

Figure 10. Illustration showing the mechanism for laser generated shock waves. In the left-hand frame, the laser strikes the target where it begins heating the material. In the right-hand frame, the laser energy has been absorbed by the target, and a plasma is expanding away from the target. The pressure generated by the plasma drives a shock wave into the target. 22

Figure 11. Plot of the various equations relating laser intensity to the ablation pressure. The "Rocket Engine Model" derived in the text assumes an absorption fraction of 70%. These calculations assume a 10 μm thick aluminum target (A=27, Z=13), a wavelength of 800 nm, and a solid density of 2.7 g/cc. See the text for references to the source materials. 25

Figure 12. Diagram illustrating the decay of a shock wave, whose initial pulse length is t_p, as the shock wave travels into a material. 28

Figure 13. This figure shows the results from HYADES simulation "AlSi08.inf". The shock pressure profile is plotted for various time delays (different colors) and a curve is fit to the pressure peaks. 28

Figure 14. Plot showing self-similar heat wave propagation from an instantaneous planar source (a) and from a steady planar source (b) through a plasma. 33

Figure 15. Illustration showing the shock wave overtaking the heat front. 35

Figure 16. Radiation intensity curves for various blackbody temperatures 37

Figure 17. Wein's Displacement Law gives the wavelength of the peak of the radiation for a blackbody of given temperature. 38

Figure 18. Diagram showing linear wave refraction and reflection at an interface. 40

Figure 19. Diagram showing linear and non-linear wave refraction and reflection at an interface. This particular case is labeled for SHG, but it is identical for THG. 45

Figure 20. Diagram showing linear and non-linear wave refraction and reflection at an interface. The third harmonic waves are shown, along with the non-linear polarization source. 50

Figure 21. Plot showing the real (red) and imaginary (blue) portions of the index of refraction for silicon. Tabulated values from Palik (solid) are compared with values from a Drude model (dotted). 57

Figure 22. The reflectivity of cold (blue) and melted (red) silicon is shown as a function of probe angle. 57

Figure 23. Plot of the skin depths for Si, GaAs, and Al 59

Figure 24. The ratio of the reflectivity of melted silicon (Drude model) to cold silicon is shown as a function of probe angle for 800 nm. The resonance effect is due to the loss of reflection at Brewster's angle for the cold material. 61

Figure 25. Plot showing the real (red) and imaginary (blue) portions of the index of refraction for GaAs. Tabulated values (solid) are compared with values from a Drude model (dotted). 62

Figure 26. The ratio of the reflectivity of melted GaAs (Drude model) to cold GaAs is shown as a function of probe angle for 800 nm. The resonance effect is due to the loss of reflection at Brewster's angle for the cold material. 63

Figure 28. Schematic showing the various components and the general layout of the THOR laser. 70

Figure 29. An illustration of the stretcher grating with the various beam hits enumerated. The grating is drawn from the perspective of the input laser beam, but it is a mirror image of the actual layout of the THOR grating. See the text for a bounce-by-bounce description. 72

Figure 30. Diagram showing the components of the regenerative amplifier cavity 73

Figure 31. Spectra of laser pulse after the oscillator and after the last amplifier in the system. (Taken with an Ocean Optics fiber spectrometer on 10/12/2006). 76

Figure 32. Beam image and line-outs of the amplified laser pulse 17ft after the last pass through the Ti:sapphire crystal. 77

Figure 33. Measured fluorescence of our 5-pass Ti:sapphire crystal (14.7mm long, pumped by 1.1 J + 1.2 J). 78

Figure 34. Beam image and line-outs of the amplified laser pulse 33ft after the entrance window of the compressor 78

Figure 35. An illustration of the compressor grating with the various beam hits enumerated. The grating is drawn from the perspective of the input laser beam. The illustration is not to scale, but the sizes are approximately correct. The grating is 40 cm diameter, and the beams sizes are drawn with a 5 cm diameter and ~ 32 nm of bandwidth. See the text for a bounce-by-bounce description. 80

Figure 36. Diagram showing the timing boxes and structure for the THOR laser. 81

Figure 37. An overhead view of the ray trace through the THOR stretcher (a) and compressor (b). 84

Figure 38. These plots demonstrate the relative effect of various orders of phase on the pulse. The input was a 30 fs FWHM Gaussian, and the amount of each phase order was chosen such that the output pulse had a width of ~ 45 fs FWHM. The effects of 2nd and 4th (or 3rd and 5th) order phase terms have similar effects on the pulse 90

Figure 39. This plot demonstrates the effect of additional material on the higher order dispersion in the THOR ray-trace model. The 4th order dispersion is minimized with ~ 4.5 m of additional fused silica, while the 5th order dispersion is minimized with ~ 5.4 m of fused silica. After running the code, I found that it is more desirable to minimize the 4th order dispersion to obtain a shorter pulse with smaller wings than to minimize the 5th order dispersion... 91

Figure 40. Optimized pulse before (top) and after (bottom) the addition of 4.5 meters of fused silica to the laser chain. The output pulse is superimposed in blue over the shorter 30 fs FWHM input pulse, shown in red. Without the fiber, the uncompensated phase causes pulse broadening and the addition of large wings to the pulse. Adding the fiber and re-optimizing the laser minimizes the phase and produces a cleaner and shorter pulse 92

Figure 41. Plot of the optimized stretcher parameters as a function of fiber length. This plot demonstrates the adjustments that would be necessary to re-compress after adding or subtracting a large amount of material from the laser chain. . 94

Figure 42. Diagram showing the alignment of the THOR stretcher and compressor (February 18, 2003). 96

Figure 43. Layout of the HeNe beam used for scanning the compressor grating angle to optimize pulse compression. 97

Figure 44. Diagram showing the spacing and layout of the goniometer mount for the 5-pass Ti:sapphire crystal. The center of the crystal needs to be placed at the center of the rotation axis of the goniometer. 100

Figure 45. Second-order single shot autocorrelation data for THOR taken October 19, 2006 103

Figure 46. Third order autocorrelation data for THOR taken on Feb 21, 2006 105

Figure 47. Diagrams showing the various target configurations. The shock driving laser is absorbed on the front surface of the target, which drives a shock wave through the material. The probe beam(s) are incident on the rear surface of the target where they interact with the shocked material. The targets that I shot consisted of Sn, Al, GaAs, or Si, while the window materials were soda lime glass (microscope slides) or (100) LiF. 108

Figure 48. Experimental layout for shocked Sn/LiF experiments. The shock drive arrives from the left, and the probe pulse arrives from the right. 110

Figure 49. Annotated picture of the probe beam layout for the shocked silicon experiments 111

Figure 50. Drawing showing the design of the aluminum vacuum chamber using in my experiments. All units are expressed in inches. 112

Figure 51. The left hand side shows images of the laser beam intensity at the plane of the target. The right hand side shows false color images of the expansion of the rear surface for each spot. Note that the intensity, shape, and size of the laser beam is directly converted into target expansion. This demonstrates the effective one dimensional nature of the shocks which is due to the large aspect ratio of spot size to the 4 μm thick targets. 114

Figure 52. Results from a LASNEX hydrocode simulation performed by Jeff Colvin. The input parameters are: Laser = 1 J, 600 ps FWHM, 0.8 μm, with a 450 μm spot size. The target is a 4 μm thick Sn foil. The Hugoniot that Jeff used results in a shock melting pressure of ~ 490 kbar. 115

Figure 53. SEM images showing the rough surface and non-homogeneous cross-section of 4 micron thick tin foils purchased from Goodfellow. 117

Figure 54. Diagram showing the cross section of the Sn/glass targets used in the experiments. The tin was deposited by thermal evaporation onto the face of an ordinary, soda lime glass, microscope slide. 118

Figure 55. An SEM cross-sectional image of the Sn/LiF targets. This image is from a piece of LiF/Sn that fractured off of the main window which caused the fracture lines in the LiF seen in the top of the image, and the tearing in the Sn at the bottom. The Sn was e-beam deposited onto the face of an optical quality LiF window. 120

Figure 56. (a) a cross-sectional view of a silicon-on-insulator (SOI) wafer. (b) a cross-sectional view of a SOI wafer after wet-etching has produced a target 121

Figure 57. Photograph of a silicon target in a target mount. The Si wafer is approximately 3 cm x 3 cm, and the two black screws are size 4-40. 122

Figure 58. The top of this figure shows various pressure profiles from a HYADES simulation using a pump laser intensity of $8x10^{11}$ W/cm^2 with a 4 μm Sn slab backed by a thick LiF window. The pressure is partially releasing from the high impedance Sn into the lower impedance LiF across the interface of the two materials. 127

Figure 59. Photograph of the experimental layout of the femtosecond laser-melting of semiconductors experiments performed in air. The overlaid lines and labels describe the path of the various beams. 132

Figure 60. Experimental layout of the femtosecond laser melting experiment. The pump pulse melts the target in < 500fs. Probe 1 is a reflectivity probe that is sensitive to the large change in the dielectric constant of semiconductors upon melting. Probe 2 is used to generate third harmonic radiation at the surface of the target.. 133

Figure 61. Images showing interferometric data from various target materials. The top left image shows very straight and uniform fringes from an inexpensive aluminum mirror, which was used as a reference. The top right image shows un-usable fringing from the structured foils purchased from Goodfellow. These foils did not have a mirror-like finish. The bottom two images show fringes obtained from free standing tin foils that were floated off of the glass substrate used in the PVD process. It was rare to find a section with relatively straight fringes, as it was much more common to find regions with distorted fringes. Although the PVD foils did have a mirror finish, residual stresses in the foils caused them to curl once removed from their substrates. 135

Figure 62. This diagram graphically illustrates the process of extracting phase information from a 2D interferometric image. First, I lineout is taken from the fringed image. It is Fourier transformed, and then filtered in spectral space. Next, the data containing frequency is shifted to zero to remove the rapidly varying phase ramp of the fringes. Finally, the spectrum is inverse-Fourier transformed to extract the phase and amplitude of the signal. The process is repeated until all of the lines have been analyzed.. 137

Figure 63. Plots showing data taken with shocked free-standing tin and aluminum targets. The top graph shows lines and equations for curve fits to each data set, along with estimated pressures taken from the Hugoniots. The bottom graph illustrates the drop in reflectivity that occurs for all targets in the experiment... 140

Figure 64. Interferometric image from the shock breakout of Sn into a LiF substrate. The laser intensity was $6x10^{12}$ W/cm^2 and the probe delay was 450 ps after the timing fiducial 141

Figure 65. Plot showing peak interferometric expansion data from the interface of Sn/LiF targets. The various peak laser intensities are plotted in different colors, and least-squares curve fits to selected ranges of data are shown in gray. The

particle velocities derived from the fits are listed next to each data set. For more data from the curve fits, see Table 9. 142

Figure 66. Pressure-particle velocity plots using the Hugoniots from Trunin and the interface velocities from the Sn/LiF data shown in Figure 65. The individual plots a, b, c & d correspond to decreasing laser intensities, starting with $6x10^{12}$ W/cm^2. 143

Figure 67 HYADES simulations (curves) are fit to four of the five Sn/LiF interface expansion data (symbols). The numbers printed next to the linear fits to the data (solid thin lines) are the slopes of the lines (i.e. interface velocities). .. 144

Figure 68. Plot of silicon peak expansion vs. probe delay under various conditions. The individual data points are described in the text. 146

Figure 69. Diagram showing the Hugoniot for silicon. The black x's show the shock velocity as a function of particle velocity, while the red +'s show the shock pressure as a function of particle velocity. The data are from Goto 1982 and Gust 1971. 148

Figure 70. The left-hand side shows filtered interferometric images from 20 μm silicon targets. The delay time for each image corresponds to the color coded lineout in the right-hand side. These vertical line-outs are taken through the peak of the expansion. 149

Figure 71. Line-outs from the expansion of 95 μm Si targets. The broad shock breakout is wider than 100 μm after 1 μm expansion. The color coded plots are arranged in order of increasing time, violet through red. 150

Figure 72. Hugoniot data from various thickness Sn targets. The error bars represent uncertainties in the curve fits to the data. Although the error bars are large, the data do lie very close to the published Hugoniot. The green arrows represent various pressures along the Hugoniot and are only included as reference points. 152

Figure 73. Plot showing the measured particle and shock velocity from experiments performed with 4 μm of Sn deposited onto 6 mm (100) LiF windows. The error bars are discussed in the text. The blue and red data correspond to peak-to-peak pulse adjustments of 0.35 and 0.5 ns, as discussed in the text. 153

Figure 74. Plot showing the Tektronix oscilloscope traces of the short pulse (black) and long pulse (blue) on the Newport photodiode used in my setup. The estimated de-convolved positions of the actual pulses are shown in red and pink, respectively. 154

Figure 75. Diagram showing reflectivity from a diffuse Sn surface. The poor quality of the data is due to the rough surface and long f/# imaging optics. 155

Figure 76. Reflectivity data from a shock breakout from Sn into a LiF substrate. The laser intensity was $6x10^{12}$ W/cm^2 and the probe delay was 450 ps after the timing fiducial 156

Figure 77. Plot showing the reflectivity of melted Sn divided by the reflectivity of cold Sn as a function of angle. My experiments probed the reflectivity of Sn at ~ 10°, as indicated by the dashed line. The expected decrease in reflectivity due to melting is < 2%. 157

Figure 78. The left graph shows expansion data as a function of probe delay time from the 2D interferometer. The right graph shows normalized target reflectivity over the same time scale. The blue squares represent data taken from free standing Sn foils, while the red triangles represent data from Sn foils supported by a soda-lime glass substrate. 158

Figure 79. An illustration on the left shows how surface fragmentation might cause scattering of the probe pulse, which would appear as a decrease in the reflectivity signal. The photo on the right is an SEM cross section of the 4 μm tin foil. The granular structure can be seen at the edge where the material has been torn, which could seed the fragmentation process 158

Figure 80. Reflectivity data from a Sn/glass target. Notice the large reflectivity fluctuations which are much larger than the drop expected upon melt. 159

Figure 81. The illustration on the left shows how pressure induced opacity in the glass window could attenuate the probe, thus reducing the reflectivity signal. The right hand plot is the Hugoniot for soda lime glass (Trunin 2001). It shows a phase transition around 150 kbar. 160

Figure 82. Plot of THG data from laser excited gallium arsenide with a pump fluence of ~ 310 mJ/cm^2. The data was taken using (100) GaAs. The THG using circularly polarized light (blue) shows a coherent artifact near t_o. This is due to temporal overlap of the s-polarized pump with the circularly polarized probe. The artifact does not occur with a p-polarized probe (purple). The SHG and THG data show a 90%-10% fall time of ~ 150 fs. 164

Figure 83. Plot of reflectivity data from laser excited gallium arsenide with a pump fluence of ~ 310 mJ/cm^2. The data was taken using (100) Si. The reflectivity data show a 10%-90% rise time of ~ 500 fs at normal incidence and ~ 350 fs at 58.5°. 165

Figure 84. Plot of THG data from laser excited silicon with a pump fluence of ~ 310 mJ/cm^2. The data was taken using (100) Si. The THG using circularly polarized light (blue) shows a coherent artifact near t_o. This is due to temporal overlap of the s-polarized pump with the circularly polarized probe. The artifact does not occur with a p-polarized probe (purple). The THG data show a 90%-10% fall time of ~ 350 fs. 166

Figure 85. Plot of reflectivity data from laser excited silicon with a pump fluence of ~ 310 mJ/cm^2. The data was taken using (100) Si. The reflectivity data show a 10%-90% rise time of ~ 430 fs both at normal incidence and 58.5°. 166

Figure 87. The top plot is of rear surface expansion of 20 μm (red) and 30 μm (blue) silicon as a function of probe delay. The bottom plot is normalized THG vs.

probe delay. The THG signal decreases for both target thicknesses. Possible explanations for this are discussed in the text. The broad light red and light blue lines are only to guide the eye. 169

Figure 88. Diagram of target surface tilt in relation to the collection optics and the collected light. (a) target slope reflects light outside of the collection cone. (b) target slope scatters light in several directions 170

Figure 89. The top graph plots the THG signal for 20 μm (light red) and 30 μm (blue) silicon as a function of probe delay. The bottom graph plots peak target slope as calculated from the interferometric data as a function of probe delay. The gray shaded region indicates the range of target slopes that reflect some light outside of the collection optics. The dark gray region above 0.1 slope indicates the expected region of complete loss of collected light. The green bounding box encompasses data that can possibly be explained by the loss of light from the collection optics. 171

Figure 90. Schematic of the long pulse portion of the laser. Most of the laser energy is diverted into this leg by the 90/10% beamsplitter. The various reflections and beams paths mainly serve to delay the pulse with respect to the compressed pulse so that they are timed up at the target. Note: diagram is not drawn to scale, but the proportions are close to accurate 179

Figure 91. Diagram showing the operation and layout of the wiring for single-shot operation of THOR 183

Figure 92. Diagram illustrating the components and positions in the delay leg. 186

Figure 93. Multiple views of the setup inside the vacuum chamber 195

Figure 94. Diagram showing a HeNe beam passing through a hole in the target while the interferometric probe reflects off of the rear surface of the target. (a) a "clean" hole through the target allows easy correlation of the target position with both probes. (b) a "dirty" hole makes correlation difficult between the probes. 198

Figure 95. A Gaussian profile is shown with the corresponding top-hat profile whose peak is the same as the Gaussian, and whose area or time integrates to 1 for a 2D spatial profile (a) or a temporal profile (b). 205

Figure 96. Schematic showing the rays and angles necessary to derive the calibration factor for the interferometer 210

CHAPTER 1. INTRODUCTION

Understanding material behavior under extreme conditions of pressure and temperature is an important area of research in physics and material science. Research in this field has contributed to advancements such as the understanding of planet and star cores (Ahrens 1975; Ahrens 1980; Nguyen and Holmes 2004), the development of shock peening for hardening materials such as turbine blades (Fairand, Wilcox et al. 1972; Montross, Wei et al. 2002), and the understanding of a wide range of projectile impacts (Luo and Ahrens 2004). These topics, as well as numerous others, all depend on knowledge of the phase, strength, and behavior of materials exposed to high pressures, whether applied statically or dynamically.

Although decades of research have yielded enormous amounts of data on a wide variety of materials, there are still many interesting topics that remain unexplored. One such area of research is the study of shock induced phase transitions. The identification of the $\alpha \rightarrow \varepsilon$ phase transition in iron established the shock compression field as separate and important scientific field in the mid-1950s (Walsh 1954; Bancroft, Peterson et al. 1956). In fact, this result, combined with a review article published by Rice, *et.al.* convinced the world that the technology developed for the nuclear weapons programs could be used to study the properties of solids under entirely new pressure regimes (Rice, McQueen et al. 1958). This led military laboratories to begin extensive studies to define high-pressure equations of state and phase diagrams for hundreds of materials. Despite the years of study that have been devoted to iron since the emergence of shock compression, it continues to be of scientific interest to this day (Kalantar, Collins et al. 2006; Kadau, Germann et al. 2007).

Along these lines, the goal of this work is to develop and implement a novel technique for studying phase transitions, such as melt, in solids. At the start of my research I became intrigued with the idea of optically detecting the time scale for a shock driven melt transition. Previous work has estimated an upper limit for the transition time at the nanosecond level (Werdiger, Eliezer et al. 1999), while the lower limit is most likely a few picoseconds for thermal transitions (Kandyla, Shih et al. 2007). What made this research interesting to me was the fact that we could theoretically observe this transition with a time resolution as low as ~100 fs through the use of a high intensity short pulse laser.

In order observe the shock driven melt transition, I need to be able to identify a change from the crystalline material to the disordered (melted) material. Professor Michael Downer suggested that I try adapting the static work of Yakovlev into a dynamic optical probe (Yakovlev and Govorkov 2001). This technique utilizes third harmonic generation (THG) from a circularly polarized femtosecond probe so that the probe is sensitive to the anisotropy of the crystalline material.

Once successfully proven, my dynamic THG diagnostic can be included at other facilities with existing diagnostics to help obtain a more complete picture of material behavior under high-pressure shock compression. In turn, this knowledge can be used to help calibrate a wide variety of simulation codes, such as those examining the high pressures of planetary cores or the compression of nuclear material using facilities such as the ASC at Lawrence Livermore National Laboratory (LLNL).

In this dissertation, I explore the shock compression of tin and silicon under pressures approaching a few Mbar with the goal of measuring the melt transition with high time resolution. The topics related to laser driven shock waves are discussed in Chapter 2. To detect the melt transition, I have developed a non-linear optical diagnostic utilizing third harmonic generation (THG) that has a temporal resolution ultimately limited by the laser pulse width. The THG diagnostic is sensitive to the crystalline symmetry of the solid, as will be discussed in Chapter 3.

All of my research has been possible due to the Texas High-intensity Optical Research (THOR) laser. THOR is a 1 J, Ti:sapphire based chirped pulse amplification (CPA) laser that was designed and built by Todd Ditmire, Gilliss Dyer, Will Grigsby, and Greg Hays in 2001. It has a pulse width as short as 40 fs, which allows excellent temporal resolution in femtosecond pump-probe experiments such as the laser melting of silicon. The design, construction, and operation of this laser is discussed in Chapter 4

The experiments that I performed are presented in Chapter 5. Here I describe the experimental layout, various laser parameters, target fabrication, and optical diagnostics. My diagnostics include 2D displacement interferometry, reflectivity, and THG. Before implementing the THG diagnostic on shock loaded materials, I first developed the dynamic probe using femtosecond laser-melting of semiconductor targets. This is the adaptation and extension of Yakovlev's experiment into the time-resolved regime. By simultaneously observing both the reflectivity and the third harmonic generation, I was able to measure and compare the time scales (< a few hundred fs) for the transition of the semiconductors into the melted state.

After working out the nuances of detecting melt through THG, I transitioned to implementing this diagnostic on shocked materials. Due to my success in detecting laser melting of Si and GaAs, I decided to explore these materials first, rather than metals, under shock loading. Discussions with Aaron Bernstein and Byoung-Ick Cho made clear the difficulty in creating etched GaAs wafers in-house. For this reason, we decided to take advantage of Byoung-Ick's extensive experience in producing Si targets. Probing of these targets revealed the following interesting behavior: THG from the ~100 kbar elastic shock compression of 95 μm thick silicon remains constant over the first ~ 3 μm of rear-surface expansion. However, THG from a ~ 300 kbar compression of 20 – 30 μm thick silicon decreases to zero faster and further than expected. Chapter 6 presents these results and discusses possible explanations for the drop in THG. Finally, I end with a summary and a look to future possibilities for this work in Chapter 7.

CHAPTER 2. SHOCK WAVE PHYSICS

In this chapter I will discuss the background information needed for the laser induced shock waves that were used in this research. In particular, I will begin by describing what a shock wave is, how one is formed, and how the material properties are related in front of and behind a shockwave. I will also discuss how real effects such as material strength and phases transitions affect the shock wave structure. Next, I will discuss how a laser is absorbed by a material to create a shock wave, and how the laser generated a propagating heat wave in the material. Finally, I will discuss how that shock wave and heat front decay with time, and how the blackbody self emission from the shock heated material depends on temperature.

2.1 Shock Waves

A shock wave is a traveling discontinuity in pressure, temperature, and density. We can see how a shock wave develops from a sound wave by looking at the bulk speed of sound c_s in a material with density ρ and isentropic bulk modulus κ.

$$c_s = \sqrt{\frac{\kappa}{\rho}} \tag{2.1}$$

The isentropic bulk modulus is defined as the derivative of stress with respect to strain,

$$\begin{aligned} \kappa &= \frac{\partial \sigma}{\partial \gamma} \\ &= -V \left.\frac{\partial P}{\partial V}\right|_S \\ &= \rho \left.\frac{\partial P}{\partial \rho}\right|_S \end{aligned} \tag{2.2}$$

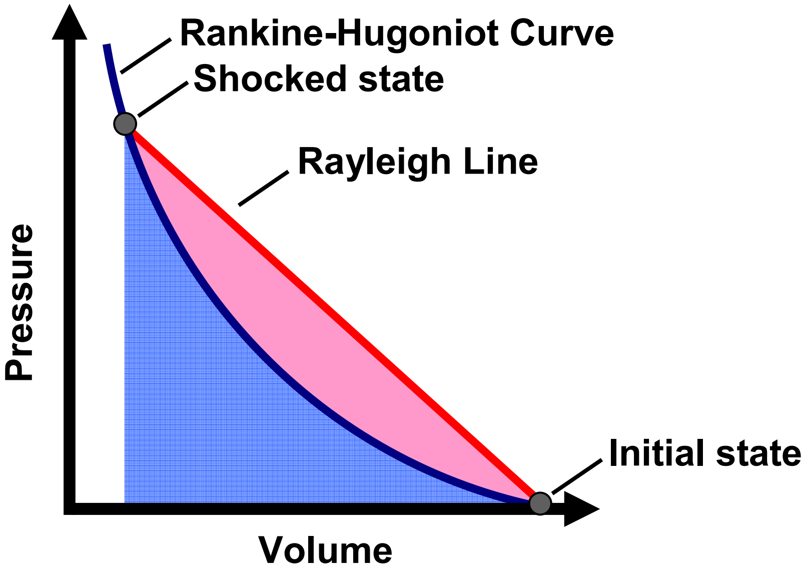

Figure 1. Diagram illustrating a normal Hugoniot curve without strength or phases transitions shown in blue. A possible shock path is shown in red (The Rayleigh line).

where σ is stress, $\gamma = dV/V$ is strain, $V = 1/\rho$ is specific volume, P is pressure, and S is entropy. In the one-dimensional longitudinal case, the stress is equal to the negative pressure, by definition. Upon simplification, this leads to a sound speed that depends on the density derivative of pressure.

$$c_s = \sqrt{\frac{\partial P}{\partial \rho}} \tag{2.3}$$

Most materials have a P-V relationship at constant entropy as shown in Figure 1, which has positive curvature. A positive curvature translates into a higher sound speed at higher pressures, which leads to the peak of a wave traveling faster than the low pressure portions. Over some distance, this causes the wave to steepen up into a discontinuity or shock wave (Figure 2).

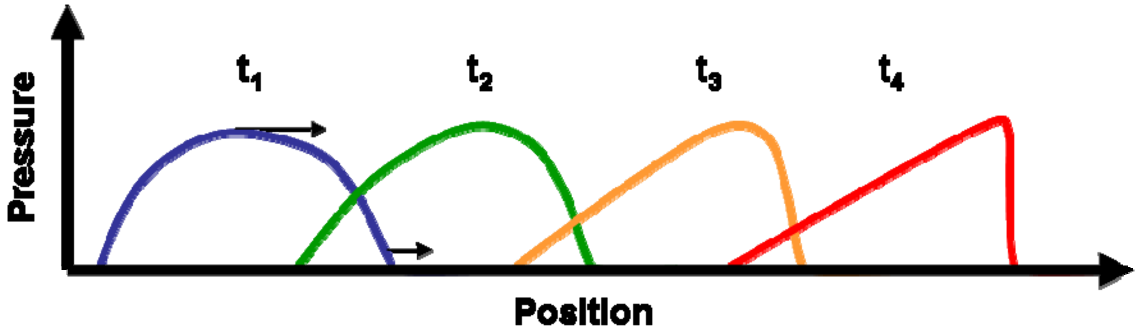

Figure 2. A high pressure disturbance can turn into a shock wave in a material a positive curvature to the P-V curve.

Three good references for the study of shock waves are the books by Meyers, Asay and Shahinpoor, and Zel'dovich and Raizer (Meyers 1994), (Asay and Shahinpoor 1993), and (Zel'dovich and Raizer 1966). On one hand, Meyer's book has a lot of information, both theoretical and experimental, on the study of shocked materials. On the other hand, Zel'dovich and Raizer's book is much more theoretical, covering the wide variety of subjects necessary to study strong explosions and related phenomena. Asay and Shahinpoor's book covers many aspects of shocked solids, from basic introduction, to detailed theory and experimental results.

2.1.2 JUMP CONDITIONS AND THE HUGONIOT

To relate the material properties behind a shock wave with those in front of the shockwave, we utilize the conservation of mass, momentum, and energy equations. These equations are sometimes known as the jump conditions, and they can be derived by considering a piston pushing on a column of material as illustrated in Figure 3. The conservation laws are listed below, as written in the laboratory reference frame with $u_o = 0$:

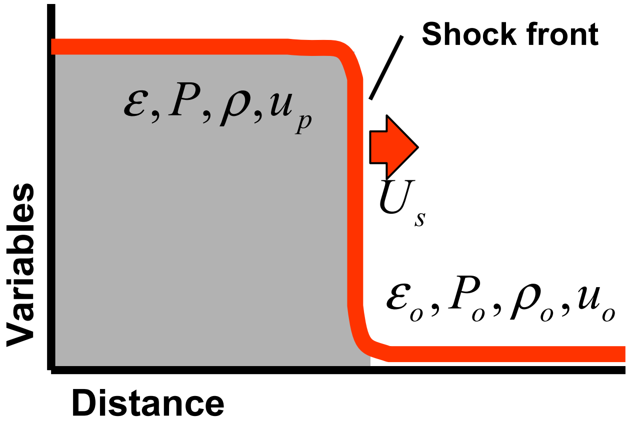

Figure 3. Diagram showing the discontinuity in material parameters on both side of the traveling shock front

conservation of mass : $\rho_o U_s = \rho(U_s - u_p)$ (2.4)

conservation of momentum : $P - P_o = (\rho_o U_s) u_p$ (2.5)

conservation of energy: $Pu_p = \frac{1}{2}(\rho_o U_s) u_p{}^2 + (\rho_o U_s)(\varepsilon - \varepsilon_o)$ (2.6)

By solving the conservation of mass equation for the shock velocity U_s, the conservation of momentum equation for the particle velocity u_p, and plugging them into the conservation of energy equation, we find one form of what is known as the *Rankine-Hugoniot* equation.

$$\varepsilon - \varepsilon_o = \frac{1}{2}(P + P_0)(V_o - V) \tag{2.7}$$

Here, ε is the internal energy density.

This curve, which relates the material states on each side of the shock front, is often referred to as the *Hugoniot,* or in Russian literature the *shock adiabat*. The Hugoniot is the collection of all possible final shocked states for a given initial state. It is important to stress that the thermodynamic path that the shock wave takes is not along the curve of the Hugoniot, but along the Rayleigh line connecting the initial and final states (Figure 1)(Asay and Shahinpoor 1993). If we consider two different initial states, the Hugoniot will, in general, be different for each of those cases.

Other forms of the Hugoniot equations can be found by plugging u_p from equation (2.5) into equation (2.4) to find U_s, or by plugging U_s into equation (2.5).

$$U_s = V_o \sqrt{\frac{(P - P_0)}{(V_o - V)}} \tag{2.8}$$

$$u_p = \sqrt{(P - P_0)(V_o - V)} \tag{2.9}$$

These three forms of the Hugoniot equation, in combination with Figure 1, reveal a few useful relationships.

1. The slope of the Rayleigh line is related to the shock velocity (Equation (2.8))
2. The area under the Rayleigh line provides the increase in internal energy (Equation (2.9))
3. The difference in area between the Rayleigh line and the Hugoniot curve provides the amount of energy associated with the irreversible processes of shock loading, as the release isentrope is often very similar to the Hugoniot curve.

To close the system of Hugoniot equations down to a function of only two variables, we need to add another equation which, for example, relates the internal energy to the pressure and volume. That equation is known as the equation of state (EOS).

To begin with, let us assume that the EOS of the material is approximated by an ideal gas with *n* degrees of freedom.

$$\varepsilon = c_v T = \frac{1}{\gamma - 1} PV \tag{2.10}$$

$$\gamma = \frac{c_p}{c_v} = \frac{n+2}{n} \tag{2.11}$$

Equation (2.7) can be re-written using this equation of state as:

$$\frac{1}{2}\left(P+P_0\right)\left(V_o-V\right) = \frac{1}{\gamma-1}\left(PV-P_oV_o\right) \tag{2.12}$$

The ideal gas EOS is not necessarily accurate at low to moderate pressures, but it becomes more applicable at very high pressures. As an example of the power of the Hugoniot equations, let us examine the strong shock limit where $P >> P_o$. After simplification of Equation (2.12), we find the theoretical peak compression for an ideal gas.

$$\frac{\rho}{\rho_o} \to \frac{\gamma+1}{\gamma-1} \tag{2.13}$$

The approach of data and simulations to this limit is illustrated in Figure 4 (Knudsen 2005).

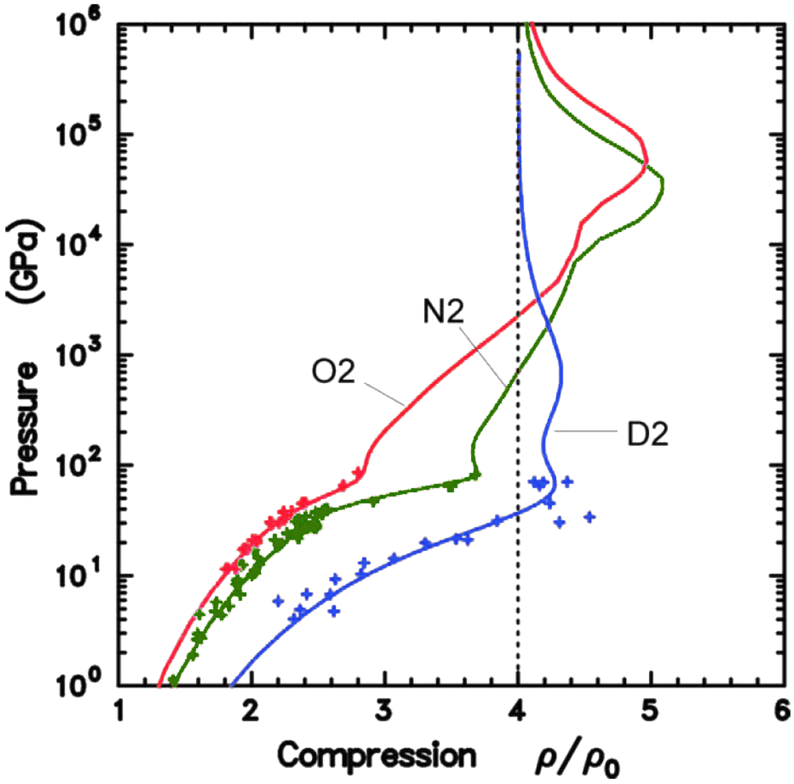

Figure 4. Plot of the theoretical Hugoniot curves and data for D_2, N_2, and O_2 at very high pressures. The peak compression of the materials all approach the theoretical limit of 4 for a monatomic gas. (The figure is adapted from Knudsen (Knudsen 2005))

2.1.3 EQUATION OF STATE

Many other forms of the equation of state exist. Quite often experimental results are used to provide coefficients for the following empirical form of the EOS (Marsh 1980; Steinberg 1991; Trunin 2001):

$$U_s = c_0 + s_1 u_p + s_2 u_p^2 + \cdots \tag{2.14}$$

For many ,materials, c_o is, or is close to, the sound speed at zero pressure. The coefficients above s_1 can often be neglected since there is a nearly linear relationship between U_s and u_p. Data from Trunin for several materials that were used in this research are listed below and plotted in Figure 5.

Si: $U_s(u_p) = 1.760 + 1.682 u_p + 0.0126 u_p^2$ $\quad 4.0 \le u_p \le 6.50$
Al: $U_s(u_p) = 5.33 + 1.356 u_p$ $\quad 0.0 \le u_p \le 6.10$
$U_s(u_p) = 6.541 + 1.158 u_p$ $\quad 6.10 \le u_p \le 22$
LiF: $U_s(u_p) = 5.130 + 1.310 u_p$ $\quad 0.0 \le u_p \le 10.10$
Sn: $U_s(u_p) = 2.437 + 1.688 u_p - 0.047 u_p^2$ $\quad 0.0 \le u_p \le 7.80$
Glass: $U_s(u_p) = 3.080 + 1.294 u_p$ $\quad 0.25 \le u_p \le 0.75$
$U_s(u_p) = 0.400 + 2.450 u_p$ $\quad 1.65 \le u_p \le 2.75$

Alternatively, tabular forms of various EOSs have been produced by combining and smoothing data and simulations to create a smooth table for use in hydrodynamic codes. One such database is the SESAME database maintained at Los Alamos National Laboratory (Lyon and Johnson 1992). It is this database that I used in my HYADES simulations, which are discussed in Section 5.2.1.

2.1.4 SHOCK IMPEDANCE

It is important to examine how shockwaves behave at an interface between two materials so that we can predict how pressures and velocities transmit and reflect (Figure 6). This is analogous to the behavior of waves on a string or light traveling thorough a material. To start with, let us assume that the two materials comprising the interface are joined together and do not separate. This restriction allows us to use the following boundary conditions for the problem, where *v* is the particle velocity, *σ* is the stress , and the subscripts *i, r,* and *t* correspond to the incoming, reflected and transmitted waves:

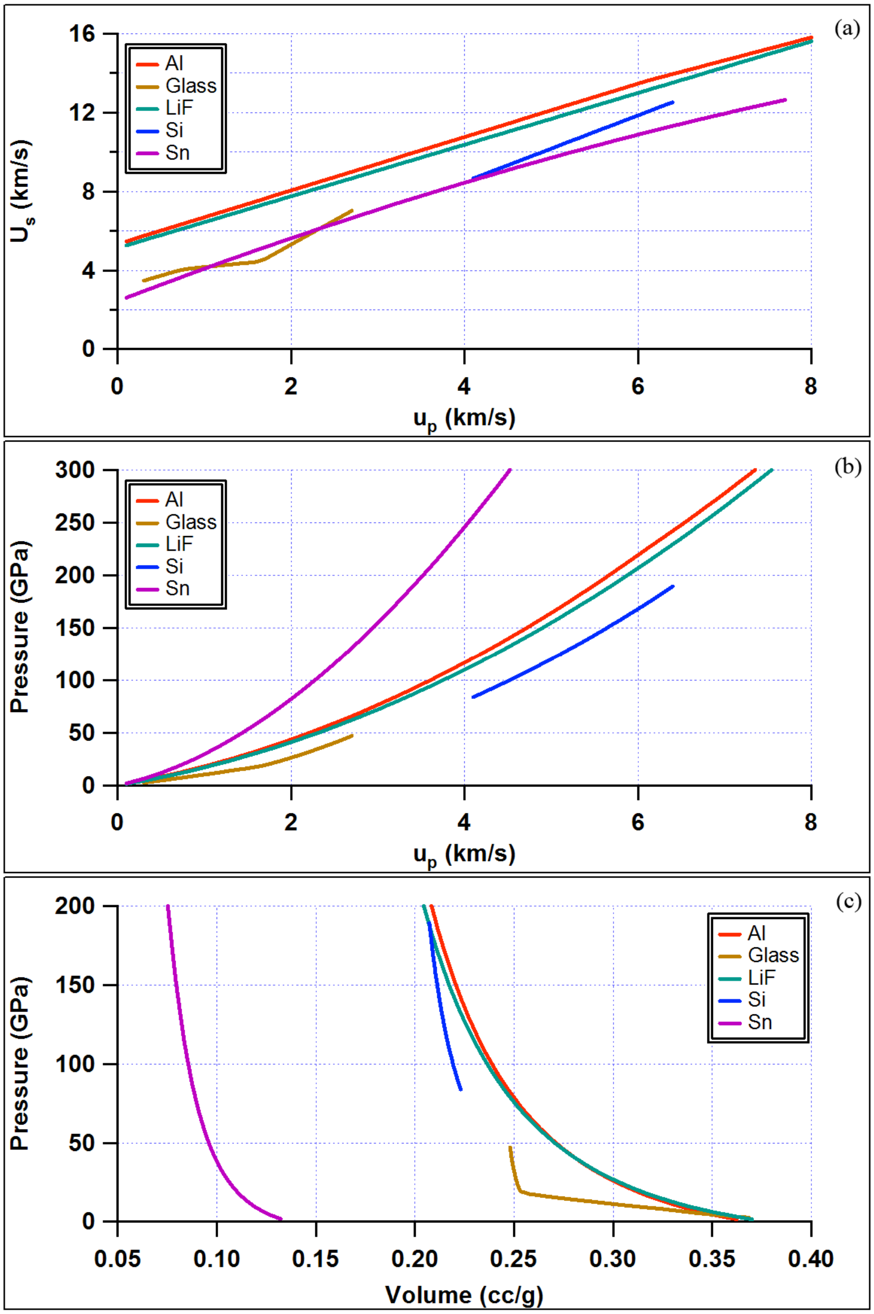

Figure 5. Plot of the various Hugoniot curves for several materials used in my research. (a) Plot of shock velocity vs. particle velocity. (b) Plot of Pressure vs. particle velocity. (c) Plot of pressure vs. specific volume. The curves are produced from the least-squares fits to EOS data, both of which are from Trunin (Trunin 2001).

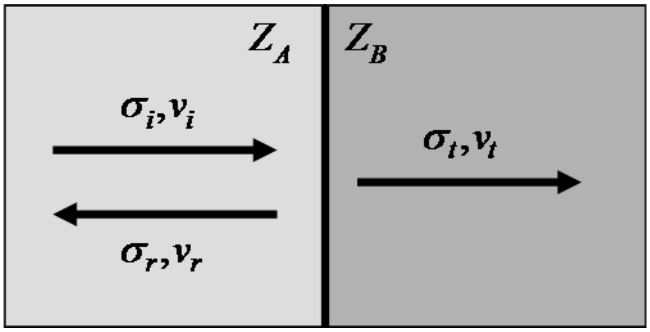

Figure 6. Diagram illustrating an incoming shock wave striking an interface between two materials, which creates a reflected and transmitted wave.

$$v_i - v_r = v_t \tag{2.15}$$

$$\sigma_i + \sigma_r = \sigma_t \tag{2.16}$$

Let us define shock impedance to be,

$$Z = \rho_o U_s \tag{2.17}$$

so that the pressure from equation (2.5) becomes

$$\sigma = Zv\,. \tag{2.18}$$

Solving equations (2.15) and (2.16) for the reflected and transmitted amplitudes in terms of the shock impedances leads to the following equations:

$$\frac{v_r}{v_i} = \frac{\dfrac{Z_B}{Z_A} - 1}{1 + \dfrac{Z_B}{Z_A}} \tag{2.19}$$

$$\frac{v_t}{v_i} = \frac{2}{1 + \dfrac{Z_B}{Z_A}} \tag{2.20}$$

$$\frac{\sigma_r}{\sigma_i} = \frac{\dfrac{Z_B}{Z_A} - 1}{1 + \dfrac{Z_B}{Z_A}} \tag{2.21}$$

$$\frac{\sigma_t}{\sigma_i} = \frac{2\frac{Z_B}{Z_A}}{1+\frac{Z_B}{Z_A}}. \tag{2.22}$$

It is instructive to consider two limiting cases to gain insight into what these equations physically mean. First, consider the case of $Z_B=0$, which is the case for vacuum. This leads to a reflected particle velocity and pressure of the opposite sign relative to the incoming wave. The transmitted particle velocity is equal to twice that of the incoming wave, while the transmitted pressure is zero. That is, the wave is releasing into vacuum, so the material continues to travel in the forward direction while sending a release (negative pressure) wave back into the material.

The second case to consider is that of $Z_B=\infty$, where the second material is an infinitely hard wall. Here, the reflected velocity and pressure equal the incoming values, while the transmitted velocity is zero, and the pressure felt at the interface is double that of the incoming wave.

Intermediate impedances fall somewhere in between these two cases. For example, let us consider a 500 kbar shock reaching a Sn/Glass interface, where $\rho_{o,Sn}$ = 2.71 g/cm^3 and $\rho_{o,glass}$ = 2.48 g/cm^3, so that Z_{Sn} = 34.9 and Z_{glass} = 17.6. Then, v_r = -0.33v_i, v_t = 1.33v_i, σ_r = -0.33 σ_i,, and σ_t = 0.67 σ_i. Here, the shock wave is partially releasing into the lower impedance glass, illustrating an impedance mismatch.

For an example where two materials are impedance matched, we will look at an Al target shocked to 1.9 Mbar backed by a LiF window. In this case, the particle velocity is ~ 5.6 km/s, so the aluminum and lithium fluoride will have shock velocities of 13.08 km/s and 12.71 km/s, respectively. Using their solid densities, this leads to a pressure reflection of only 2.6%, which is an effective shock impedance match.

2.2 Shock Waves in Solids

2.2.1 MATERIAL STRENGTH

Real materials do not always behave hydrodynamically, like a liquid, as was assumed in Figure 1. Hydrodynamic behavior ignores any complicating factors such as material strength or phase transitions. When these behaviors are accounted for in a Hugoniot, they often show up as one or more cusps in the P-V curve (Figure 7). The point where these cusps meet is a discontinuity in the slope, and it is at this point that the actual phase change or plastic flow transition occurs

The structure of a shock wave generated in such a material depends on the amplitude of the drive pressure, which affects the path in P-V space. At low pressures, the shock has a single wave structure and remains in the first state of the material, as shown by the shortest path in (Figure 7). In contrast, at intermediate pressures, the

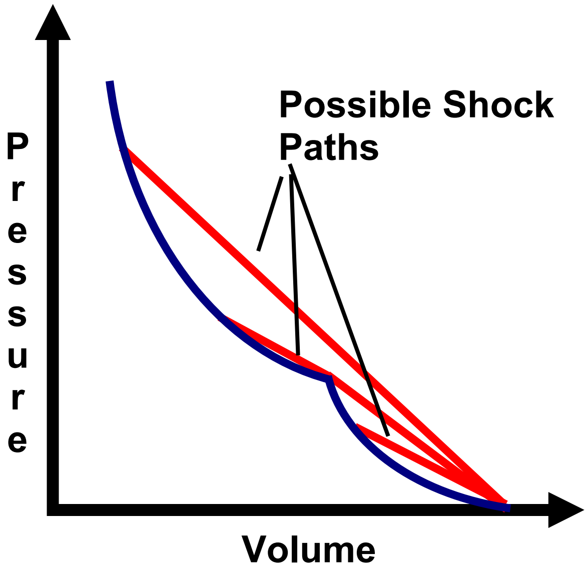

Figure 7. Hugoniot for a material with strength or a phase transition.

material reaches the second state and there is a two wave structure with shock velocities related to the slope of the two Rayleigh lines, as the middle path illustrates. The first wave takes the material to the discontinuity in the first state, while the second wave is the transformation wave that results in the second state of the material. The third option shown in (Figure 7) is for a high pressure shock the path of the longest Rayleigh line. In this case, there is only a single wave structure, traveling faster than any of the previous waves, that transforms the material directly into the second state.

In many materials, this first state of the material is the elastic regime, where only longitudinal compression is observed. After the pressure returns to zero, the elastically compressed material is able to return to its initial state, since there is no permanent deformation. When the pressure becomes larger than the Hugoniot elastic limit (HEL), the material begins to undergo permanent plastic deformation. Hydrostatic (volumetric) compression is an example of this second state of compression. After the pressure is released, the material does not return to its original dimensions, as the structure has been permanently altered.

Typical elastic limits for metals are in the range of 1 - 50 kbar, while the HEL for LiF and sapphire are ~ 1 kbar and 120 – 210 kbar, respectively. For most of the experiments performed in this work, the shock pressures (0.1 – 1 Mbar) are much higher than the HEL, so plastic deformation is expected. However, the onset of plastic flow can be time dependent such that not all experiments performed above the HEL become plastic (Loveridge-Smith, Allen et al. 2001). In this case, the velocity of dislocations (crystallographic defects) was low enough that the silicon sample remained elastic over the time scale of their diagnostics.

2.2.2 PHASE TRANSITIONS

The second effect that can create a multiple shock wave structure is that of phase transitions. As a shockwave transforms a material from one point on the Hugoniot to another point, its path may cross a phase transition region. If this happens, then the shock wave will transform the material into that second phase. One of the first to be studied and now the most well known transformation is that of iron, which undergoes the $\alpha \rightarrow \varepsilon$ (BCC to HCP) phase transition at ~ 13 GPa (Walsh 1954; Bancroft, Peterson et al. 1956).

In addition to solid-solid phase transitions, shock waves can also drive melt and re-solidification transitions, depending on the phase diagram and the Hugoniot of a material. An excellent review article involving various phase transitions was published by Duvall and Graham (Duvall and Graham 1977).

One material where the Hugoniot crosses the melt curve at a relatively low pressure is tin. A phase diagram for tin is shown in (Figure 8) (Werdiger, Eliezer et al. 1999). The Hugoniot (dotted line) is shown to intersect the melt curve (solid line) at 292 kbar. At pressures higher than this, tin melts upon shock loading. Various release isentropes (dashed lines) are shown labeled with their peak pressures. For pressures between 205 kbar and 292 kbar the material releases into the melt region of the phase diagram. For pressures below 205 kbar the material never melts, even upon release.

Based on these data, I began studying laser shocked tin, with the goal of detecting the shock melting transition and measuring its duration. The results from these experiments will be discussed in Chapter 6.

Another material that melts upon shock loading, albeit at higher pressures, is silicon. Very little data exists in the literature on the precise behavior of silicon under high pressures, which leads to a large region of uncertainty in phase space. To constrain the pressure-temperature region where I believe it does melt, I examined the published

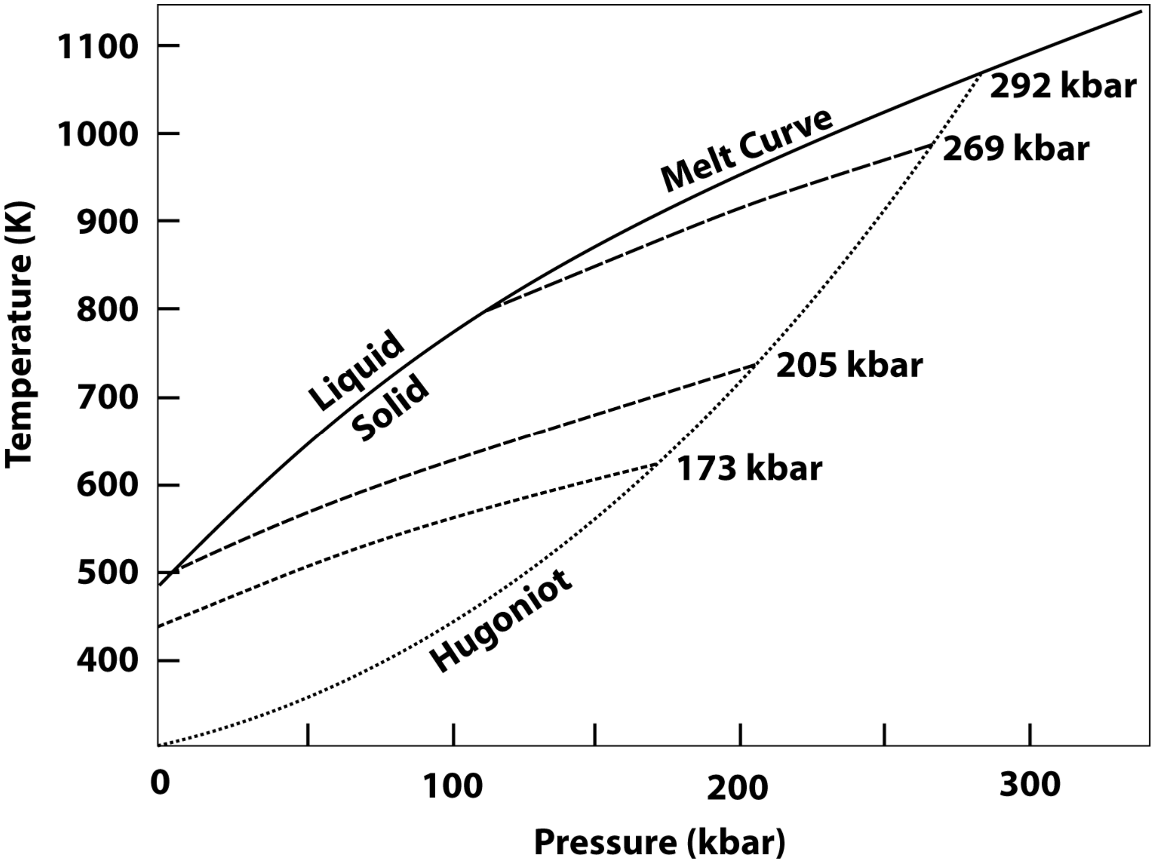

Figure 8. Phase diagram for tin. The melt curve, Hugoniot, and various release isentropes are shown. The image is adapted from Werdiger 1999.

simulations and experimental results and plotted the boundaries that I found in Figure 9. The boundaries from this region include a temperature range from Ng and a pressure range from Voronin (Ng, Celliers et al. 1995; Voronin, Pantea et al. 2003). Despite the lack of data on the high pressure shock structures of silicon, it turns out to be a good specimen to study from a diagnostics standpoint. It has a relatively high non-linear susceptibility which increases the intensity of third harmonic generation, and it is available in various wafer thicknesses with a very flat surface finish, which allows nice interference images to be made.

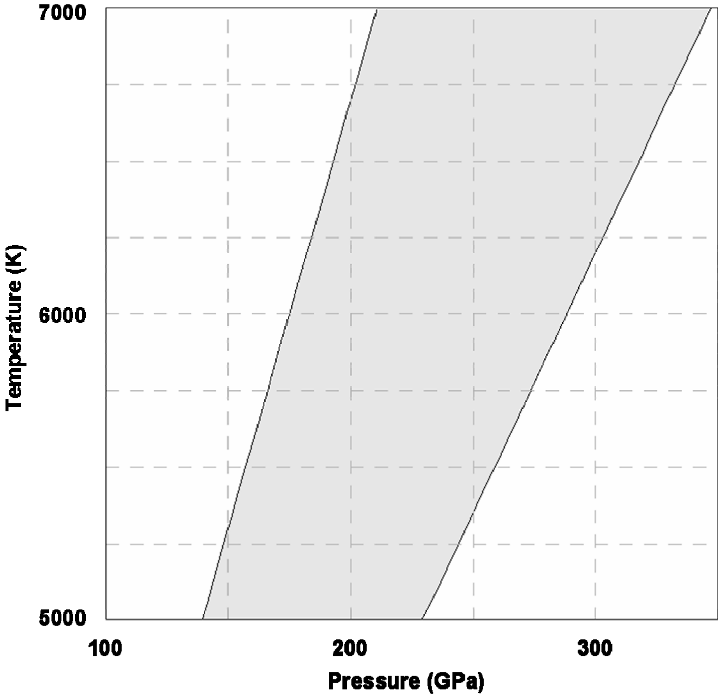

Figure 9. Inequality plot showing the region where silicon should melt upon shock loading. The temperature limits are from Ng 1995, while the pressure limits are due to the uncertainty in the slope of the melt region from Voronin 2003.

2.3 Laser-Mater Interaction

Shock waves can be created by many different sources. In the laboratory, they are often created by impacts or energy deposition by way of high-explosives (McQueen and Marsh 1960), gas guns (Chhabildas, Barker et al. 1992), rail guns (Rashleigh and Marshall 1978), and lasers (Fairand and Clauer 1979; Obenschain, Whitlock et al. 1983). Each method has its benefits, but the only source that can also have a precisely synchronized material probe is the laser. There are two main experimental methods in which a laser can drive a shock wave through a solid. One way is to focus the laser onto a flyer plate that accelerates across a vacuum gap and impacts the target material (Paisley

1990). This method typically requires a larger amount of energy than the second method, and also requires a large amount of characterization to understand the flyer plate behavior. In flyer plate experiments, researchers are concerned about such things as the flyer planarity, tilt, velocity, and density.

The second method is simply to focus the laser directly onto the target material and let the plasma pressure create the shock wave that traverses the target (Fairand and Clauer 1979). In this technique, which I have utilized for the research in this dissertation, researchers are concerned about the shape and smoothness of the laser intensity profile, as well as the temporal shape of the main pulse and any pre-pulses.

2.3.1 ROCKET ENGINE BLOW-OFF MODEL OF SHOCK GENERATION

Let us consider the basic physics of how an energy source, such as a laser, can create a pressure wave in a target. In particular, we want to examine how the ablation pressure of the plasma scales with the input laser intensity. As the laser hits the target, a fraction of the energy is absorbed near the critical density (see Section 2.3.4) and creates an expanding plasma. Let us assume that a fraction α of the total laser energy goes into the kinetic energy of the expanding material, so that

$$\alpha E_{laser} = \frac{1}{2} m v^2 \tag{2.23}$$

To simplify the equations, assume that the motion is one dimensional. To convert energy into intensity, divide the laser energy by area *A* and time *t*.

$$I = \frac{E_{laser}}{A \cdot t} \tag{2.24}$$

$$\alpha I = \frac{1}{2} \frac{m}{A \cdot t} v^2 \tag{2.25}$$

The blown off mass per area per time is simply

$$\frac{m}{A \cdot t} = \rho v \tag{2.26}$$

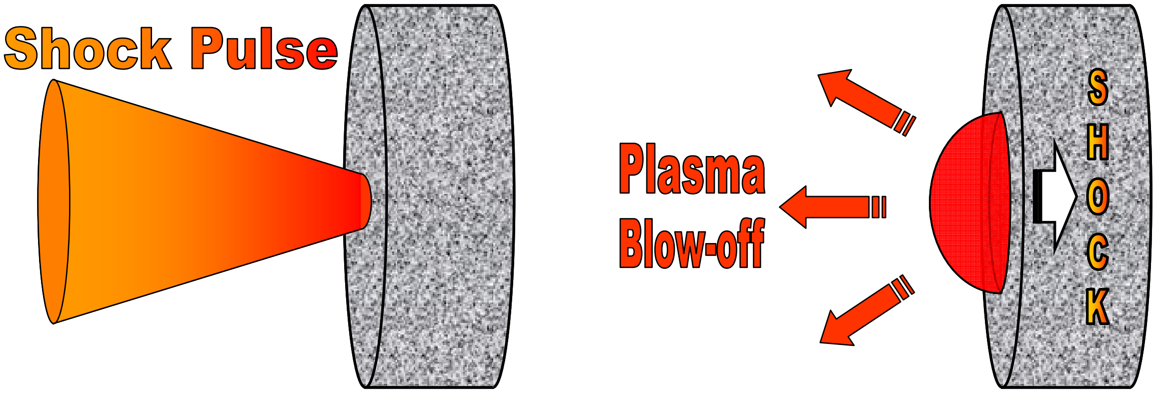

Figure 10. Illustration showing the mechanism for laser generated shock waves. In the left-hand frame, the laser strikes the target where it begins heating the material. In the right-hand frame, the laser energy has been absorbed by the target, and a plasma is expanding away from the target. The pressure generated by the plasma drives a shock wave into the target.

As the material heats up, it tries to expand (Figure 10). Since one side of the plasma is fixed at the target surface, the plasma must expand in the opposite direction. Combining these equations, and then solving for velocity we find

$$\alpha I = \frac{1}{2}\rho v^3 \tag{2.27}$$

$$v = \left(\frac{2\alpha I}{\rho}\right)^{1/3} \tag{2.28}$$

Conservation of momentum requires that a pressure be generated at the target, due to the plasma expanding in the opposite direction.

$$P = \rho v^2 \tag{2.29}$$

We can plug velocity into the formula for pressure to get

$$P = \rho^{1/3}\left(2\alpha I\right)^{2/3} \tag{2.30}$$

We see that the ablation pressure scales sub-linearly with laser intensity, and has a weak dependence on density. The density can be estimated by assuming that all of the laser absorption occurs at the critical density (Equation (2.42)), which is where the laser frequency equals the electron plasma frequency. The electron density is converted into an ion density by assuming an ionization state of the material, Z*, so that the ion density is represented by the following equation.

$$\begin{aligned}\rho_{ion} &= n_i m_p \\ &= \frac{n_{cr}}{Z^*} m_p \\ &= \frac{\omega^2 m_e \varepsilon_o}{e^2} \frac{m_p}{Z^*}\end{aligned} \tag{2.31}$$

$$\rho_{ion}\left[g/cm^3\right] \approx \frac{0.00187}{Z^*\left(\lambda[\mu m]\right)^2} \tag{2.32}$$

The density can be inserted into Equation (2.30) to yield:

$$P = \left((2\pi c)^2 \frac{m_e m_p \varepsilon_o}{Z^* e^2}\right)^{1/3} \left(\frac{2\alpha I}{\lambda}\right)^{2/3} \tag{2.33}$$

Plugging into equation (2.33) some parameters typical for the performance of our laser system (energy=1 J, diameter=0.5 mm, pulse width = 600 ps, laser wavelength = 800 nm, ionization state = 5, absorption fraction = 0.7, ion density = 0.0006 g/cm^3) we find the pressure ≈ 0.43 Mbar.

2.3.2 EMPIRICAL SHOCK PRESSURE

Although the absolute results from the rocket engine model are an overestimate, the scaling laws are approximately correct, as can be seen by comparing with the following empirical and theoretical expressions:

- Max reported the following expression, where *A* is the mass number, *Z* is the atomic number, the laser intensity *I* has units of W/cm^2 and the wavelength λ has units of µm (Max, Lindl et al. 1983).

$$P\ [\text{Mbar}] = 12\left(\frac{I\ \left[\text{W/cm}^2\right]}{10^{14}}\right)^{2/3} \left(\frac{1}{\lambda\ [\mu\text{m}]}\right)^{2/3} \left(\frac{A}{2Z}\right)^{1/3} \tag{2.34}$$

- In an inertial confinement fusion review paper, Lindl modified Max's result (Lindl 1995).

$$P\ [\text{Mbar}] = 8.6\left(\frac{I\ \left[\text{W/cm}^2\right]}{10^{14}}\right)^{2/3}\left(\frac{1}{\lambda\ [\mu\text{m}]}\right)^{2/3} \tag{2.35}$$

- Mora theoretically found the following expression, where Z^* is the ionization number, and t is the pulse width in ns (Mora 1982).

$$P\ [\text{Mbar}] = 11.6\left(\frac{I\ \left[\text{W/cm}^2\right]}{10^{14}}\right)^{3/4}\left(\frac{1}{\lambda\ [\mu\text{m}]}\right)^{1/4}\left(\frac{A}{2Z}\right)^{7/16}\left(\frac{3.5}{Z^* t[\text{ns}]}\right)^{1/8} \tag{2.36}$$

- Batani modified Mora's equation to make it time-independent, and found the following expression for aluminum, using A = 27 and $Z = Z^*$ = 13 (Batani, Stabile et al. 2003).

$$\begin{aligned} P\ [\text{Mbar}] = 15.36&\left(\frac{I\ \left[\text{W/cm}^2\right]}{10^{14}}\right)^{4/5}\left(\frac{1}{\lambda\ [\mu\text{m}]}\right)^{4/15} \times \\ &\left(\frac{1}{\rho_o\ \left[\text{g/cm}^3\right]}\right)^{1/15}\left(\frac{1}{d\ [\mu\text{m}]}\right)^{2/15} \end{aligned} \tag{2.37}$$

- For shockwaves in aluminum, Henis published the following empirical relation (Henis and Eliezer 1993).

$$P\ [\text{Mbar}] = \frac{12.25\left(\frac{I\ \left[\text{W/cm}^2\right]}{10^{14}}\right)^{0.785}}{1+0.0057\left(\frac{I\ \left[\text{W/cm}^2\right]}{10^{14}}\right)^{-0.725}} \tag{2.38}$$

- Eliezer (Eliezer, Gazit et al. 1990) adapted an equation from an extensive study covering UV-IR laser ablation (C. R. Phipps, Turner et al. 1988)

$$P\ [\text{Mbar}] = 0.23(A)^{7/16}\left(\frac{I\ \left[\text{W/cm}^2\right]}{10^{12}}\right)^{3/4}\left(\frac{1}{\lambda\ [\mu\text{m}]}\right)^{1/4}\left(\frac{1}{Z}\right)^{9/16}\left(\frac{1}{t\ [\text{ns}]}\right)^{1/8} \tag{2.39}$$

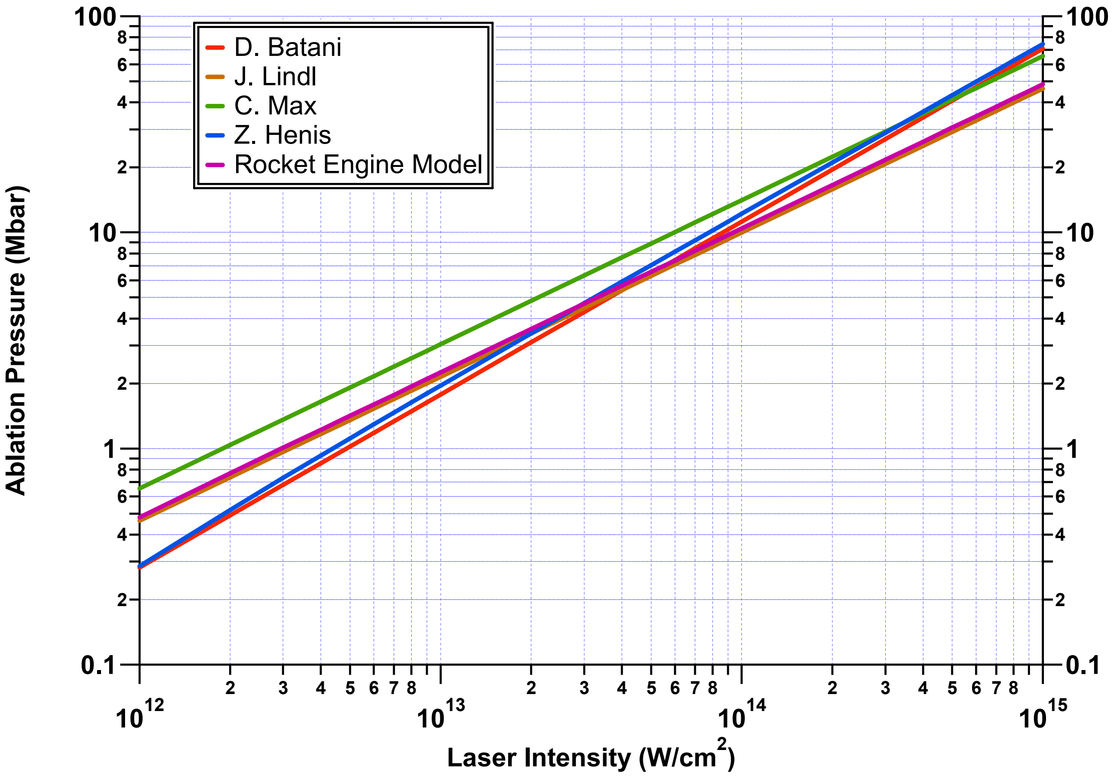

Figure 11. Plot of the various equations relating laser intensity to the ablation pressure. The "Rocket Engine Model" derived in the text assumes an absorption fraction of 70%. These calculations assume a 10 µm thick aluminum target (A=27, Z=13), a wavelength of 800 nm, and a solid density of 2.7 g/cc. See the text for references to the source materials.

These relations are compared with the rocket engine model in (Figure 11). As the figure shows, all of these models fall within a factor of two from each other. It is important to remember that these equations estimate the shock pressure in the case that the drive intensity is turned on for the duration of the shock. For many shock waves, including those studied in this research, the input pulse has a shorter temporal duration than the shock transit time, so the pressure will begin to attenuate.

2.3.3 TAYLOR-SEDOV SELF SIMILAR EXPANSION

In the limit that the temporal duration of energy input into the system is much shorter than the propagation time of interest, the shock wave evolves into a decaying blast wave. This is particularly applicable for point explosions in the atmosphere, but it can also give insight into the decay of shockwaves in thick materials.

If this blast wave evolves in a purely hydrodynamic manner, the expansion can be characterized in terms of its initial conditions and dimensionless quantities. The only initial conditions of importance are the input energy of the explosion E and the background material density ρ_o. By combining these quantities in such a way that the units reduce to only length and time, we arrive at the ratio of the energy of the blast wave to the density of the background material. For planar geometry, this ratio has the units of length^3/time^2. Consequently the similarity variable will be:

$$\xi = x(t)\left(\frac{\rho_0}{Et^2}\right)^{\frac{1}{3}} \tag{2.40}$$

The blast wave position x will evolve according to the equation:

$$x(t) = \xi_o\left(\frac{E}{\rho}\right)^{1/3} t^{2/3} \tag{2.41}$$

Table 1 summarizes the results for other geometries. To see how other hydrodynamic variables evolve, it is necessary to use the conservation of momentum, equation (2.5). The shock pressure is proportional to the square of the velocity, so we arrive at the relation showing the pressure decay with increasing time or position. This decay is a consequence of the energy expanding into 1, 2, or 3 dimensions. Although this self-similar treatment does not strictly hold true for shockwaves in solids, it is instructive to study this limiting case to get an estimate for how a decaying shockwave evolves.

Table 1. Scaling laws for a blast wave in different geometries.

	Density Units	Units of (E/ρ)	Shock Position $r(t)$	Shock Velocity $u(t)=\frac{\partial r(t)}{\partial t}$	Shock Pressure $P(t)\propto u(t)^2$
Planar	$\frac{\text{mass}}{\text{length}}$	$\frac{m^3}{s^2}$	$\propto t^{\frac{2}{3}}$	$\propto t^{\frac{-1}{3}}$	$\propto t^{\frac{-2}{3}} \propto r^{-1}$
Cylindrical	$\frac{\text{mass}}{\text{area}}$	$\frac{m^4}{s^2}$	$\propto t^{\frac{2}{4}}$	$\propto t^{\frac{-1}{2}}$	$\propto t^{-1} \propto r^{-2}$
Spherical	$\frac{\text{mass}}{\text{volume}}$	$\frac{m^5}{s^2}$	$\propto t^{\frac{2}{5}}$	$\propto t^{\frac{-3}{5}}$	$\propto t^{\frac{-6}{5}} \propto r^{-3}$

2.3.3.2 Shock Pressure Decay with Thickness

To understand better the process of how a shock wave begins to decay in a material, we will examine the evolution of a shock wave driven for a duration of τ_p (see Figure 12). In the time τ_p, the shock front will propagate to $x_{s,1}=U_s\tau_p$. At this point the drive is turned off, causing a release wave to begin propagating behind the shock wave. The rarefaction (release) wave travels at the sound speed of the compressed material plus the particle velocity ($u_r=C+u_p$). This velocity is faster than U_s for normal materials $\left(\partial^2 P/\partial\rho^2>0\right)$, which means that the faster traveling release wave will catch up to the shock front at position $x_{s,3}=U_s\tau_p\left(u_p+C\right)/\left(u_p+C-U_s\right)$. After this point, the release wave begins to decrease the peak pressure of the shock wave. As the pressure decreases, so will the shock velocity, causing the shock wave to slow down. This is the reasoning behind the shock pressure and velocity decay that was predicted in the self-similar expansion theory shown in (Table 1).

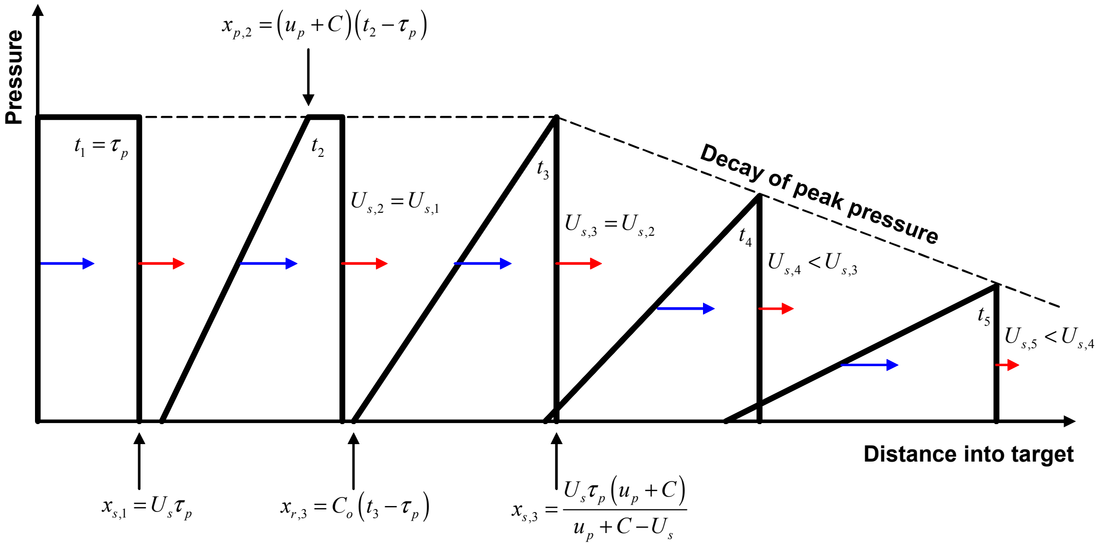

Figure 12. Diagram illustrating the decay of a shock wave, whose initial pulse length is t_p, as the shock wave travels into a material.

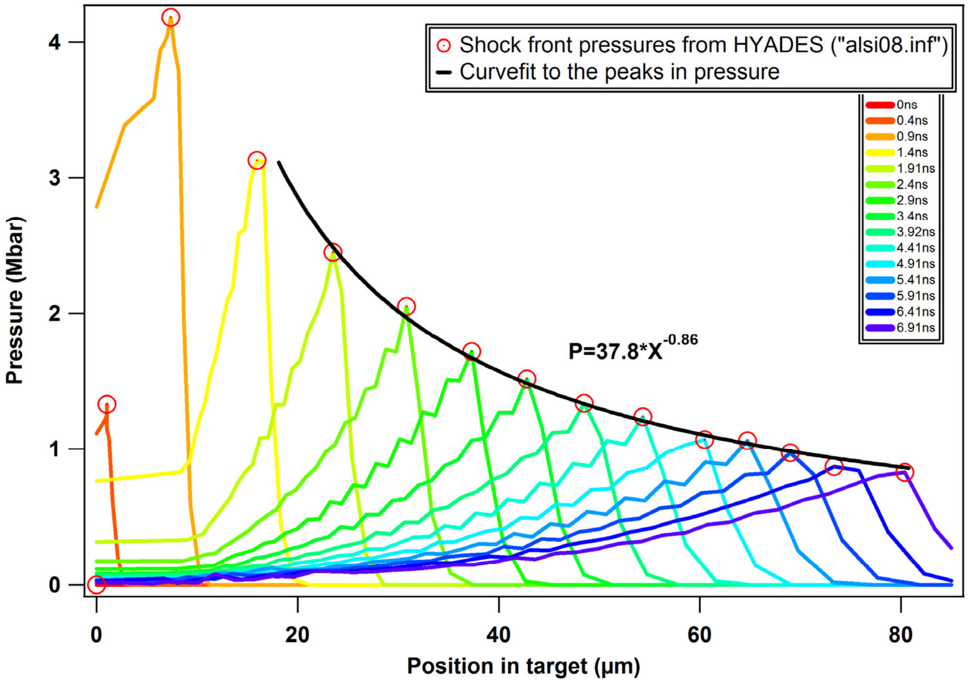

Figure 13. This figure shows the results from HYADES simulation "AlSi08.inf". The shock pressure profile is plotted for various time delays (different colors) and a curve is fit to the pressure peaks.

A numerical hydrodynamic simulation showing the propagation of a shockwave into silicon is shown in (Figure 13). This HYADES simulation (Appendix Appendix F) used a laser pulse ($I = 1.5\text{x}10^{13}$ W/cm^2, $\lambda = 800$ nm, $\tau_\text{p} = 460$ ps FWHM) peaked at 0.8 ns in the simulation. The target material was 300 μm of silicon, with a 300 nm overcoat of aluminum to absorb the laser. A curve fit to the peak pressures is displayed in the figure, and reveals an exponent close to that predicted by the self-similar solution. The fit was performed over the range of 18 to 80 μm in the plot so that the shock had sufficient time to begin decaying.

2.3.4 ABSORPTION MECHANISMS

Let us examine the laser absorption process in more detail. To begin with, the low intensity leading edge of the laser pulse will begin to ionize and heat a thin layer of the atoms in the target. These atoms will expand away from the surface, creating a plasma density gradient that spans from very low density at the leading edge to solid density at the target. Somewhere in between these extremes, the electron density equals the critical density n_{cr} for the incoming laser light.

$$n_{cr}\ [cm^{-3}] = \frac{\omega^2 m_e \varepsilon_o}{e^2} \approx \frac{1.1\times10^{21}}{\left(\lambda[\mu m]\right)^2} \tag{2.42}$$

It is this point where the laser frequency is equal to the plasma frequency, and the laser is unable to penetrate any further. At higher densities, the plasma responds faster than the laser oscillation and blocks the electric field. This means that the laser light will only be absorbed before the critical density through collisional (inverse bremsstrahlung) absorption, or near the critical density through resonant absorption, where the laser field resonantly drives an electron plasma wave that then transfers energy into the plasma.

For the intensities studied in this research, inverse bremsstrahlung (IB) is the primary mechanism of laser absorption (Shay, Haas et al. 1978; Kaushik and Godwal 1987). Simulations show that 60 - 80% of the laser energy is absorbed by the material in the range of 10^{13} - 10^{14} W/cm^2 (Kruer 1988; Kruer 2005; Regan, Epstein et al. 2007). IB occurs through a process where electrons oscillating in the field of the laser collide with an ion and absorb energy from the laser. The fraction of energy absorbed by this collisional process can be written as:

$$f_A = 1 - \exp\left(-\frac{8\nu_{ei}^{*}L}{3c}\right) \qquad (2.43)$$

where ν_{ei}^{*} is the electron-ion collision rate at the critical density and L is the plasma scale length (Kruer 1988). The scaling of the collision rate provides insight into the efficiency of IB in various plasma regimes.

$$\nu_{ei} = \frac{1}{\tau_{ei}} \propto \frac{nZ}{\theta^{3/2}} \qquad (2.44)$$

As the plasma density n increases, collisions increase, but as the temperature $\theta = k_B T_e$ increases, collisions decrease. The decrease in collisions with increasing temperature (and laser intensity) is due to the smaller cross-section for collisions at higher temperatures.

2.3.5 HEAT CONDUCTION

Once the energy from the laser is deposited into the target plasma, it propagates through the target by heat conduction. The energy balance equation governing heat flow can be written as

$$\rho c_p \frac{\partial T}{\partial t} = -\nabla \bullet S + W \qquad (2.45)$$

where c_p is the specific heat at constant pressure, S is the heat flux, and W is the energy release per unit time per unit volume from external sources (Zel'dovich and Raizer 1966).

The conductive heat flux is proportional to the temperature gradient, to first order, where κ is the thermal conductivity.

$$S = -\kappa \, \nabla T \tag{2.46}$$

From this, we can re-write the energy equation as:

$$\rho c_p \frac{\partial T}{\partial t} = -\nabla \bullet \left(-\kappa \, \nabla T \right) + W \tag{2.47}$$

If the heat conduction changes very little with temperature, the heat conduction becomes linear with *T*.

$$\rho c_p \frac{\partial T}{\partial t} = \kappa \, \nabla^2 T + W \tag{2.48}$$

More realistically, the heat conduction in a plasma does depend on temperature in the following manner, when using SI units (Kruer 1988):

$$\kappa = \frac{4 \left(k_B T_e \right)^{5/2}}{\sqrt{m_e} Z e^4 \ln \Lambda} \left(4 \pi \varepsilon_o \right)^2 \tag{2.49}$$

The Coulomb logarithm can be written (Huba 2007):

$$\ln \Lambda \approx 24 - \ln \left(\frac{\sqrt{n_e [cm^{-3}]}}{T_e [eV]} \right) \tag{2.50}$$

2.3.5.1 Flux Limiting

Kruer's thermal conductivity is identical to that found by both Spitzer and Braginskii, except for the numerical cofactor and small higher order correction factors (Braginskii 1958; Spitzer 1962).

$$\kappa = \frac{n_e k_B T_e}{m_e} \tau_e \tag{2.51}$$

$$\tau_{e,Braginskii} = \frac{3 \sqrt{m_e} \left(k_B T_e \right)^{3/2}}{4 \sqrt{2\pi} Z n_e e^4 \ln \Lambda} \left(4 \pi \varepsilon_o \right)^2 \tag{2.52}$$

$$\tau_{e,Spitzer} = 20 \left(\frac{2}{\pi} \right)^{3/2} \frac{\sqrt{m_e} \left(k_B T_e \right)^{3/2}}{Z n_e e^4 \ln \Lambda} \left(4 \pi \varepsilon_o \right)^2 \tag{2.53}$$

These definitions show that the thermal conductivity is higher at higher temperatures, and lower at lower temperatures. This is analogous to the sound speed vs. pressure relationship that we explored earlier in describing the building of a shock front. In this case, the heat flow forms a heat front that travels into the material.

Now we will examine the heat flow at sharp gradients, such as at the heat front. The local electron temperature scale length is defined as the

$$L \equiv \frac{T_e}{\nabla(T_e)} \tag{2.54}$$

We can use $k_B T_e = \frac{1}{2} m_e v_e^2$ and the above equation to simplify the heat flux equation.

$$\begin{aligned} S &= -\kappa \nabla T \\ &= \left(\frac{n_e k_B T_e}{m_e} \tau_e \right) \left(\frac{k_B T_e}{L} \right) \\ &\approx \frac{n_e k_B T_e}{m_e} \tau_e \frac{m_e v_e^2}{L} \end{aligned} \tag{2.55}$$

When the electron mean free path $\lambda = v_e \tau_e$ becomes equal to or greater than the plasma scale length *L*, the heat flux equation predicts that thermal energy is transported faster than the free streaming limit,

$$S_{fs} \approx f \, n_e v_e k_B T_e \tag{2.56}$$

To compensate for this, heat conduction models often include a flux limiter, $f \approx 1\% - 10\%$, which keeps the heat flux below the maximum physically allowed limit (Malone, McCrory et al. 1975; Kruer 1988). This is the reason it is important to change the default flux limiter in the HYADES code, as discussed in Section 5.2.1.2.

2.3.5.2 Heat Flow Examples

The thermal conductivity can be generalized from equations (2.49) and (2.51)to the following form, where a is a numerical factor from equations (2.49), (2.52), or (2.53):

$$\kappa = a\left(k_B T_e\right)^n \tag{2.57}$$

The one-dimensional heat flow equation is now written as:

$$\frac{\partial T}{\partial t} = a\frac{\partial}{\partial x}\left(T^n \frac{\partial T}{\partial x}\right) \tag{2.58}$$

Zel'dovich found an exact self-similar solution for this equation with an instantaneous planar heat input, which is listed below and plotted in (Figure 14 a):

$$T(x,t) = T_c(t)\left(1 - \frac{x^2}{x_f^2(t)}\right)^{2/5} \tag{2.59}$$

$$T_c(t) = \frac{Q}{2x_f(t)}\frac{9\Gamma\left(\frac{9}{10}\right)}{2\sqrt{\pi}\Gamma\left(\frac{2}{5}\right)} \tag{2.60}$$

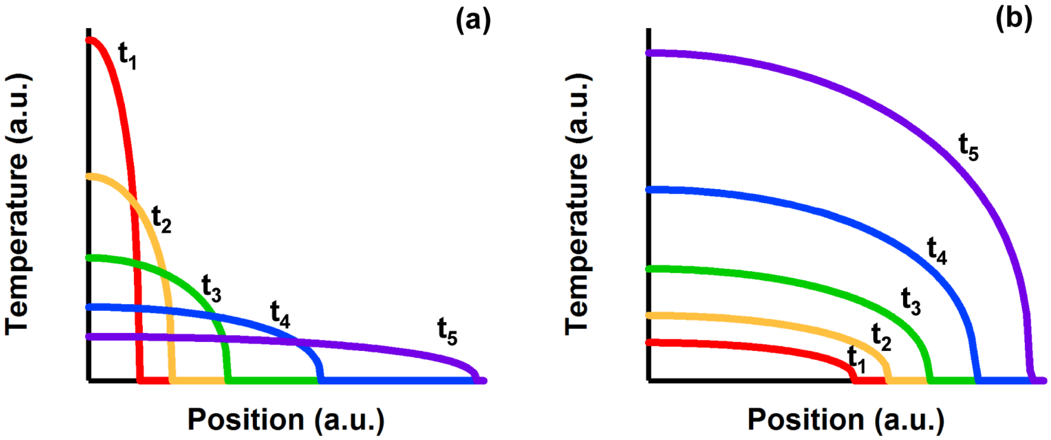

Figure 14. Plot showing self-similar heat wave propagation from an instantaneous planar source (a) and from a steady planar source (b) through a plasma.

$$
\begin{aligned}
Q &= \int_{-\infty}^{\infty} T dx \\
&= \frac{\mathrm{E}}{\rho c_p}
\end{aligned}
\tag{2.61}
$$

$$
x_f(t) = \xi_o \left(a Q^{5/2} t \right)^{2/9} \tag{2.62}
$$

$$
\xi_o = \left(\frac{\left(\frac{9}{2}\right)^{7/2} 2^{-3/2}}{\left(\frac{5}{2}\right) \pi^{5/4}} \right)^{2/9} \left(\frac{\Gamma\left(\frac{9}{10}\right)}{\Gamma\left(\frac{2}{10}\right)} \right)^{5/9} \tag{2.63}
$$

This solution shows that the heat front position x_f decays as $t^{2/9}$. E is the energy per unit area released at $t = 0$, T_c is the temperature at the origin (the solution is symmetric about $x = 0$), Γ is the mathematical gamma function, and x_f is the position of the heat front.

As a comparison, consider the case of one dimensional heat flow due to a steady planar heat source in time (Figure 14 b). This situation better approximates a steady long pulse laser drive of a shock wave. In the approximation that the temperature gradient is linear, we can estimate the gradient to be

$$
\nabla T \approx \frac{T}{x_f} \tag{2.64}
$$

Now we can simplify equation (2.46) to:

$$
S = a \left(k_B T_e \right)^n \frac{\left(k_B T_e \right)}{x_f} \tag{2.65}
$$

Using conservation of energy, we can set the heat energy equal to the ideal gas energy:

$$
S\ A\ t = \left(\frac{3}{2} n_e k_B T \right)_e \left(x_f A \right) \tag{2.66}
$$

S is the heat flux, t is time, A is the cross-sectional area, and x_f is the heat front position. Rearranging this equation to solve for the thermal energy gives:

$$k_B T_e = \frac{2}{3}\frac{St}{n_e x_f} \tag{2.67}$$

Plugging this expression into equation (2.65) and solving for the front position reveals:

$$x_f = \left(\frac{2}{3}\right)^{\frac{n+1}{n+2}} (a)^{1/(n+2)} (S)^{n/(n+2)} \left(\frac{t}{n_e}\right)^{\frac{n+1}{n+2}} \tag{2.68}$$

This solution shows that the heat front position in a plasma (n = 5/2) decays as $t^{7/9}$, which has a slower decay than the case of instantaneous heat input. It makes sense that the heat propagation will be more sustained in the case of steady heat input because energy is continually being added to the system.

We can set the heat front position equal to the shock front position to find the time that the shock waves catches up with the heat wave (Figure 15). This time can then be used with the shock velocity to find the position x_{cr} where the shock wave out-runs the heat wave. For a plasma with $n \approx 5/2$, this position is:

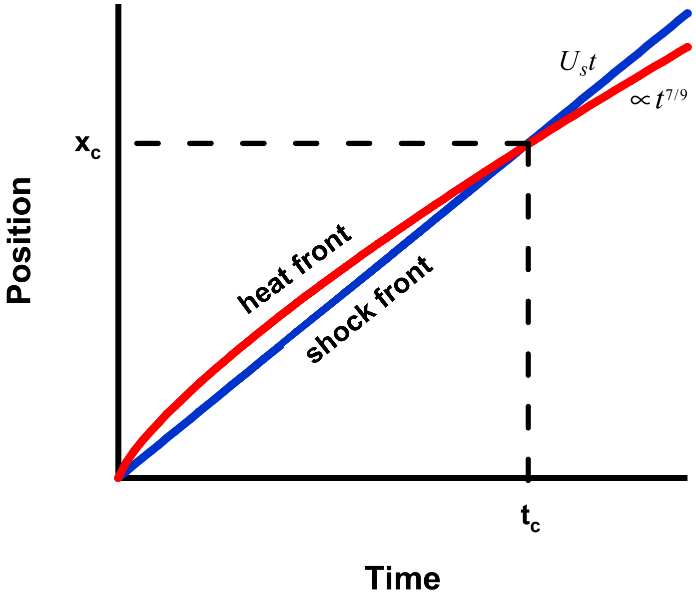

Figure 15. Illustration showing the shock wave overtaking the heat front.

$$x_{cr} = (2/3)^{7/2}(a)(S)^{5/2}(n_e U_s)^{-7/2} \tag{2.69}$$

As an example, assume we convert 20% of a laser ($I = 10^{13}\ \ W/cm^2$) into heat, driving a 10^4 m/s shock wave through solid density aluminum ionized to a charge state of three. In this case, $\ln\Lambda \approx 5$, $a \approx 4\times10^{69}$, $n_e = 2\times10^{29} m^{-3}$, and the crossing point is near 150 nm into the target. In contrast, if the laser intensity was $I = 10^{15}\ \ W/cm^2$ and $U_s = 20$ km/s, the critical depth would be around 0.5 µm. According to these self-similar solutions, the shock wave will not be traversing cold material until after it has overtaken the heat wave. Although these values are only rough estimates, they do illustrate the point that the heat front can affect an experiment performed at high intensities or with thin targets if the parameters are chosen improperly.

2.3.6 BLACKBODY RADIATION

As a material undergoes shock compression, not only are the density and pressure increased, but so is the temperature. In fact, many shock experiments measure the light emission from a material to estimate the temperature (Ng, Parfeniuk et al. 1985; Ng, Parfeniuk et al. 1985; Celliers, Ng et al. 1992; Löwer, Kondrashov et al. 1998). The basic connection between light emission and temperature of a heated body is related through the Planck equation for blackbody emission.

The Planck equation provides the amount of energy per unit volume per unit frequency interval radiated at equilibrium with a frequency ν (Zel'dovich and Raizer 1966).

$$U_\nu(\nu) = \frac{8\pi h\nu^3}{c^3}\frac{1}{e^{h\nu/k_B T} - 1} \tag{2.70}$$

We can convert this into wavelength space by multiplying by the differential of frequency ν.

$$d\nu = \frac{c}{\lambda^2} d\lambda \tag{2.71}$$

To find the radiated power per unit area from a surface at temperature *T*, multiply the above energy density by c/4.

$$I_\lambda(\lambda) = \frac{2hc}{\lambda^5} \frac{1}{e^{hc/\lambda k_B T} - 1} \tag{2.72}$$

This intensity per unit wavelength is plotted for several temperatures in (Figure 16). For reference later note that the radiation peaks at 266 nm for ~ 1 eV blackbodies (shown in orange).

It is often useful to locate the wavelength corresponding with the peak of the radiated intensity (Figure 17). This relation is known as Wein's Displacement law.

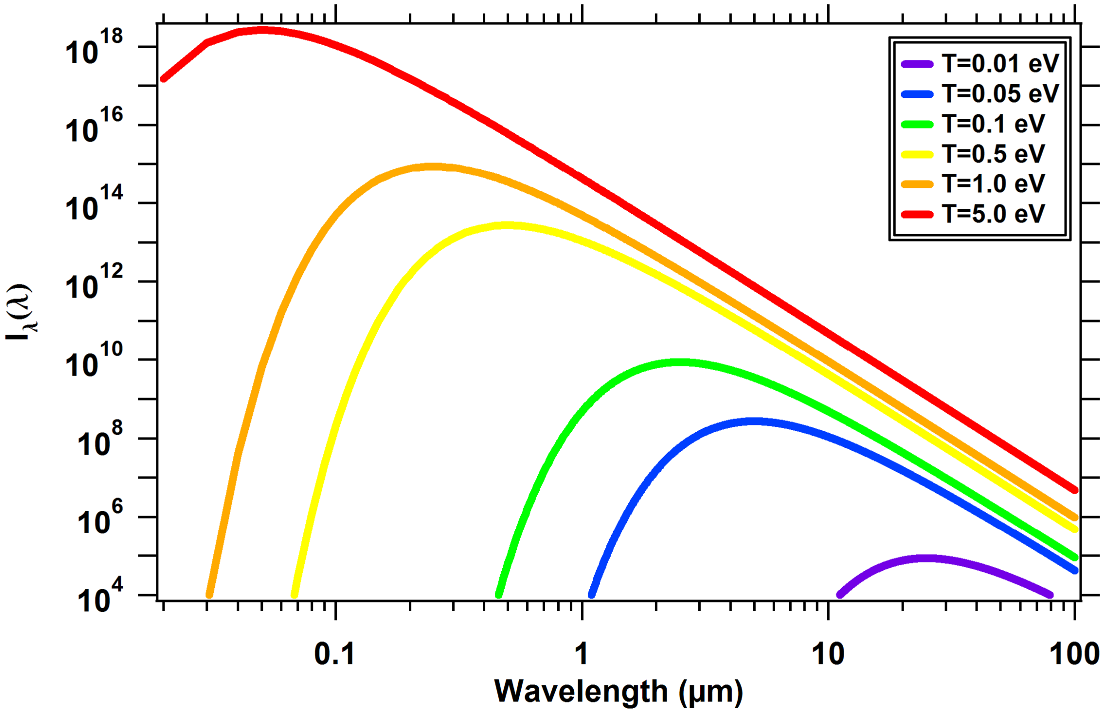

Figure 16. Radiation intensity curves for various blackbody temperatures

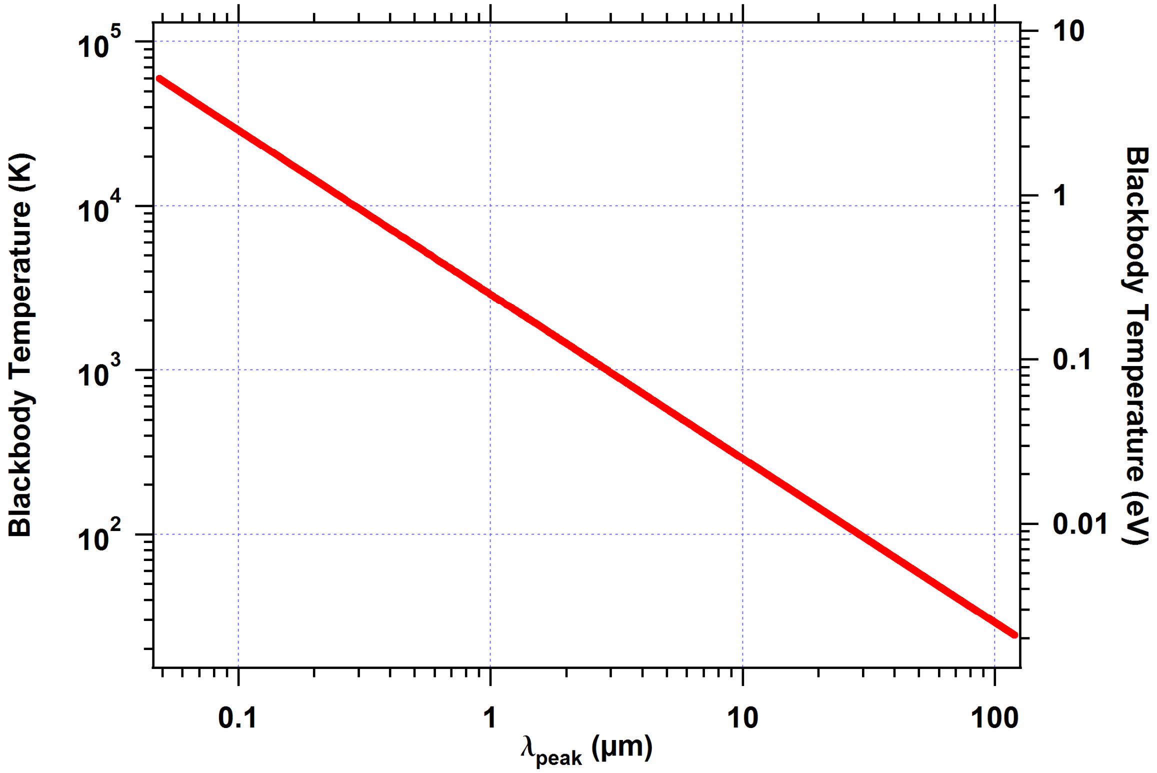

Figure 17. Wein's Displacement Law gives the wavelength of the peak of the radiation for a blackbody of given temperature.

$$\lambda_{peak} = \frac{2898[\mu m]}{T[K]} \tag{2.73}$$

From this relation, we see that a 1 eV blackbody does radiate most strongly at 250 nm. This fact, combined with a calculated temperature of ~ 13,000 K for silicon shocked to 1.5 Mbar (Ng and Ao 2003), indicates that there will be significant blackbody emission near the third harmonic of an 800 nm laser. This will be discussed further in Section 6.3.2.

CHAPTER 3. OPTICAL PROBING OF SURFACES

In this chapter, I discuss some of the linear and non-linear interactions at boundaries between dielectric materials. In particular, I derive Snell's law and the Fresnel equations that describe reflection and refraction, and then I extend this to second and third harmonic waves which use the non-linear forms those equations. Next I go through the derivation of second and third harmonic generation, primarily in the reflection geometry since that is the component I measure in my experiments. I then discuss the dielectric constant of a material, and how materials with a metallic behavior can often be modeled with a Drude model. Finally, I end with a discussion of previous research regarding linear and non-linear optical probing of laser-melted semiconductors. This discussion serves as a background for my own experiments which will be discussed in Chapter 5 and Chapter 6.

3.1 Linear Reflectivity

The interaction of electromagnetic radiation with interfaces between materials is an event that we experience every day. From the distortion of your hand behind a glass of water, to the glaring reflection of the sun off of a car hood, optical refraction and reflection play important roles in our lives. The following section discusses and derives several of the equations that govern such actions. The derivations primarily focus on waves in reflection to correspond with the diagnostics that will be discussed in Chapter 5.

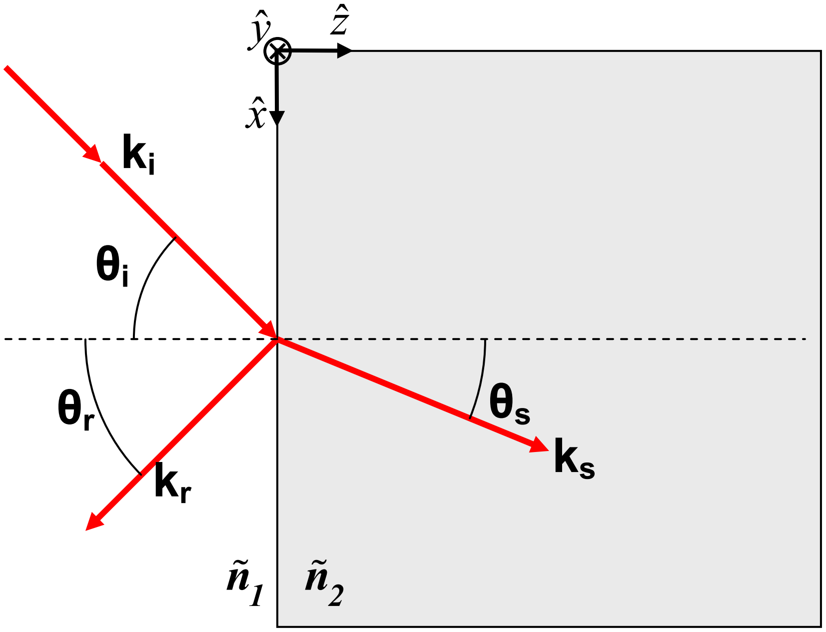

Figure 18. Diagram showing linear wave refraction and reflection at an interface.

3.1.1 DERIVATION OF SNELL'S LAW

Below, in Figure 18, is an illustration of an incident wave intersecting a linear material with index of refraction $\tilde{n}_2$. The angles, amplitudes and phases of the exiting waves depend on the input polarization, the input angle, and the indices of refraction, $\tilde{n}_1$ and $\tilde{n}_2$, for materials 1 and 2.

Waves at each wavelength must satisfy conservation of momentum at the boundary. Namely, the portions of the wave vectors parallel to the interface plane must be equal for each wavelength.

$$\begin{gathered} \vec{k}_i \cdot \hat{x} = \vec{k}_r \cdot \hat{x} = \vec{k}_s \cdot \hat{x} \\ k_i \sin(\theta_i) = k_r \sin(\theta_r) = k_s \sin(\theta_s) \end{gathered} \tag{3.1}$$

3.1.1.1 Linear Snell's Law and Fresnel Equations

Rewriting the wave vectors as,

$$\begin{aligned} k_i = k_r &= \tilde{n}_1(\omega)\frac{\omega}{c} \\ k_s &= \tilde{n}_2(\omega)\frac{\omega}{c} \end{aligned} \tag{3.2}$$

allows the simplification of equation (3.1) into the well known Snell's Law.

$$\tilde{n}_1(\omega)\sin(\theta_i) = \tilde{n}_2(\omega)\sin(\theta_s) \tag{3.3}$$

This equation relates the angles of reflection and refraction to the indices of refraction of the materials, however, it tells us nothing about the amplitudes of the waves.

To determine the amplitudes of the waves, we must use the Fresnel equations. These equations are used to relate the amplitudes of the outgoing waves at an interface to the incoming wave. That is, the reflected, E^R, and refracted or transmitted, E^T, wave amplitudes are related to the input wave amplitude, E^i, according to,

$$\begin{aligned} E^R &= E_\perp^{\ R} + E_{\|}^{R} \\ &= F_\perp^{\ L,R} E^i + F_{\|}^{L,R} E^i \end{aligned} \tag{3.4}$$

$$\begin{aligned} E^T &= E_\perp^{\ T} + E_{\|}^{T} \\ &= F_\perp^{\ L,T} E^i + F_{\|}^{L,T} E^i \end{aligned} \tag{3.5}$$

, where L indicates the linear Fresnel factor, and $\perp$ and $\|$ indicate the *s-polarized* and *p-polarized* components, respectively. The Fresnel equations for reflection of the fields are,

$$r_s = F_\perp^{\ L,R} = \frac{\tilde{n}_1(\omega)\cos(\theta_i) - \tilde{n}_2(\omega)\cos(\theta_s)}{\tilde{n}_1(\omega)\cos(\theta_i) + \tilde{n}_2(\omega)\cos(\theta_s)} \tag{3.6}$$

$$r_p = F_{\|}^{L,R} = \frac{\tilde{n}_1(\omega)\cos(\theta_s) - \tilde{n}_2(\omega)\cos(\theta_i)}{\tilde{n}_1(\omega)\cos(\theta_s) + \tilde{n}_2(\omega)\cos(\theta_i)} \tag{3.7}$$

, and the Fresnel equations for transmission of the fields are,

$$t_s = F_\perp^{\ L,T} = \frac{2\tilde{n}_1(\omega)\cos(\theta_i)}{\tilde{n}_1(\omega)\cos(\theta_i) + \tilde{n}_2(\omega)\cos(\theta_s)} \tag{3.8}$$

$$t_p = F_{\parallel}^{L,T} = \frac{2\tilde{n}_1(\omega)\cos(\theta_i)}{\tilde{n}_1(\omega)\cos(\theta_s) + \tilde{n}_2(\omega)\cos(\theta_i)} \tag{3.9}$$

See Section 3.3 for examples and plots using these equations.

3.1.1.2 Non-Linear Snell's Law

If we now look at the behavior of second harmonic waves generated at the interface, we find the so called non-linear Snell's Law equations. This derivation follows just as before, except for the changes in the definitions of the wave numbers.

$$\vec{k}_r^{\,2\omega} \cdot \hat{x} = \vec{k}_s^{\,2\omega} \cdot \hat{x} = 2\vec{k}_s^{\,1\omega} \cdot \hat{x} \tag{3.10}$$

Upon further simplification, these equations reduce to,

$$\tilde{n}_1(2\omega)\sin(\theta_r^{2\omega}) = \tilde{n}_1(\omega)\sin(\theta_i) \tag{3.11}$$

$$\tilde{n}_1(\omega)\sin(\theta_i) = \tilde{n}_2(2\omega)\sin(\theta_s^{2\omega}) \tag{3.12}$$

If we generate third harmonic (TH) in addition to second harmonic (SH), another identical set of equations will be produced if 3ω is substituted for 2ω in equations (3.11) and (3.12).

3.2 Harmonic Generation in Reflection Geometry

3.2.1 SECOND HARMONIC GENERATION AT AN INTERFACE

3.2.1.1 General Solution

Let us consider what happens when an electromagnetic wave of frequency ω_1 and wave vector $\vec{k}_1$ propagates in a non-linear medium. The non-linearity will couple the wave with itself and will generate a polarization wave at the harmonics of the fundamental frequency, $\omega_n = n\omega_1$ where *n=2,3…*, with a wave vector given by $\vec{k}_n = n\vec{k}_1$. The effective non-linear polarization source (NLS) term is defined by,

$$\vec{P}^{NLS}(2\omega_1) = \hat{p}P^{NLS}(\omega_2) = \chi(\omega_2 = 2\omega_1) : \vec{E}^T\vec{E}^T e^{i\left(\vec{k}_s\cdot\vec{r}-2\omega_1 t\right)} \tag{3.13}$$

To find the amplitude of the harmonic waves that are generated at an interface, we need to look at the equations governing the various waves. This derivation follows similar to that of (Bloembergen and Pershan 1962). Let's start with Maxwell's equations. In SI units, they are:

$$\nabla\times\vec{E} = -\mu\frac{\partial\vec{H}}{\partial u} \tag{3.14}$$

$$\nabla\times\vec{H} = J + \varepsilon\frac{\partial\vec{E}}{\partial t} \tag{3.15}$$

The non-linear susceptibility of medium 2 will give rise to a polarization at the harmonic frequencies.

$$\vec{k}_s = 2\vec{k}_{t,\omega_1} \tag{3.16}$$

To ease comparison with most of the existing literature, let us switch to CGS units and plug the source into Maxwell's equations, which become

$$\nabla\times\vec{E} = -\frac{\mu}{c}\frac{\partial^2\vec{H}}{\partial u^2} \tag{3.17}$$

$$\nabla\times\vec{H} = \frac{4\pi}{c}\frac{\partial\vec{P}^{NLS}}{\partial t} + \frac{\varepsilon}{c}\frac{\partial\vec{E}}{\partial t} \tag{3.18}$$

Next, we take the curl of equation (3.17) and plug in equation (3.18).

$$\nabla\times\nabla\times\vec{E}^{2\omega} + \frac{\varepsilon_2(2\omega)}{c^2}\frac{\partial^2\vec{E}^{2\omega}}{\partial t^2} = -\frac{4\pi}{c^2}\frac{\partial^2\vec{P}^{NLS}(2\omega)}{\partial t^2} \tag{3.19}$$

By using the following vector identity with Gauss' Law with zero charge density, we can simplify equation (3.19).

$$\nabla\times\nabla\times\vec{E} = \nabla\left(\nabla\cdot\vec{E}\right) - \nabla^2\vec{E} \tag{3.20}$$

$$\nabla\cdot\vec{E} = \frac{\rho}{\varepsilon} \tag{3.21}$$

If we assume a harmonic time dependence to the solution, we get:

$$\nabla^2\vec{E}^{2\omega} + \frac{\varepsilon_2(\omega_2)\omega_2^{\,2}}{c^2}\vec{E}^{2\omega} = -\frac{4\pi\omega_2^{\,2}}{c^2}\vec{P}^{NLS}(\omega_2)e^{i\left(\vec{k}_s\cdot\vec{r}-\omega_s t\right)} \tag{3.22}$$

This is the usual wave equation with a source added to the right hand side. The general solution will be of the form of the homogeneous solution plus a particular solution of the inhomogeneous equation (Bloembergen and Pershan 1962),

$$\begin{aligned}\vec{E}^{2\omega,T} &= \hat{e}_t A^{2\omega,T} e^{i\left(\vec{k}_t\cdot\vec{r}-\omega_2 t\right)} - \frac{4\pi\omega_2^{\,2}}{c^2}\frac{\vec{P}^{NLS}(\omega_2)}{\left|k_t\right|^2-\left|k_s\right|^2}\left(\hat{p}-\frac{\vec{k}_s\left(\vec{k}_s\cdot\hat{p}\right)}{\left|k_t\right|^2}\right)e^{i\left(\vec{k}_s\cdot\vec{r}-\omega_2 t\right)} \\ \vec{H}^{2\omega,T} &= \frac{c}{\omega_2}\left(\vec{k}_t\times\hat{e}_t\right)A^{2\omega,T}e^{i\left(\vec{k}_t\cdot\vec{r}-\omega_2 t\right)} - \frac{4\pi\omega_2^{\,2}}{c^2}\frac{\vec{P}^{NLS}(\omega_2)}{\left|k_t\right|^2-\left|k_s\right|^2}\frac{c}{\omega_2}\left(\vec{k}_s\times\hat{p}\right)e^{i\left(\vec{k}_s\cdot\vec{r}-\omega_2 t\right)}\end{aligned} \tag{3.23}$$

Here, $\hat{e}_t$ and $\hat{e}_r$ are the transmitted and reflected polarization vectors. The usual plane wave solution to the homogenous wave equation in vacuum is

$$\begin{aligned}\vec{E}^{2\omega,R} &= \hat{e}_r A^{2\omega,R} e^{i\left(\vec{k}_r\cdot\vec{r}-\omega_2 t\right)} \\ \vec{H}^{2\omega,R} &= \frac{c}{\omega_2}\left(\vec{k}_r\times\hat{e}_r\right)A^{2\omega,R}e^{i\left(\vec{k}_r\cdot\vec{r}-\omega_2 t\right)}\end{aligned} \tag{3.24}$$

In order to solve these equations, we need to satisfy the necessary boundary conditions at the linear / non-linear interface, as depicted in Figure 19. The input wave is labels with an *i,* “Source” waves at the fundamental frequency are labeled with an *s*, transmitted waves at the harmonic frequency are labeled with a *t*, and reflected waves at the harmonic frequency are labeled with an *r*.

3.2.1.2 Perpendicular Polarization

Let us first assume that our incoming beam is *s-polarized*. That is, $\vec{E} \parallel \hat{y}$, and $\vec{H}$ lies in the plane of incidence. This leads to the transmitted wave solution,

$$E_\perp^{\,2\omega,T} = A_\perp^{\,T} e^{i\left(\vec{k}_t\cdot\vec{r}\right)} + \frac{4\pi\omega_2^{\,2}}{c^2}\frac{\vec{P}^{NLS}(\omega_2)}{\left|k_s\right|^2-\left|k_t\right|^2}e^{i\left(\vec{k}_s\cdot\vec{r}\right)} \tag{3.25}$$

and the reflected wave solution,

$$E_\perp^{\,2\omega,R} = A_\perp^{\,R} e^{i\left(\vec{k}_r\cdot\vec{r}\right)} \tag{3.26}$$

where the following relations have been used.

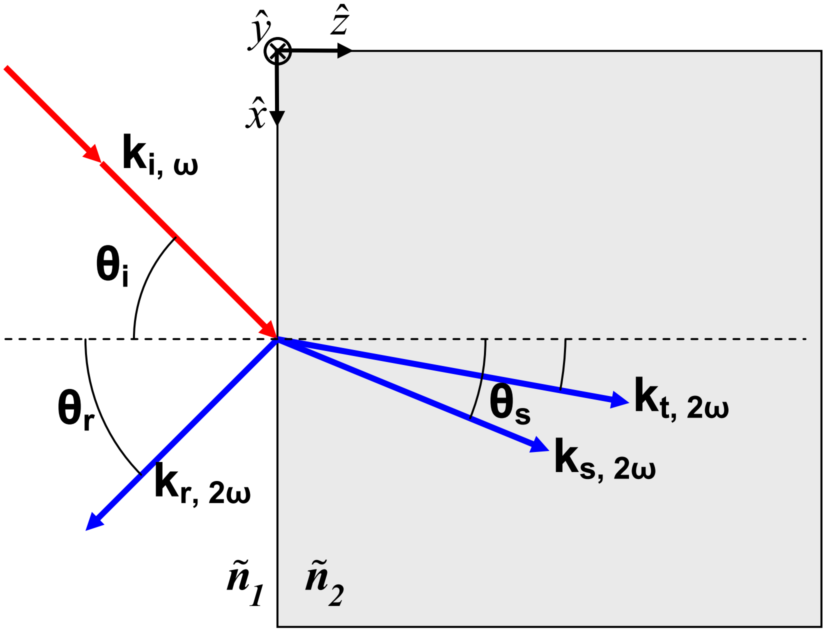

Figure 19. Diagram showing linear and non-linear wave refraction and reflection at an interface. This particular case is labeled for SHG, but it is identical for THG.

$$\begin{aligned} |k_t| &= \tilde{n}_2(\omega_2)\frac{\omega_2}{c} \\ |k_s| &= \tilde{n}_2(\omega_1)\frac{\omega_2}{c} \\ |k_r| &= \tilde{n}_1(\omega_2)\frac{\omega_2}{c} \end{aligned} \tag{3.27}$$

The complex index of refraction in the incident medium is $\tilde{n}_1$, while the complex index of refraction for the non-linear medium on the right hand side of Figure 19 is $\tilde{n}_2$

The boundary conditions at the interface require that the tangential components of E and H be continuous. Specifically, this means that $\vec{E}_y$ and $\vec{H}_x \propto \left(\vec{k}\times\vec{E}\right)_x$ be continuous. In equation form, these two requirements become, respectively,

$$E_\perp^{2\omega,R} = A_\perp^{T} + \frac{4\pi\omega_2^2}{c^2}\frac{\vec{P}_\perp^{NLS}(\omega_2)}{|k_s|^2-|k_t|^2} \tag{3.28}$$

$$-|k_r|E_\perp^{2\omega,R}\cos(\theta_r) = |k_t|A_\perp^{T}\cos(\theta_t) + |k_s|\frac{4\pi\omega_2^2}{c^2}\frac{\vec{P}_\perp^{NLS}(\omega_2)}{|k_s|^2-|k_t|^2}\cos(\theta_s) \tag{3.29}$$

Here, θ_t is the angle of the harmonic wave transmitted into material 2, θ_s is the angle of the transmitted fundamental wave, and θ_r is the angle of the reflected harmonic wave. Solve equation (3.28) for the homogenous solution, $A_\perp^{T}$, and plug it into equation (3.29). After some basic algebra, the following equation remains:

$$E_\perp^{2\omega,R} = \frac{4\pi\omega_2^2}{c^2}\frac{\vec{P}_\perp^{NLS}(\omega_2)}{|k_s|^2-|k_t|^2}\frac{k_t\cos(\theta_t)-k_s\cos(\theta_s)}{k_r\cos(\theta_r)+k_t\cos(\theta_t)} \tag{3.30}$$

Using equation (3.27), we finally get

$$\begin{aligned}E_\perp^{2\omega,R} &= \frac{4\pi\vec{P}_\perp^{NLS}(\omega_2)}{\varepsilon_s-\varepsilon_t}\frac{n_t\cos(\theta_t)-n_s\cos(\theta_s)}{n_r\cos(\theta_r)+n_t\cos(\theta_t)}\\ &= \frac{4\pi\vec{P}_\perp^{NLS}(\omega_2)}{|\tilde{n}_2(\omega)|^2-|\tilde{n}_2(2\omega)|^2}\frac{\tilde{n}_2(2\omega)\cos(\theta_t)-\tilde{n}_2(\omega)\cos(\theta_s)}{\tilde{n}_1(2\omega)\cos(\theta_r)+\tilde{n}_2(2\omega)\cos(\theta_t)}\end{aligned} \tag{3.31}$$

By plugging in a specific form of the non-linear source (equation (3.13)), we can simplify this equation so that it is dependent only on known quantities.

$$\begin{aligned}P_\perp^{NLS}(\omega_2) &= \chi(\omega_2)\left|E_\perp^{2\omega,T}\right|^2\\ &= \chi(\omega_2)\left(F_\perp^{L,T}(\theta_i)\right)^2\left|E_\perp^{1\omega,i}\right|^2\end{aligned} \tag{3.32}$$

$$\begin{aligned}E_\perp^{2\omega,R} &= \frac{4\pi\chi}{|\tilde{n}_2(\omega)|^2-|\tilde{n}_2(2\omega)|^2}\frac{\tilde{n}_2(2\omega)\cos(\theta_t)-\tilde{n}_2(\omega)\cos(\theta_s)}{\tilde{n}_1(2\omega)\cos(\theta_r)+\tilde{n}_2(2\omega)\cos(\theta_t)}\\ &\quad\times\left(\frac{2\tilde{n}_1(\omega)\cos(\theta_i)}{\tilde{n}_1(\omega)\cos(\theta_i)+\tilde{n}_2(\omega)\cos(\theta_s)}\right)^2\left|E_\perp^{1\omega,i}\right|^2\end{aligned} \tag{3.33}$$

$F_\perp^{L,T}(\theta_i)$ is the linear Fresnel equation for transmission from equation (3.8). We can simplify this solution one more step, to the form in (Bloembergen and Pershan 1962), by multiplying by $\tilde{n}_2(2\omega)\cos(\theta_t)-\tilde{n}_2(\omega)\cos(\theta_s)/\tilde{n}_2(2\omega)\cos(\theta_t)-\tilde{n}_2(\omega)\cos(\theta_s)$ and using equations (3.12) and (3.3) (Snell's Laws).

$$E_{\perp}^{2\omega,R} = \frac{4\pi\chi}{\tilde{n}_2(2\omega)\cos(\theta_t)+\tilde{n}_2(\omega)\cos(\theta_s)}\frac{1}{\tilde{n}_1(2\omega)\cos(\theta_r)+\tilde{n}_2(2\omega)\cos(\theta_t)} \times\left(\frac{2\tilde{n}_1(\omega)\cos(\theta_i)}{\tilde{n}_1(\omega)\cos(\theta_i)+\tilde{n}_2(\omega)\cos(\theta_s)}\right)^2\left|E_{\perp}^{1\omega,i}\right|^2 \tag{3.34}$$

The intensity of the reflected, s-polarized, second harmonic wave is,

$$I_{\perp}^{2w,R} = \left|E_{\perp}^{2w,R}\right|^2 \tag{3.35}$$

3.2.1.3 Parallel Polarization

Now, let's change our assumption to that of a *p-polarized* fundamental wave. That is, $\vec{H} \parallel \hat{y}$ and $\vec{E}$ lies in the plane of incidence (the x-z plane). In this situation, the equations are complicated by the fact that the non-linear polarization source is not required to be perpendicular to its wave vector. We will let α be the angle between $\vec{P}$ and $\vec{k}_s$ in the following equations, such that

$$\vec{P}_{\parallel}^{NLS} = P_{\parallel}^{NLS}\sin(\alpha)\hat{t} + P_{\parallel}^{NLS}\cos(\alpha)\hat{l} \tag{3.36}$$

where $\hat{t}$ and $\hat{l}$ lie in the x-z plane and are perpendicular and parallel to $\vec{k}_s$, respectively. Once again, we apply the boundary conditions ($\vec{E}_y$ and $\vec{H}_x \propto \left(\vec{k}\times\vec{E}\right)_x$ are continuous) to equations (3.23) and (3.24) to get:

$$\begin{aligned} -E_{\parallel}^{2\omega,R}\cos(\theta_r) &= A_{\parallel}^{2\omega,T}\cos(\theta_t) - \frac{4\pi\omega_2^2 P_{\parallel}^{NLS}(\omega_2)}{c^2}\left(\begin{aligned}&\frac{\sin(\alpha)\cos(\theta_s)}{|k_t|^2-|k_s|^2}\\ &+\frac{\cos(\alpha)\cos(\theta_s)}{|k_t|^2}\end{aligned}\right)\\ -|k_r|\,E_{\parallel}^{2\omega,R} &= -|k_t|\,A_{\parallel}^{2\omega,T} + |k_s|\frac{4\pi\omega_2^2 P_{\parallel}^{NLS}(\omega_2)}{c^2}\frac{\sin(\alpha)}{|k_t|^2-|k_s|^2}\end{aligned} \tag{3.37}$$

Following this, plug in the definitions of the various wave vectors to simplify the above equation.

$$\begin{aligned}-E_{\parallel}^{2\omega,R}\cos(\theta_r) &= A_{\parallel}^{2\omega,T}\cos(\theta_t) + 4\pi P_{\parallel}^{NLS}(\omega_2)\left(\begin{array}{c}\dfrac{\sin(\alpha)\cos(\theta_s)}{\varepsilon_s-\varepsilon_t}\\ -\dfrac{\cos(\alpha)\cos(\theta_s)}{\varepsilon_t}\end{array}\right)\\ -\tilde{n}_r E_{\parallel}^{2\omega,R} &= -\tilde{n}_t A_{\parallel}^{2\omega,T} - \tilde{n}_s 4\pi P_{\parallel}^{NLS}(\omega_2)\frac{\sin(\alpha)}{\varepsilon_s-\varepsilon_t}\end{aligned} \tag{3.38}$$

Eliminate $A_{\parallel}^{2\omega,T}$ from both equations using algebra, solve for $E_{\parallel}^{2\omega,R}$,then multiply by $\cos(\theta_t)/\cos(\theta_t)$ to finally arrive at,

$$\begin{aligned}E_{\parallel}^{2\omega,R} = &\frac{-4\pi P_{\parallel}^{NLS}(\omega_2)}{\varepsilon_s-\varepsilon_t}\left(\frac{\tilde{n}_t\cos(\theta_s)-\tilde{n}_s\cos(\theta_t)}{\tilde{n}_t\cos(\theta_r)+\tilde{n}_r\cos(\theta_t)}\right)\sin(\alpha)\\ &+\frac{4\pi P_{\parallel}^{NLS}(\omega_2)}{\varepsilon_t}\left(\frac{\tilde{n}_t\sin(\theta_s)}{\tilde{n}_t\cos(\theta_r)+\tilde{n}_r\cos(\theta_t)}\right)\cos(\alpha)\end{aligned} \tag{3.39}$$

Here, the dielectric constants and indices of refraction are related to the wave vectors by equation (3.27). In the case of an isotropic material (or a cubic material with only a small anisotropy), $\alpha = 90°$, which will get rid of the right hand side, and simplify the equation. We can plug in the non-linear source, along with $\alpha = 90°$, to simplify the equation to,

$$\begin{aligned}P_{\parallel}^{NLS}(\omega_2) &= \chi(\omega_2)\left|E_{\parallel}^{2\omega,T}\right|^2\\ &= \chi(\omega_2)\left(F_{\parallel}^{L,T}(\theta_i)\right)^2\left|E_{\parallel}^{1\omega,i}\right|^2\end{aligned} \tag{3.40}$$

$$\begin{aligned}E_{\parallel}^{2\omega,R} = &\frac{-4\pi\chi}{\left|\tilde{n}_2(\omega)\right|^2-\left|\tilde{n}_2(2\omega)\right|^2}\left(\frac{\tilde{n}_2(2\omega)\cos(\theta_s)-\tilde{n}_2(\omega)\cos(\theta_t)}{\tilde{n}_2(2\omega)\cos(\theta_r)+\tilde{n}_1(2\omega)\cos(\theta_t)}\right)\\ &\times\left(\frac{2\tilde{n}_1(\omega)\cos(\theta_i)}{\tilde{n}_1(\omega)\cos(\theta_s)+\tilde{n}_2(\omega)\cos(\theta_i)}\right)^2\left|E_{\parallel}^{1\omega,i}\right|^2\end{aligned} \tag{3.41}$$

The intensity of the reflected, p-polarized, second harmonic wave is,

$$I_{\parallel}^{2w,R} = \left|E_{\parallel}^{2w,R}\right|^2 \tag{3.42}$$

3.2.2 THIRD HARMONIC GENERATION AT AN INTERFACE

3.2.2.1.1 Non-linear Source Considerations

The derivation of third harmonic generation (THG) in the reflection geometry proceeds in a similar manner as SHG in the above section. The generalization of the NLS term from equation (3.13) is given by,

$$\vec{P}^{NLS}(3\omega_1) = \hat{p}P^{NLS}(\omega_3) = \chi\left(\omega_3 = 3\omega_1\right) : \vec{E}^T \vec{E}^T \vec{E}^T e^{i\left(\vec{k}_s \cdot \vec{r} - 2\omega_1 t\right)} \tag{3.43}$$

In general, the point group symmetry of the non-linear material imposes certain restrictions on the form of the susceptibility. That is, equation (3.43) must be invariant under the allowed symmetry operations of the medium. For cubic crystals having point symmetry 432, $\bar{4}3m \text{ or } m3m$, this results in a simplification to,

$$\vec{P}_i^{NLS} = 3C_{1122}E_i(\vec{E}\cdot\vec{E}) + \left(C_{1111} - 3C_{1122}\right)E_i^3 \tag{3.44}$$

For an isotropic material, $C_{1111} = 3C_{1122}$, it can be seen that a linearly polarized input electric field will produce a NLS wave that is also polarized in the same direction, with $\chi = 3C_{1122}$. As another special case, an *s-polarized* input wave oriented along the [001] direction of a (100) oriented cubic non-linear material will also produce a NLS wave that is polarized in the same direction, but this time with $\chi = C_{1111}$.

As an example of a more complicated situation, let us consider the case of a *p-polarized* input wave incident upon a crystal whose axes are oriented along the x, y, z axes. This situation is depicted in Figure 20. The fundamental electric field inside the medium is written as,

$$\vec{E}^{1\omega,T} = E_{\|}^{1\omega,i}\cos\left(\theta_t\right)\hat{x} + 0\hat{y} + E_{\|}^{1\omega,i}\sin\left(\theta_t\right)\hat{z} \tag{3.45}$$

The NLS components are found by combining the transmitted electric field with equation (3.44).

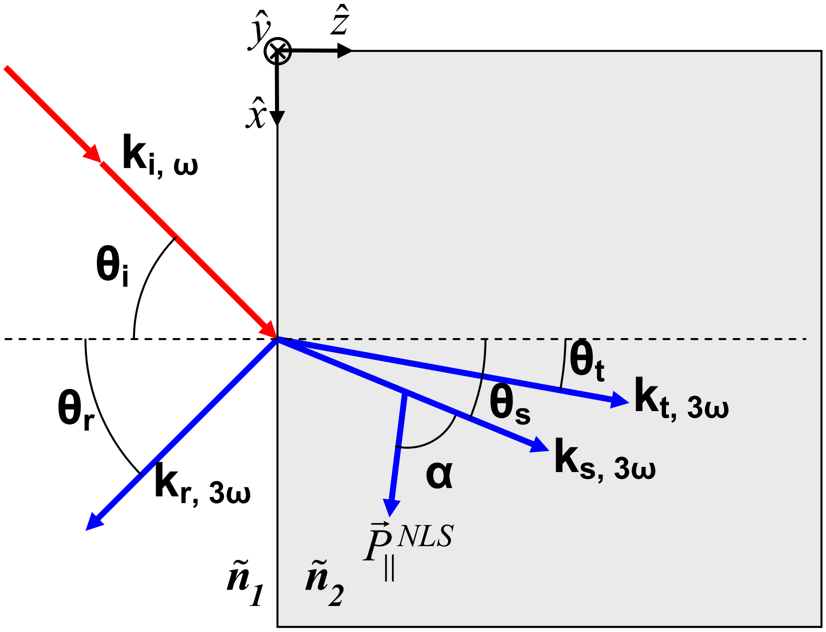

Figure 20. Diagram showing linear and non-linear wave refraction and reflection at an interface. The third harmonic waves are shown, along with the non-linear polarization source.

$$\begin{aligned}
&\vec{P}_{\parallel}^{NLS}\cdot\hat{x} = 3C_{1122}\left(E_{\parallel}^{1\omega,i}\right)^{3}\cos\left(\theta_t\right)+(C_{1111}-3C_{1122})\left(E_{\parallel}^{1\omega,i}\right)^{3}\left(\cos\left(\theta_t\right)\right)^{3}\\
&\vec{P}_{\parallel}^{NLS}\cdot\hat{y} = 0\\
&\vec{P}_{\parallel}^{NLS}\cdot\hat{z} = 3C_{1122}\left(E_{\parallel}^{1\omega,i}\right)^{3}\sin\left(\theta_t\right)+(C_{1111}-3C_{1122})\left(E_{\parallel}^{1\omega,i}\right)^{3}\left(\sin\left(\theta_t\right)\right)^{3}
\end{aligned} \tag{3.46}$$

Again, let α be the angle between $\vec{P}_{\parallel}^{NLS}$ and $\vec{k}_s$, which allows us to write,

$$\begin{aligned}
P_{\parallel}^{NLS}\sin\left(\alpha\right) &= \vec{P}_{\parallel}^{NLS}\cdot\hat{x}\cos\left(\theta_t\right)+\vec{P}_{\parallel}^{NLS}\cdot\hat{z}\sin\left(\theta_t\right)\\
P_{\parallel}^{NLS}\cos\left(\alpha\right) &= \vec{P}_{\parallel}^{NLS}\cdot\hat{x}\sin\left(\theta_t\right)-\vec{P}_{\parallel}^{NLS}\cdot\hat{z}\cos\left(\theta_t\right)
\end{aligned} \tag{3.47}$$

By plugging equations (3.45) and (3.46) into equation (3.47) and using trigonometric identities, we can relate the NLS to the input parameters according to,

$$\begin{aligned} P_{\parallel}^{NLS}\sin\left(\alpha\right) &= \left(3C_{1122}+(C_{1111}-3C_{1122})\frac{\left(3+\cos\left(4\theta_t\right)\right)}{4}\right)\left(E_{\parallel}^{1\omega,i}\right)^3 \\ P_{\parallel}^{NLS}\cos\left(\alpha\right) &= \left((C_{1111}-3C_{1122})\frac{\left(\sin\left(4\theta_t\right)\right)}{4}\right)\left(E_{\parallel}^{1\omega,i}\right)^3 \end{aligned} \tag{3.48}$$

3.2.2.2 Linearly Polarized Input

To derive the THG equations, the following relations must be altered from their definitions given in the SHG section.

$$\begin{aligned} 2\omega &\rightarrow 3\omega \\ \omega_2 &\rightarrow \omega_3 \end{aligned} \tag{3.49}$$

$$\vec{k}_s = 3\vec{k}_{t,\omega_1} \tag{3.50}$$

$$\begin{aligned} P_{\parallel}^{NLS}(\omega_3) &= \chi\left(\omega_3\right)\left|E_{\parallel}^{3\omega,T}\right|^3 \\ &= \chi\left(\omega_3\right)\left(F_{\parallel}^{L,T}\left(\theta_i,\alpha\right)\right)^3\left|E_{\parallel}^{1\omega,i}\right|^3 \end{aligned} \tag{3.51}$$

$$\begin{aligned} P_{\perp}^{NLS}(\omega_3) &= \chi\left(\omega_3\right)\left|E_{\perp}^{2\omega,T}\right|^3 \\ &= \chi\left(\omega_3\right)\left(F_{\perp}^{L,T}\left(\theta_i\right)\right)^3\left|E_{\perp}^{1\omega,i}\right|^3 \end{aligned} \tag{3.52}$$

The intensity of the reflected, s-polarized, third harmonic wave from an s-polarized input wave is,

$$\begin{aligned} I_{\perp}^{3\omega,R} = &\left(\frac{4\pi\left|\chi\right|}{\tilde{n}_2\left(3\omega\right)\cos\left(\theta_t\right)+\tilde{n}_2\left(\omega\right)\cos\left(\theta_s\right)}\right)^2 \\ &\times\left(\frac{1}{\tilde{n}_1\left(3\omega\right)\cos\left(\theta_r\right)+\tilde{n}_2\left(3\omega\right)\cos\left(\theta_t\right)}\right)^2 \\ &\times\left(\frac{2\tilde{n}_1\left(\omega\right)\cos(\theta_i)}{\tilde{n}_1\left(\omega\right)\cos(\theta_i)+\tilde{n}_2\left(\omega\right)\cos(\theta_s)}\right)^6\left|E_{\perp}^{1\omega,i}\right|^6 \end{aligned} \tag{3.53}$$

For conceptualization, this can be thought of as a combination of linear and non-linear Fresnel factors.

$$I_{\perp}^{3\omega,R} = 16\pi^2\left|\chi\right|^2\left|F_{\perp}^{NL,R}\left(\theta_i\right)\right|^2\left|F_{\perp}^{L,T}\left(\theta_i\right)\right|^6\left|E_{\perp}^{1\omega,i}\right|^6 \tag{3.54}$$

The intensity of the reflected, p-polarized, third harmonic wave from a p-polarized input wave is incident upon an isotropic material and is given by,

$$I_{\parallel}^{3\omega,R}=\left(\frac{4\pi|\chi|}{\tilde{n}_2(3\omega)\cos(\theta_s)+\tilde{n}_2(\omega)\cos(\theta_t)}\right)^2$$
$$\times\left(\frac{1}{\tilde{n}_2(3\omega)\cos(\theta_r)+\tilde{n}_1(3\omega)\cos(\theta_t)}\right)^2$$
$$\times\left(\frac{2\tilde{n}_1(\omega)\cos(\theta_i)}{\tilde{n}_1(\omega)\cos(\theta_s)+\tilde{n}_2(\omega)\cos(\theta_i)}\right)^6\left|E_{\parallel}^{1\omega,i}\right|^6 \tag{3.55}$$

As expected, at normal incidence, $\theta_i=\theta_r=\theta_t=\theta_s=0$, and equations (3.53) and (3.55) reduce to the same value.

3.2.2.3 Circularly Polarized Input

Let us assume that a right circularly polarized wave is normally incident upon a (100) oriented, cubic non-linear material. The incident electric field can be written as,

$$\vec{E}=E_o\hat{x}+iE_o\hat{y} \tag{3.56}$$

The non linear polarization source from the generalization of equation (3.13) is,

$$\vec{P}_i^{NLS}=3C_{1122}E_i(\vec{E}\cdot\vec{E})+(C_{1111}-3C_{1122})E_i^3 \tag{3.57}$$

After plugging in our circularly polarized incident beam, we have ,

$$\vec{E}\cdot\vec{E}=E_o^2-E_o^2=0 \tag{3.58}$$

$$\vec{P}^{NLS}=(C_{1111}-3C_{1122})E_o^3(\hat{x}-i\hat{y}) \tag{3.59}$$

However, for an isotropic material, $C_{1111}=3C_{1122}$, which shows that we will have no third harmonic generation. If the material is anisotropic, $C_{1111}\neq 3C_{1122}$, THG is allowed.

In the anisotropic case, we can explain the allowance of THG in the following manner (Burns 1971). Each 3ω photon that is generated annihilates three 1ω photons. That is, the net change in angular momentum is,

$$\begin{aligned}\Delta m &= \left|+3\hbar - (-\hbar)\right| \\ &= \left|4\hbar\right|\end{aligned} \tag{3.60}$$

Angular momentum of the system must be conserved, so it is taken up by the crystal lattice (Simon and Bloembergen 1968). But, the (100) oriented cubic lattice can only absorb angular momentum in units of $4\hbar$ because of the four-fold symmetry of the problem. If we were incident upon a (111) face, there is only a three fold axis of symmetry, and angular momentum can only be absorbed in units of $3\hbar$. This explains why THG is disallowed from (111) orientations of cubic materials, but it is allowed for (100) orientations. In contrast, SHG using circularly polarized light is allowed for (111), but disallowed for (100) because of the quanta of angular momenta that the crystal is allowed to absorb.

The above mentioned loss of THG in an isotropic material can be exploited to characterize the anisotropy of a cubic material. In other words, if a crystalline (anisotropic) material somehow becomes isotropic, the THG signal will disappear. This is the rational behind the experiments described in Chapter 5 and Chapter 6, as well as previously published studies (Wang, Bomback et al. 1986; Yakovlev and Govorkov 2001; Gundrum, Averback et al. 2007).

3.3 Dielectric Constant

The Fresnel equations derived in the previous section relate the material index of refraction to the polarization, angle of incidence, and the reflectivity of electromagnetic waves striking the material. However, in an experiment, we often measure the reflectivity, polarization, and the angle with the intent of reconstructing the index of refraction. In general, the index of refraction at each wavelength is a complex number composed of a real and an imaginary part. This makes it impossible to determine both parts with only one measurement. One method around this problem is to describe the index of refraction with a single parameter.

3.3.1 DRUDE MODEL

The particular parameterization we will explore is the modified Drude model, which expresses the complex dielectric function as a function of frequency.

$$\varepsilon(\omega) = 1 + \chi_{interband}(\omega) + \chi_{Drude}(\omega) \tag{3.61}$$

Here, $\chi_{\mathrm{int}\,erband}(\omega)$ represents the contribution of interband transitions to the dielectric constant and is equal to the dielectric constant of the material in the absence of any excitations. $\chi_{Drude}(\omega)$ represents the contribution due to the effect of free carriers (electrons and holes) in the material. To derive the Drude contribution, we consider the motion of a free electron with charge *e* and momentum $\vec{p}$ in the presence of an applied electric field *E*. The equation of motion is

$$\frac{d\vec{p}}{dt} = -\frac{\vec{p}}{\tau} - e\vec{E} \tag{3.62}$$

This equation assumes that an electron will collide and lose its momentum in an average time τ. Assuming the electric filed oscillates with frequency ω, the solution becomes,

$$\vec{p}(\omega) = \frac{-e\vec{E}(\omega)}{-i\omega + \frac{1}{\tau}} \tag{3.63}$$

We can relate the electron motion to the current generated by the electrons.

$$\vec{J} = -N_e e \frac{\vec{p}}{m_e} = \sigma(\omega)\vec{E} \tag{3.64}$$

Using Maxwell's equation in SI units (equation (3.15)),

$$
\begin{aligned}
\nabla\times\vec{H} &= \sigma\vec{E}+\varepsilon_o\frac{\partial\vec{E}}{\partial t} \\
&= \sigma\vec{E}-i\omega\varepsilon_o\vec{E} \\
&= -i\omega\left(\frac{\sigma}{-i\omega}+\varepsilon_o\right)\vec{E} \\
&= -i\omega\varepsilon\vec{E}
\end{aligned}
\tag{3.65}
$$

we can find the dielectric constant of the material.

$$
\begin{aligned}
\varepsilon &= \varepsilon_o+\frac{i\sigma}{\omega} \\
&= \varepsilon_o\left(1+\frac{i\sigma}{\varepsilon_o\omega}\right) \\
&= \varepsilon_o\left(1+\chi\right)
\end{aligned}
\tag{3.66}
$$

The electrical conductivity of the material, $\sigma(\omega)$, is related to the susceptibility χ by,

$$
\chi(\omega)=\frac{i\sigma(\omega)}{\varepsilon_o\omega}=-\frac{N_e e^2}{\varepsilon_o m_e\omega^2}\left(\frac{1}{1+\frac{i}{\omega\tau}}\right)
\tag{3.67}
$$

This is simply the Drude contribution, which can be re-written as

$$
\begin{aligned}
\chi_{Drude} &= -\left(\frac{\omega_p}{\omega}\right)^2\frac{1}{1+\frac{i}{\omega\tau}} \\
&= -\frac{\omega_p{}^2\tau^2}{1+\omega^2\tau^2}+i\frac{\omega_p{}^2\tau}{\omega\left(1+\omega^2\tau^2\right)}
\end{aligned}
\tag{3.68}
$$

The plasma frequency, ω_p, is the resonant oscillation frequency of the free electrons.

$$
\omega_p=\sqrt{\frac{N_{e,h}e^2}{\varepsilon_o m_e}}
\tag{3.69}
$$

The number density of free carriers is given by $N_{e,h}$, the electron mass is m_e, the electron charge is e, and the permittivity of free space is ε_o. A “Drude metal” is a material that is dominated by free carriers, instead of by interband transitions, so the dielectric function becomes

Table 2. Index of refraction data used in this dissertation for gallium arsenide, silicon, and amorphous silicon. The cold data comes from Palik while the Drude model parameters are discussed in the text.

		GaAs			**Si**			**a-Si**		
		800nm	**400nm**	**266nm**	**800nm**	**400nm**	**266nm**	**800nm**	**400nm**	**266nm**
Cold	**n**	*3.682*	*4.373*	*3.67*	*3.692*	*5.57*	*1.831*	*3.89*	*4.275*	*2.00*
	k	*0.086*	*2.146*	*3.32*	*0.006*	*0.387*	*4.426*	*0.13*	*2.20*	*2.90*
Drude	**n**	*2.770*	*1.340*	*0.780*	*3.802*	*1.767*	*0.988*			
	k	*4.200*	*2.809*	*2.015*	*6.029*	*4.055*	*2.960*			

$$\varepsilon(\omega) = 1 - \frac{\omega_p{}^2\tau^2}{1+\omega^2\tau^2} + i\frac{\omega_p{}^2\tau}{\omega\left(1+\omega^2\tau^2\right)} \tag{3.70}$$

The dielectric function is the square of the complex index of refraction, which can be separated into real and imaginary parts.

$$\begin{aligned} \varepsilon(\omega) &= \tilde{n}(\omega)^2 \\ &= \left(n(\omega) + ik(\omega)\right)^2 \\ &= \left(n(\omega)^2 - k(\omega)^2\right) + i\left(2n(\omega)k(\omega)\right) \end{aligned} \tag{3.71}$$

Using the above formulas, we can now relate the real and imaginary parts of the index of refraction to the measured parameters, assuming the optical response of the material under consideration is dominated by free carriers.

As an example, Figure 21 plots the tabulated index of refraction (Palik 1985) and a Drude model for silicon, assuming τ=212 fs, and ω_p=2.523x10^{16} s^{-1} (Li and Fauchet 1987). The linear Fresnel formulas have been combined with the Drude model to produce Figure 22, which shows the reflectivity of cold and molten Si at 800 nm. As silicon melts, it becomes more metallic (using the Drude model) and thus reflects more of the 800 nm probe. It is instructive to look at the ratio of the two curves in Figure 22, which give the reflectivity of the melted silicon normalized to that of cold silicon. This ratio can then be compared to experimental results, as will be described in Chapter 6.

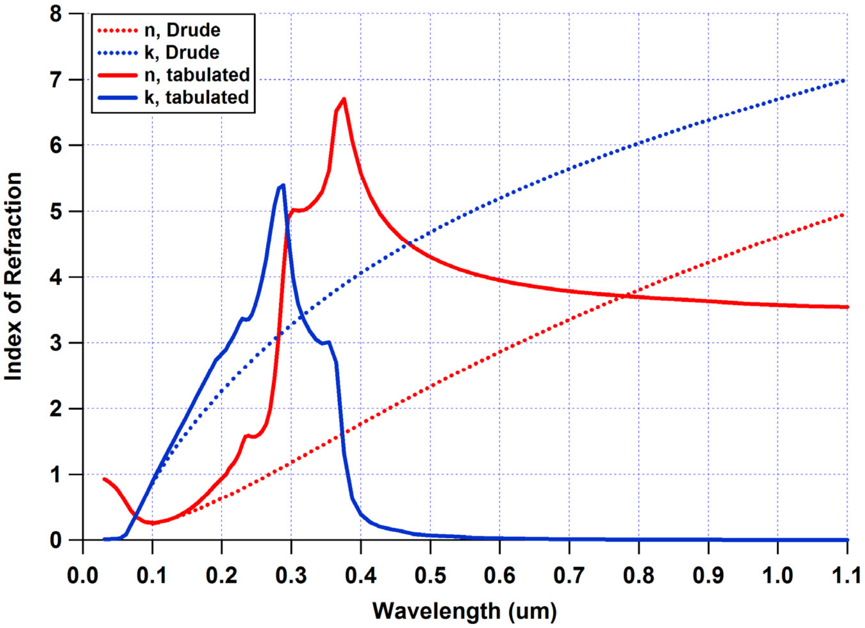

Figure 21. Plot showing the real (red) and imaginary (blue) portions of the index of refraction for silicon. Tabulated values from Palik (solid) are compared with values from a Drude model (dotted).

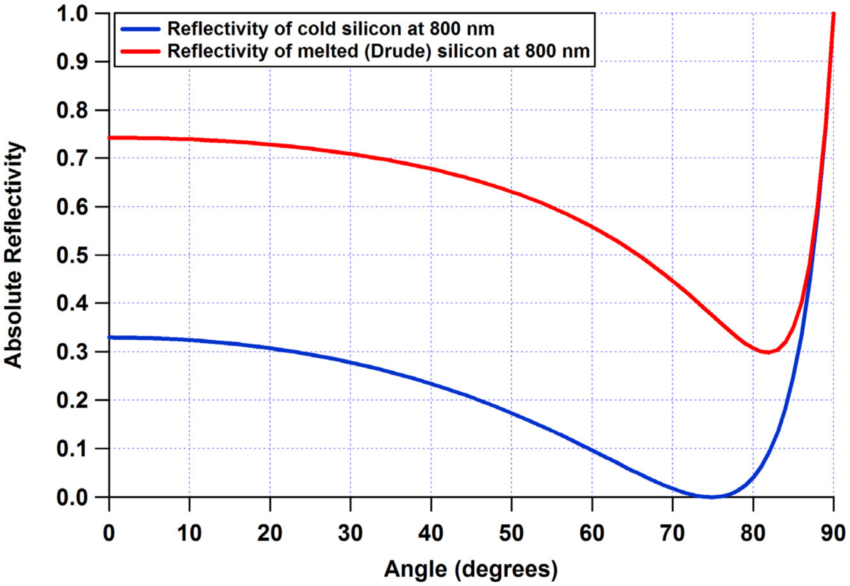

Figure 22. The reflectivity of cold (blue) and melted (red) silicon is shown as a function of probe angle.

3.3.2 SKIN DEPTH

As mentioned in the previous section, the index of refraction has both a real and imaginary component. As shown in equation (3.24), the electric field has spatial and temporal dependence.

$$\vec{E}\left(\vec{r},t\right)=\hat{e}Ae^{i\left(\vec{k}\cdot\vec{r}-\omega t\right)} \tag{3.72}$$

Since the wave vector k_1 is proportional to the index of refraction $\tilde{n}=n+ik$, any imaginary portion will cause the wave amplitude to decay.

$$\left|k_1\left(\omega\right)\right|=\frac{\tilde{n}\left(\omega\right)\omega}{c} \tag{3.73}$$

$$\begin{aligned} E &= Ae^{i\left(\frac{\tilde{n}(\omega)\omega x}{c}-\omega t\right)} \\ &= Ae^{i\left(\frac{n(\omega)\omega x}{c}+\frac{ik(\omega)\omega x}{c}-\omega t\right)} \\ &= Ae^{-\left(\frac{k(\omega)\omega x}{c}\right)}e^{i\left(\frac{n(\omega)\omega x}{c}-\omega t\right)} \end{aligned} \tag{3.74}$$

The intensity of the wave is proportional to the square of the field, so the intensity will decay as:

$$\begin{aligned} I(x) &= I_o e^{-\alpha x} \\ \alpha &= \frac{2k\left(\omega\right)\omega}{c} \end{aligned} \tag{3.75}$$

where α is known as the absorption. The intensity will decrease by 1/e after the wave propagates a distance $x=1/\alpha$. This distance is known as the skin depth, and it is plotted for various materials in Figure 23. Notice that Si and GaAs are much less absorbing in the IR than Al. However, in the UV, the semiconductors act like a metal and have short skin depths. This concept helps to explain the decrease in THG signal in Section 6.3.1.

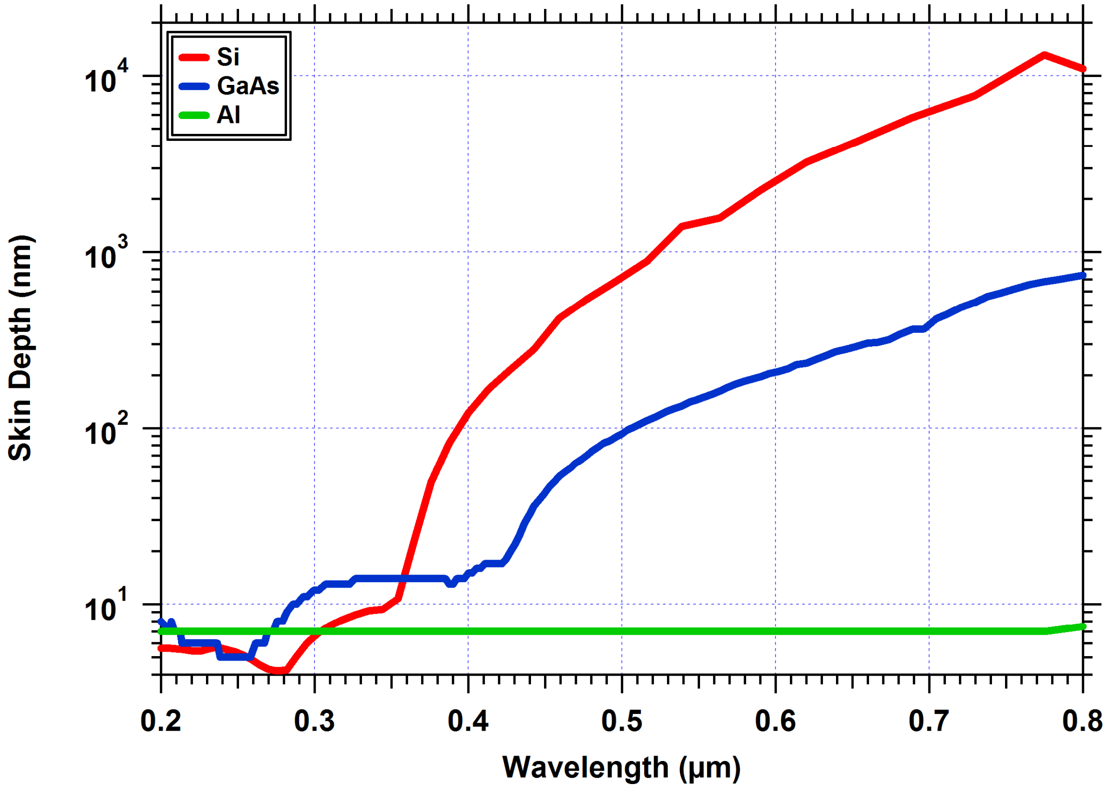

Figure 23. Plot of the skin depths for Si, GaAs, and Al

3.4 Probing of Laser-Melted Semiconductors

3.4.1 HARMONIC GENERATION

Harmonic generation (HG) is a powerful technique for probing long-range crystalline order. In particular, HG can help identify the dynamics that occur upon laser-induced melting. In pump probe experiments, second harmonic generation (SHG) has been used to identify a transformation of crystalline GaAs to a centrosymmetric electronic state within 100 fs (Saeta, Wang et al. 1991). It has also been used to discover a loss of cubic order in crystalline silicon within 150 fs of intense laser excitation (Tom, Aumiller et al. 1988). Tom, *et. al.* discovered that 75 fs laser excitation of silicon above a threshold fluence causes bulk atomic disorder with a 1/e time constant of ~ 100 fs . In contrast, they found that the electronic properties, as determined by linear reflectivity, did not reach those of molten silicon for several hundred femtoseconds. This indicated that silicon was melting non-thermally before the lattice had time to thermally equilibrate. The dense electron-hole plasma created by the ultra-fast optical excitation weakens the atomic bonds, causing disorder in the lattice. This non-thermal process skips the "normal" thermal transfer of energy from the electronic system to the lattice by phonon emission., as the atoms remain cold for several hundred femtoseconds or more (Sokolowski-Tinten and von der Linde 2000; Kim 2001).

For many materials and crystallographic orientations, SHG is not dipole allowed in the bulk material, so detection of the small surface generated signals can be very difficult, especially for single shot type experiments (Tom, Aumiller et al. 1988). For this reason, we are exploring the ultra-fast third harmonic (TH) response of materials under femtosecond excitation. THG is bulk-allowed in most crystalline materials, but disappears in isotropic media with circularly polarized excitation, as discussed in Section 3.2.2.3 (Burns and Bloembergen 1971). It is this change in THG that I explore in my experiments, and I use this technique to detect order/disorder transitions in shocked materials.

3.4.2 REFLECTIVITY

As discussed in the sections above, the linear reflectivity is sensitive to the electronic structure of materials. In particular, the reflectivity of semiconductors changes quite noticeably upon melting due to a large change in the index of refraction. This change is caused by the excitation of electrons into the conduction band, which produces a metallic-like state. The real and imaginary parts of the index of refraction for Si are

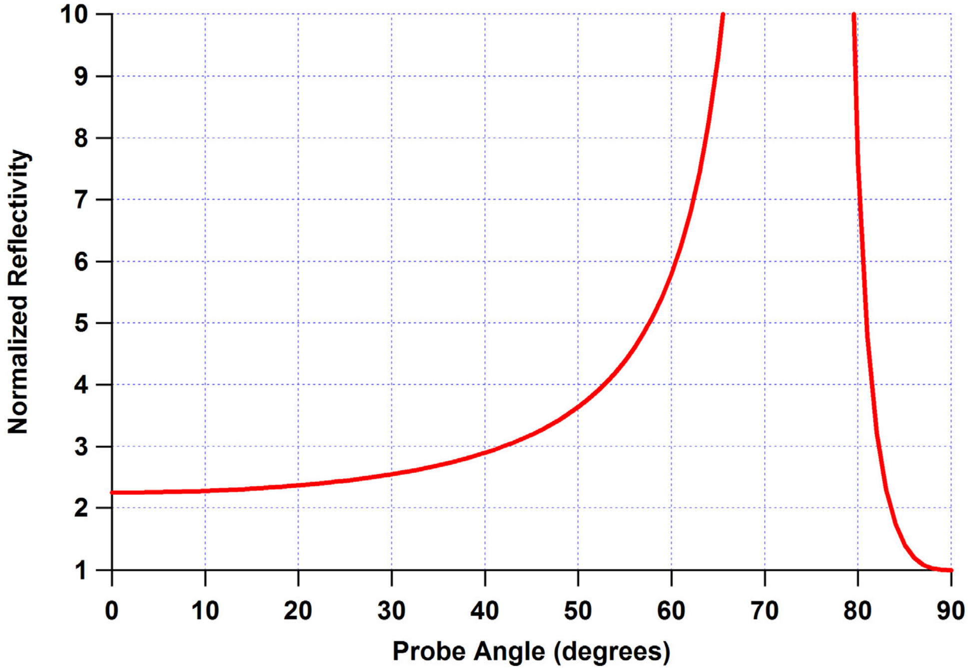

Figure 24. The ratio of the reflectivity of melted silicon (Drude model) to cold silicon is shown as a function of probe angle for 800 nm. The resonance effect is due to the loss of reflection at Brewster's angle for the cold material.

shown in Figure 21. Combining this data with the Fresnel equations produces the reflectivity curves in Figure 22. Division of the melted (Drude) reflectivity by the “cold” reflectivity produces a plot of normalized reflectivity at 800 nm as a function of angle (Figure 24). Notice for comparison with results later that the calculated reflectivity is 5.28 times larger than the reference “cold” silicon, while at normal incidence, the reflectivity is 2.26 times larger.

GaAs is not well modeled by a Drude model under all excitation levels. However, at pump fluences greater that ~ 80 mJ/cm^2, the parameters $\omega_p = 1.83\times10^{16}$ s^{-1} and $\tau = 0.2$ fs match ellipsometric data, indicating that the Drude model is acceptable for calculating the dielectric constant (Huang, Callan et al. 1998). Using these parameters, the index of refraction can be calculated (Figure 25), and the normalized reflectivity for strongly excited GaAs can be found by way of the Fresnel equations (Figure 26). Other Drude parameters reported in the literature (Table 3) lead to slightly different indices of refraction which only affect the reflectivity by < ±4% at the listed angles (Huang, Callan et al. 1998; Temnov, Sokolowski-Tinten et al. 2006).

It is these normalized reflectivities for melted Si and GaAs that I will compare with the experimental results in Section 6.3.1. In particular, the Fresnel equations combined with Drude modes predict the reflectivity values for Si and GaAs to increase by factors of 2.26 and 2.02 at normal incidence, and by factors of 5.28 and 4.32 at 58.5° off of normal.

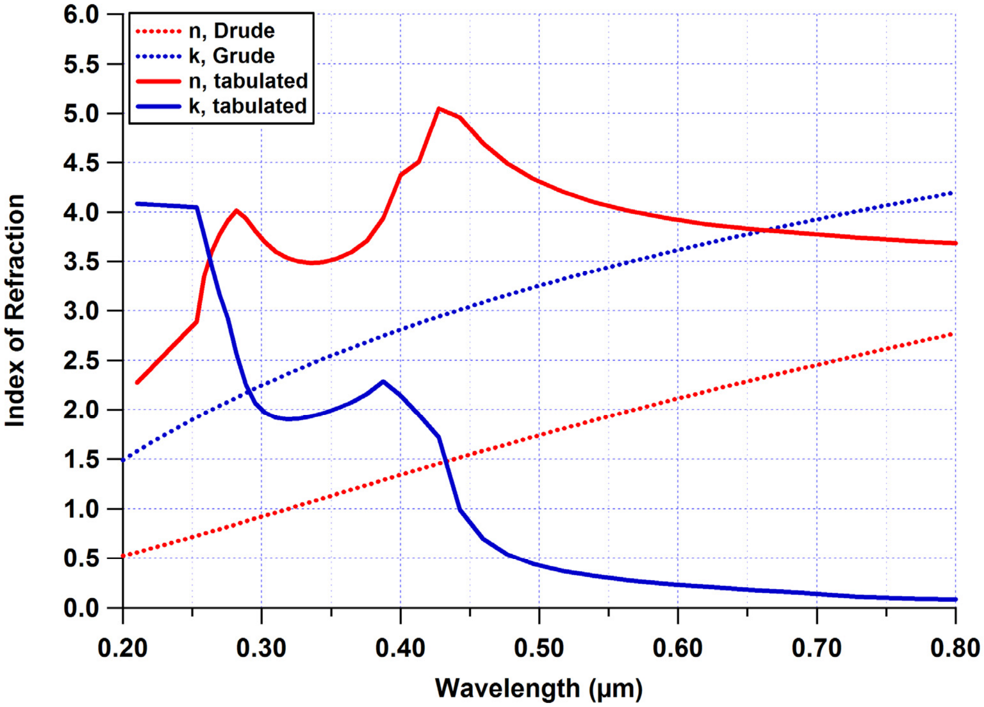

Figure 25. Plot showing the real (red) and imaginary (blue) portions of the index of refraction for GaAs. Tabulated values (solid) are compared with values from a Drude model (dotted).

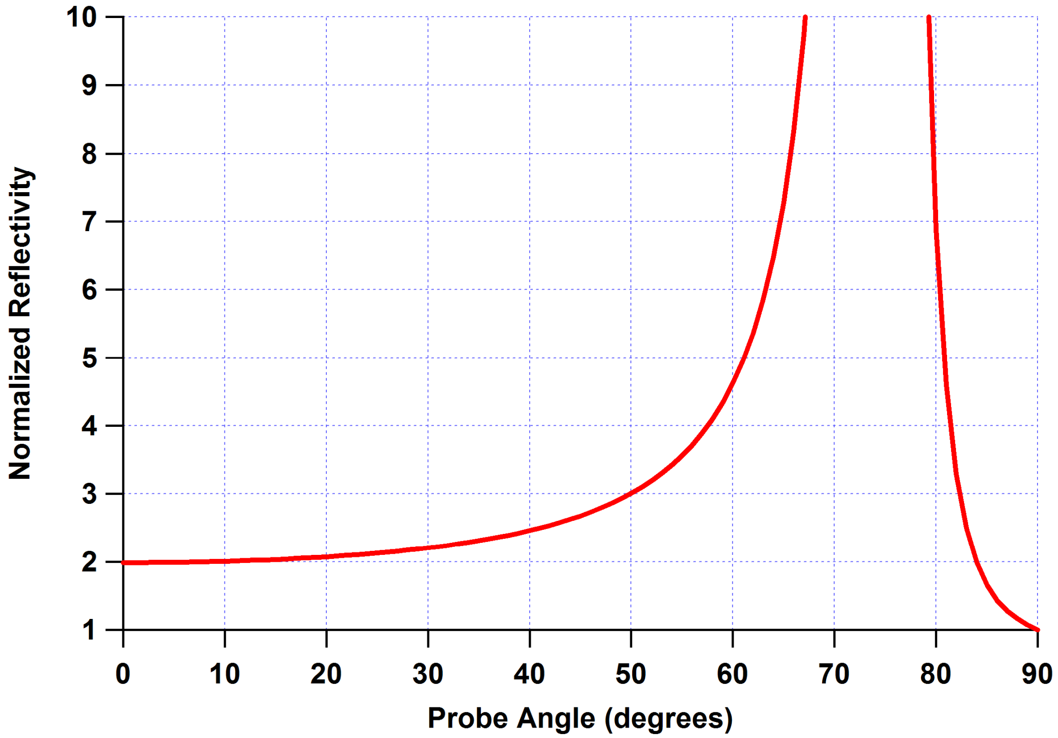

Figure 26. The ratio of the reflectivity of melted GaAs (Drude model) to cold GaAs is shown as a function of probe angle for 800 nm. The resonance effect is due to the loss of reflection at Brewster's angle for the cold material.

Table 3. Various Drude model parameters for GaAs, with the increase in reflectivity upon melting factor listed for two different angles. The parameters come from Temnov 2006 and Huang 1998.

						Factor of Reflectivity Increase	
λ (nm)	τ (fs)	N_e (cm^{-3})	ω_p (s^{-1})	n	k	**@ 0°**	**@ 58.5°**
800	0.125	1.95E+23	2.49E+16	3.418	4.427	1.98	4.15
800	0.15	1.90E+23	2.45E+16	3.514	4.833	2.06	4.49
800	0.135	2.10E+23	2.58E+16	3.608	4.799	2.05	4.43
800	0.2	1.03E+23	1.83E+16	2.65	3.56	1.98	4.21
					Average	2.02	4.32
					StdDev	0.04	0.17

CHAPTER 4. THOR LASER DESCRIPTION

This chapter discusses the background and techniques for generating high-intensity short pulse lasers. It chronicles the design and development of the THOR laser that was built at the University of Texas in 2001 and 2002, and discusses information relevant to the use and maintenance of the system. For information related to the modeling of the energetics of the laser, please reference Greg Hays' dissertation published in August 2007.

4.1 Laser Background

A laser is a device that emits photons in a coherent beam. These photons are generated in an optical cavity surrounding a gain medium that amplifies the light. Energy is stored in the gain medium by some form of excitation, and it later extracted by photons traveling back and forth in the optical cavity. The extracted photons were created by stimulation from the first spontaneous photons, which is why the word "LASER" is an acronym for "light amplification by stimulated emission of radiation."

Since the development of the laser (Maiman 1960), scientists have been striving to reach higher and higher laser power. Initially, lasers increased in power by amplification to higher energies, but damage to the gain media and optics of the system fundamentally limited the peak intensities that could be reached. Intensity is proportional to energy and inversely proportional to pulse width and beam size, so there are only two methods to amplify to higher energies without damage; physically increase the beam size, or increase the temporal pulse length. The first method, which has been pioneered by large national lab type facilities, is to increase the diameter of the beam and corresponding optics so that the intensity is reduced below the damage limit. This path quickly leads to very physically large and expensive laser systems such as Nova and the National Ignition Facility (NIF) at Lawrence Livermore National Laboratory (LLNL).

4.1.1 CHIRPED PULSE AMPLIFICATION

The second method to achieve a high intensity laser involves lengthening the pulse in time. For a good review of this field, see (Backus, Durfee et al. 1998). The now common way to do this is to take advantage of the broad bandwidth of a short pulse laser (bandwidth is inversely proportional to pulse width, from the uncertainty principle) by manipulating the frequencies (called stretching) so that they are distributed in the pulse as a function of time. In many cases, this dispersion of the frequencies is created by a pulse stretcher, which is typically two diffraction gratings with an imaging telescope between them (Figure 27) (Martinez 1987; Pessot, Maine et al. 1987). Although great progress was achieved with this design, these systems were limited in pulse widths to upwards of 100 fs due to the chromatic and spherical aberrations of the telescope. Many alternative designs have since been developed, but they each have their own benefits and drawbacks (Lemoff and Barty 1993; Banks, Perry et al. 2000).

By broadening the pulse width, it is now safe to amplify to higher energies than otherwise would be possible. However, the fluence must still remain below the damage level of the gain media and optics. After amplification, the longer pulse has more energy than the non-stretched pulse would have, but it still does not have a higher intensity. In order to reach higher intensities, the frequency manipulation of the pulse that we performed earlier must be undone, which is called compressing. The revolutionary idea that broad-bandwidth pulses could be compressed in time with the use of diffraction

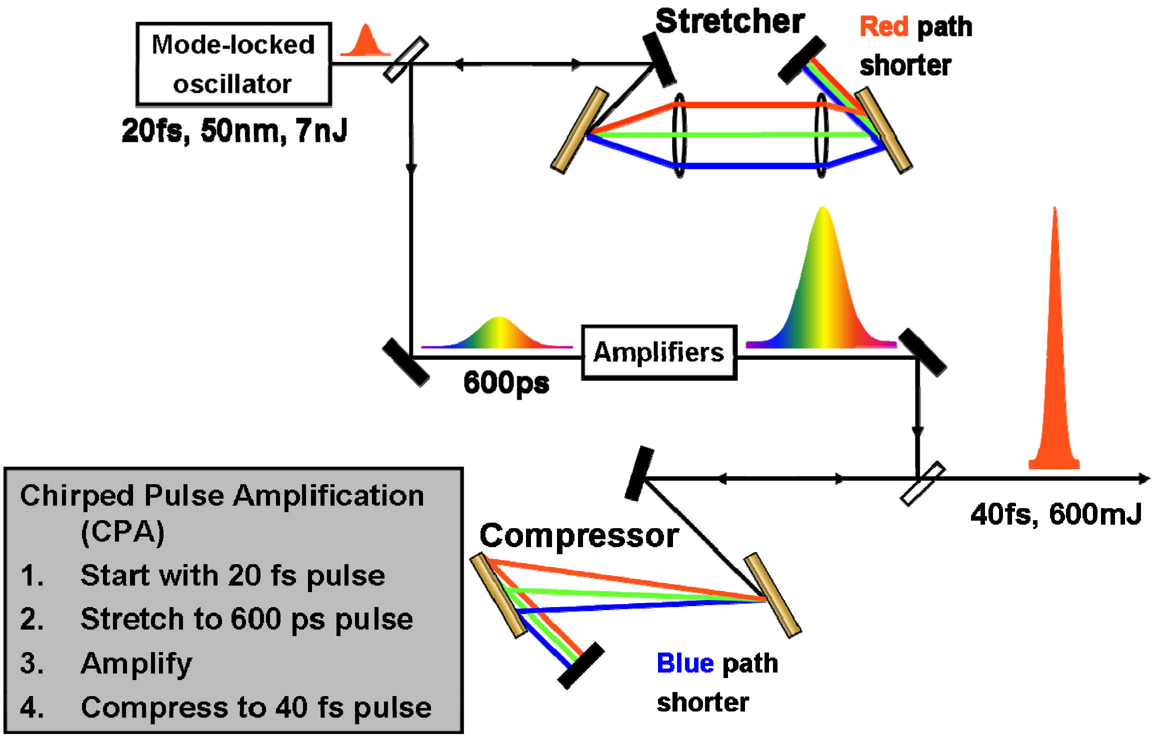

Figure 27. Schematic illustrating the method of chirped pulse amplification (CPA).

gratings was discovered by (Treacy 1969) and further developed by (Martinez 1987). By properly compressing the higher energy stretched pulse, a higher intensity laser is finally obtained. This method of stretching, amplifying, and compressing is called chirped pulse amplification (CPA), which was pioneered in the mid-1980's (Strickland and Mourou 1985). The predominantly linear phase sweep across the pulse bandwidth is where the term "chirped" comes from, as this sweep in frequencies is analogous to the rising or falling pitches of many bird chirps.

4.1.2 TIME-BANDWIDTH PRODUCT

As mentioned above, the uncertainty principle limits the minimum pulse width and spectral width product. It is instructive to derive the relation between these two quantities to measure the quality of compression. The electric field of a transform limited ultra-short laser pulse can be written as,

$$E(t) = A(t) \cdot e^{i(k \cdot x - \omega_o t)} \tag{4.1}$$

where *A(t)* is often a Gaussian envelope.

$$A(t) = A_o \cdot e^{\frac{-t^2}{\tau_p{}^2}} \tag{4.2}$$

We are primarily interested in the intensity of the pulse, which is the magnitude squared of the electric field.

$$I(t) = |E(t)|^2 = A_o{}^2 \cdot e^{\frac{-2t^2}{\tau_p{}^2}} \tag{4.3}$$

The full-width-at-half-maximum (FWHM) of the intensity is related to τ_p, the 1/e^2 width, as

$$\Delta t = \tau_p \sqrt{2 \cdot Ln(2)} \approx 1.1774 \cdot \tau_p \tag{4.4}$$

Oftentimes, we measure the spectrum of the pulse, so it is useful to know the spectral intensity of the pulse, which is found by taking the square of the magnitude of the Fourier transform of the temporal electric field.

$$\begin{aligned} S(\omega) = |F[E(t)]|^2 &= \left| \frac{1}{\sqrt{2\pi}} \int_{-\infty}^{\infty} E(t) \cdot e^{i\omega t} dt \right|^2 \\ &= \frac{\tau_p{}^2 A_o{}^2}{2} Exp\left[\frac{-(\omega - \omega_o)^2 \tau_p{}^2}{2} \right] \end{aligned} \tag{4.5}$$

For comparison of various pulses, the FWHM of the spectral intensity can be expressed in the following forms with various units:

$$\Delta\omega = \frac{\sqrt{8Ln(2)}}{\tau_p} \approx \frac{2.355}{\tau_p} \tag{4.6}$$

$$\Delta\nu = \frac{\Delta\omega}{2\pi} = \frac{\sqrt{2Ln(2)}}{\pi\tau_p} \simeq \frac{0.375}{\tau_p} \tag{4.7}$$

$$\Delta\lambda = \frac{c}{{\nu_o}^2}\Delta\nu = \frac{{\lambda_o}^2}{c}\frac{\sqrt{2Ln(2)}}{\pi\tau_p} \simeq \frac{1.25\times10^{-9}{\lambda_o}^2}{\tau_p} \tag{4.8}$$

By combining the FWHM of the spectral and temporal intensity, we find what is known as the time-bandwidth product for a Gaussian pulse.

$$\begin{aligned}\Delta t\cdot\Delta\nu &= \frac{2\cdot Ln(2)}{\pi} \\ &\approx .441\end{aligned} \tag{4.9}$$

This time-bandwidth product is the uncertainty principle for a perfectly Gaussian pulse. We can transform this to more convenient units using equation (4.8). Doing so allows the time-bandwidth product to be rewritten as

$$\Delta t\cdot\Delta\lambda = \frac{2\cdot Ln(2)}{\pi}\frac{{\lambda_o}^2}{c} \tag{4.10}$$

For 800 nm light, this can be written as

$$\Delta t\cdot\Delta\lambda \approx 941 fs\cdot nm \tag{4.11}$$

This equation is handy for determining the minimum pulse length attainable for a given spectral bandwidth. For example, given a 44.5 nm Gaussian shaped spectrum from the THOR oscillator, we find the bandwidth limited pulse width to be 21.2 fs. After amplification to ~ 1 J, the THOR laser has a 27.5 nm Gaussian shaped spectrum, which leads to a bandwidth limited pulse width of 34.2 fs. In reality, it is very difficult to have a perfectly flat spectral phase on such a laser pulse, so the pulse width is almost always wider than the bandwidth limit, which leads to a time-bandwidth product > 0.441. In the case of the THOR laser, the time-bandwidth product = 0.516.

4.1.3 TI:SAPPHIRE CHARACTERISTICS

Titanium doped sapphire (Al_2O_3) (Ti:sapphire) based laser systems work very well for producing a short laser pulse due to the large bandwidths that they can amplify.

Ti:sapphire has a large emission spectrum that reaches from ~650 to 1100 nm, with a peak gain around 790 nm, and it has a large absorption spectrum centered around 500 nm (Moulton 1986).

The excited population lifetime of Ti:sapphire is about 3 μs around room temperature, so the pump energy must be stored in the crystal in a time scale shorter than or equal to this lifetime. This restriction effectively rules out flashlamp pumping, since flashlamps typically release their energy over durations longer than ~ 100 μs. The common method to excite Ti:sapphire is to pump it with another laser that emits in the green region. Nd:YAG, Nd:YVO_4, and Ar:ion lasers produce 532 nm, 532 nm, and 514 nm, respectively, and thus work well for pumping Ti:sapphire.

4.2 THOR Specifics

The laser that I helped design and build is the Texas High-intensity Optical Research (THOR) laser (Figure 28). This laser system is based on the master oscillator, power amplifier (MOPA) scheme, where a seed pulse is generated in an oscillator cavity, and later amplified in one or more amplifier stages that increase the energy.

4.2.1 OSCILLATOR

The heart of the THOR laser is the Femotosource Kerr-lens modelocked Ti:sapphire oscillator. It is currently pumped by a Spectra Physics Millennia Vs DPSS laser. The Millennia outputs ~4.5 W of green laser light, which is focused into the Ti:sapphire crystal of the oscillator. When mode-locked, the oscillator produces ~20 fs, 8 nJ laser pulses at a repetition rate of ~73 MHz (a pulse separation of ~ 13.7 ns). This nm results in an average power of ~600 mW. These laser pulses have a bandwidth of ~45

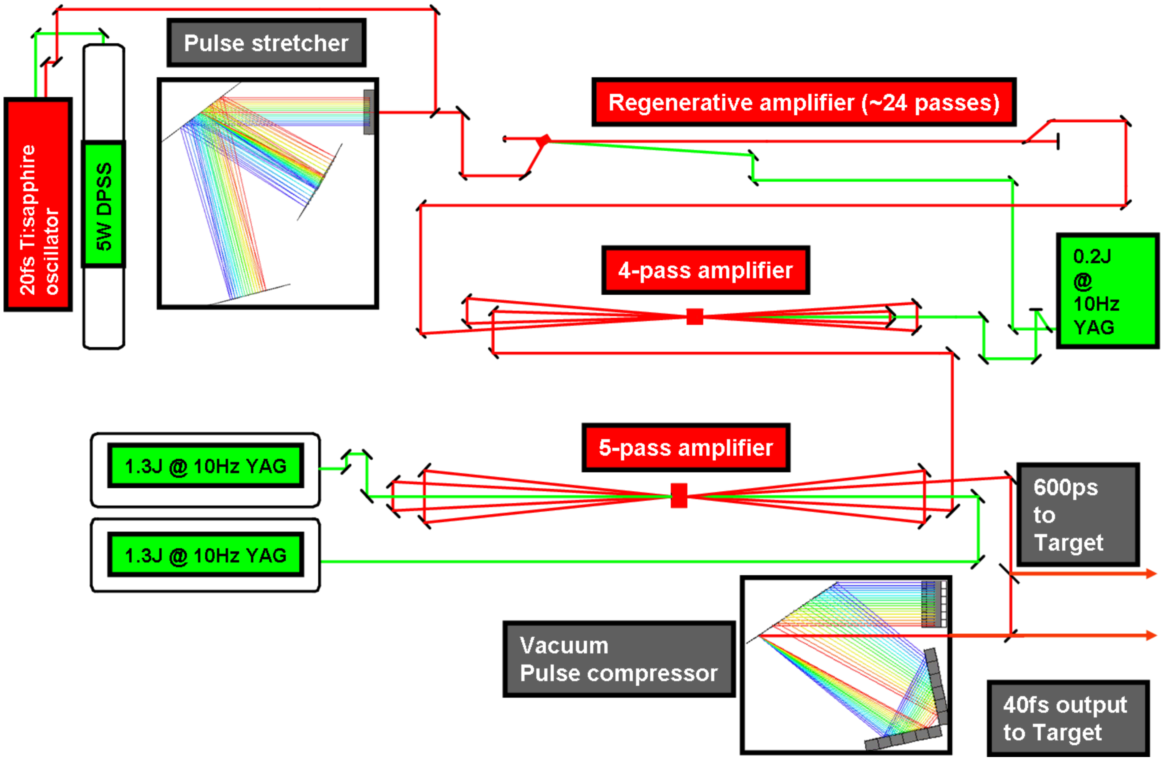

Figure 28. Schematic showing the various components and the general layout of the THOR laser.

FWHM, with a full width near 100 nm.

4.2.2 ISOLATION

These pulses then pass through two isolation stages to protect the oscillator from back-reflections and feedback. The first stage contains a faraday rotator surrounded by two calcite polarizers. This provides an extinction ratio of ~1000:1 for forward traveling light as compared to backward traveling light. The next isolation stage consists of a fast on-off Lasermetrics Pockels cell surrounded by two calcite polarizers. The Pockels cell switches to and from its half-wave voltage within ~5 ns. This stage provides an additional ~ 1000x extinction for light not traversing the crystal during the energized state. It is this Pockels cell that we call the “pulse slicer”, as it slices out 10 pulses per second, and dumps the other 73 MHz minus 10 Hz pulses into the polarizer.

4.2.3 STRETCHER

After the isolation stage, the beam is pseudo-collimated by a 2 m lens, before it is periscoped up into the pulse stretcher. There are two irises to be used for alignment into the stretcher; one just outside the Plexiglas box, and one on the inside of the box. These are only needed if things get bumped, and the beam no longer enters and exits the stretcher properly.

We have designed our stretcher based on the LLNL design (Banks, Perry et al. 2000) that utilizes all reflective optics in an on-axis configuration. A 40 cm wide, 1480 line/mm diffraction grating was manufactured at LLNL with a 2 inch horizontal mirror stripe across the center. This stripe, together with an 1130 mm focal length spherical mirror and a flat mirror (both 30 cm diameter) at the focal plane, replace the telescope that is contained in other designs. Benefits to this design include the elimination of chromatic aberrations due to the lack of transmissive optics, and the relative ease of alignment due to the on-axis optics and the use of a single diffraction grating. The stretcher is double passed by vertically offsetting the beam with a roof-top mirror pair to stretch the pulse from ~ 100 fs to 600 ps. This vertical offset also allows the pulse to clear the top of the stretcher injection mirror, where it is periscoped down to the table for injection into the 5 m long polarization maintaining fiber.

The vertical placement of the beams on the grating follows according to Figure 29. This figure is drawn from the point of view of the input beam, not the grating normal. The stretcher beam takes the following path: the input beam, #1, strikes the grating and diffracts off to the spherical mirror. The reflected beam, #2, reflects off of the mirror stripe on the grating and is sent to the flat mirror. This reflected beam, #3, returns to the mirror stripe below the mid-point and reflects off toward the spherical mirror. This reflection, #4, strikes the grating below the mirror stripe, and is directed to the vertical rooftop mirror pair to be offset further down (vertically). The beam paths reverse themselves, and the exit beam, #8, exits just a bit higher than the input beam.

This fiber adds the necessary dispersion, which is discussed in the phase modeling section, so that the pulse compressor can later recompress the pulse down to ~ 40 fs after amplification. After traveling through the fiber, the beam exits the second fiber launcher with a clean Gaussian mode, thanks to the spatial filtering performed by the single-mode nature of the fiber. Normally, the coupling losses into and out of the fiber and launchers allow ~ 30-40% transmission through the fiber assembly. From here, the beam transmits through a small diameter Faraday rotator isolation package so that light ejected upstream from the regenerative amplifier does not damage the output end of the fiber.

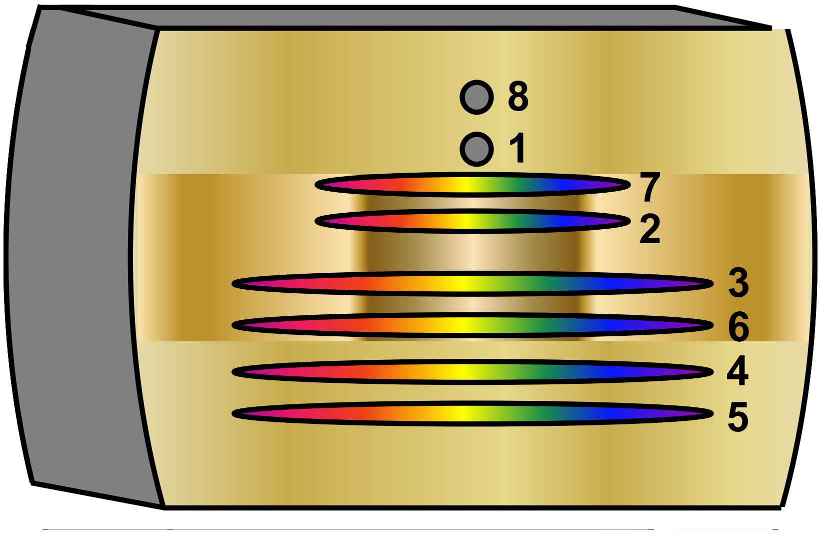

Figure 29. An illustration of the stretcher grating with the various beam hits enumerated. The grating is drawn from the perspective of the input laser beam, but it is a mirror image of the actual layout of the THOR grating. See the text for a bounce-by-bounce description.

4.2.4 REGENERATIVE AMPLIFIER

After the isolator, the beam is injected into the regenerative amplifier (regen) cavity by reflecting off of the face of the Brewster cut Ti:sapphire crystal. The cavity consists of two mirrors separated by ~ 91 inches , a Ti:sapphire crystal, a Pockels cell, and a thin film polarizer (Figure 30). The end mirror near crystal is a 5 m radius of curvature high-reflector, while the mirror near the polarizer is a flat zero degree high-reflector. The regen contains a 5 mm x 10 mm x 10 mm Brewster-cut Ti:sapphire crystal (absorption $\alpha = 2.6$/cm) that is pumped by ~ 45 mJ from the output of a BigSky CFR-400 laser. The pump is focused down to a 2 mm diameter, thus creating a peak pump fluence of 1 J/cm^2. After passing the mid-point of the cavity, the pulse polarization is rotated to p-polarization by a Medox dual-pulse fast on/off Pockels cell. The Medox turns on just before the injected pulse passes through, and it turns off before the pulse travels back through in the opposite direction. Once the pulse is trapped in the cavity, it makes ~ 24 round trips (~ 15.5 ns each), gaining an amplification of ~ 10^6. The thin film polarizer (TFP) serves to reject s-polarized ASE in the cavity, but it also ejects the pulse after the final pass through the Medox where the pulse polarization is rotated horizontally.

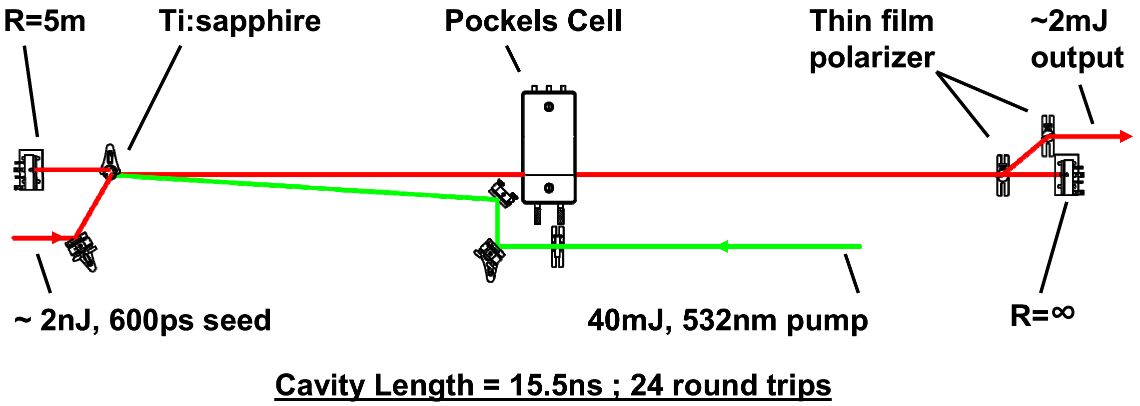

Figure 30. Diagram showing the components of the regenerative amplifier cavity

After ejection, the ~ 1 mm diameter pulse reflects off one more TFP before entering the "pulse cleaner" isolation stage, which consist of two parallel calcite polarizers surrounding, a half waveplate, and a Lasermetrics Pockels cell. This isolation stage will attenuate any leakage from the regen, including both pulse leakage from each round trip and amplified spontaneous emission (ASE). After isolation, the amplified pulse has an energy of ~ 1-2 mJ.

4.2.5 4-PASS AMPLIFIER

From here, the pulse is pseudo-collimated with a 2.5 m lens to correct for the divergence from the regen before it passes through the Uniblitz shutter and enters the 4-pass "bow-tie" amplifier. The shutter is used to modify the repetition rate of the laser for various experiments that need to run at rates between single shot and 10 Hz operation.

The 4-pass contains a 10 mm diameter, 20 mm long Brewster-cut Ti:sapphire crystal ($\alpha = 1.05$/cm) manufactured by Crystal Systems. This crystal is pumped by the reminder of the Big Sky laser output, which is typically near 110 mJ, and focused to a spot size of 2.5 mm which creates a peak pump fluence of 1.5 J/cm^2. This pump laser is timed up to fire just prior to the entrance of the seed pulse into the regen, which leads to a delay between pumping of the 4-pass and extraction of the energy. Luckily, the ~ 3 μs lifetime is greater than the ~ 385 ns delay between excitation and extraction, so only ~ 10% of the atoms have time to decay. After four passes through the crystal, the seed has an energy of ~ 20 mJ, and a spot size of ~ 2 mm FWHM.

4.2.6 5-PASS AMPLIFIER

The output of 4-pass amplifier is periscoped up in height before entering a beam expanding vacuum spatial filter (VSF), which expands the beam size to ~ 1 cm. The 2nd lens of this telescope assembly is placed less than a focal length away from the pinhole of the VSF because we need the beam to diverge slightly to counteract the thermal lens that is present in the 5-pass power amplifier.

The 5-pass amplifier consisted of a 20 mm diameter x 20 mm long (now 15 mm) Ti:sapphire (α = 2.30/cm) crystal from Crystal Systems. The thermal lens is caused by the radial extraction of heat from this cylindrical crystal into the surrounding water-cooled copper mount. The crystal is carefully wrapped in a thin layer of indium foil, to increase the surface area of thermal contact before being clamped in the copper mount. The temperature gradient between the hot region of pump laser absorption and the cool heat sink creates a gradient in the index of refraction, which acts as a weak positive lens. We measured the focal length of this thermal lens to be on the order of 50 - 100 m.

The thermal load is due to the 5-pass being double pumped with two Spectra Physics PRO 350 YAG lasers, one per each side of the crystal. The PROs each contribute ~ 1.3 J of 532 nm light in ~ 8 ns. After 5-passes, the 800 nm seed pulse is amplified up to ~ 1.1 J (Table 4) with a pulse width of ~ 550 ps FWHM due to gain-narrowing of the spectrum (Figure 31). The beam profile is shown in Figure 32.

The large size of the 5-pass Ti:sapphire crystal (20 mm diameter, 20 mm length) combined with the high pump-fluence (~ 1.5 J/cm^2) makes it easy for transverse parasitic oscillations to occur. These transverse lasing modes start with ASE that bounces back and forth across the crystal face, where they see high gain on each pass. These parasitic oscillations reduce the excited atom density that the seed pulse will see, which lowers the overall gain. To minimize parasitics in our crystals, we purchased rough ground crystals, and then painted the edges of them with a Sharpie magic marker. The ground edges serve to scatter the light in random directions, rather than reflect it back in the region of high gain, and the black marker helps to absorb light that reaches the edge, rather than

Table 4. Amplification data from the 5-pass amplifier (taken 10/6/2006). PRO 1 energy = 1.14 J, PRO 2 energy = 1.22 J, as measured at the crystal

Amplification Stage	Energy (mJ)	Gain Factor
0	17	-
1	64	3.8
2	200	3.1
3	470	2.4
4	770	1.6
5	950	1.2

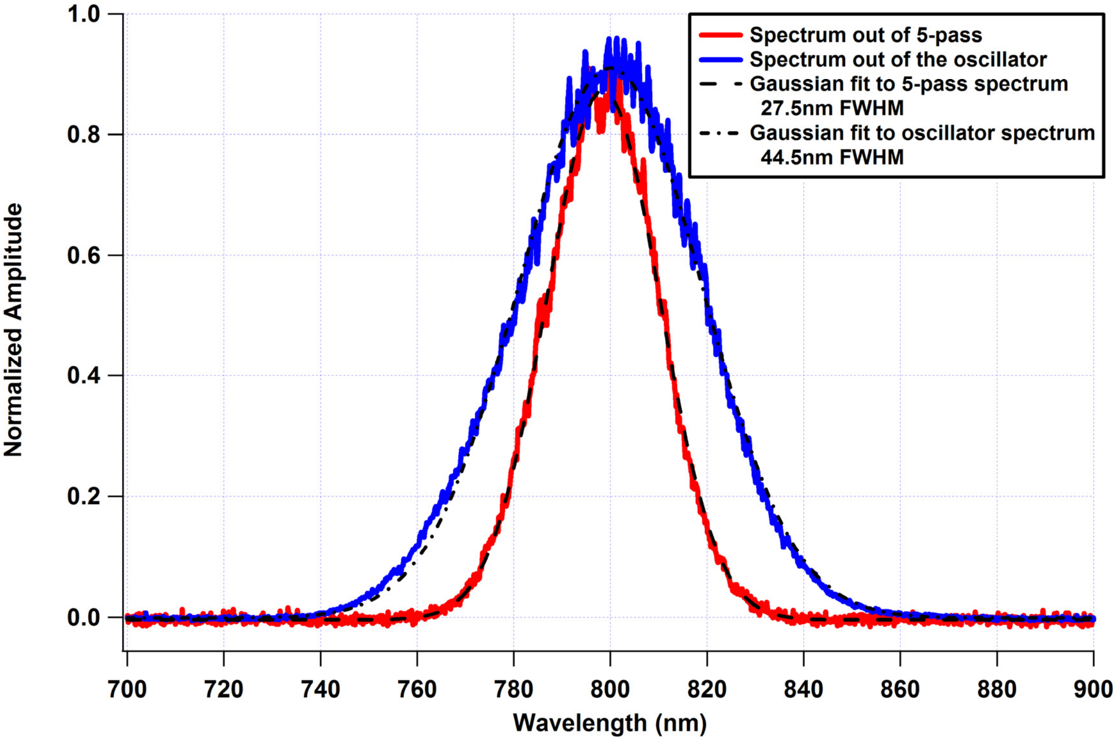

Figure 31. Spectra of laser pulse after the oscillator and after the last amplifier in the system. (Taken with an Ocean Optics fiber spectrometer on 10/12/2006).

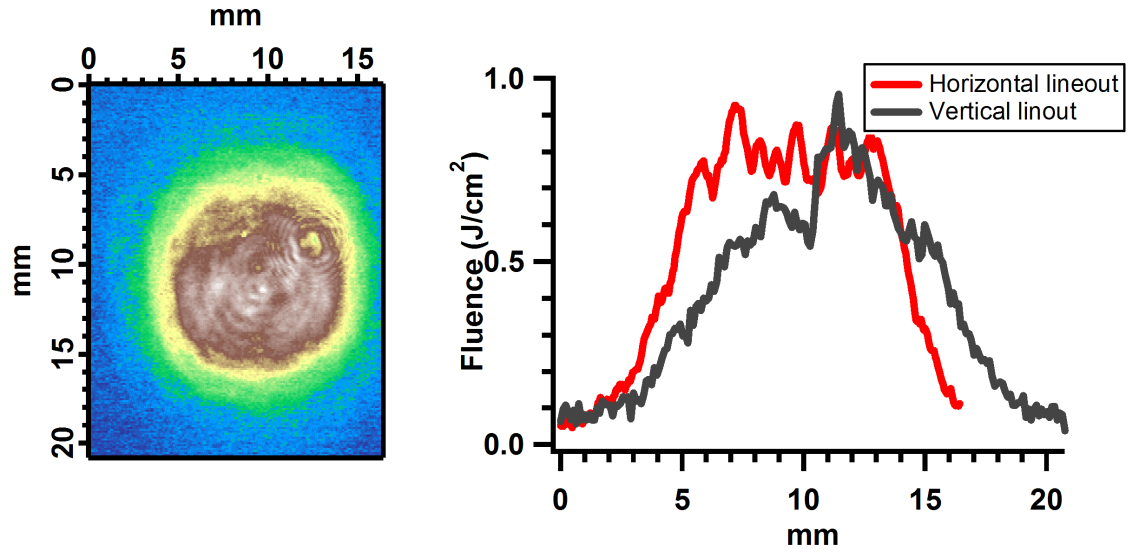

Figure 32. Beam image and line-outs of the amplified laser pulse 17ft after the last pass through the Ti:sapphire crystal.

reflect it. We found that these two measures were necessary and sufficient to prevent parasitic oscillations in our amplifiers (Figure 33).

After amplification, the beam leaves the laser table and crosses over to the compressor table where it enters a polarization rotating periscope that raises the beam to the compressor height. The beam passes through a second VSF that expands the beam up to ~5 cm FWHM with hard clipping at ~75 mm full width due to the 3” collimation lens. This collimated and filtered beam has a peak fluence of ~ 50 mJ/cm^2 (Figure 34), which is well below the ~ 300 mJ/cm^2 damage fluence of the gold coated compressor gratings. The beam travels through an AR coated window into the vacuum compressor, where it is compressed down to ~ 40 fs, with about 60% energy throughput.

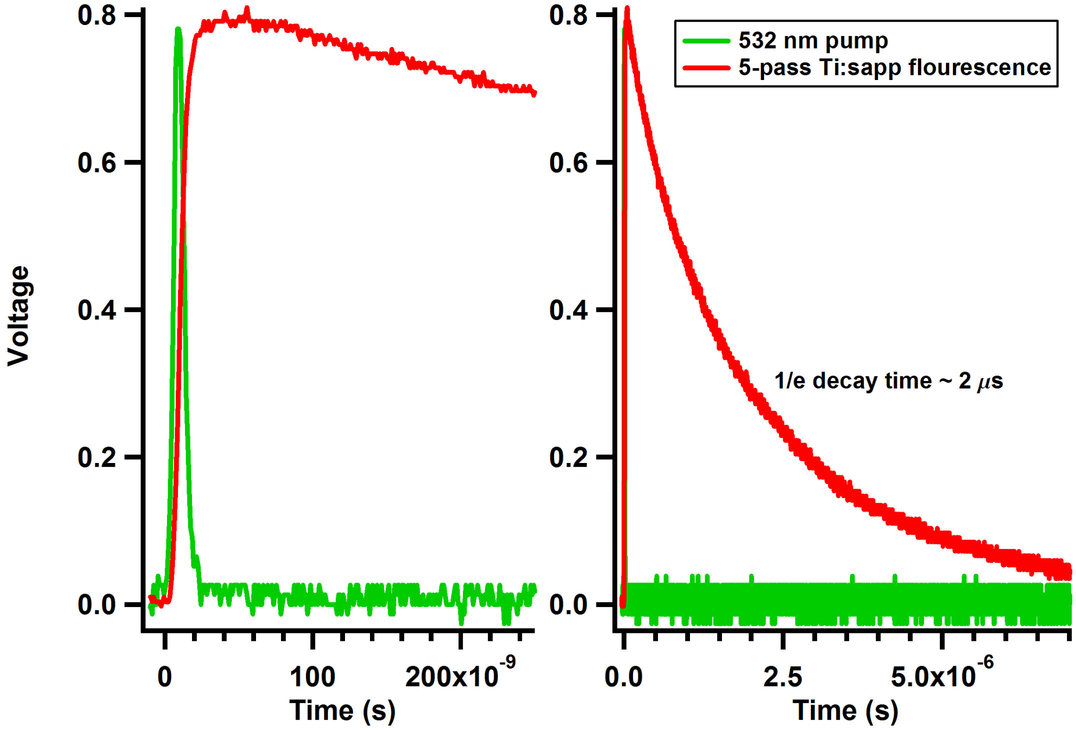

Figure 33. Measured fluorescence of our 5-pass Ti:sapphire crystal (14.7mm long, pumped by 1.1 J + 1.2 J).

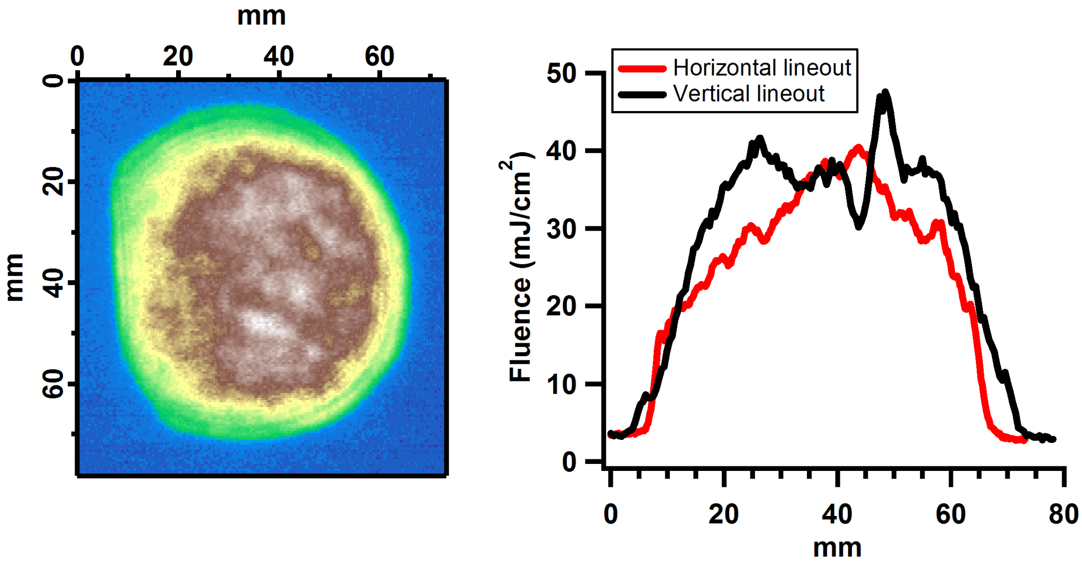

Figure 34. Beam image and line-outs of the amplified laser pulse 33ft after the entrance window of the compressor

4.2.7 COMPRESSOR

Our pulse compressor is of a single grating design, utilizing a 40 cm wide, 1480 line/mm diffraction grating purchased from LLNL. It uses a pair of 28 cm x 16 cm mirrors as a horizontal retro-reflector to fold the compressor in half so that the same grating is used on each “end” of the standard two grating compressor. The compressor utilizes a pair of 17 cm x 10 cm mirrors as a vertical roof-top mirror to double pass the pulse and offset the output beam from the input beam. Due to the large beam size involved, the optics of the compressor are quite large. In fact, it is the size of the optics, but more importantly the grating, that limit the spectral transmission of the compressor.

Specifically, the large compressor diffraction grating is difficult and expensive to manufacture, so it is this element in THOR that limits the minimum pulse width in our design of the laser. The optics are only able to transmit ~ 70 nm of bandwidth (cutoff), which limits THOR to a minimum of ~28 fs, transform limited. This means that there is no point in building a laser with a bandwidth larger than ~ 35 nm FWHM, because it will get clipped in the compressor. More discussion on the design of the stretcher and compressor will follow in section 4.3.

The compressor beam strikes the grating on both sides of the midpoint according to Figure 35. The input beam, #1, enters the compressor below the midpoint of the grating and off to the right hand side. It diffracts off and is retro-reflected by the horizontal roof top mirror pair. This beam, #2, strikes the grating as a spatially dispersed beam to the left of the input and diffracts off toward the vertical rooftop mirror pair. This pair raises the beam just enough to not overlap the input beam and the process reverses until the output beam, #4, exits just above the input.

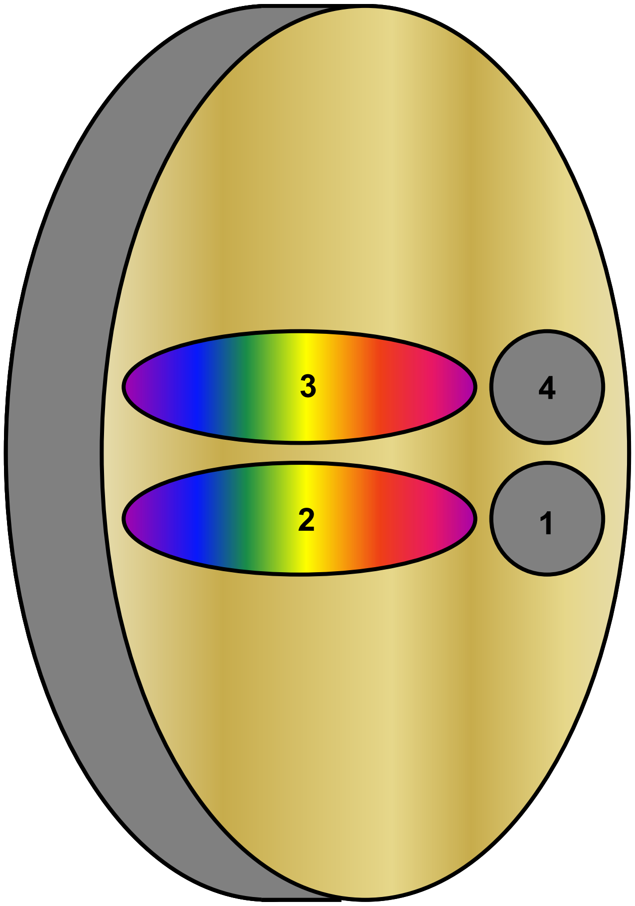

Figure 35. An illustration of the compressor grating with the various beam hits enumerated. The grating is drawn from the perspective of the input laser beam. The illustration is not to scale, but the sizes are approximately correct. The grating is 40 cm diameter, and the beams sizes are drawn with a 5 cm diameter and ~ 32 nm of bandwidth. See the text for a bounce-by-bounce description.

4.2.8 TIMING SYSTEM

In order to operate a laser such as THOR, many pieces of equipment must be electrically triggered at very specific times. For example, the pump lasers must arrive in the crystals before the seed pulse, and the Pockels cells must fire at precisely the right moment to allow passage of the laser pulse. To accomplish these goals, we utilize numerous commercial digital delay generators from Stanford Research Systems (model # DG535). The schematic for the timing and triggering system is shown in (Figure 36).

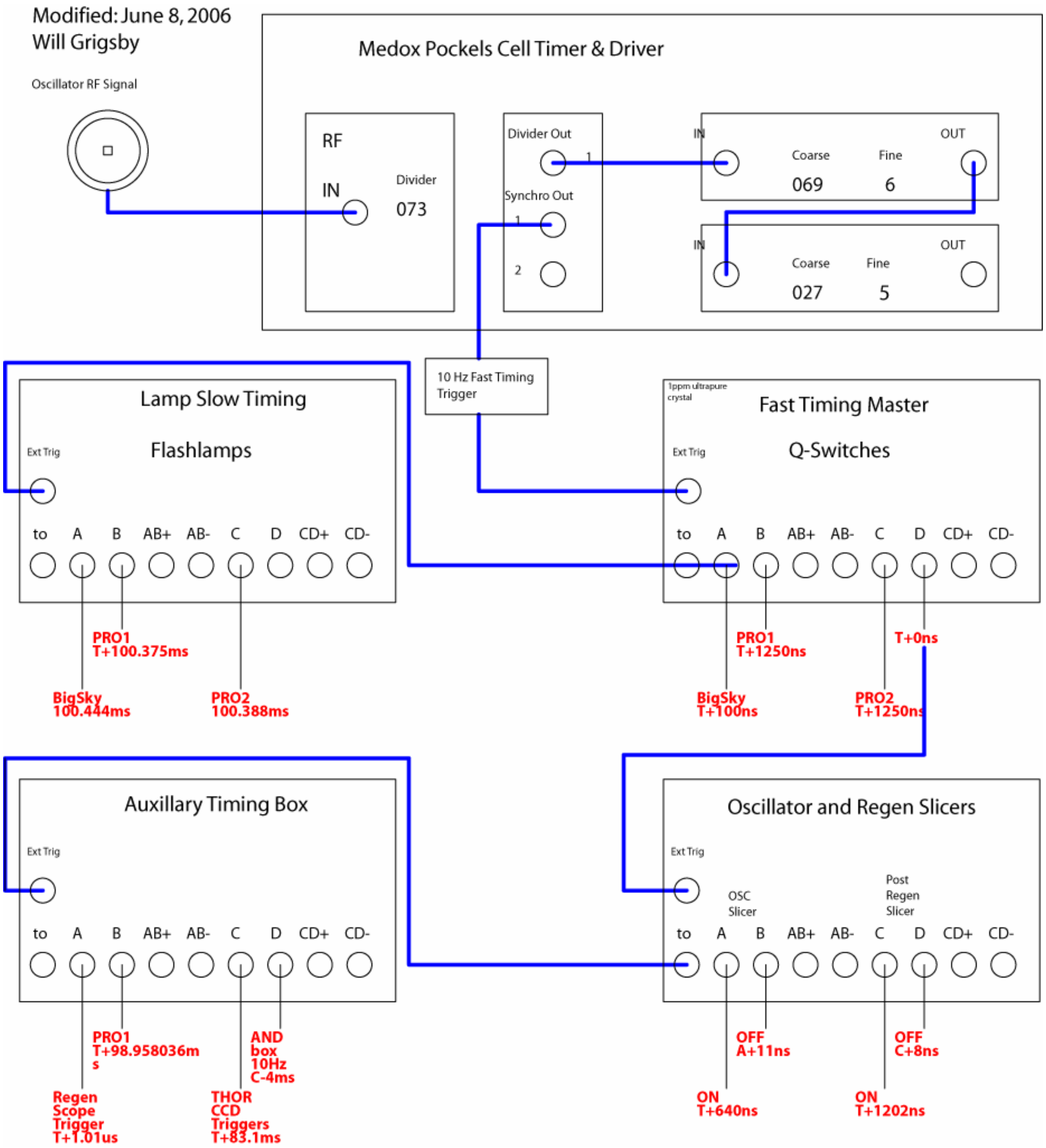

Figure 36. Diagram showing the timing boxes and structure for the THOR laser.

Before we can create delays for the laser, we must synchronize the timing to the laser pulses. This is done by slaving the master clock of the system to the RF train of optical pulses from the oscillator. This optical to electrical pulse conversion is done with a photodiode that is located just inside the stretcher box near the oscillator. This is schematically represented in the top left corner of Figure 36. The ~ 73 MHz train of pulses is input into the control driver box for the Medox Pockels cell, which requires a pulse voltage of ~ 1 V. If the pulse signal drops to < ~ 0.5 V, then the timing system becomes unstable. Inside the control box, the frequency is down-converted to nearly 10 Hz operation, and this newly created signal is then used to trigger the digital delay generators that control THOR. This signal is input into the external trigger of the master DG in the top right hand corner.. The frequency is nearly 10 Hz because the Medox driver divides the oscillator frequency, which is not exactly 73 MHz, by the clock division multiplier of 73×10^5.

The DG535s typically have timing jitter ~ 10^{-8} of the longest delay (i.e. a delay of 1 s will cause variations less than 10 ns, while a delay of 1 ms causes tens of picoseconds variations). For this reason, the relatively slow timing delays of the flashlamps (100 ms) are isolated to the top left DG, while the high-sensitivity fast timing delays of the Q-switches (1000 ns) and Pockels cells are isolated in their own DGs in the top right and bottom right of the figure, respectively. The various outputs of the delay generators are run to the trigger inputs on the various laser components using an array of RG58 BNC connected cables.

4.3 Phase Modeling

In designing the THOR laser, I modeled the phase of the laser pulse in order to predict the output pulse we could achieve. The pulse acquires spectral phase dispersion in all of the different system components. First, the stretcher imposes a large amount of high-order phase on the spectrum of the pulse. As it travels through the amplifier chain, material will further add to the phase because different spectral components travel at different speeds, given by $c/n(\omega)$. Finally, the pulse is sent through a compressor, which is designed to undo the phase applied by the rest of the system. If we succeed in canceling out all of the phase, we are left with essentially the same pulse that we started off with (neglecting gain narrowing, and other effects.) To ease mathematical calculations and to allow us to model the phase, we can expand it in a power series.

$$\begin{aligned}\phi(\omega) = \phi(\omega_o) + \beta_1(\omega-\omega_o) + \frac{1}{2!}\beta_2(\omega-\omega_o)^2 + \frac{1}{3!}\beta_3(\omega-\omega_o)^3 \\ + \frac{1}{4!}\beta_4(\omega-\omega_o)^4 + \mathrm{O}(\omega^5)\end{aligned} \tag{4.12}$$

where

$$\beta_m = \left.\frac{\partial^m f}{\partial \omega^m}\right|_{\omega_o} \tag{4.13}$$

β_2 represents the group-velocity dispersion (GVD), β_3 represents the third-order dispersion (TOD), β_4 represents the fourth-order dispersion (FOD), and so on.

Our model for the Texas High-Intensity Optical Research (THOR) laser uses a ray-tracing code (Optica 1995) to calculate the physical path lengths for each wavelength through the stretcher and compressor (Figure 37). The phase of the light is related to this path length x by the following equation:

$$\phi(\omega) = \frac{\omega}{c} n(\omega) x \tag{4.14}$$

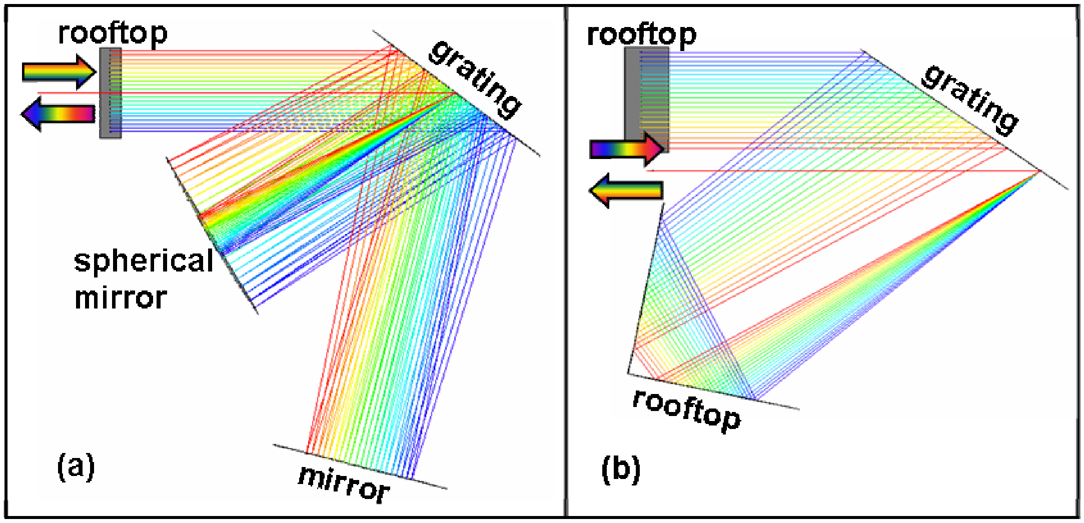

Figure 37. An overhead view of the ray trace through the THOR stretcher (a) and compressor (b).

The β coefficients for the phase expansion (Equation (4.12)) can be found by curve-fitting a polynomial to the phase data calculated using Equation (4.14) and the data from the ray-trace output.

In order to calculate the dispersion of light through optical materials, we need to express the index of refraction $n(\omega)$ as a function of frequency. Material indices of refraction are typically given by Sellmeier equations of the form

$$n^2 = 1 + \sum_{j=1}^{m} \frac{\alpha_j \omega_j^2}{\omega_j^2 - \omega^2} \tag{4.15}$$

where ω_j is the j^{th} resonant frequency at which radiation is absorbed by bound electrons oscillations, and α_j is the strength of the j^{th} resonance. Once again, we fit a polynomial to the calculated phase using the Sellmeier equation and the physical path length and extract the material dispersion coefficients of the system.

Table 5. List of various orders of dispersion caused by passing through 112 cm BK7 glass

	My code results	(Fittinghoff 1998)
GVD	5.00×10^4 fs^2/rad	5.04×10^4 fs^2/rad
TOD	3.59×10^4 fs^3/rad^2	3.57×10^4 fs^3/rad^2
FOD	-1.19×10^4 fs^4/rad^3	-1.14×10^4 fs^4/rad^3
5th order	3.76×10^4 fs^5/rad^4	5.45×10^4 fs^5/rad^4

To test our code, we used it to calculate the dispersion a pulse would acquire after traveling through 112cm of BK7 glass. The coefficients are given in (Table 5), and they agree very well with the results of similar calculations reported by Fittinghoff (Fittinghoff, Walker et al. 1998). The very small discrepancies that do exist are due to slight variations in various published Sellmeier equations.

To model the THOR laser, we begin in the following manner. Instead of starting with the stretcher, as the real THOR system does, we start by optimizing the parameters in the compressor. This is because the larger beam sizes and limited optic sizes in the compressor place strict limitations on what is physically possible. We want to disperse our input pulse (assume 30 fs) to 600 ps, while still passing the maximum bandwidth possible within the limitations set by the physical beam and substrate sizes. The parameters available for adjusting the compressor are the angle of incidence of the laser upon the grating, and the position and angle of the horizontal retro-reflector.

Once this is complete, the code then uses the physical path lengths of the various materials (

Table 6) to calculate the dispersion through the amplifier chain. From here, the code adjusts the stretcher parameters to cancel out the phase due to material and compressor dispersion. The stretcher only has two adjustable parameters: the angle of incidence and the distance of the spherical mirror from the center of the grating. The flat mirror distance is set so that it is a focal length away from the spherical mirror, with a reflection off of the mirror stripe on the grating surface. A minimization routine iteratively minimizes both the GVD and TOD by adjusting these two parameters. A Fourier transform of the phase modulation on the pulse spectrum yields the output pulse shape, so we are able to detect and analyze any pedestals or wings on the pulse.

Ideally, when the coefficients for the stretcher, compressor, and material are added together, each order of phase should sum to zero (phase "zero-ing"). This would result in a short and clean output pulse. However, in reality, there is always some residual phase that cannot be compensated for. My code examined the effects of the separate phase orders, and found that even (or odd) orders of phase have a similar qualitative effect on the output pulse (Figure 38). "Phase balancing" uses this fact to optimize the output pulse. In other words, 2nd order phase is used to cancel out some 4th order phase of opposite sign. Similarly, 3rd order phase can cancel some 5th order phase of opposite sign. However, for our set-up, we quickly found that the large fourth order dispersion due to the spherical aberration in the stretcher created phase that was not easily compensated.

Our initial ray-traced laser design, when optimized using phase balancing (phase "zeroing" was unfavorable), had an output pulse of ~45 fs FWHM (Figure 40). As the figure shows, there are still large modulations in the pulse wings, making this pulse unsuitable for most experiments. By examining the different phase orders, we found that additional material dispersion was needed to be able to compensate for the residual phase.

My code predicts that ~ 4.5 meters (Figure 39)of fused silica will allow us to stretch and amplify a 30 fs input pulse into a recompressed 33.4 fs pulse. The phase coefficients for both of these arrangements are shown in Table 7, while the optimized grating angles and grating spacing parameters for various lengths of extra material are plotted in Figure 41.

Table 6. List of material for the THOR laser. All units are in millimeters, and all materials are broken down by type and description. Depending on the current state of the laser, some of these values might be different. For example, if a different fiber length is used, or if the number of regen trips is changes, then the values in this chart will need to be changed.

Description	**BK7**	**Fused Silica**	**Calcite (o)**	**Terbium Glass**	**Crystal Quartz**	**DKDP (o)**	**EOT Terbium Glass**	**Ti:sapphire (e)**	**Air**
Output coupler + wedge	4.8								
PD Beamsplitter		9.0							
Spect. Beamsplitter		9.0							
Isolation Stage									
Polarizer			21						
OFR				53.6					
Waveplate					0.5				
Polarizer			21						
Pockels cell window		4							
Pockels cell crystal						20			
Pockels cell window		4							
Polarizer			21						
Lens		4							
Additional Material									
Fiber coupler lens		4							
Fiber		4300							
Fiber coupler lens		4							
EOT Isolator									
Polarizer			16						
Waveplate					3.9				
Crystal							21		
Polarizer			16						
Regen (2*24 passes)									
Ti:sapphire crystal								480	
Pockels cell crystal						960			

TFP	421								
Ejection from regen									
Pockels cell crystal						20			
Polarizer			21						
Pockels cell window		4							
Pockels cell crystal						20			
Pockels cell window		4							
Waveplate					0.5				
Lens	6.4								
Polarizer			21						
Ti:sapphire (4 passes)								80	
Spatial Filter									
Lens	6.4								
Window	6.35								
Lens	6.4								
Ti:sapphire (5 passes)								100	
Spatial Filter									
Lens	6.4								
Window	6.35								
Lens	15								
Compressor Window	25.4								
Air (approximate for system)									350 m
TOTALS (mm)	**504.5**	**4346**	**137**	**53.6**	**4.9**	**1020**	**21**	**660**	**350 m**

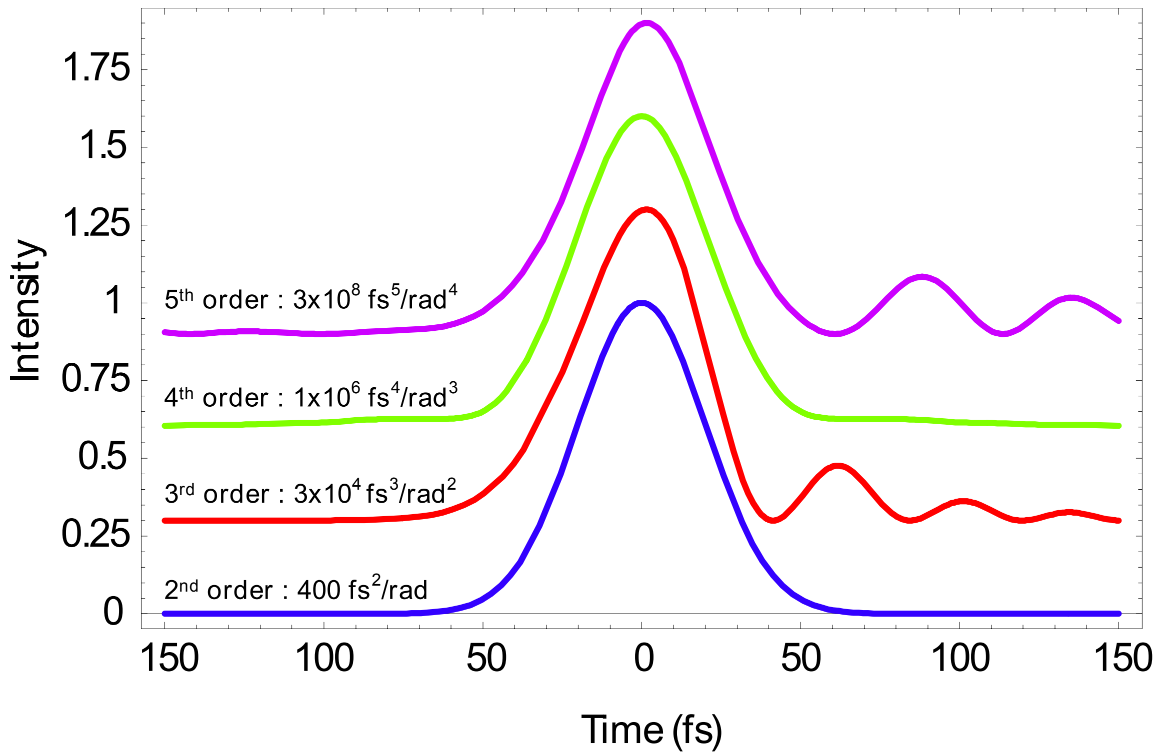

Figure 38. These plots demonstrate the relative effect of various orders of phase on the pulse. The input was a 30 fs FWHM Gaussian, and the amount of each phase order was chosen such that the output pulse had a width of ~ 45 fs FWHM. The effects of 2nd and 4th (or 3rd and 5th) order phase terms have similar effects on the pulse.

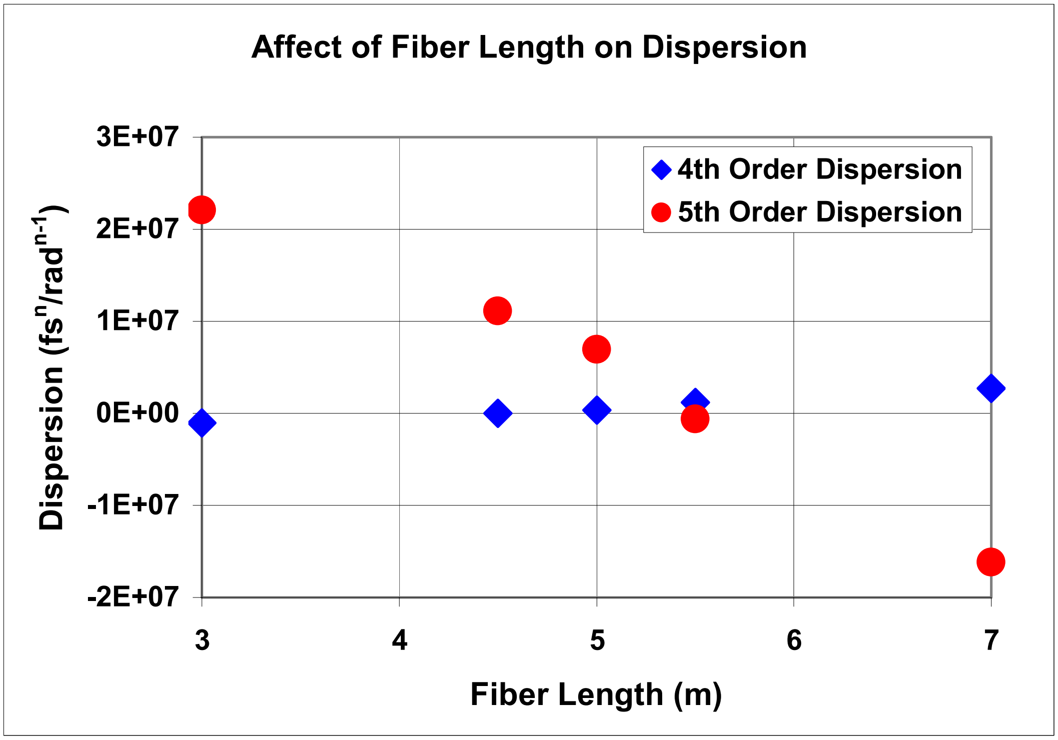

Figure 39. This plot demonstrates the effect of additional material on the higher order dispersion in the THOR ray-trace model. The 4th order dispersion is minimized with ~ 4.5 m of additional fused silica, while the 5th order dispersion is minimized with ~ 5.4 m of fused silica. After running the code, I found that it is more desirable to minimize the 4th order dispersion to obtain a shorter pulse with smaller wings than to minimize the 5th order dispersion..

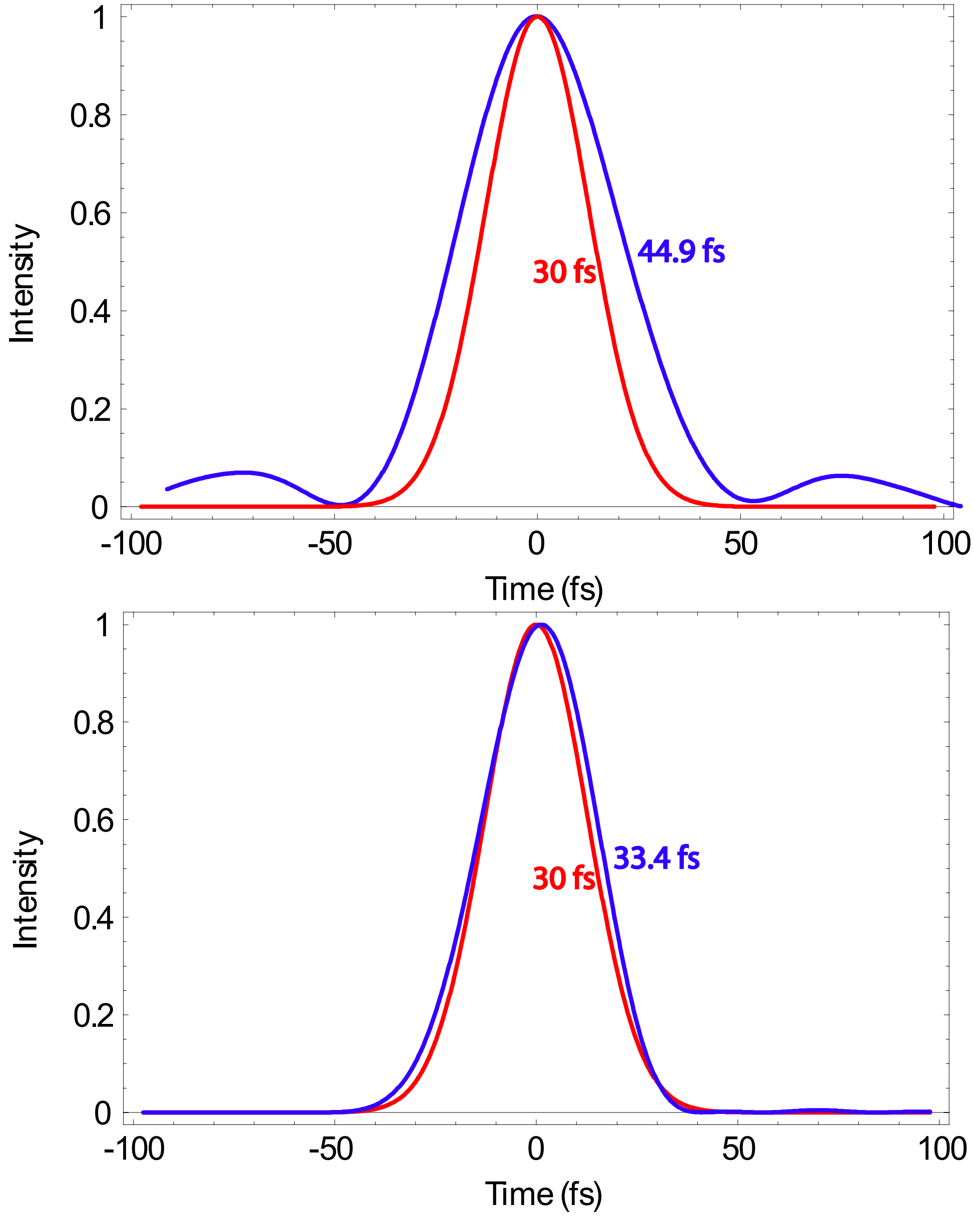

Figure 40. Optimized pulse before (top) and after (bottom) the addition of 4.5 meters of fused silica to the laser chain. The output pulse is superimposed in blue over the shorter 30 fs FWHM input pulse, shown in red. Without the fiber, the uncompensated phase causes pulse broadening and the addition of large wings to the pulse. Adding the fiber and re-optimizing the laser minimizes the phase and produces a cleaner and shorter pulse

Table 7. Phase coefficients for two different configuration of the laser system. The top half describes the configuration when there is no additional material installed in the laser chain. The parameters have been optimized for compression down to ~ 45 fs. The bottom half describes the configuration when there is 450 cm of extra fused silica added to the laser chain. The parameters have been re-optimized for compression down to ~ 33.6 fs. The adjustable laser parameters are the angle of incidence on the stretcher grating and the spherical mirror spacing from the center of the diffraction grating.

No fiber, 57.7547° , 68.23 cm				
	GVD (fs^2/rad)	TOD (fs^3/rad^2)	FOD (fs^4/rad^3)	5OD (fs^5/rad^4)
Stretcher	-1.575E+07	4.949E+07	-2.161E+08	1.204E+09
Compressor	1.564E+07	-4.959E+07	2.129E+08	-1.158E+09
Material	1.140E+05	8.002E+04	-3.560E+05	2.104E+06
Total	**1.616E+03**	**-2.115E+04**	**-3.525E+06**	**4.805E+07**

4.5m fused silica fiber, 56.1228° , 64.3641 cm				
	GVD (fs^2/rad)	TOD (fs^3/rad^2)	FOD (fs^4/rad^3)	5OD (fs^5/rad^4)
Stretcher	-1.575E+07	4.949E+07	-2.161E+08	1.204E+09
Compressor	1.547E+07	-4.970E+07	2.165E+08	-1.195E+09
Material	2.767E+05	2.038E+05	-4.074E+05	2.265E+06
Total	**1.503E+01**	**-4.048E+03**	**-1.008E+04**	**1.112E+07**

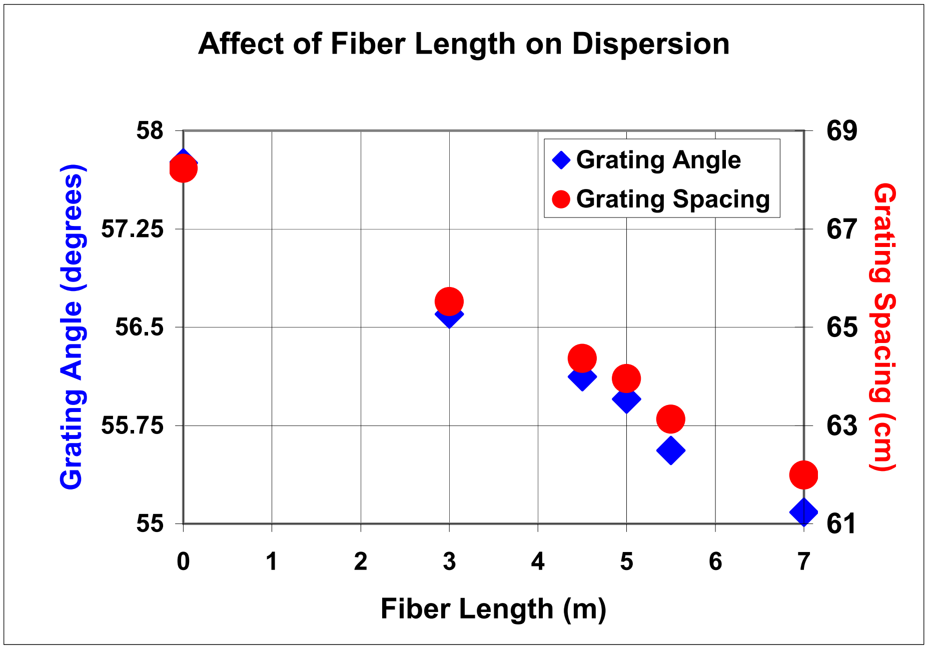

Figure 41. Plot of the optimized stretcher parameters as a function of fiber length. This plot demonstrates the adjustments that would be necessary to re-compress after adding or subtracting a large amount of material from the laser chain.

To install the additional material needed in the laser, we considered two different methods. Our first option was to insert an ~ 9.3 cm fused silica rod into the regenerative amplifier (regen). Because the rod is a pure material with a well known Sellmeier equation, we can accurately model and predict how it will affect our compressibility. However, a rod of this type is relatively expensive, and not adjustable. If, in the process of assembling the laser, we are forced to change the number of passes in our regen, our ability to compress down to 33 fs would be compromised. Also, to minimize etalon effects, the rod ends must be polished at an angle, which will change the alignment of our regen cavity, and thus the pointing through the rest of the system.

The other option, which we chose to implement, was to pass the stretched pulse through a 4.5-meter length of optical fiber. Polarization-maintaining (PM) fiber was most desirable, because our regen only allows s-polarized light to enter. Single mode (non-PM) fiber will convert our polarized laser into un-polarized light, thus creating a loss of energy when coupled into the regen.

There are a few complications that could have arisen with this solution. For example, the stress in the fiber creates a non-symmetric index of refraction, which, combined with other fiber dispersion effects is not easily predicted, so our imparted phase may not be exactly what we calculate. Despite this possible problem, we decided to move forward with the fiber solution. We believed that its strengths outweighed its weaknesses. Once we purchased the laser-fiber coupling mechanisms, it would be relatively easy and inexpensive to change the length of fiber, thus allowing the system to be easily updated, depending on future needs. Also, the process of coupling the pulse into and out of the fiber serves to spatially filter the pulse spatial profile and eases mode matching into the regen.

4.4 Construction

THOR construction took place over the course of ~ 1.5 years, with the primary builders being Greg Hays, Will Grigsby, Gilliss Dyer, and Todd Ditmire. The laser was built in stages, with each component being completed before moving to the next part. Some of the trickier parts of the construction will be discussed in this section.

4.4.1 STRETCHER AND COMPRESSOR ALIGNMENT

The optics of the stretcher and compressor are large, heavy, and expensive. For these reasons, care must be taken in aligning them. Once the gratings are mounted, it is necessary to adjust them so that the grooves run vertically, and so that the surface is normal to the table. To ensure vertical grooves, we diffracted a leveled beam from the mode-locked oscillator off of the grating and used a long construction level to ensure that the diffracted line was horizontal. To ensure that the face of any of the optics are normal to the table, we aligned a HeNe through two irises separated by a long distance and adjusted the mirrors until the beam was reflected back through the irises. A similar method was used to align the retro-reflectors in the stretcher and compressor.

After these preparations, we positioned the optics according to (Figure 42). The input beams to the stretcher and compressor strike the diffraction grating at 56.16° and 53.0°, respectively. These angles and the distances shown in the figure were extracted from my ray-trace model of THOR. To determine the angles for the alignment HeNe beams, I used the grating equation, which relates the incident angle θ_i and the diffracted angle θ_m (relative to the grating normal) to the diffracted order m, the wavelength λ, the index of refraction of the surrounding medium n, and the distance between grooves d.

$$Sin(\theta_m) - Sin(\theta_i) = \frac{m\lambda}{nd} \tag{4.16}$$

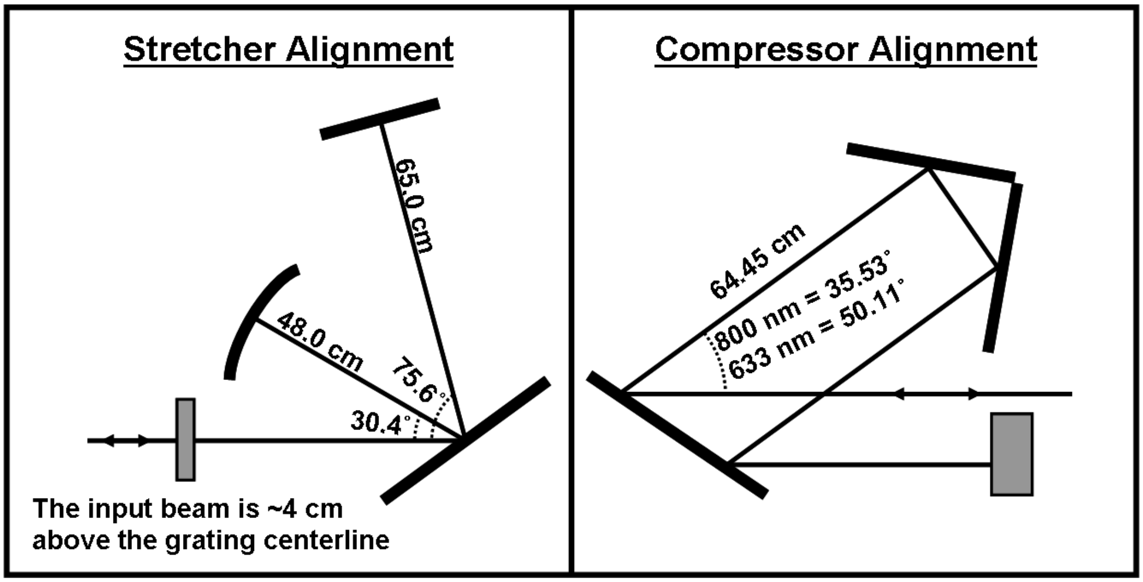

Figure 42. Diagram showing the alignment of the THOR stretcher and compressor (February 18, 2003).

Calculations for the THOR system were performed assuming a surrounding medium of air with an index of refraction of 1.000877. An alignment beam from the oscillator, at 800 nm, or from a HeNe at 633 nm, can be used with multiple irises to define the orientation of the optics. We used the grid on the table to position the irises at their precise locations, and then moved the optics until the beams transmitted through the irises.

In order to optimize pulse compression once the laser was built, we undertook a program to systematically scan the compressor grating angle and then optimize the rooftop mirror spacing for each position. A full scan range of ~3 degrees (Figure 43) provided enough change that we could find the approximate position which should yield a minimum pulse width.

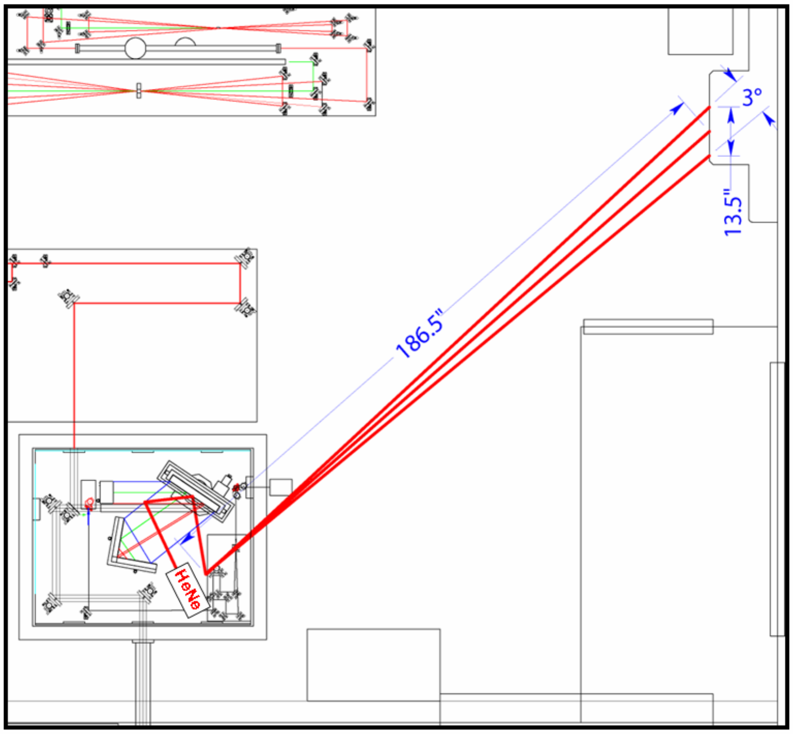

Figure 43. Layout of the HeNe beam used for scanning the compressor grating angle to optimize pulse compression.

4.4.2 REGENERATIVE AMPLIFIER ALIGNMENT

When building the regen from scratch, or replacing components, it can take a while to get the cavity into good alignment. Our method involved using the stretched seed beam, although a HeNe can be used. In my experience, the attenuation of the HeNe from the dielectric mirrors made the use of the 800 nm seed pulse necessary. We reflected the seed off of the crystal face down a line on the table. We placed two irises toward each end of the cavity, and centered them up on the beam. Next, the flat reflecting mirror was centered on the beam and adjusted so that the beam passed back through both partially closed irises. Finally, the curved mirror was centered on the beam and adjusted so that the beam traveled back through the irises. A rough alignment was done with the IR viewer, but precise alignment was performed while looking at the spots transmitted though the flat mirror to a CCD camera. Once the spots were centered, the cavity was *very* close to alignment.

4.5 Pre- & Post-Pulses

It is important to be able to measure the laser pulse from THOR so that we can better understand the laser-target interaction that takes place. We need to know not only the peak intensity and pulse width, but also the amplitude and position of any pre-pulses. We have built and used several diagnostics for measuring these properties.

4.5.1 SPECTROMETER

Although a spectrometer doesn't directly measure the temporal structure of the laser pulse, it can be used to estimate the structure based on the Fourier transform relationship between time and frequency. For example, when analyzing the spectrum of the amplified THOR laser, at one point we noticed that it contained a slight modulation in the amplitude. By analyzing the Fourier transform of two short pulses separated in time by *dt*, we can find a relation between spectral modulation and temporal separation of the pulses to compare with the measured data. First, we define the envelope of the electric field of two Gaussian pulses as

$$E_1(t) = \sqrt{\frac{1}{\pi}}\cdot\frac{1}{T}\cdot e^{\left(\frac{-t^2}{T^2}\right)} \tag{4.17}$$

$$E_2(t) = \sqrt{\frac{1}{\pi}}\cdot\frac{1}{T}\cdot e^{\left(\frac{-(t-\Delta t)^2}{T^2}\right)} \tag{4.18}$$

The Fourier transform of the electric field gives us the spectrum of the pulse

$$E_1(\omega) = \int_{-\infty}^{\infty} E_1(t)dt = e^{-\frac{1}{4}(\omega\cdot T)^2} \tag{4.19}$$

$$E_2(\omega) = \int_{-\infty}^{\infty} E_2(t)dt = e^{-\frac{\omega}{4}\left(4i\cdot\Delta t+\omega\cdot T^2\right)} \tag{4.20}$$

The spectral intensity of the two pulses is

$$\begin{aligned} I(\omega) &= \left|E_1(\omega)+E_2(\omega)\right|^2 \\ &= e^{-(i\cdot\omega\cdot\Delta t)-\left(\frac{T^2\omega^2}{2}\right)}\cdot\left(1+e^{i\cdot\omega\cdot\Delta t}\right)^2 \\ &= 4Cos\left(\frac{\omega\cdot\Delta t}{2}\right)^2 e^{-\frac{1}{2}(\omega\cdot T)^2} \end{aligned} \tag{4.21}$$

This is simply a Gaussian intensity envelope, with a cosine-squared modulation imposed. Two consecutive maxima or minima are separated by 2π, which allows us to solve for the wavelength in terms of the temporal separation.

$$\frac{\Delta t\cdot\omega_1}{2} - \frac{\Delta t\cdot\omega_2}{2} = 2\pi \tag{4.22}$$

$$\frac{1}{\lambda_1} - \frac{1}{\lambda_2} = \frac{1}{\Delta t\cdot c} \tag{4.23}$$

$$\Delta\lambda = \frac{\lambda_o}{\frac{c\cdot\Delta t}{\lambda_o}-1} \tag{4.24}$$

Experimentally, we can easily measure the pulse spectrum, so it is more convenient to express the temporal separation in terms of the spectral modulation spacing.

$$\Delta t = \frac{\lambda_o}{c}\left(\frac{\lambda_o}{\Delta\lambda}+1\right) \qquad (4.25)$$

Before we installed the 5-pass Ti:sapphire crystal into a goniometer mount (to carefully align the rotation) (Figure 44), we measured a modulation separation of ~ 3.9 nm. Using equation (4.25) reveals a pulse separation of ~ 550 fs, which was verified using the 2nd order autocorrelator. Once the goniometer was installed, we carefully adjusted the rotation of 5-pass crystal about its z-axis so that the modulation was minimized. The modulation arose because of to the differing indices of refraction along the different axes of the Ti:sapphire crystal. As the seed pulse passed through the crystal, part of the pulse was along the fast axis, and part of it was along the slow axis, thus generating a post-pulse.

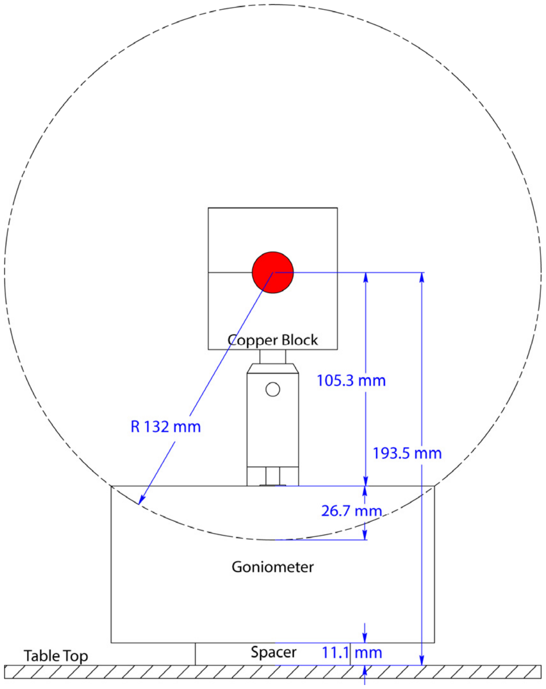

Figure 44. Diagram showing the spacing and layout of the goniometer mount for the 5-pass Ti:sapphire crystal. The center of the crystal needs to be placed at the center of the rotation axis of the goniometer.

4.5.2 2$^{\mathrm{ND}}$ ORDER AUTOCORRELATOR

The second diagnostic that we have to measure temporal information from the laser pulse is a 2nd order autocorrelator. This diagnostic is useful for measuring the pulse length and pre/post-pulse structure of an ultra-short laser. Knowing the pulse length is useful in determining if the pulse is bandwidth limited (a measure of the quality of compression), and it is also needed to calculate the intensity of the pulse. In order to measure pulses in the femtosecond to picosecond range, we must use the pulse itself as the detector. One way to do this is with a 2nd order single-shot autocorrelator.

In an autocorrelator, the pulse is combined with itself in such a way as to provide information on the correlated signal, thus it is an autocorrelation. A single shot autocorrelator overlaps two copies of the pulse at slight angle with respect to each other in a non-linear medium (Ishida, Yajima et al. 1985). Here, the non-linear medium allows the generation of second harmonic light only when the two pulses are overlapped inside of the crystal. Because of the tilt between the two beams, temporal overlap between the beams is translated into spatial overlap, which can be measure using an ordinary CCD camera. The spatial width of the autocorrelation on the detector is related to the temporal width of the autocorrelation of the pulse, based on the geometry of the setup.

In order to de-convolve the actual laser pulse width from the autocorrelation width, it is instructive to examine the problem with analytical equations. The autocorrelation of a laser pulse is defined as:

$$C(\tau) = \int_{-\infty}^{\infty} I(t)I(t-\tau)dt \tag{4.26}$$

Using the definition of a Gaussian pulse from equation (4.3) gives the following result:

$$C(\tau) = \int_{-\infty}^{\infty} A_o{}^4 e^{-\frac{2t^2}{\tau_p{}^2}} e^{-\frac{2(t-\tau)^2}{\tau_p{}^2}} dt \tag{4.27}$$
$$= A_o{}^4 \tau_p \frac{\sqrt{\pi}}{2} e^{-\frac{\tau^2}{\tau_p{}^2}}$$

The FWHM of this autocorrelation is

$$\Delta\tau = 2\tau_p \sqrt{\ln(2)} \tag{4.28}$$

,which leads to a ratio of the pulse width to the autocorrelation width of

$$\frac{FWHM_{pulse}}{FWHM_{AC}} = \frac{\Delta t}{\Delta\tau} = \frac{2\tau_p\sqrt{2\times\ln(2)}}{2\tau_p\sqrt{\ln(2)}} = \frac{1}{\sqrt{2}} \tag{4.29}$$

If, instead of a Gaussian intensity profile, we use a sech^2 profile ($I = A_o \operatorname{sech}\left(t/\tau_p\right)^2$, the time-bandwidth product and the autocorrelation correction factor become:

$$\Delta\nu\Delta t = \frac{4}{\pi^2}\operatorname{arccosh}\left(\sqrt{2}\right)^2 \approx 0.315 \tag{4.30}$$

$$\frac{FWHM_{pulse}}{FWHM_{AC}} \approx 0.648 \tag{4.31}$$

A figure showing an example 2nd order single shot autocorrelation of the THOR laser is shown with the averaged lineout in (Figure 45). Note that the de-convolution factor for a Gaussian pulse shape is used to be consistent with my choice of Gaussian pulses throughout this thesis.

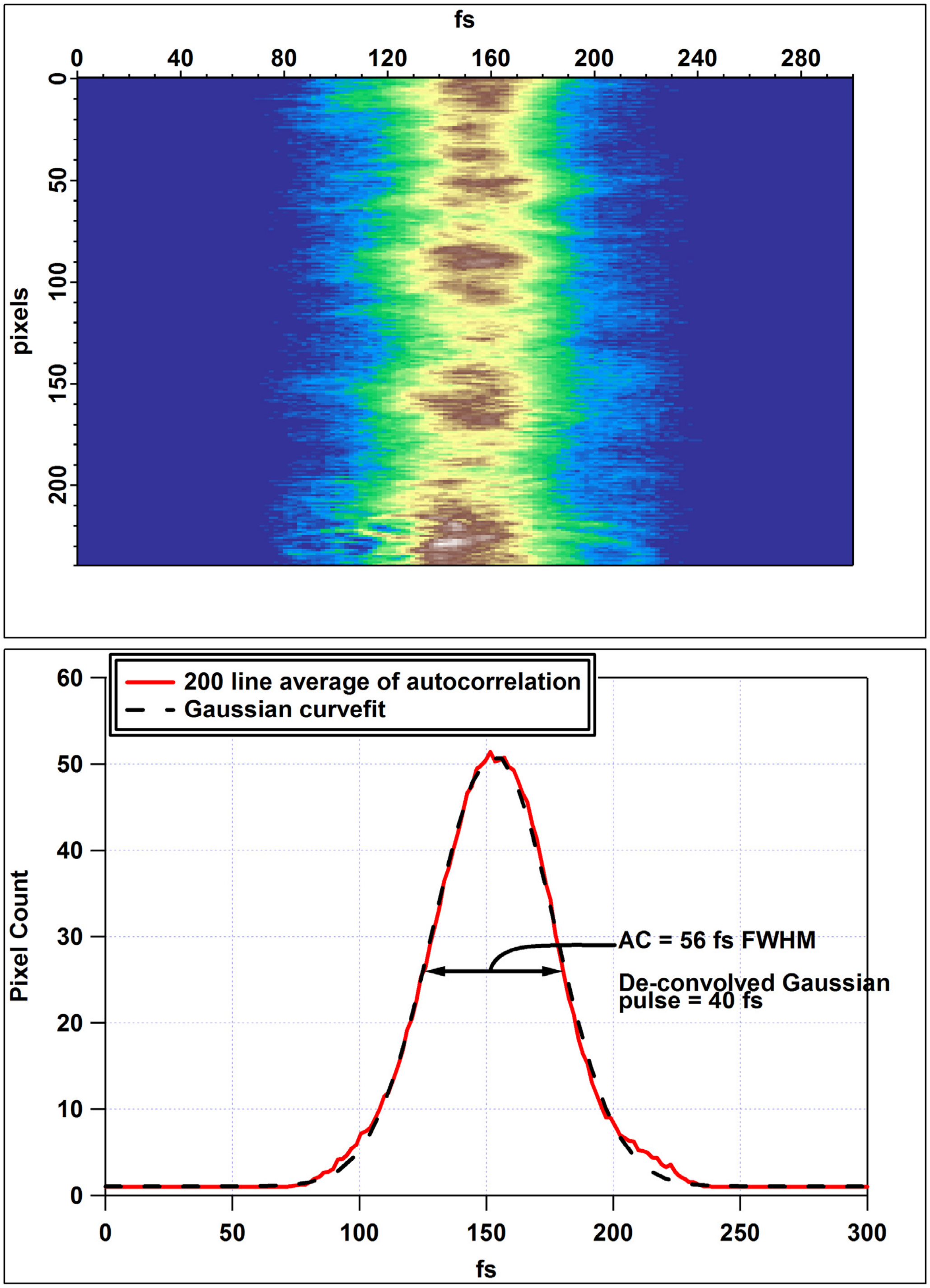

Figure 45. Second-order single shot autocorrelation data for THOR taken October 19, 2006.

4.5.3 3RD ORDER AUTOCORRELATOR

One problem with a 2nd order autocorrelator is that the resulting signal is symmetric about t_o. It is unable to distinguish a pre-pulse from a post-pulse because of this symmetry. The extension of an autocorrelator to the third order solves this problem.

In a 3rd order autocorrelator, the pulse is combined with a doubled version of itself. In practice, this works by first sending the pulse into a 2nd harmonic doubling crystal before splitting the two colors with a dichroic beamsplitter. Once the pulses are split, the delay between them needs to be adjusted before they are combined in a second non-linear crystal that generates a 3rd harmonic pulse. This 3ω pulse is a correlation between the 1ω and the 2ω, where the 2ω acts like a delta function that is swept across the fundamental pulse. It is this action that distinguishes between pre- and post-pulses.

The tripling process is weak, compared with the 1ω and 2ω pulses, so care must be taken to properly isolate the 3ω. In our setup, we reflected the 3ω off of two dichroic beam splitters before passing the pulse through at least three interference filters located before the PMT detector. We used ordinary glass microscope slides as attenuators in order to be able to measure the large dynamic range between the peak and the pre/post-pulses and the ASE.

The data from the third order autocorrelation THOR taken on Feb 21, 2006 is plotted in (Figure 46). Pre-pulses, those with negative time delay, provide the most trouble for experiments, since they modify the target before the laser arrives. However, it is likely that some of these pulses are artifacts from the optics in the autocorrelator. Unfortunately, we have not yet been able to absolutely identify those pulses.

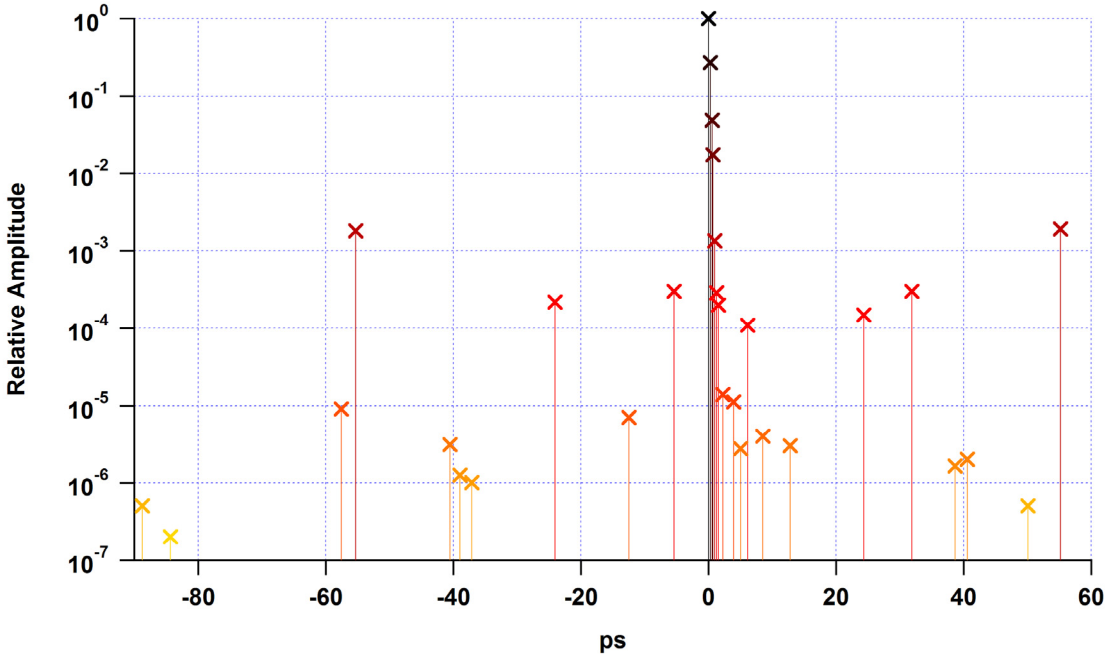

Figure 46. Third order autocorrelation data for THOR taken on Feb 21, 2006.

4.6 Future Improvements

Now that the laser has been in use for several years, there are a few changes and upgrades that could improve the laser operation. Some of these items may be difficult or impractical to implement, but never the less, they would be welcome additions to the lab. In particular, it would be very helpful in the day-to-day operation of THOR if we had a few more measuring devices installed in the laser.

Considering the trouble we have had with Pockels cells timing changes and accidental waveplate rotations, it would be nice to have a pair of photodiodes positioned after the post-regen slicer to measure the pulse contrast ratio out of the regen. This would a convenient way to measure the pre-pulses and ASE levels from the regen, which are dependent on the Medox and Lasermetrics Pockels cells timing.

It would also be useful to monitor the condition of the PRO lasers in real-time. A pair of CCD cameras could monitor the beam quality of the lasers, so we could quickly discover damage in the beams and observe the progress of damage once it occurs. Additionally, it would be helpful to install a pair of photodiodes or other detectors that monitor the Q-switched energy from the PROs. They could easily be calibrated with the power meter so that the health of the lasers could be quickly assessed several times throughout the day. It would also make it easier to optimize the SHG crystal in the lasers if a drop in power is detected.

Since we are adding a few more cameras, combined with the need for several cameral diagnostics in each experiment, it would be helpful to purchase one or more additional frame grabbers, so that multiple diagnostics can be operated concurrently.

Although these upgrades are not necessary, if money becomes available, they would certainly improve the laser operation, as well as helping to minimize and catch problems much faster than is currently possible.

CHAPTER 5. EXPERIMENTAL DESCRIPTION

The description of my experiments begins with preliminary steps that work toward the goal of detecting shock induced melting. First, the shock drive must be characterized to ensure repeatability and it must be calibrated so that the shock pressure is known in each experiment. To this end, I performed simulation of the laser-mater interaction and the subsequent hydrodynamic behavior, as well as acquired experimental data on the particle and shock velocities for comparison with published Hugoniots. To acquire this data, I developed and implemented a 2D short pulse interferometer that measured the displacement of the various target surfaces. Next, diagnostics for detecting melt must be developed and tested. For this reason, I studied the reflectivity of the shocked surface, as well as monitored the generation of third harmonics at the surface. These diagnostics are sensitive to the melt transition by way of the changing optical properties. Finally, the above diagnostics were combined with a characterized shock drive to attempt to observe shock melting.

5.1 General Experimental Layout

For all of the following experiments, I used the THOR laser system to both shock and probe my targets (Figure 47). As discussed in Chapter 4, THOR is a Ti:sapphire chirped pulse amplification system, with a Gaussian shaped stretched pulse width of ~ 600 ps FWHM. After amplification to ~ 1 J, the beam was split into two parts. Most of the energy was diverted into the shock driving beam (~700 mJ) which contained a delay leg that allowed the beam to arrive at the target at the same time as the probe beam. The probe beam was created by sending the energy not contained in the shock beam into the pulse compressor where it was compressed to ~ 40 fs before traveling to the target chamber. The short temporal duration of the probe pulse allowed the acquisition of time-resolved images of the rear surface using an ordinary CCD camera. In order to shock and probe a fresh surface for each shot, an XYZ translation stage was used to raster the target between shots.

Beyond these similarities, many of the experiments were performed with slight, but sometimes important, differences in the experimental layout. For example, early experiments using Goodfellow foils and some freestanding PVD foils (to be discussed in Section 5.1.3) were performed on an optical table in an ambient air atmosphere. Experience taught me that the shock driving laser with an intensity of order 10^{11} to 10^{12}W/cm^2 will ionize air and dynamically decrease the energy deposited in the target

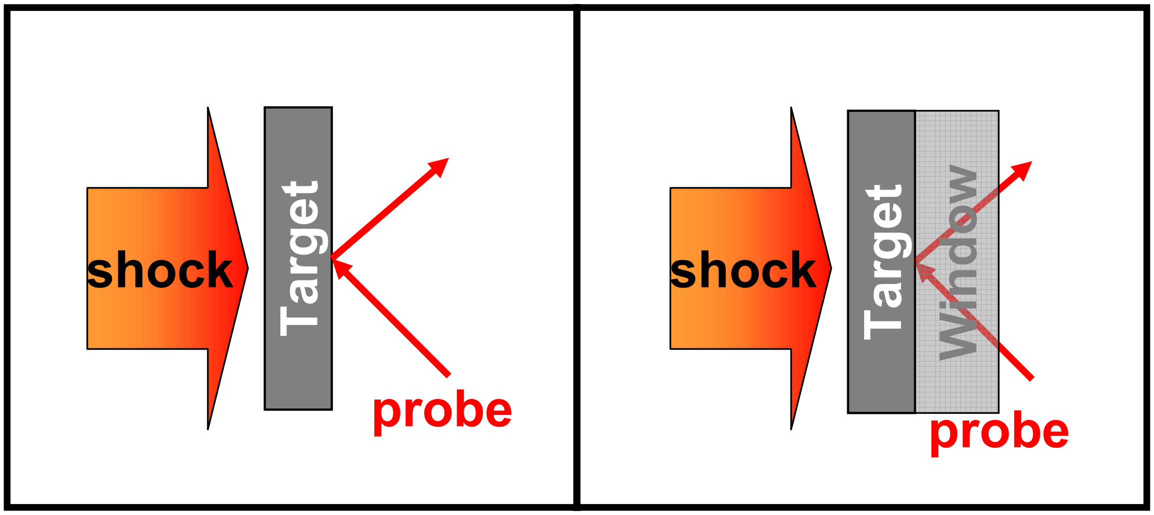

Figure 47. Diagrams showing the various target configurations. The shock driving laser is absorbed on the front surface of the target, which drives a shock wave through the material. The probe beam(s) are incident on the rear surface of the target where they interact with the shocked material. The targets that I shot consisted of Sn, Al, GaAs, or Si, while the window materials were soda lime glass (microscope slides) or (100) LiF.

material. To remedy this problem, experiments performed with PVD Sn and Al foils deposited onto glass microscope slides were performed with a flowing He atmosphere in the focal volume of the drive laser. The reason I switched to He is that it has a higher ionization threshold, and it was relatively cheap and easy to obtain. Experience with this setup revealed that the flowing He caused a significant amount of turbulence in the focal volume of the laser. This turbulence created shot-to-shot variations and distortions in the focal spot, thus making data less reproducible and more scattered.

The final experimental layout (used for Sn/LiF and Si targets) involved moving the target and focal volume of the pump laser into vacuum. In order to do so, I designed a vacuum chamber that would work with my multiple probe layouts (Figure 48 and Figure 49). Performing these experiments under vacuum removed the possibility of ionization of the surrounding atmosphere due to the pump and probe laser intensities.

A schematic of the chamber design is shown in Figure 50. It was constructed by the UT Physics Department machine ship from aluminum, primarily for weight purposes and ease of machining. The flanges all seal with o-rings, and their designs were copies of the flanges attached to the blue clamshell chamber in the THOR lab. This chamber was not designed for ultra high vacuum, which allowed the use of o-ring seals that permit easy connection of flanges and was determined to be superior to copper gaskets in this regard.

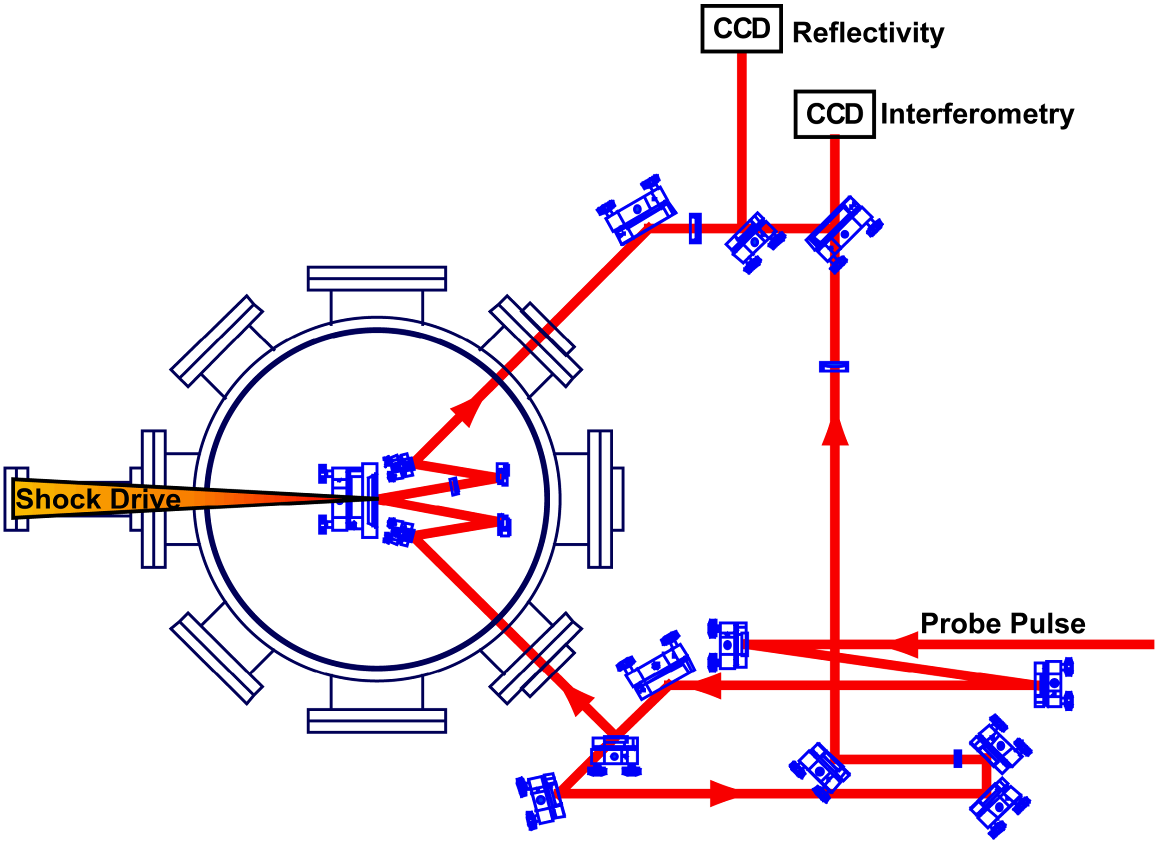

Figure 48. Experimental layout for shocked Sn/LiF experiments. The shock drive arrives from the left, and the probe pulse arrives from the right.

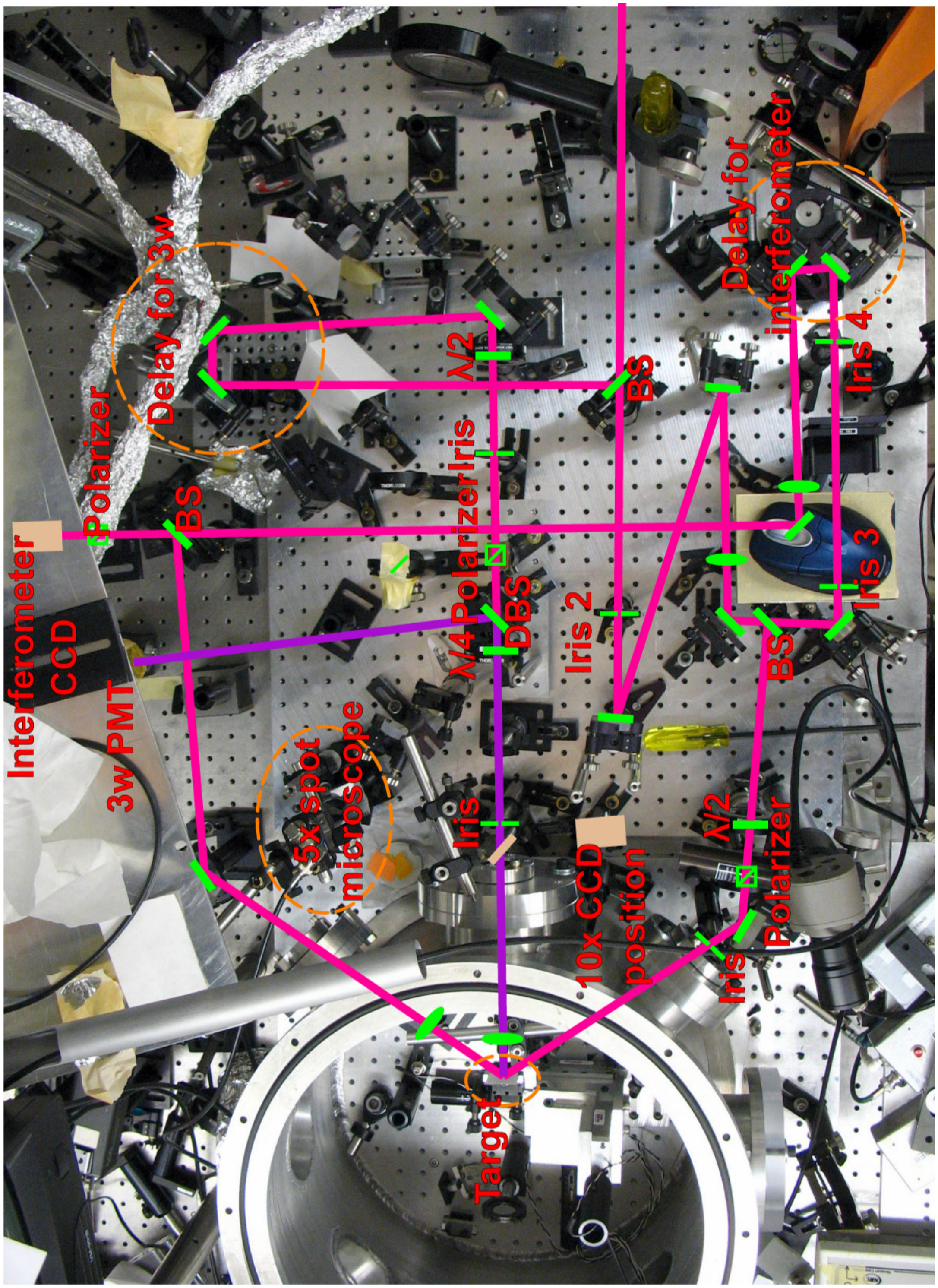

Figure 49. Annotated picture of the probe beam layout for the shocked silicon experiments

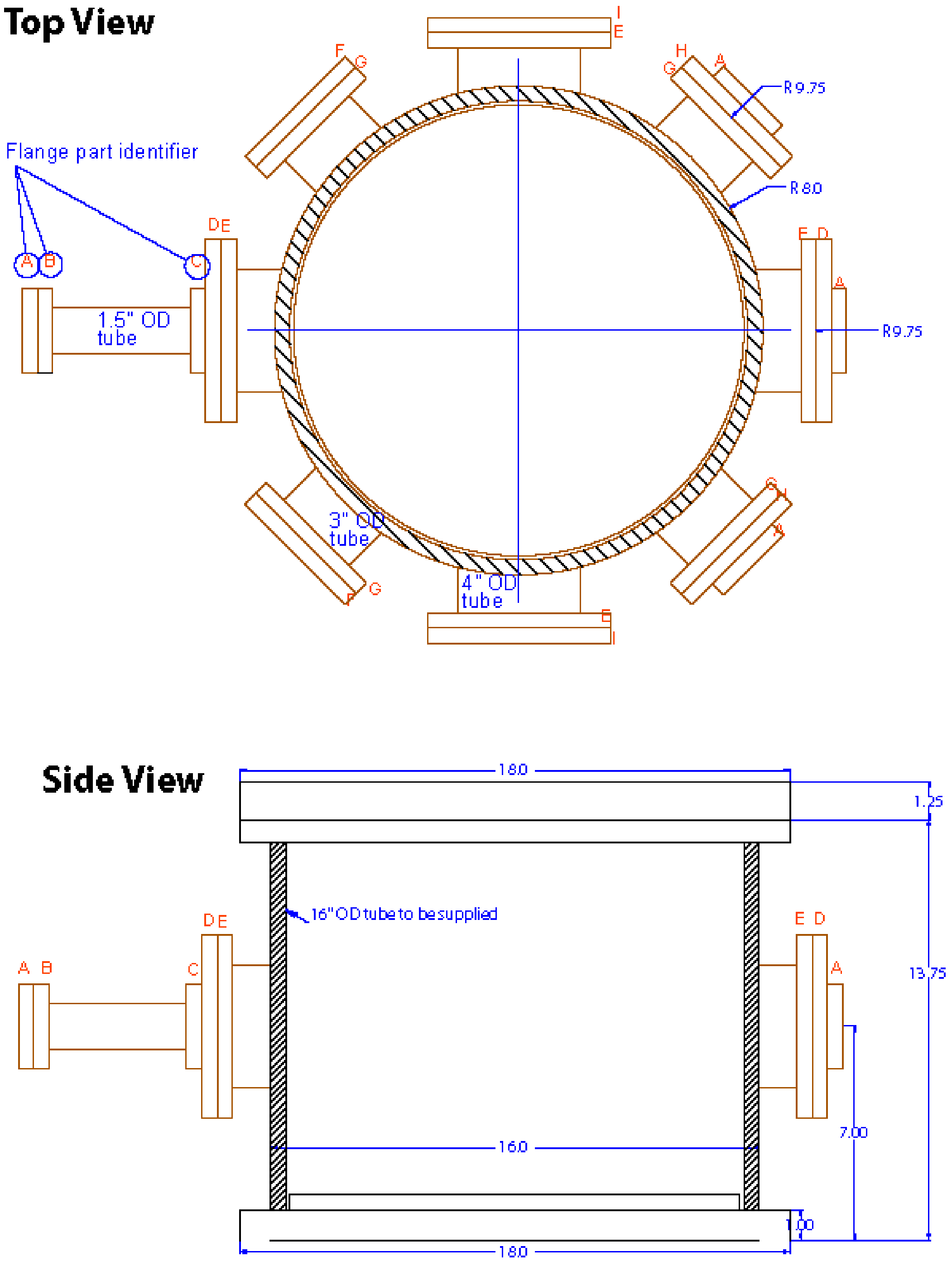

Figure 50. Drawing showing the design of the aluminum vacuum chamber using in my experiments. All units are expressed in inches.

5.1.1 SHOCK DRIVING LASER PULSE

In all of my experiments, the shock-driving laser was focused with an f/20 lens down to a diameter of between twenty and several hundred microns FWHM. This laser pulse drove an ablation-driven shock wave which traveled through the target (Trainor, Shaner et al. 1979). Since the energy in the pulse was more or less fixed, I used the spot size to adjust the laser intensity incident on the target. For the 4 μm Sn and Al foils, I typically used a spot size of order 100-300 μm (Figure 51). This created a laser intensity of order 10^{12} W/cm^2, and it helped create an approximately one-dimension shock wave. The spot size to target thickness ratio was much greater than the usual limit of 3 used to distinguish a 1D shock.

On the other hand, the Si wafers that I shocked were much thicker (10 – 95 μm), thus allowing the release wave to overtake the shock front, causing the shock wave to decay as it propagated through the targets. For this reason, I had to increase the laser intensity on the front surface so that the shock pressure remained high enough at the rear surface to probe the regions of interest. This led me to use much smaller spot sizes, of order 25-50 μm FWHM. The trouble with going to such a small spot is that the shock wave has two-dimensional effects due to the small width to thickness ratio. In this case, the shock wave not only decays with depth into the target due to the release from the front, but also decays from the edge effects from the sides.

5.1.2 PROBE LASER PULSE

The probe pulses used in my experiments typically had pulse durations of ~ 50 fs and energies in the 10 μJ to 1 mJ range, depending on how tightly the spot was focused. This led to probe intensities of order 10^9 to 10^{12} W/cm^2, where the lower intensities were typically used for reflectivity and interferometry, and the higher intensities were used to generate second and third harmonics.

After compression of the short pulse probe, the beam entered a delay stage located on a 1 m long rail. This stage allowed the relative timing between the probe and the shock to be adjusted. For coarse adjustments of several millimeters, I slid the cart on the rail and used the rail markings to determine the location. For fine adjustments down to

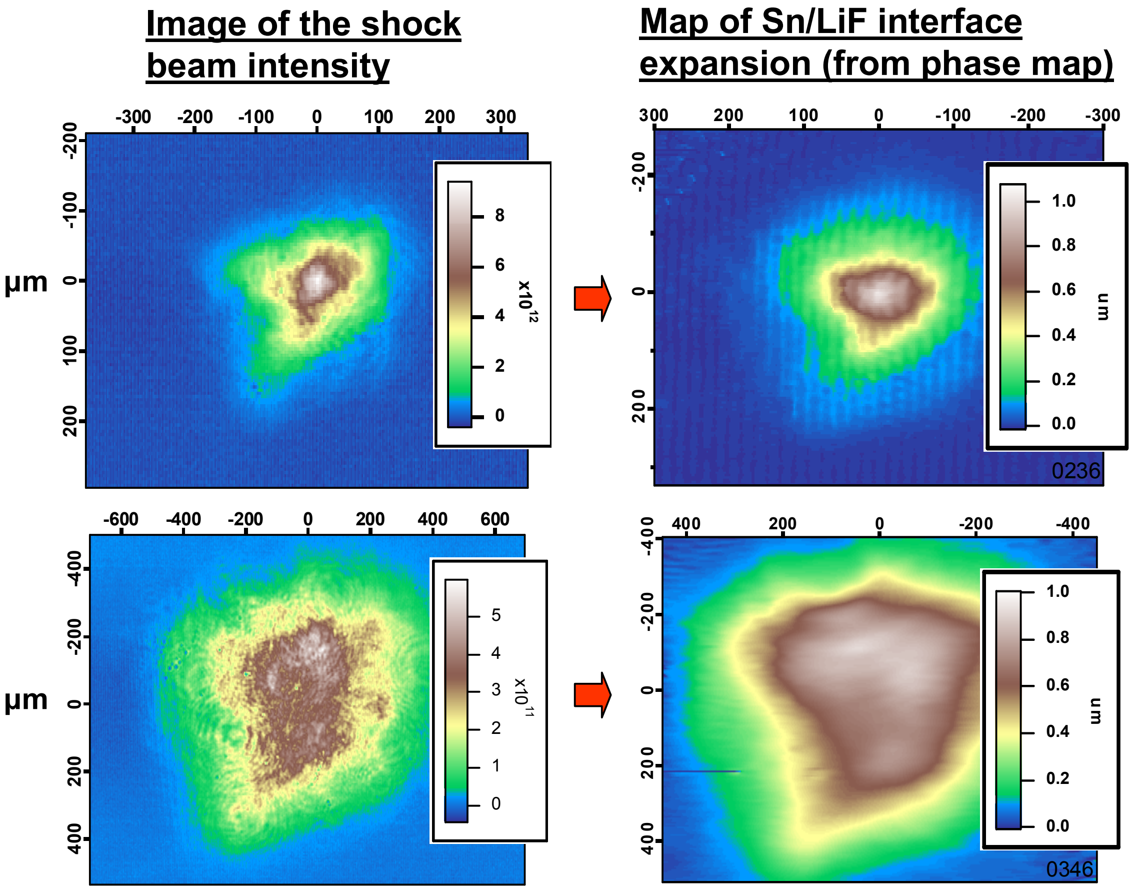
Image of the shock beam intensity

Map of Sn/LiF interface expansion (from phase map)

Figure 51. The left hand side shows images of the laser beam intensity at the plane of the target. The right hand side shows false color images of the expansion of the rear surface for each spot. Note that the intensity, shape, and size of the laser beam is directly converted into target expansion. This demonstrates the effective one dimensional nature of the shocks which is due to the large aspect ratio of spot size to the 4 μm thick targets.

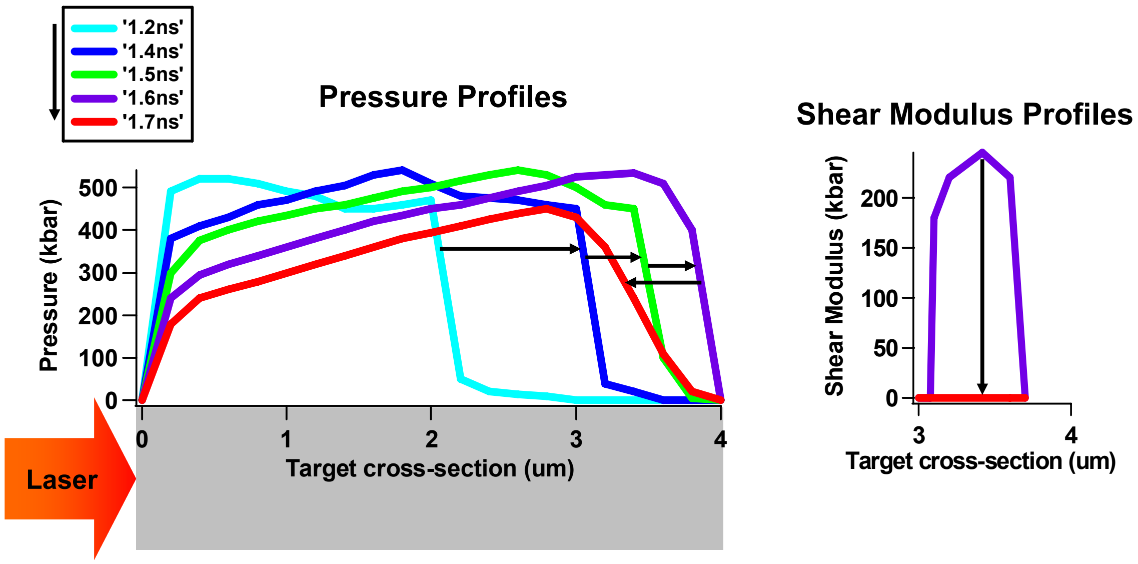

Figure 52. Results from a LASNEX hydrocode simulation performed by Jeff Colvin. The input parameters are: Laser = 1 J, 600 ps FWHM, 0.8 µm, with a 450 µm spot size. The target is a 4 µm thick Sn foil. The Hugoniot that Jeff used results in a shock melting pressure of ~ 490 kbar.

~ 10 µm, I adjusted the micrometer stage located on top of the cart. The alignment and timing procedures are discussed in much more detail in Appendix A.

5.1.3 TARGETS

To study shock induced melting, it is important to choose a solid material that will melt within an accessible pressure range. Because of this constraint, I chose to initially study Sn, due to the relatively low melting pressure of ~ 490 kbar (Figure 52). Jeff Colvin at LLNL ran simulations of shocked tin using parameters similar to what the THOR laser can achieve. The target thickness of 4 µm was chosen so that the shock would not have time to decay due to the 600 ps FWHM Gaussian temporal profile, but it would have time to steepen up into a shock.

Later experience in developing my THG diagnostic led me to explore semiconductor targets (Si and GaAs), since their non-linear susceptibilities are typically higher than those of many metals (Burns and Bloembergen 1971). For this reason, I have shocked and probed a variety of targets in many different configurations. In this section, I will elaborate on the specifics of each target, as well as provide information on how they were purchased or manufactured.

5.1.3.1 Tin

I studied free standing Sn targets so that I could examine the free surface behavior of a shock melted target, as in Jeff Colvin's simulations. Initial foils were purchased commercially from www.goodfellow.com, but they did not have sufficient thickness uniformity or quality. Their foils were produced by an electroplating process using a copper substrate, which left a very uneven free surface (Figure 53).

Discussions with Todd Ditmire led to making my own free-standing foils. This process involved coating a microscope slide with a diluted solution of liquid soap and water, before depositing the tin on the slide. After deposition, the foil could be "floated" off of the slide by immersion in water. It was sometimes necessary to encourage the foil to lift off of the glass with a razor blade, followed by gently shaking the submerged slide. As pieces of the foil floated off, they were captured using surface tension and installed on a specially designed mount for installation on the target holder. They were held onto the target holder with superglue or the force from the surface tension of a carefully placed drop of water

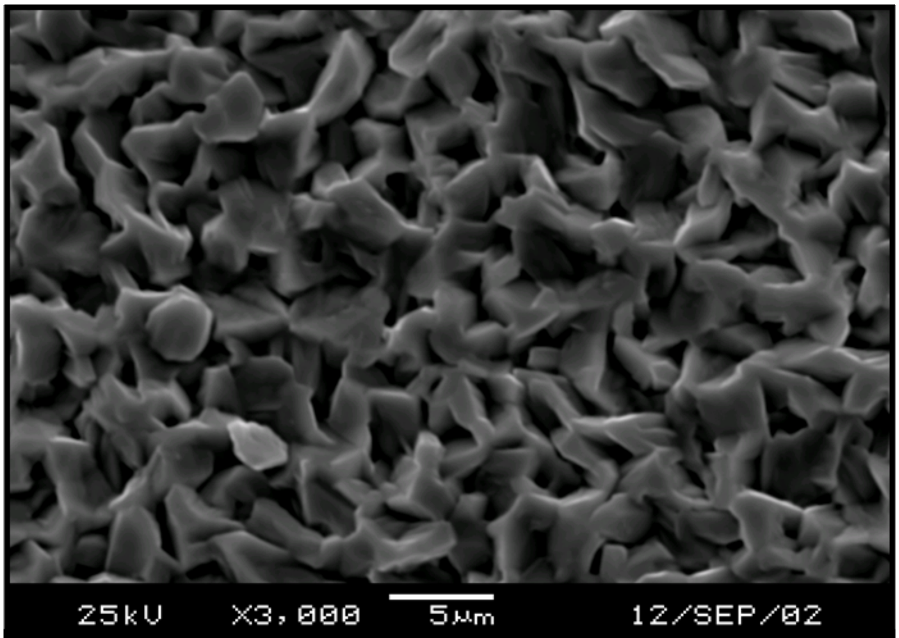

“Free” surface from electroplating process

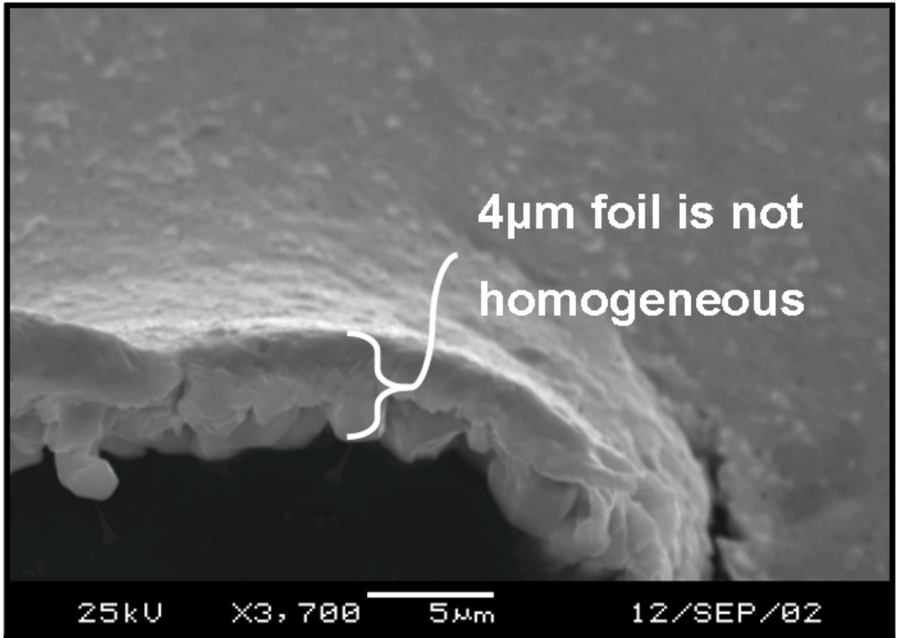

Cross section view

Figure 53. SEM images showing the rough surface and non-homogeneous cross-section of 4 micron thick tin foils purchased from Goodfellow.

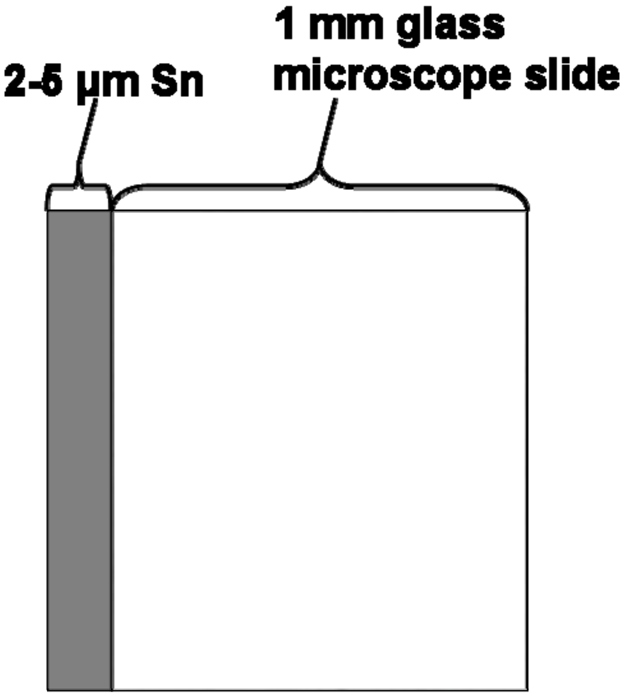

Figure 54. Diagram showing the cross section of the Sn/glass targets used in the experiments. The tin was deposited by thermal evaporation onto the face of an ordinary, soda lime glass, microscope slide.

The early deposited tin targets were made by a Physical Vapor Deposition (PVD) process, thermal evaporation, in the third floor cryogenics/vacuum shop of RLM. A resistive heating element located inside a vacuum bell jar heated a "boat" containing Sn above its melting point, 232°C. The evaporated metal traversed the vacuum and impacted glass microscope slides held above the source, where it cooled and re-crystallized (Figure 54). The process continued until the desired thickness of metal was deposited.

It was later discovered, after conversations with Alan Jankowski at LLNL, that leaving the substrates at room temperature will produce a less than solid density foil. However, if the substrates are held at an elevated temperature just below the melting point of the source metal, then the deposited metal will approach solid density

(Jankowski, Ferreira et al. 2005). This is due to the fact that metal vapor will tend to stick wherever it lands on a cold substrate, but it will retain some kinetic energy when landing on a hot substrate. This energy allows the atoms to migrate short distances on the surface to fill in the lattice and reach a lower energy state. Future target manufacturing should take this fact into consideration. Unfortunately, the third floor shop does not have the ability to heat substrates in the vacuum chamber.

5.1.3.2 Sn/Glass

While these floated foils were more uniform in density than the commercial foils, the macroscopic curvature and roughness of the foils made clean interferometry fringes difficult to achieve. It was primarily this reason which led us to the use of foils supported by a transparent window. The window was used as a support structure for the thin foil, and also as a medium to confine the rear surface of the target to prevent material ejecta. These targets were initially made by depositing the Sn directly onto glass slides, without the thin soapy film.

5.1.3.3 Sn/LiF

As per the above mentioned conversations with Alan Jankowski, it was necessary to find a manufacturer capable of depositing Sn on a substrate at an elevated temperature. Much searching led me to use Evaporated Coatings Inc. (www.evaporatedcoatings.com) for the deposition process. Single crystal lithium fluoride was used as a substrate window because it has been experimentally shown to be transparent up to at least 1.6 Mbar (Asay and Shahinpoor 1993). Also, transitioning to a larger 2" diameter substrate/target allowed for more data to be continuously taken while the chamber was under vacuum. The LiF windows (2” diameter, 6mm thick, (100) orientation) were purchased from www.crystaltechno.com and were sent off for coating. Although details of the exact process they used were unavailable, the foils did have a much higher quality than those produced in-house (Figure 55).

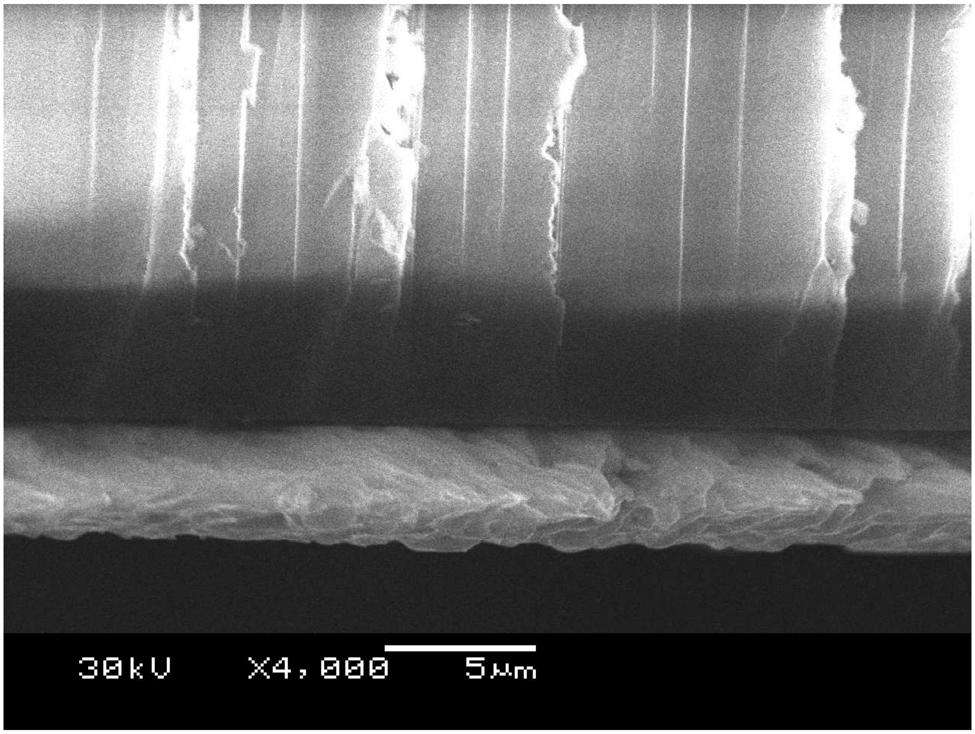

Figure 55. An SEM cross-sectional image of the Sn/LiF targets. This image is from a piece of LiF/Sn that fractured off of the main window which caused the fracture lines in the LiF seen in the top of the image, and the tearing in the Sn at the bottom. The Sn was e-beam deposited onto the face of an optical quality LiF window.

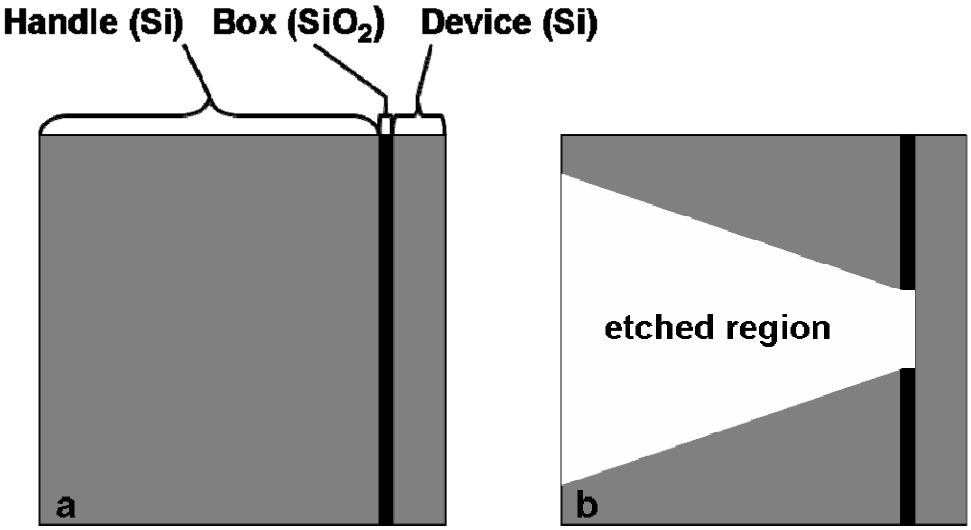

Figure 56. (a) a cross-sectional view of a silicon-on-insulator (SOI) wafer. (b) a cross-sectional view of a SOI wafer after wet-etching has produced a target.

5.1.3.4 Si

The Si targets were made by etching a silicon-on-insulator wafer (Figure 56). The wafers used in this experiment were purchased from www.ultrasil.com, and consisted of a thick handle (~500 µm Si), a thin buried oxide (box, ~ 1-5 µm SiO_2), and a device of various thicknesses (10-95 µm Si). In the etching process, regions of the handle were etched away to reveal the box. With a different process, the exposed box was then etched away while leaving the Si unharmed to reveal a small section of the Si device layer. It is this device layer that served as the target. A photo showing a section of the wafer with many target sites is provided in Figure 57.

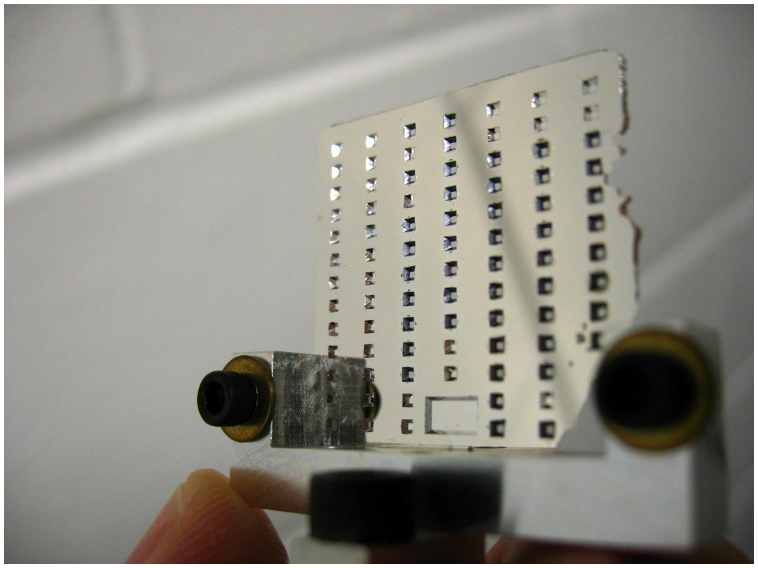

Figure 57. Photograph of a silicon target in a target mount. The Si wafer is approximately 3 cm x 3 cm, and the two black screws are size 4-40.

After completion of the etching processes, it was necessary to coat several skin depths of aluminum onto the front surface of the Si target so that the energy is absorbed at the surface, rather than throughout the bulk. This is because a shockwave is more quickly formed when energy is deposited in a smaller volume, rather than distributed over a larger volume, so it is better for the pump energy to encounter a material with short skin depth, rather than a long skin depth. The choice of Al over Si is due to the skin depth of 800 nm light in Si being ~ 10 μm, while it is only ~ 7.5 nm in Al. To ensure absorption at the surface, I typically used ~ 100 nm of aluminum as the absorptive layer.

5.2 Shock Wave Characterization

5.2.1 SIMULATIONS

For most shock experiments, it is beneficial to simulate the material behavior using modeling software. The material thicknesses and laser drive intensity can be input into the code so that approximate velocities and pressures can be extracted to guide the experiment. Simulations of both the laser-target coupling and of the subsequent shock wave evolution in the target were run using HYADES, which is a one-dimensional radiation and hydrodynamics code developed by Jon Larsen (Larsen and Lane 1994). It uses Lagrangian coordinates, where the frame of reference is inside the material, not in the laboratory frame. This code solves the hydrodynamic conservation equations and advances them over small time steps to simulate a given problem. In defining the parameters to run a simulation, the material is partitioned into n zones, whose coordinates are the surrounding $n+1$ mesh points. This staggered mesh is required for the finite difference equations to maintain stability.

5.2.1.1 Zone Size

One of the trickiest parts of running a realistic simulation is in picking the correct zone sizes. Unfortunately, as you increase the number of zones, the computational time increases very rapidly, so a balance must be found. In laser driven shock wave simulations, there are two main scale-lengths that define the problem. The first requirement is that the material cannot move farther than the width of the zone in one time step. This is known as the Courant limit. So, to increase the time resolution, the mesh points need to be closer together, thus increasing the number of zones.

The second important scale length is the skin depth of the laser in the target material. It is important that the incident laser energy get spread over several zones to produce a more accurate result. To do so requires that the first several zones be thinner than the skin depth. However, we cannot make all of the zones that thin, as HYADES limits the maximum number of zones to $<$ 999. Also, if we want the code to execute in a reasonable amount of time, we cannot have this many zones, and we can't have them all less than a skin depth.

To compromise, the zone thicknesses must be adjusted throughout the problem so that a balance can be found between execution time and accurate results. However, this adjustment needs to be smooth so that the finite difference equations remain stable. The smooth adjustment of the zone thicknesses is known as feathering. Feathering is the matching of each successive zone width with its neighbors to within a defined percentage. For example, a region feathered by 10% could have Δx_n = 1 mm, while Δx_{n-1} = 0.909 mm and Δx_{n+1} = 1.1 mm. More generally, the following equations define feathering:

$$\begin{aligned}(\Delta x)_n &= r(\Delta x)_{n-1} \\ &= r^{n-1}(\Delta x)_0\end{aligned} \tag{5.1}$$

$$\begin{aligned}T &= \sum_{n=0}^{NZ}(\Delta x)_n \\ &= \left(\frac{1-r^{NZ}}{1-r}\right)(\Delta x)_0\end{aligned} \tag{5.2}$$

Here, $(\Delta x)_0$ is the thickness of the first zone, T is the total thickness, NZ is the number of zones, and r is the feathering ratio. For increasing zone thicknesses, r > 1, and for decreasing thicknesses, r < 1. After taking a class at LLNL on the use of HYADES, I was given two differing recommendations on the maximum amount of feathering that should occur; Jon Edwards told us to keep feathering within 5% and Jeff Colvin suggested keeping it within 20%.

The last concern with zone thicknesses has to do with so called “mass matching” at an interface between two materials. It is important to adjust the zone size, by feathering or otherwise, at an interface between two different densities to maintain stability of the equations. Unfortunately, there is no way to mass-match across a solid-vacuum interface, so feathering down to small zones must be attempted.

Typically, a problem is started with large zones so that the user can obtain a rough estimate of the results within a short execution time. If everything appears correct, then the number of zones is increased. After obtaining these results, they are compared with the previous ones. If they agree, then the problem has converged to a solution with the given number of zones. If the results disagree, then the number of zones is increased, the problem is run again, and the process repeats.

5.2.1.2 Simulation Parameters, EOS, etc.

Other parameters that are necessary to adjust in a HYADES simulation include the equation of state, the ionization model, the material strength and/or melting models, and simulation control parameters, many of which are listed and discussed in the HYADES manual.

Discussion with Jon Larsen revealed the importance of adjusted the flux limiter parameter in simulations where there is a steep temperature or density profile. He believes that it should be ~ 0.05, which agrees with a published recommended value of 0.03 times the free streaming limit (Dendy 1993; Swift, Tierney et al. 2004).

I have found that the equation of state used in the simulation can have a drastic effect on the ability of the code to execute properly. For example, when I used HYADES

EOS 402 for laser induced shock waves in tin, I continually received an error message. After discussion with Jon Larsen, he became concerned about the validity of the EOS in my region of interest. After examining the EOS, by exporting the data with the HYADLIBM program, I discovered that there was very little data around the STP region and the code was having trouble interpolating the points in between. It was after this effort that I tried various equations of state, including the QEOS (More, Warren et al. 1988) and others from the SESAME library (Lyon and Johnson 1992), that I discovered the results were not very sensitive to the EOS used (except for an ideal gas EOS). I contacted the T-1 division of LANL (http://t1web.lanl.gov/newweb_dir/t1sesame.html) to obtain the non-classified SESAME EOS database so that I could try other tables.

An example of HYADES results, along with the target configuration used in the simulation, are shown in Figure 58. In this case, the pressure profiles at various delay times are plotted in laboratory coordinates. The results from this and more HYADES simulations are included along with experimental data in Chapter 6.

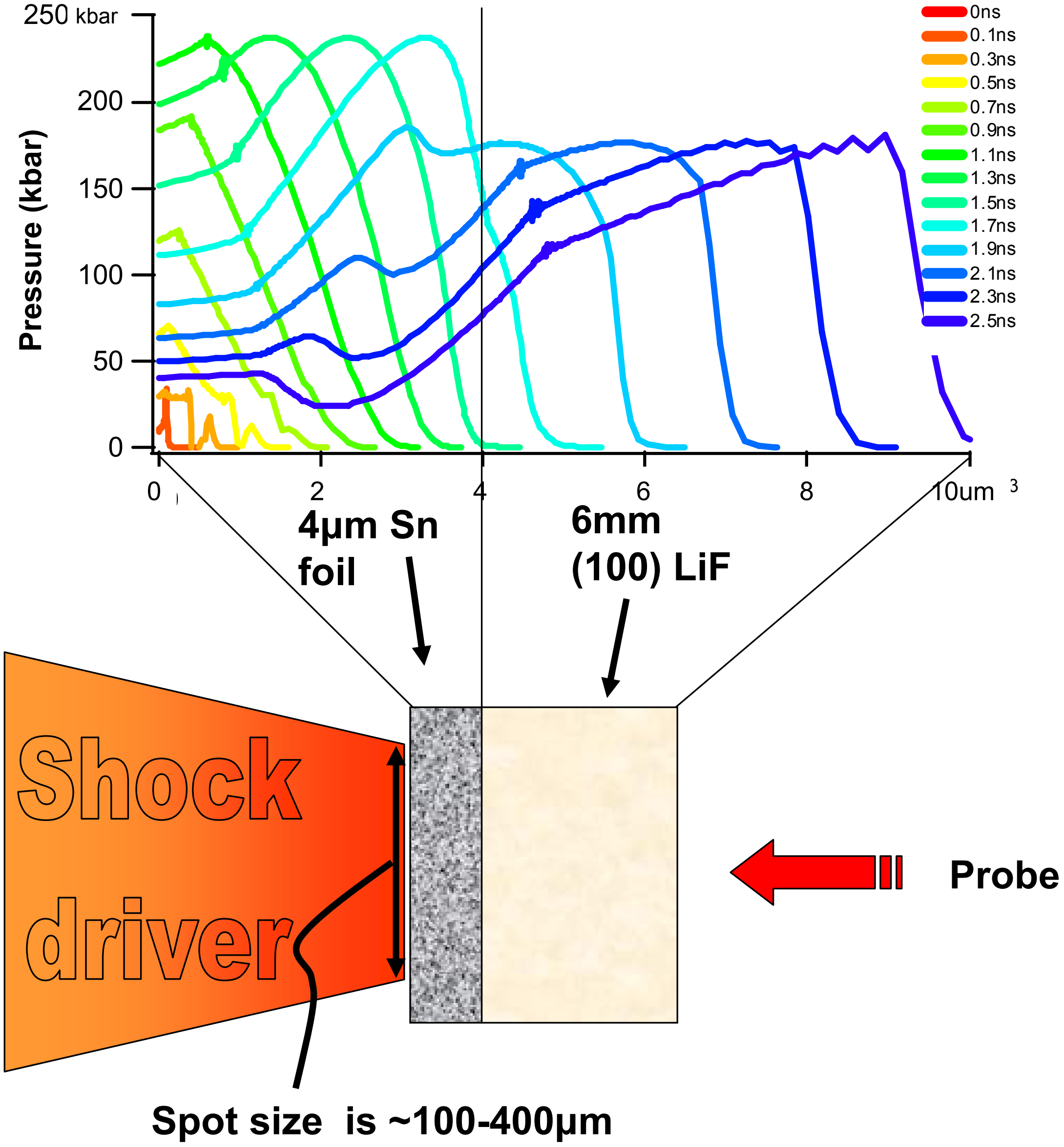

Figure 58. The top of this figure shows various pressure profiles from a HYADES simulation using a pump laser intensity of 8×10^{11} W/cm^2 with a 4 µm Sn slab backed by a thick LiF window. The pressure is partially releasing from the high impedance Sn into the lower impedance LiF across the interface of the two materials.

5.2.2 INTERFEROMETRY

The main diagnostic used to experimentally determine shock parameters was a 2D short pulse Mach-Zehnder style interferometer that probed through the back surface of the supporting window (if applicable) and reflected off of the target interface or rear surface. This displacement interferometer displays a shift in the fringe location where the surface expands, due to a change in phase between the reference and target arms of the interferometer. In the case of most of my experiments, which used a more-or-less Gaussian shock spot whose size was smaller than the probe, the phase due to the expansion changes somewhat smoothly up to the peak of the expansion. This 2D phase map (see Figure 51) provides spatial data on the expansion across the range of laser intensities contained in the pump pulse.

The target arm of the interferometer traveled into the vacuum chamber, reflected off of the target interface, and was then imaged onto the face of a CCD camera located outside of the chamber (Figure 48). The reference arm of the interferometer was located completely outside of the chamber and was adjusted to have equal imaging optics and equal optical delay to the probe arm. A combining beamsplitter was placed before the CCD, and adjustments were made to straighten and optimize the fringes on the camera. Before each shot was taken, a reference image was saved so that the change in surface position due to the shock wave could be measured accurately.

Additionally, to ease data analysis and aid in accuracy, it was beneficial to have smooth and straight fringes in the reference image. In order for this to occur, I estimate the surface flatness needs to be < ~ 3 μm across the region of interest. Surfaces with optical quality specifications, such as the glass slides and LiF windows, produce very flat and smooth surfaces that easily create a linear phase ramp on the CCD. This linear ramp manifests itself as a screen full of straight fringes. Although I tried to use vertical fringes in my experiments, other orientations can be used if the analysis software is modified to handle the different orientation.

5.2.3 REFLECTIVITY

The reflectivity of shocked materials is sensitive to the conditions at the rear surface of the target. In particular, if a solid melts upon shock-loading, then the reflectivity is expected to change. Also, if the target rear surface fragments upon shock release, then the reflectivity is expected to decrease due to absorption and scattering of the probe light. Additionally, reflectivity serves as a nice monitor of the rear surface during target and laser beam alignment. It is these reasons that led me to include reflectivity as one of my diagnostics.

Although the reflectivity of the targets could be extracted from the interferometric data, it was often helpful to use a dedicated CCD camera to capture the reflectivity image. This was done by inserting a beamsplitter in the target arm of the interferometer so that a portion of the light imaged from the target surface was sent to the reflectivity CCD. Once again, a reference image was taken before each shot so that a normalized reflectivity signal could be obtained. Depending on availability of laboratory equipment, the CCD camera was occasionally a 16 bit camera, which provided a larger dynamic range, at the expense of processing and data transfer times. On other occasions, a normal 8 bit Pulnix, Sony, or Cohu camera was used.

In addition to the shock experiments, I also performed femtosecond laser-melting experiments where I used reflectivity as a diagnostic. For the latter experiments, I collected a CCD image of the target for the data, but for early experiments I used a focused probe beam that I imaged onto a Thorlabs DET210 photodiode. These early results did not provide spatial information, but they did provide nanosecond scale temporal information. These results are discussed in Chapter 6.

5.2.4 THIRD HARMONIC GENERATION

As discussed in Section 3.2.2.3, third harmonic generation from circularly polarized light is sensitive to the crystalline symmetry of the material. However, THG is typically a weak process, which makes it difficult to explore in the single shot nature of shock wave experiments. For this reason, I developed the THG diagnostic using a more repeatable and high repetition rate experiment. That experiment is the laser melting of semiconductors using femtosecond laser pulses. In these experiments, I monitored the linear reflectivity and THG from the surface of the Si or GaAs wafer while pumping the same side of the target with a laser fluence near the melting threshold. For GaAs, I also monitored SHG.

The THG diagnostic operates by measuring the third harmonic light generated in reflection at the rear surface of the target from a circularly polarized, normally incident, 800 nm probe. The THG was measured using a Hamamatsu UV sensitive side-on PMT biased to ~ -1000 V. The PMT was connected to our Tektronix oscilloscope to record the data. Initial data at low pressures were clean and noise free, so a simple ratio of the measured THG to the average reference THG provided the normalized data. However, when I studied higher pressures, the signal due to electronic noise, plasma light, and blackbody signal grew to be comparable in size the THG data, so I began saving the oscilloscope traces so that I could study the temporal signal to try to differentiate between THG and spurious signals. I found it quite helpful to view the probe and reference data on the same graph so that I could easily identify the location of the THG peak. These results will be discussed in Section 6.3.2. A picture showing the physical layout of this experiment is shown in Figure 59, while a schematic drawing is shown in Figure 60. The pump beam was a 40 fs pulse with a fluence of a few hundred mJ/cm^2 that was incident onto the target at an angle of ~ 17° off of normal. This pump pulse non-thermally melted the semiconductor in less than a few hundred femtoseconds. I utilized a wide angle, 58.5°, reflectivity probe to detect the large increase in reflectivity that occurs near Brewster's angle (Figure 26). At normal incidence, the circularly polarized harmonic generating probe was focused onto the target at a fluence less than 100 mJ/cm^2 to keep from damaging the target. The residual 800 nm not involved in THG was directed onto a photodiode so that reflectivity at normal incidence could be recorded.

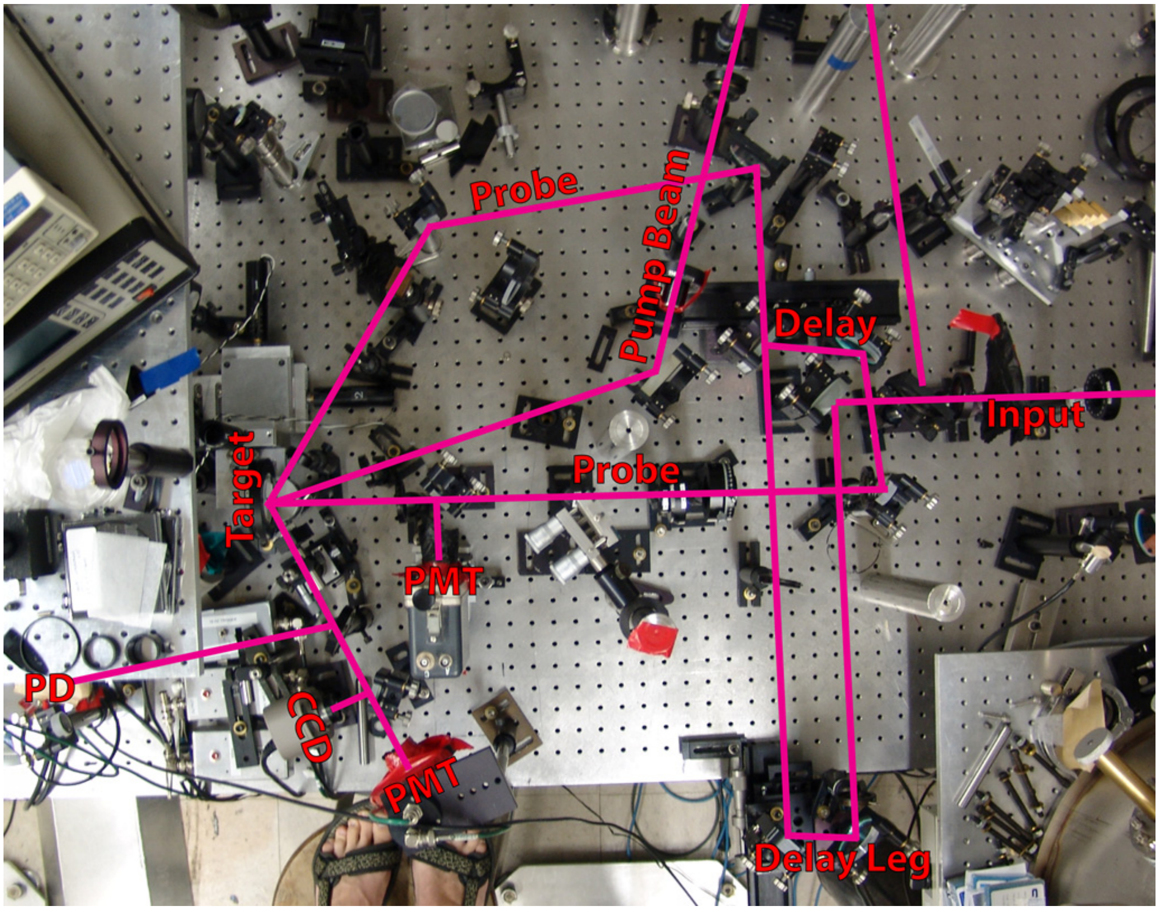

Figure 59. Photograph of the experimental layout of the femtosecond laser-melting of semiconductors experiments performed in air. The overlaid lines and labels describe the path of the various beams.

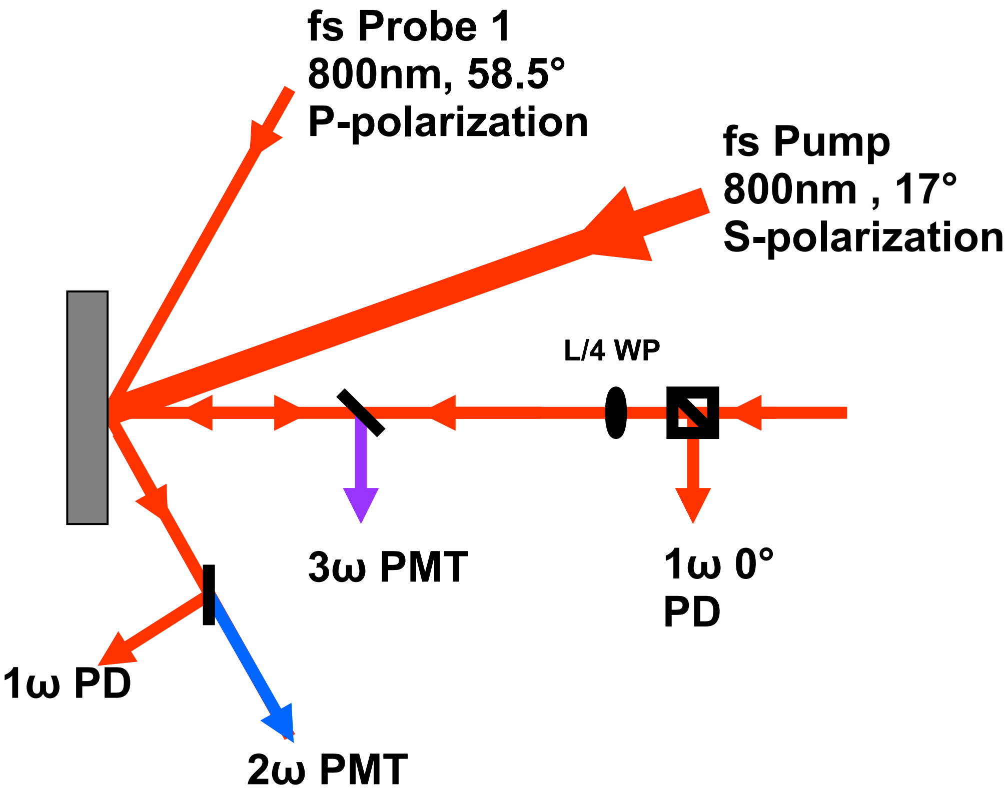

Figure 60. Experimental layout of the femtosecond laser melting experiment. The pump pulse melts the target in < 500fs. Probe 1 is a reflectivity probe that is sensitive to the large change in the dielectric constant of semiconductors upon melting. Probe 2 is used to generate third harmonic radiation at the surface of the target.

CHAPTER 6. RESULTS AND ANALYSIS

In this chapter, I present and summarize the data from my research on laser driven shock waves and detection of melting. I begin by discussing results from characterization of laser-driven shock waves in my various targets. Next, data and related analysis for the THG diagnostic are presented. I discuss the development and testing of the diagnostic using laser melting of semiconductors and show how these results demonstrate successful operation of the THG technique. After the diagnostic development, I discuss the data and conclusions from probing shock loaded silicon targets.

6.1 Shock Characterization

I explored a variety of Sn targets, as discussed in Section 5.1.3, using reflectivity and interferometry, when possible. Some target types produced relatively poor data, while some produced much cleaner data. Un-disturbed interferometric images from various targets illustrate the extremes in data quality, as shown in Figure 61. The Goodfellow foils are not flat enough to produce quality interferograms, and the free standing PVD foils produce mixed quality results. The targets that were attached to a backing window produced much cleaner fringes similar to those of an aluminum mirror. These were the Sn/glass, Sn/LiF, and semiconductor wafer targets.

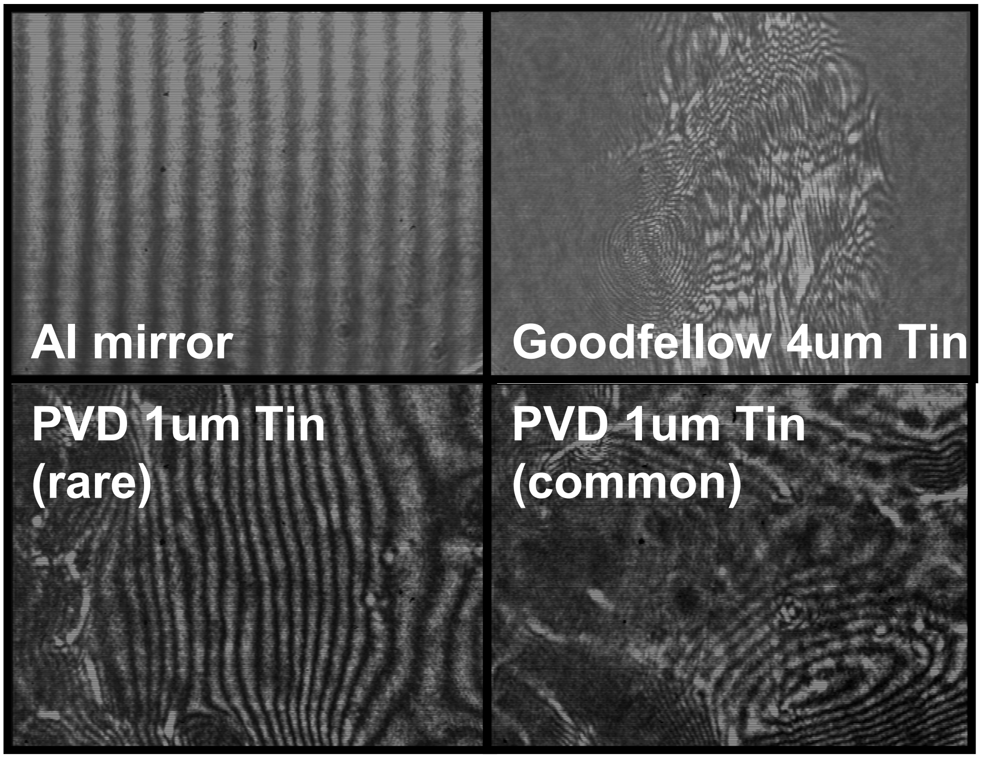

Figure 61. Images showing interferometric data from various target materials. The top left image shows very straight and uniform fringes from an inexpensive aluminum mirror, which was used as a reference. The top right image shows un-usable fringing from the structured foils purchased from Goodfellow. These foils did not have a mirror-like finish. The bottom two images show fringes obtained from free standing tin foils that were floated off of the glass substrate used in the PVD process. It was rare to find a section with relatively straight fringes, as it was much more common to find regions with distorted fringes. Although the PVD foils did have a mirror finish, residual stresses in the foils caused them to curl once removed from their substrates.

6.1.1 INTERFEROMETRY ANALYSIS

In order to extract useful results from the interferometric data, it must be processed to extract the phase. This section will discuss the procedures I applied to extract the phase, which I developed in IGOR (Wavemetrics).

My interferometric data was acquired using an 8 bit CCD camera connected to a frame grabber card (CyberOptics Imagenation PXC). The interlaced nature of the cameras we used, combined with the temporally short pulses of our lasers, produced images with data only on every other horizontal line (similar to analog TV signals). Deletion of these empty lines produces a rectangular array of data that is then ready for visualization and analysis.

The interferometer records shifts in phase between its two optical arms. It is this phase that we want to extract so we may determine the amount of expansion of the target. We use a procedure similar to Takeda *et. al*. to extract this phase (Figure 62) (Takeda, Ina et al. 1982). First, the data is Fourier transformed to produce the spectral amplitude and phase. The spectrum typically has a large peak near DC that can be ignored, and will have a symmetric peak on both sides of the origin near the frequency of the fringes in the image. It is the region around this symmetric second peak that we are interested in, so the spectrum is filtered by multiplying by a super-Gaussian filter with a width 5-10 times greater than the peak's width. The now filtered spectrum is inverse-Fourier transformed back to real space so that the amplitude and phase maps can be extracted. The amplitude is a measure of the target reflectivity, while the phase is a related to the observed fringe shifts.

The phase returned by the inverse Fourier transform is modulo 2π, so these discontinuities must be removed by a process called phase unwrapping. In the simplest case, unwrapping involves locating all of the phase jumps and adding or subtracting a multiple of 2π until the entire surface is smooth and continuous. In reality, the data is never clean enough for this process to produce a complete result.

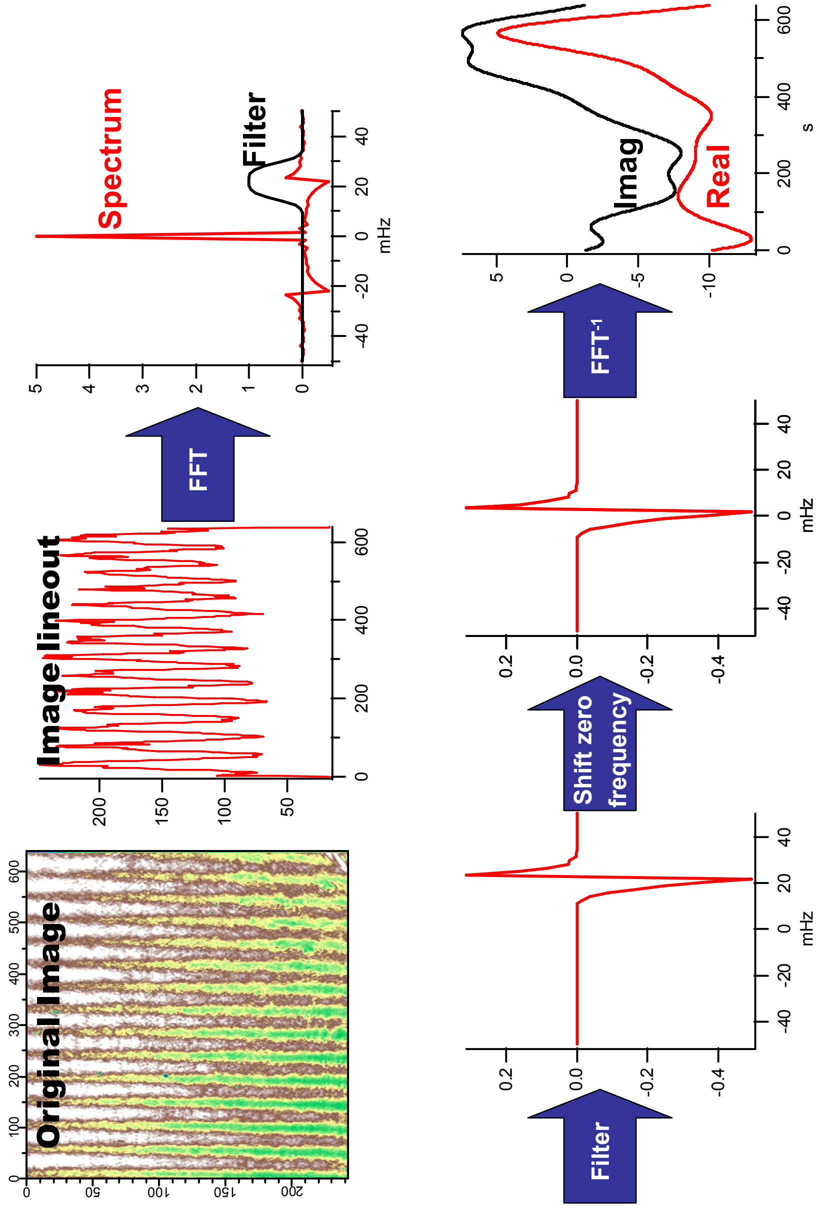

Figure 62. This diagram graphically illustrates the process of extracting phase information from a 2D interferometric image. First, I lineout is taken from the fringed image. It is Fourier transformed, and then filtered in spectral space. Next, the data containing frequency is shifted to zero to remove the rapidly varying phase ramp of the fringes. Finally, the spectrum is inverse-Fourier transformed to extract the phase and amplitude of the signal. The process is repeated until all of the lines have been analyzed.

Noise in the image, dust on the optics, and sharp phase jumps tend to break the unwrapping process such that a continuous phase map is not attainable. However, typical data can be processed with more advanced techniques to produce a more realistic phase map (Ghiglia and Pritt 2001). Ghiglia and Pritt's excellent book provides the C code for nine different methods of phase unwrapping. I compiled these source codes into command-line executable programs that I called from within IGOR. Through experience, I found that Flynn's minimum weighted discontinuity algorithm (Flynn 1997) provided the best results in a reasonable amount of time for the actual data interferograms. However, I typically used Goldstein's residue and branch cut algorithm (Goldstein, Zebker et al. 1988) or the quality guided algorithm (Bone 1991) to unwrap the reference shots more quickly than when using Flynn's method.

The unwrapped phase has a large linear component due to the slope of fringes across the image, but this background map can be removed by subtracting off the phase from an analyzed reference shot that was acquired before the shock. After the background subtraction, the remaining phase is indicative of target expansion. Equation (E.9), which is reproduced here, allows us to relate the phase to the distance that the target expanded, *d*,

$$d = \frac{\lambda \cdot \phi(x,y)}{4\pi n \cdot Cos\left(\theta\right)} \tag{6.1}$$

where n is the index of refraction in the window, θ is the angle of the probe beam inside of the window (relative to the surface normal), and $\phi(x,y)$ is the unwrapped phase shift from the analysis of the interferogram. The resulting displacement map reveals the shape of the rear surface expansion, from which the peak expansion, size of the breakout region, and slope of the expansion can all be determined.

In order to be consistent, I measured the peak expansion of the target, and not an average over the spot. Although there are variations of the peak, this method reduces the need to assume a certain shape of the expansion. This is important, considering that the shock beam profile tends to morph from shot to shot. If I only recorded the expansion at the "center" of the spot, the data would be more scattered due to the position of peak expansion drifting for each shot.

6.1.2 INTERFEROMETRIC DATA – TIN/SODA LIME GLASS

Interferometric data from experiments performed using Sn and Al foils has been analyzed as discussed above, and the peak expansion for each shot is plotted in the top of Figure 63. Each target's rear surface expansion data, represented by different colors, were fit by lines whose equations are included in the plot. The slope of the line is equal to the free surface velocity, which is approximately equal to twice the particle velocity (see Section 2.1.4). The particle velocities are then compared with the published Hugoniot to obtain the estimated pressures, as shown in red text on the plot. These pressures are lower than the expected melt pressure for tin (~ 490 kbar), so more experiments were performed to try to reach higher shock pressures.

6.1.3 INTERFEROMETRIC DATA – TIN/LITHIUM FLOURIDE

To reach higher pressures, I had to increase the laser intensity incident on the targets. In these experiments using Sn/LiF targets, I used five different laser intensities to drive shock waves into the targets. An example 2D interferogram is shown in Figure 64. I measured the displacement of the Sn/LiF interface as a function of probe delay for each of these five intensities. The maximum displacement that I could probe was limited by the fringe size relative to the shock spot, and also by the contrast between adjacent fringes on the CCD. For example, interferometric data for the 1×10^{13} W/cm^2 scan did not

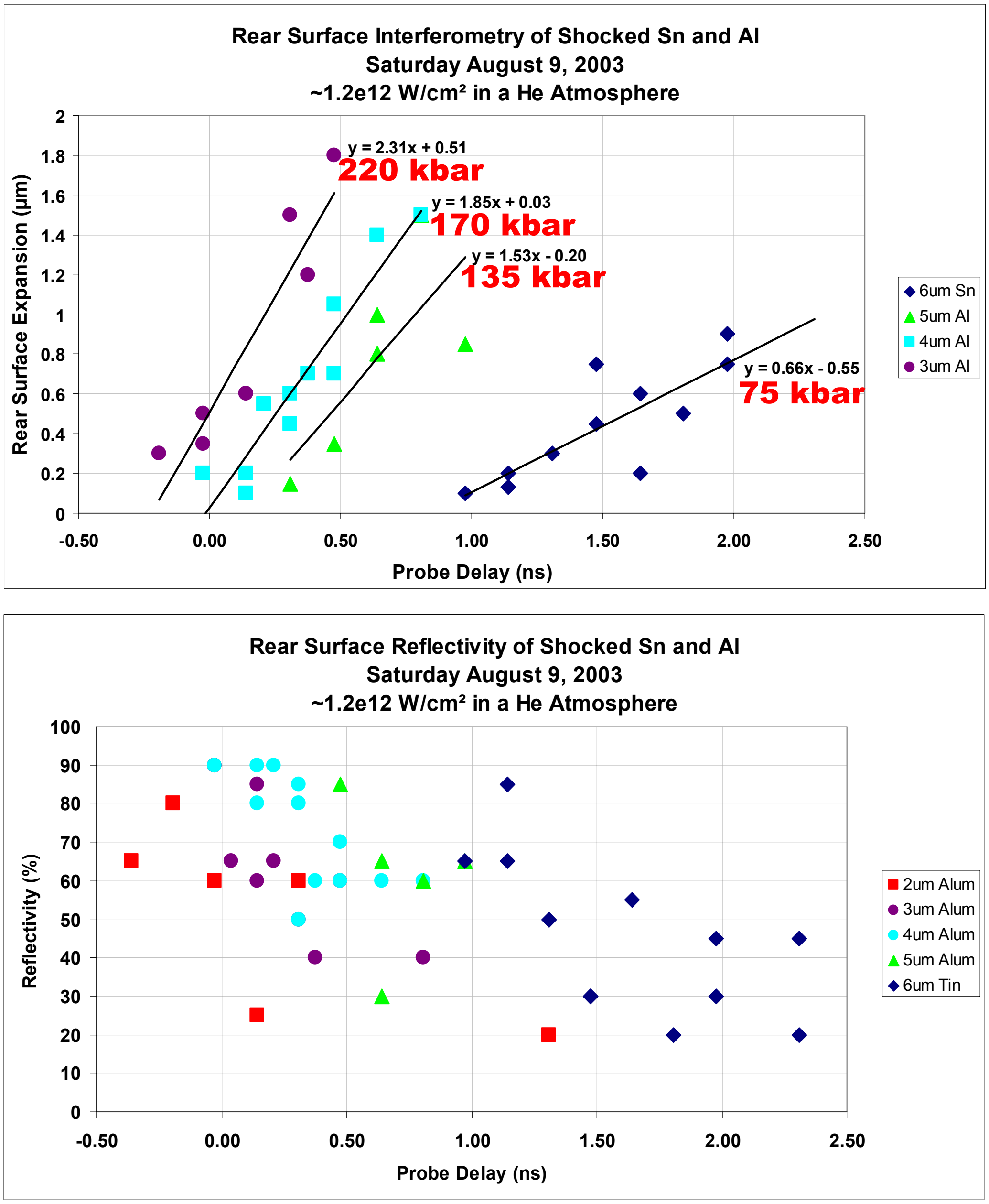

Figure 63. Plots showing data taken with shocked free-standing tin and aluminum targets. The top graph shows lines and equations for curve fits to each data set, along with estimated pressures taken from the Hugoniots. The bottom graph illustrates the drop in reflectivity that occurs for all targets in the experiment.

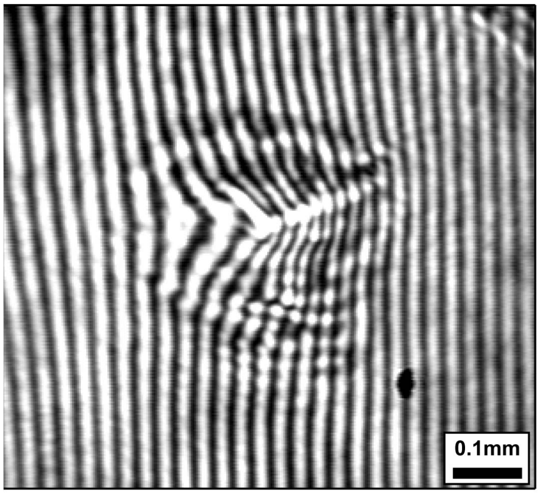

Figure 64. Interferometric image from the shock breakout of Sn into a LiF substrate. The laser intensity was 6x10^{12} W/cm^2 and the probe delay was 450 ps after the timing fiducial

extend past 0.6 μm because of the small spot size on the CCD. For the other scans, where the fringes were distinguishable, I was able to observe up to a 2.1 μm expansion.

As before, a line was fit to the linear portion of the expansion data, using a least-squares algorithm, to determine the particle velocity at shock breakout (see Figure 65). The shock impedance mismatch between the tin and the lithium fluoride was accounted for so that the interface velocity could be converted into a particle velocity of the bulk tin (Figure 66). This particle velocity was then combined with Hugoniot data for tin (Figure 5) to estimate the pressure observed at the interface within the target. This pressure is compared with results from HYADES simulations in Figure 67 and in Table 8.

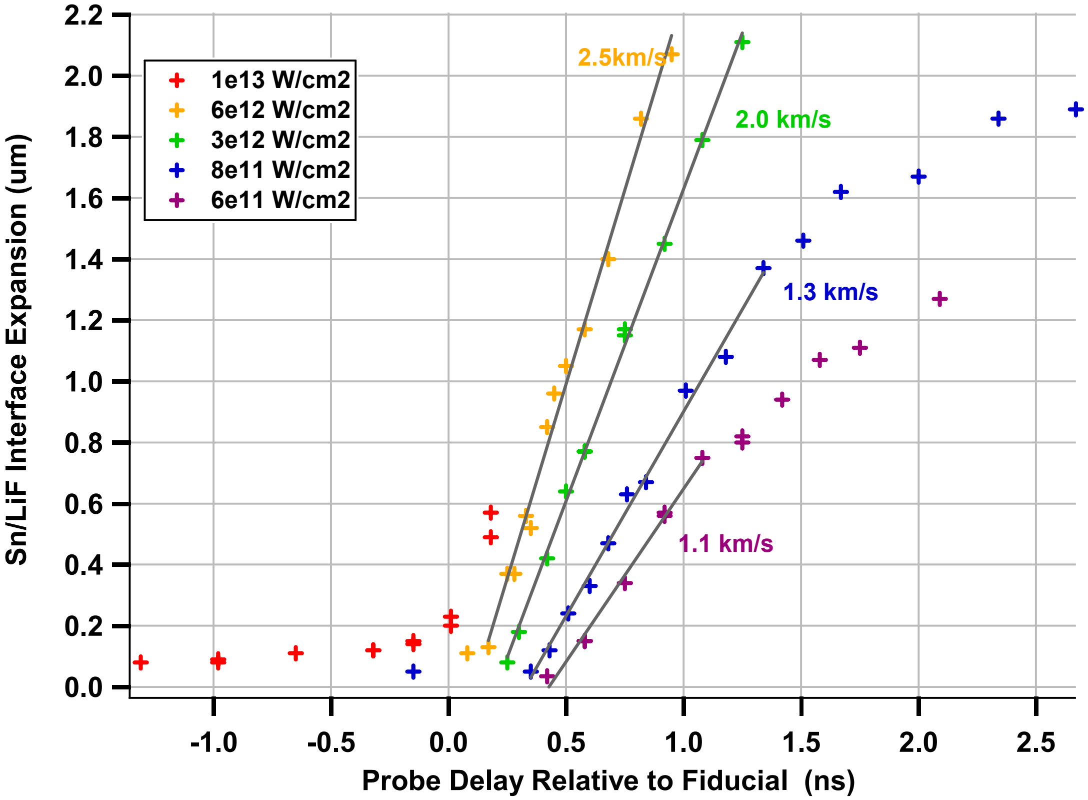

Figure 65. Plot showing peak interferometric expansion data from the interface of Sn/LiF targets. The various peak laser intensities are plotted in different colors, and least-squares curve fits to selected ranges of data are shown in gray. The particle velocities derived from the fits are listed next to each data set. For more data from the curve fits, see Table 9.

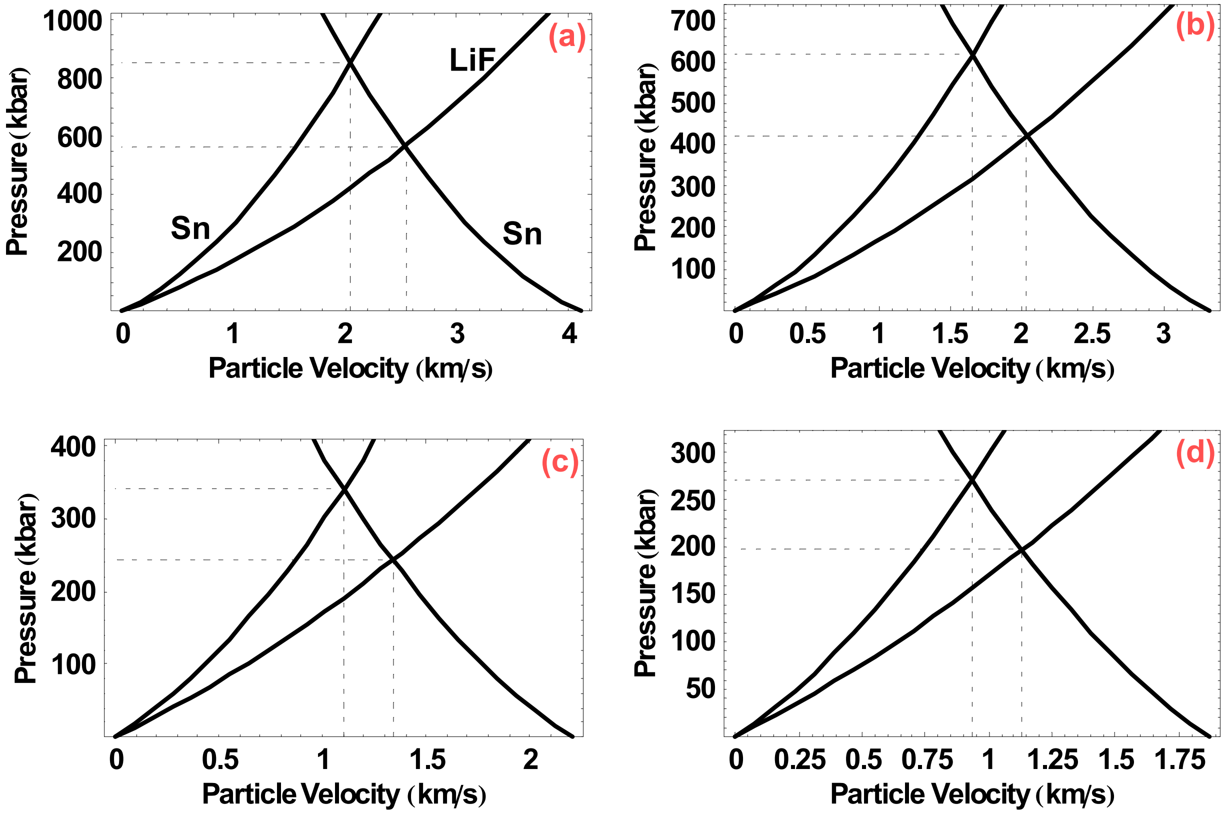

Figure 66. Pressure-particle velocity plots using the Hugoniots from Trunin and the interface velocities from the Sn/LiF data shown in Figure 65. The individual plots a, b, c & d correspond to decreasing laser intensities, starting with $6x10^{12}$ W/cm^2.

Table 8. Experimental Results Combined with Simulation Parameters

Incident Laser Intensity (W/cm^2)	**Pressure From Measured U_p Using the Hugoniot (±30kbar)**	**Laser Intensity Used in HYADES Simulation (W/cm^2)**	**Pressure From HYADES Simulation (kbar)**
$6x10^{11}$	271	$8x10^{11}$	237
$8x10^{11}$	341	$1.5x10^{12}$	380
$3x10^{12}$	617	$3x10^{12}$	645
$6x10^{12}$	853	$5x10^{12}$	950
$1x10^{13}$	N/A	N/A	N/A

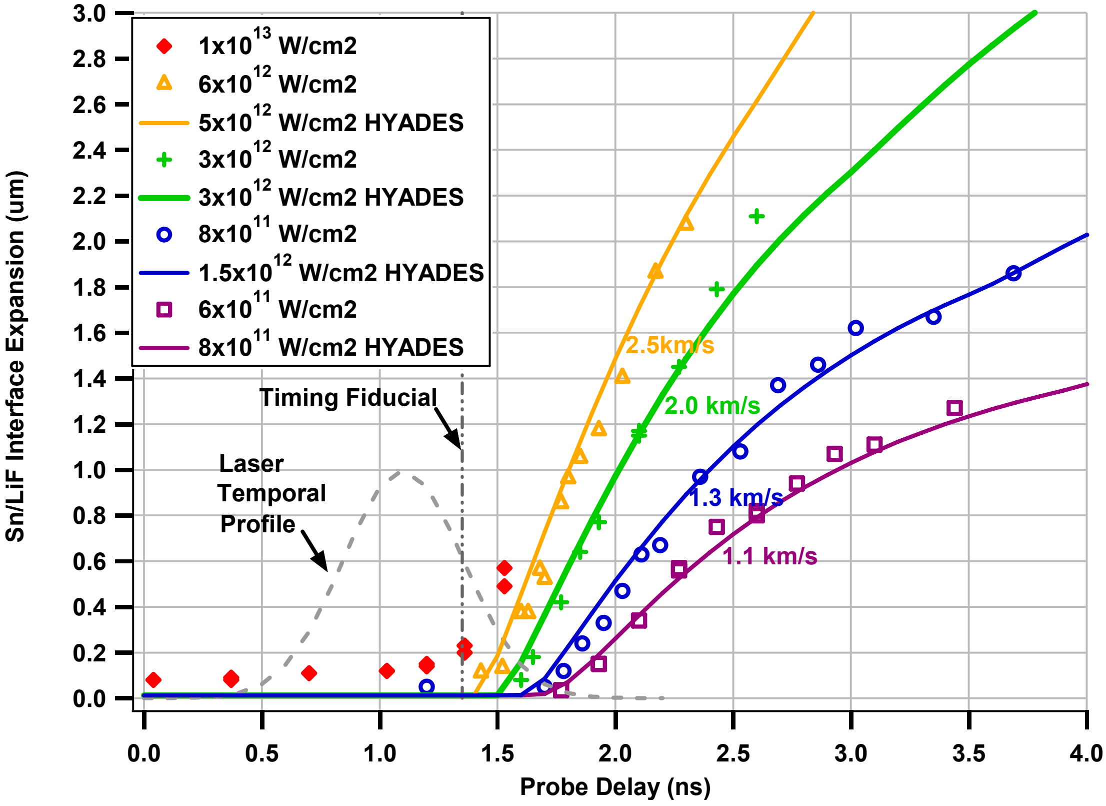

Figure 67 HYADES simulations (curves) are fit to four of the five Sn/LiF interface expansion data (symbols). The numbers printed next to the linear fits to the data (solid thin lines) are the slopes of the lines (i.e. interface velocities).

Table 9. Table of parameters from the curve fits to the Sn/LiF data plotted in Figure 65.

Incident Laser Intensity (W/cm^2)	Sn U_p (µm/ns)	ΔU_p (µm/ns)	$t_{transit}$ (ns)	$\Delta t_{transit}$ (ns)	$t_{transit}$ +0.5 (ns)	Sn U_s (µm/ns)	$\Delta d_{thickness}$ (nm)	ΔU_s (nm/ns)
6x10^{11}	.93	0.05	0.427	-0.054	0.927	4.313	200	468.2
8x10^{11}	1.10	0.04	0.326	-0.040	0.826	4.842	200	474.1
3x10^{12}	1.66	0.03	0.201	-0.013	0.701	5.706	200	389.2
6x10^{12}	2.05	0.08	0.110	-0.019	0.610	6.555	200	534.2

6.1.4 MATCHING OF SIMULATIONS WITH SN/LIF DATA

Simulations of both the laser-target coupling and of the subsequent shock wave evolution in the target were run using HYADES, with 150 mesh points spanning 4 μm of tin (feathered 5% for both surfaces) and 100 mesh points spanning 21 μm of lithium fluoride (feathered 5% from the front to the back). An example file is provided in Appendix G. The EOSs used were SESAME #2160 and #7270 for tin and lithium fluoride, respectively. Results from these simulations were initially used to predict the approximate laser intensity necessary to shock melt tin at the rear surface of the target. These results agreed well with the initial LASNEX simulations that Jeff Colvin performed. After the experiments were carried out, HYADES simulations were used to match the Sn/LiF interface expansion to measured data. The laser intensity parameter was slightly adjusted in the simulations until a match to the target expansion data was made. As Figure 67 shows, the resulting simulations match the data very well. Additionally, the intensities necessary in three of the four simulations agree perfectly with the measured intensities, within error (Table 8).

6.1.5 INTERFEROMETRIC DATA – SILICON

I was unable to detect THG from tin targets without causing damage to the surface. This is because the conversion efficiency of THG from tin was so small that I had to increase the laser intensity which in turn created a plasma at the surface. In order to generate a measurable amount of THG without damage to a target, I decided to performed experiments on silicon wafers, which generate THG much more efficiently. For these experiments, the shock driving laser contained ~ 700 – 750 mJ of energy in

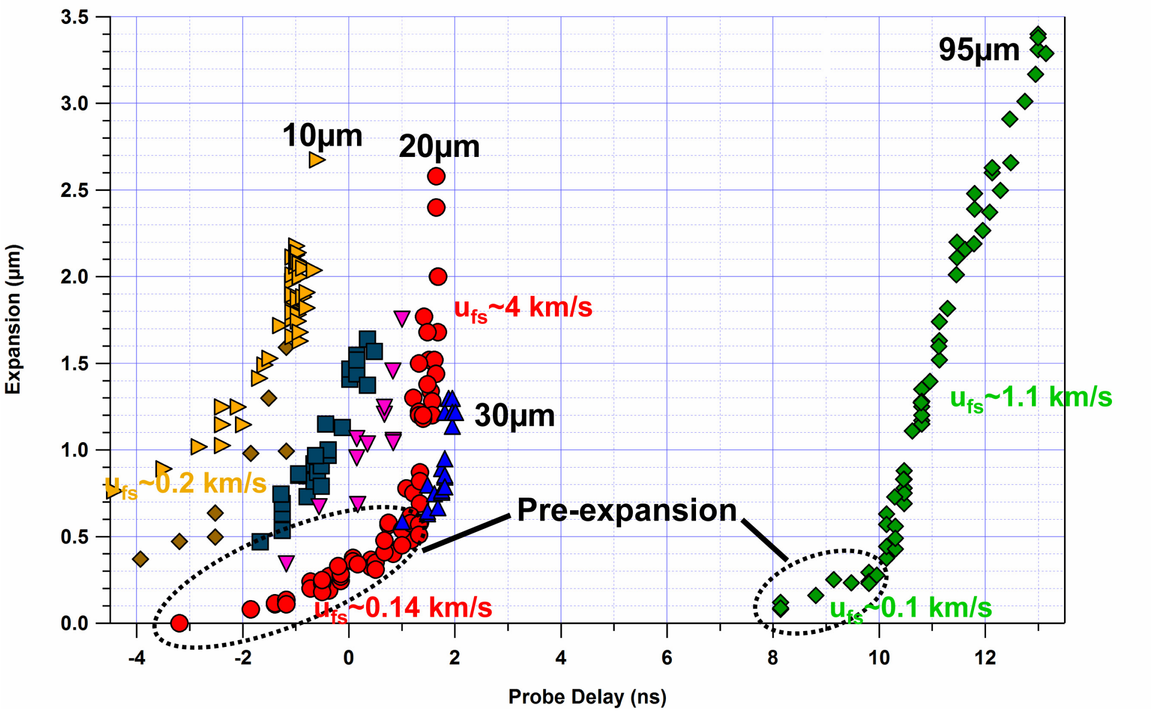

Figure 68. Plot of silicon peak expansion vs. probe delay under various conditions. The individual data points are described in the text.

varying spot sizes that resulted in laser intensities that varied between 1×10^{13} and 2×10^{14} W/cm^2. The various targets, combined with various incident laser intensities, produced the data in Figure 68. In this figure, data located toward the right-hand side is generally from a thicker target, while data located toward the left-hand side indicates a thinner target. The exceptions to this rule are the cases where the same target thickness was shot with different laser intensities. The higher intensities cause a higher pressure, which cause a higher shock velocity, which leads to an earlier shock breakout.

The yellow triangles represent data taken with 10 µm Si targets and a laser intensity of ~ 2×10^{14} W/cm^2. Unfortunately, during these shots, the laser contained several ns-scale pre-pulses from a misalignment of a waveplate in the post-regen isolation stage. This led to pre-pulses with amplitudes of 4×10^{-4} times the main peak, located at 15, 30, and 45 ns before the peak. These pre-pulses caused an additional 0.4 μm expansion in the rear surface, as compared with data taken when the pre-pulses were minimized, shown in brown diamonds. The laser was adjusted so that the pre-pulses were no higher than 10^{-6} of the main peak.

The dark blue squares in the graph represent data taken with 10 μm targets and a lower laser intensity of $\sim\ 2\times10^{13}\ \text{W/cm}^2$. The pre-expansion arrives at a later time than the previous data, due to the cooler plasma and slower heat and shock front velocities.

The data for the pink triangles were taken with 20 μm targets and a laser intensity of $\sim\ 2\times10^{14}\ \text{W/cm}^2$. Based on comparisons with the brown diamond data, the pre-expansion wave front appears to be traveling with a velocity ~ 3 km/s.

The red circles represent data taken with 20 μm targets and a lower laser intensity of $\sim\ 2\times10^{13}\ \text{W/cm}^2$. These data show the first real transition from motion due to target pre-expansion to motion due to shock breakout. The break in the velocity of the expansion occurs near the 0.6 μm expansion point, with the pre-expansion having a free surface velocity of ~ 0.14 km/s and the shocked free surface velocity of ~ 4 km/s. From equation (2.20), we find $u_p \approx 2$ km/s, which corresponds to a shock pressure of ~ 300 kbar, according to the silicon Hugoniot (Figure 69) from published literature (Goto, Sato et al. 1982). Sample line-outs from various delay times are plotted in Figure 70.

The blue triangles in Figure 68 represent data taken with 30 μm targets and a laser intensity of $\sim\ 1\times10^{14}\ \text{W/cm}^2$. These data seem to cover the end of the pre-expansion and the very beginning of the shock expansion. Unfortunately, the data are too scattered to estimate a reliable free-surface velocity and pressure. However, we can compare these

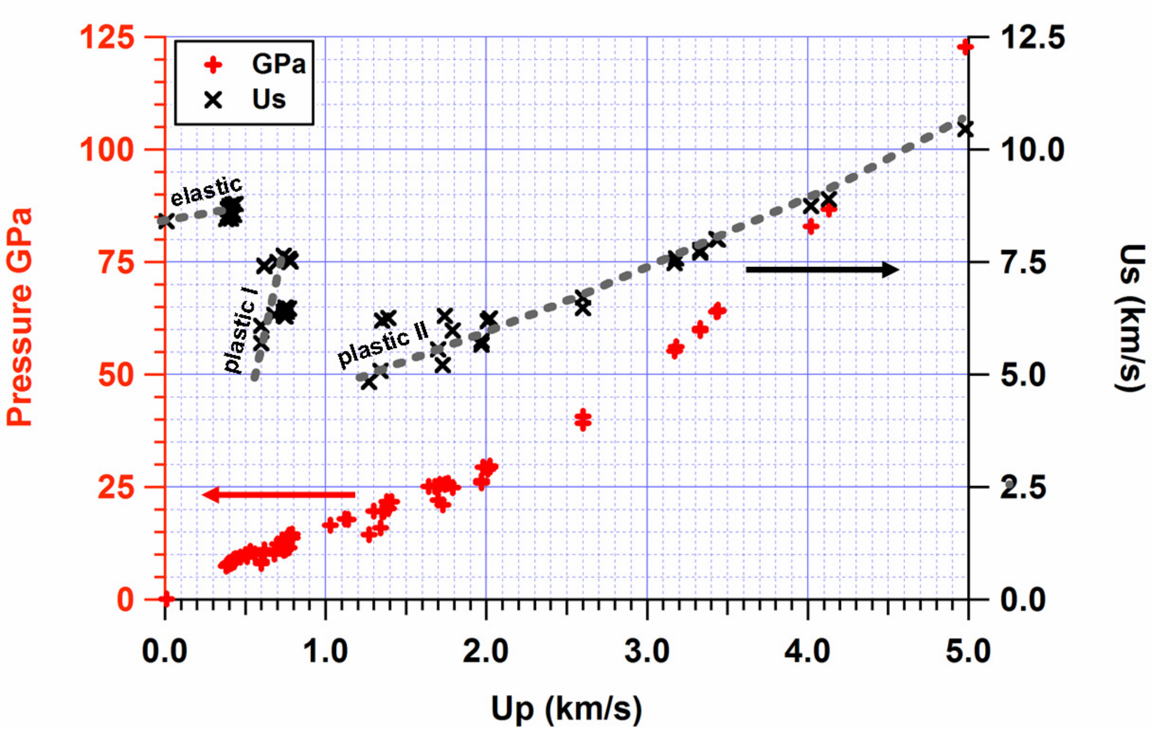

Figure 69. Diagram showing the Hugoniot for silicon. The black x's show the shock velocity as a function of particle velocity, while the red +'s show the shock pressure as a function of particle velocity. The data are from Goto 1982 and Gust 1971.

data with the pink triangles to estimate the shock velocity at around 6-10 km/s, which bound the published elastic sound speed of ~ 9 km/s for (100) silicon.

In all of the above silicon experiments, the small spot-size combined with the slope of the target make it difficult to extract any expansion data from the interferograms above 1.5 to 2 μm expansion. Because of this, it is difficult, if not impossible, to tell where any shock front breakout is, as the target surface is strongly distorted by the large expansion of the small spot size region. The only clear exception to this so far has been the data represented by the red circles.

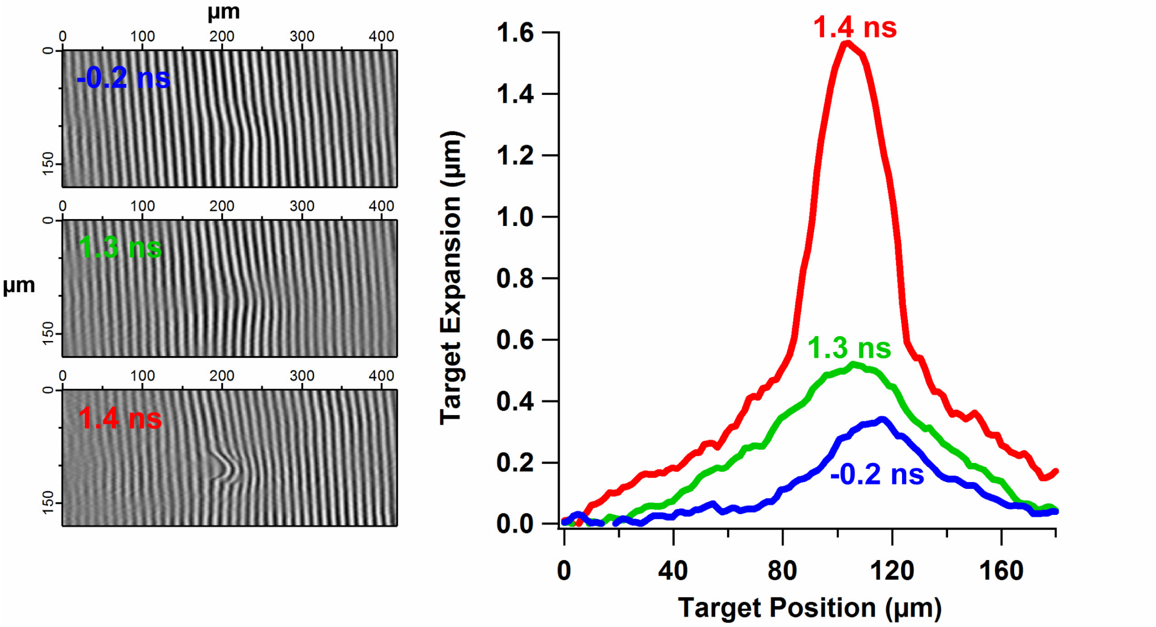

Figure 70. The left-hand side shows filtered interferometric images from 20 μm silicon targets. The delay time for each image corresponds to the color coded lineout in the right-hand side. These vertical line-outs are taken through the peak of the expansion.

Finally, we reach the green diamonds, which represent data taken with 95 μm silicon and laser intensities of ~ 2×10^{13} W/cm^2 on and ~ 6×10^{13} W/cm^2. This experimental data, in contrast with the previous data, created a large spot size, as shown in Figure 71. This is due to the two dimensional spreading of the shock front over the thicker target into an almost spherical wave. This allowed much cleaner interferometric data to be obtained, and led to less scatter in the data.

The fact that the 95 μm expansion does not depend on intensity indicates that the shock velocity and particle velocity for this breakout are independent on pressure over the range tested. This can only be true if the shock breakout is due to an elastic wave, such as that generated at the HEL. This conclusion agrees nicely with the measured free

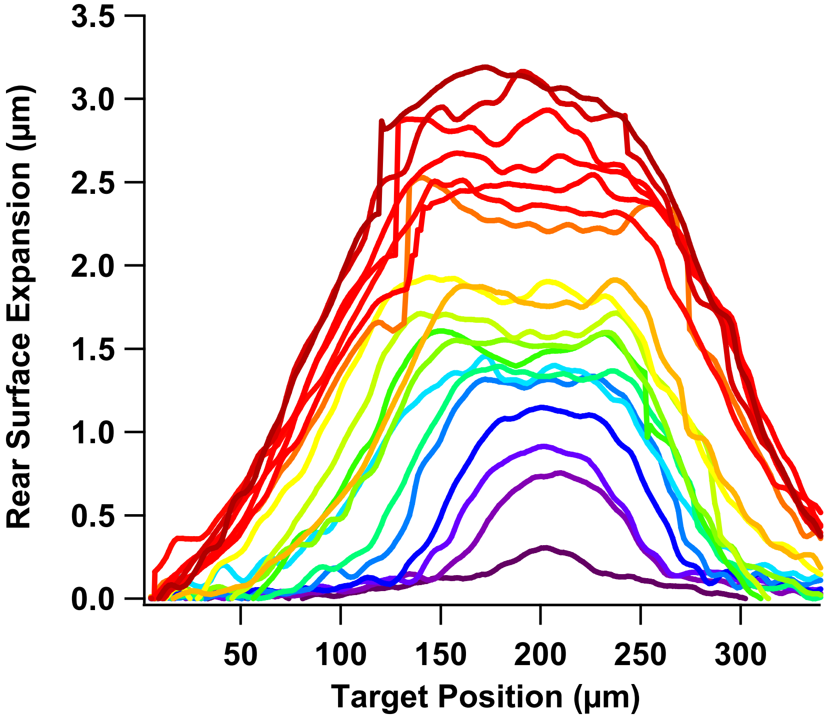

Figure 71. Line-outs from the expansion of 95 µm Si targets. The broad shock breakout is wider than 100 µm after 1 µm expansion. The color coded plots are arranged in order of increasing time, violet through red.

surface velocity of ~ 1.1 km/s, which corresponds to a particle velocity of ~ 0.5 km/s and a pressure of ~ 100 kbar.

It is interesting to note that the pre-expansion continues to persist in the data, all the way past the 95 µm thick targets. However, it appears that the amount of pre-expansion and the free surface velocity that occurs before shock breakout decrease for increasing propagation distance. This could be due to a stronger than expected decaying heat wave, as discussed in section 2.3.5.2., hot electron penetration through the target, pre-pulse effects from the laser shock, or some other mechanism. It is quite possible that interesting results lie in further experimental investigation of this phenomenon. If the demonstrated decreasing trend of the pre-expansion continues, it appears that its effect would be negligible by a probe delay of ~ 20 ns, corresponding to a target thickness of ~ 200 μm.

6.1.6 HUGONIOT MEASUREMENTS

In experiments where both the shock velocities and the particle velocities can be estimated, I was able to compare my data with published Hugoniot data. In my work to date, the error bars have been quite large due to uncertainties in the velocities. However, with more shots and statistics, the error bars could be reduced, with the eventual goal of independently adding new data to Hugoniot databases. Realistically, this goal is quite a ways off, but it should be possible.

In relatively early experiments in my work, I succeeded in shocking various thickness Sn foils. From this data, I could find the particle velocity from the slope of the expansion data, and the horizontal intercept could be related to the transit time, and thus the shock velocity. My experimental Hugoniot data points are shown as blue squares in Figure 72. The error bars are due to uncertainties in the slope of the expansion (twice the particle velocity) and the time of breakout. For comparison, these data are compared with data from the Russian shock database (Bushman, Lomonosov et al. 2003).

In my experiments with Sn/LiF targets, I also found shock and particle velocities for various pressures through the use of multiple laser intensities. Hugoniot data points extracted from the Sn/LiF experiments of Figure 67 are plotted in Figure 73. The uncertainty in shock velocity,

$$U_s = \frac{d_{thickness}}{t_{transit}} \tag{6.2}$$

$$\Delta U_s = \frac{\Delta d_{thickness}}{t_{transit}} - \frac{d_{thickness}}{t_{transit}^{2}} \Delta t_{transit} \tag{6.3}$$

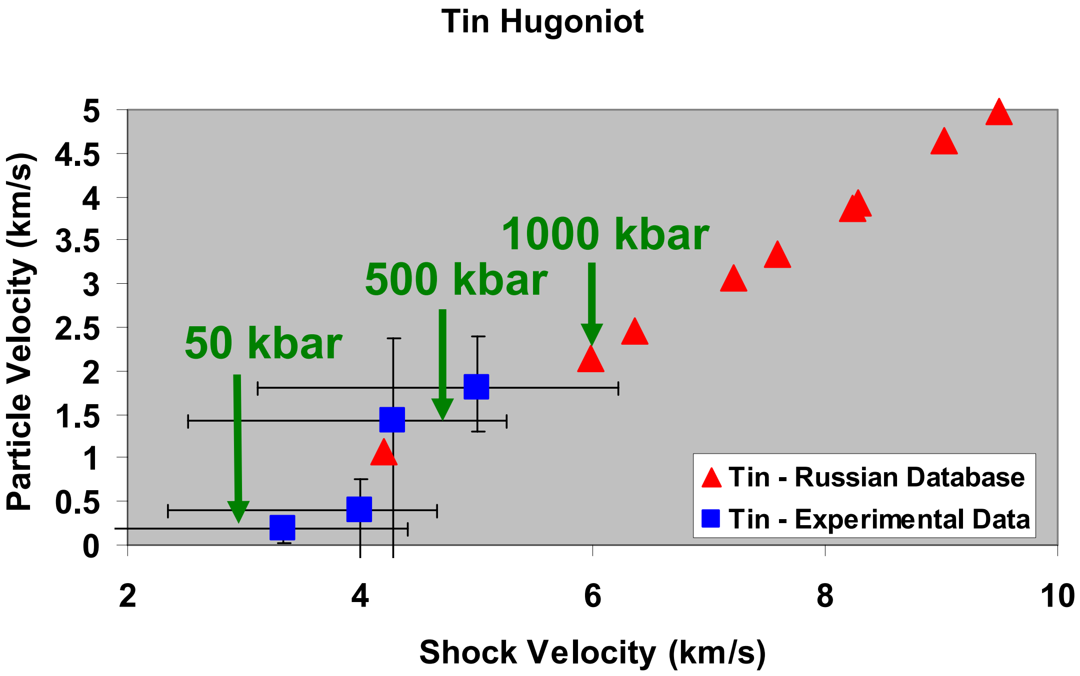

Figure 72. Hugoniot data from various thickness Sn targets. The error bars represent uncertainties in the curve fits to the data. Although the error bars are large, the data do lie very close to the published Hugoniot. The green arrows represent various pressures along the Hugoniot and are only included as reference points.

was calculated by assuming a target thickness uncertainty of 200 nm, a transit time uncertainty given by the lease squares curve fit, and a transit time equal to the results of the curve fit plus the 0.5 ns offset discussed below. The uncertainty in particle velocity was taken from the curve fit results listed in Table 9.

In order to determine the shock velocity, the shock transit time and the target thickness must be known. The difficult task is to determine accurately the transit time, since it is difficult to say when the shock wave starts, given the thin nature of the targets and the Gaussian shape of the drive pulse. However, to make an estimate of the transit time, I tried to de-convolve the pulse timings from the measured photodiode signals. The

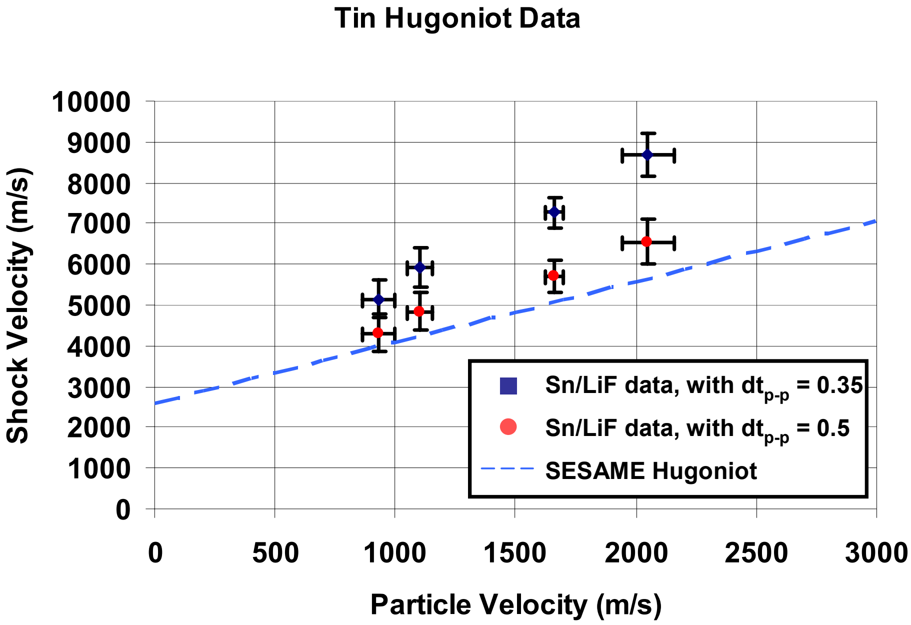

Figure 73. Plot showing the measured particle and shock velocity from experiments performed with 4 µm of Sn deposited onto 6 mm (100) LiF windows. The error bars are discussed in the text. The blue and red data correspond to peak-to-peak pulse adjustments of 0.35 and 0.5 ns, as discussed in the text..

estimated "actual" signals are a de-convolution of the detector response from the measured signals. The de-convolution was done by adjusting the temporal offset of the actual pulses so that their shapes overlapped with the photodiode signals at a normalized amplitude of ~ 5%. This level was chosen as an estimate for the first visible response of the rising voltage on the oscilloscope. The de-convolved pulse widths are found by assuming that the pulse widths add in quadrature.

$$\left(dt_{measured}\right)^2 = \left(dt_{pulse}\right)^2 + \left(dt_{detector}\right)^2 \tag{6.4}$$

The measured FWHM of the photodiode traces are 641 ps and 855 ps for the short and long pulses, respectively. The photodiode has a rise time of ~ 50 ps, so the measured short pulse FWHM effectively characterizes the response of the 1 GHz oscilloscope.

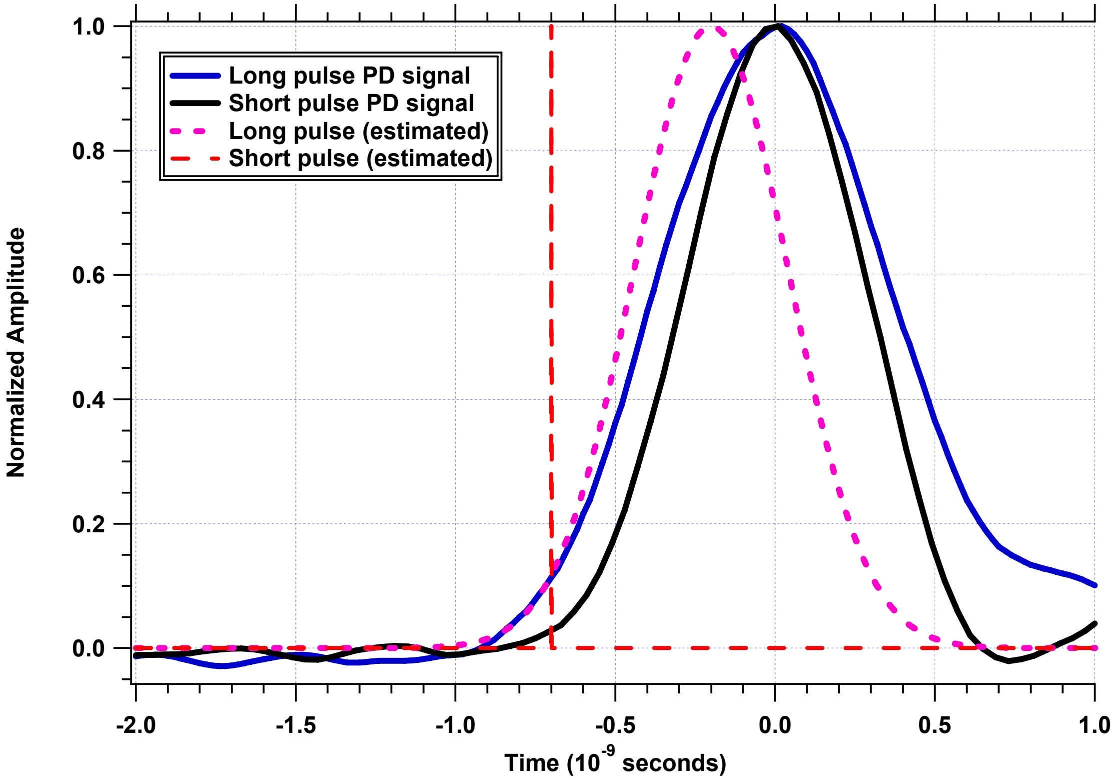

Figure 74. Plot showing the Tektronix oscilloscope traces of the short pulse (black) and long pulse (blue) on the Newport photodiode used in my setup. The estimated deconvolved positions of the actual pulses are shown in red and pink, respectively.

Using Equation (6.4), the actual pulse width of the long pulse can be estimated as 570 ps. This estimated long pulse is plotted in pink in Figure 74, along with the ~ 40 fs short pulse plotted in red.

From this analysis, the actual peak-to-peak pulse separation is found to be 0.5 ns when the temporal separation between the photodiode signals is adjusted to zero. This means that the t_o timing fiducial used in my probe delay should be approximately t = -0.5 ns. However, HYADES simulations fit the data when the peak-to-peak pulse separation is 0.35 ns. This discrepancy and its effects are illustrated in Figure 73, which plots the data for the two sets of shock velocities found by assuming different peak-to-peak separations. At this point, we must conclude that there is not enough data to make accurate estimates of the shock velocities observed in this experiment. More data will need to be taken with different thickness targets to resolve this issue.

6.2 Reflectivity

In addition to interferometry, I also examined the reflectivity of various shocked targets. The reflectivity from shocked Goodfellow foils is shown in Figure 75. This figure illustrates the excessive scattering from the un-shocked, as well as shocked surface, and explains why I don not have any interferograms from these targets. The shocked image in the bottom of the figure should show a sharp decrease in reflectivity of the melted region, but scattering from the target and issues with the imaging system cause it to blur.

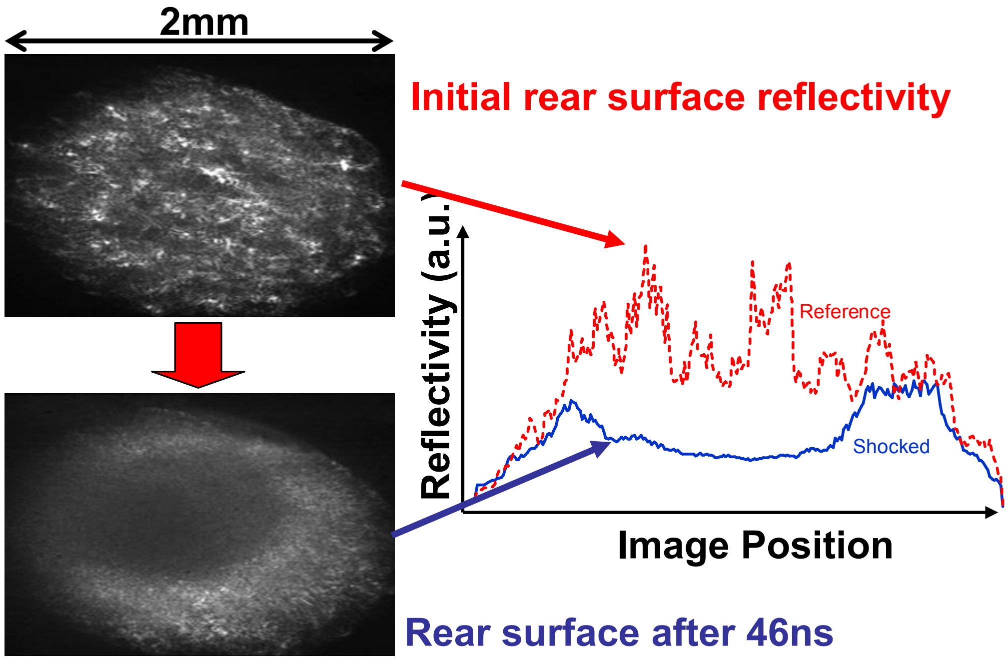

Figure 75. Diagram showing reflectivity from a diffuse Sn surface. The poor quality of the data is due to the rough surface and long f/# imaging optics.

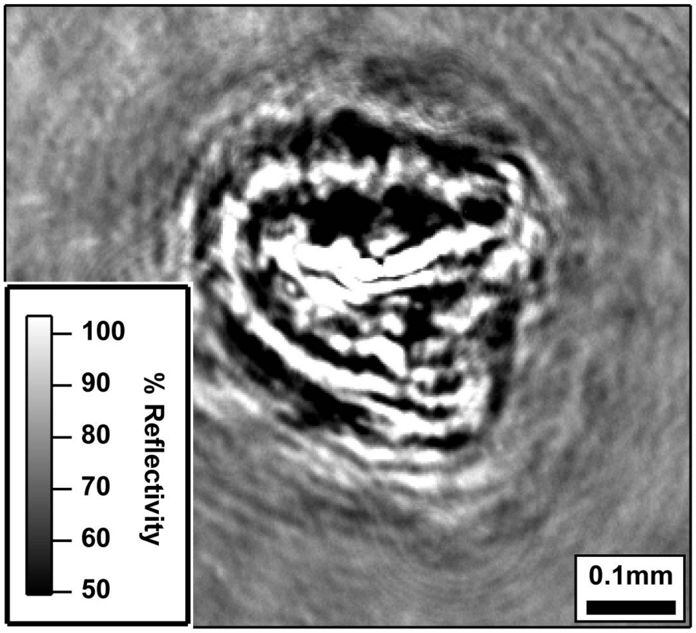

Figure 76. Reflectivity data from a shock breakout from Sn into a LiF substrate. The laser intensity was 6x10^{12} W/cm^{2} and the probe delay was 450 ps after the timing fiducial

As a comparison, Figure 76 presents an example image from shocked Sn/LiF targets. These reflectivity images generally show a flat region of uniform reflectivity surrounding the shock breakout region, which show a sharp transition at the shock boundary. However, this decrease is much greater than is expected for melted Sn. A graph of the normalized reflectivity for melted Sn as a function of angle using a Drude model and the Fresnel equations is presented in Figure 77. As the figure shows, the reflectivity should decrease < 2% at the experimental angle of incidence of 10°.

Other targets also demonstrated a decrease in normalized reflectivity to nearly zero, which was much greater than expected . Results from various freestanding PVD targets are displayed in the bottom of Figure 63 and in right side of Figure 78. Since all of these foils demonstrated a rapid reflectivity drop, I became concerned that the target surface

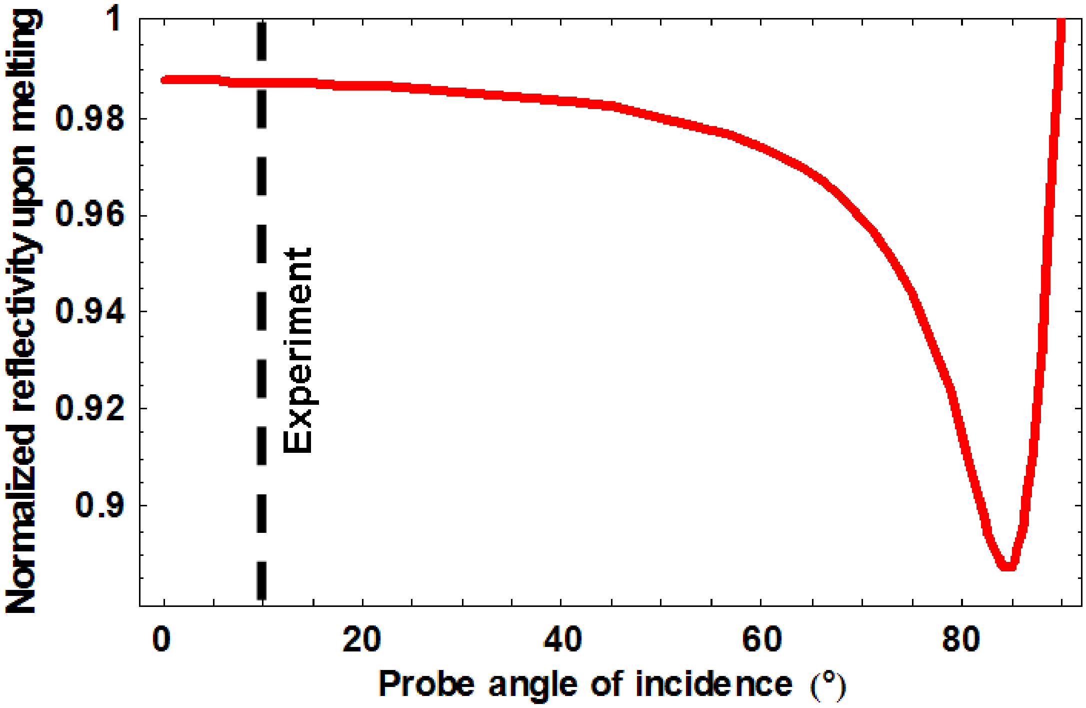

Figure 77. Plot showing the reflectivity of melted Sn divided by the reflectivity of cold Sn as a function of angle. My experiments probed the reflectivity of Sn at ~ 10°, as indicated by the dashed line. The expected decrease in reflectivity due to melting is < 2%.

was fragmenting upon shock breakout (Figure 79), causing the probe light to be scattered away from the detector. To test this hypothesis, I performed experiments where I did not remove the PVD foil from the glass microscope slide substrate. For these experiments, I shocked the free surface of the targets, and probed through the glass substrate to observe the interface expansion and the surface reflectivity. This raw data is shown in Figure 80 and the analyzed data is presented as red triangles in Figure 78. The surprise result from these experiments was that the reflectivity from both types of targets decreases at approximately the same rate. In fact the reflectivity decreased to 60% by the time the target surface had only expanded ~ 200 nm.

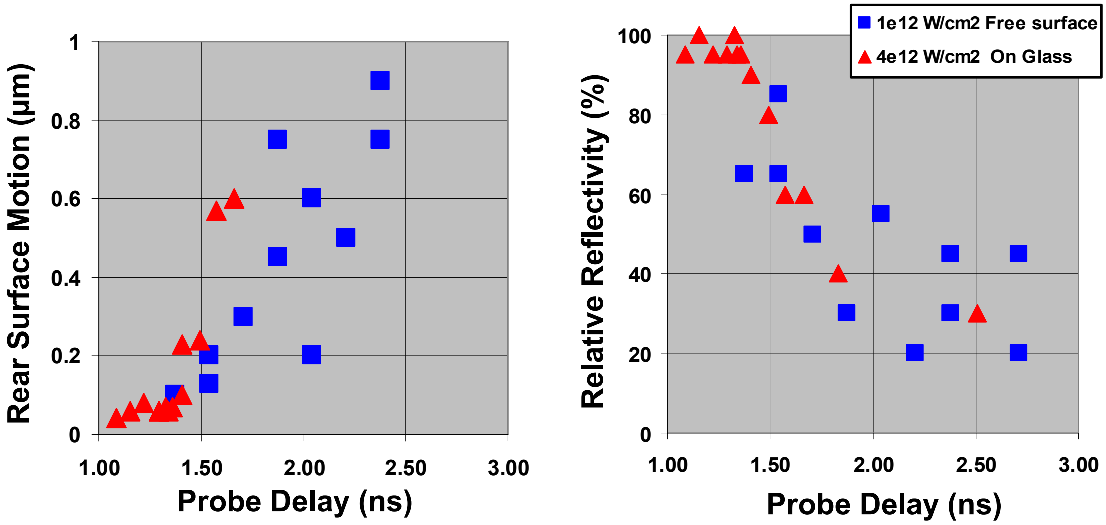

Figure 78. The left graph shows expansion data as a function of probe delay time from the 2D interferometer. The right graph shows normalized target reflectivity over the same time scale. The blue squares represent data taken from free standing Sn foils, while the red triangles represent data from Sn foils supported by a soda-lime glass substrate.

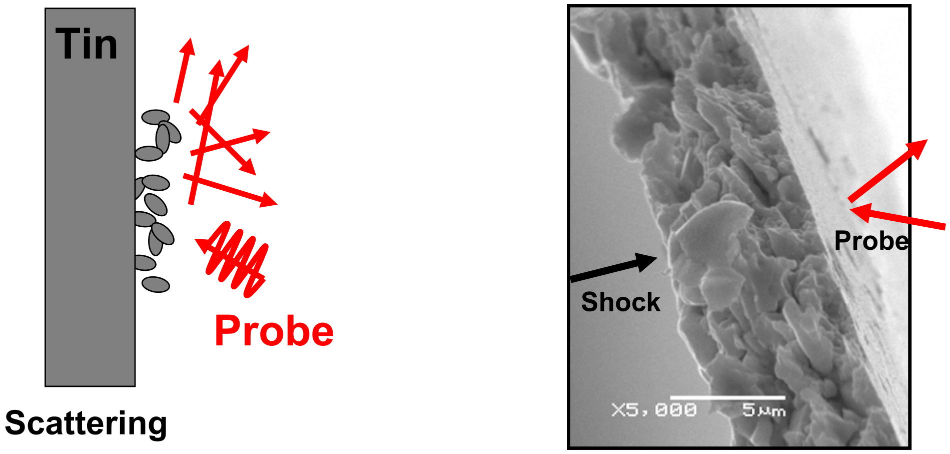

Figure 79. An illustration on the left shows how surface fragmentation might cause scattering of the probe pulse, which would appear as a decrease in the reflectivity signal. The photo on the right is an SEM cross section of the 4 µm tin foil. The granular structure can be seen at the edge where the material has been torn, which could seed the fragmentation process

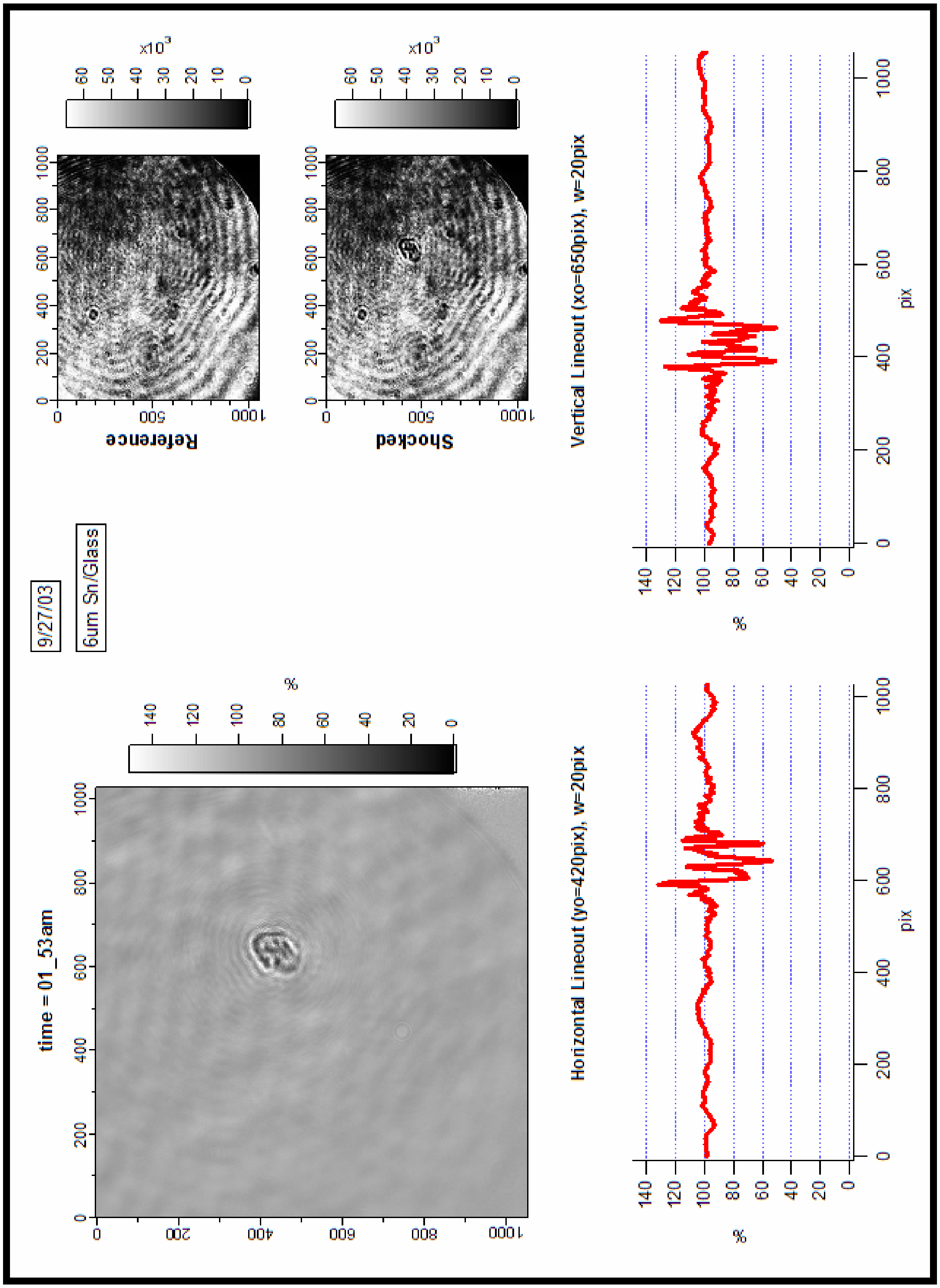

Figure 80. Reflectivity data from a Sn/glass target. Notice the large reflectivity fluctuations which are much larger than the drop expected upon melt.

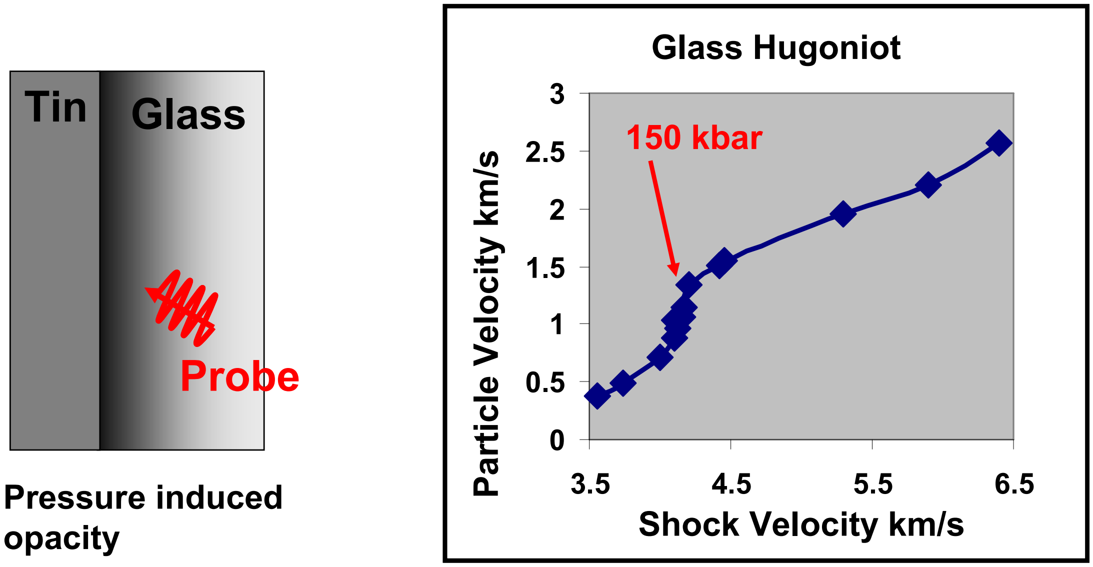

Figure 81. The illustration on the left shows how pressure induced opacity in the glass window could attenuate the probe, thus reducing the reflectivity signal. The right hand plot is the Hugoniot for soda lime glass (Trunin 2001). It shows a phase transition around 150 kbar.

Upon further investigation, I found that the Hugoniot data on soda lime glass shows a phase transition in the pressure range of these experiments, and it is quite possible that the phase transition alters the transparency of the glass (Figure 81) (Trunin 2001).

To eliminate both the fragmentation and the glass phase transition, I decided to use lithium fluoride substrates to support the tin targets. This decision was made due to the published transparent behavior of LiF as a supporting window in shock experiments up to 1.6 Mbar (Asay and Shahinpoor 1993). However, as Figure 76 shows, the reflectivity behavior is still unexpected. The large fluctuations tend to have a ring-like structure, pointing to the possibility that they are caused by an interference effect. Regardless of the cause, the observed reflectivity variations are much larger than the expected few percent change that occurs upon melting. Therefore, reflectivity appears to be an unacceptable diagnostic for melting in this experimental campaign. More work must be done before any conclusions can be drawn from this data, and before it can be compared to the work by Swift (Swift, Tierney et al. 2005).

6.3 THG

6.3.1 DIAGNOSTIC DEVELOPMENT USING FEMTOSECOND LASER EXCITATION OF SILICON AND GALLIUM ARSENIDE

In this section I describe my experiments performed on laser melting of silicon and gallium arsenide. The purpose of these experiments is to serve as a test bed for the THG diagnostic, with the goal of probing shock-melted solids. If the THG diagnostic works as expected, then it should be able to detect the ultra-fast melting transition that has been studied by previous researchers using reflectivity and SHG. By comparing my results with published results, I have identified that the THG diagnostic is able to detect melting of Si and GaAs.

As the probe pulse delay was scanned relative to the pump pulse, a fast (less than 500 fs) transition was detected by both the reflectivity diagnostic, as well as the third harmonic diagnostic (see Figure 82 through Figure 85). This agrees with previously published results (Tom, Aumiller et al. 1988; Sokolowski-Tinten and von der Linde 2000). This drop in harmonic generation (GaAs and Si) indicates a loss of electronic structuring of the target (GaAs), which is confirmed by the large increase in the reflectivity probes (GaAs and Si). The increase in reflectivity agrees within ~ 10% with calculations using the Fresnel equations to predict the change in reflectivity upon melting (Figure 83 and Figure 85). This change is due to the dielectric constant approaching that of a liquid (Drude) metal. As was shown in section 3.2, the linear dielectric constant affects harmonic generation at a surface through the linear Fresnel equations, which determine the penetration of the probe light into the material. The harmonic intensity is proportional to the fundamental field to the *2j* power, where *j* is the harmonic order, so the field amplitude has a large effect on the harmonic amplitude. I tabulated data for Si and GaAs in (Table 10) to illustrate this point. For example, the THG from an oxide/Si and an oxide/GaAs interface are given respectively by,

$$\frac{I_{melt}}{I_{cold}} \propto \frac{0.37^6 \times 0.33^2}{0.56^6 \times 0.32^2} = 0.08 \tag{6.5}$$

$$\frac{I_{melt}}{I_{cold}} \propto \frac{0.63^6 \times 0.52^2}{0.70^6 \times 0.24^2} = 2.42 \tag{6.6}$$

The decreased penetration of the fundamental field into melted Si causes weaker harmonic generation than in the case of GaAs, where the slightly lower penetration is offset by the larger non-linear Fresnel factor. In these calculations, the oxide layers are assumed to have an index of refraction of 2 and 1.453 for GaAs (Potter 1969) and Si (Palik 1985), respectively.

Table 10. Table listing the calculated linear and non-linear Fresnel factors, which depend on the dielectric constant, along with the relative intensity of the harmonics generated in reflection from cold and melted Si or GaAs.

		GaAs, SHG		**GaAs, THG**		**Si, THG**	
		Air/Sample	**Oxide/Sample**	**Air/Sample**	**Oxide/Sample**	**Air/Sample**	**Oxide/Sample**
Cold	$\lvert F_{\parallel}^{L,T}\rvert$	0.36	0.57	0.43	0.70	0.43	0.56
	$\lvert F_{\parallel}^{NL,R}\rvert$	0.41	0.27	0.27	0.24	0.34	0.32
	$I \propto \lvert F_{\parallel}^{L,R}\rvert^{2j} \lvert F_{\parallel}^{NL,R}\rvert^{2}$	*0.0028*	*0.0072*	*0.0004*	*0.0068*	*0.0007*	*0.0034*
Melt	$\lvert F_{\parallel}^{L,T}\rvert$	0.32	0.50	0.35	0.63	0.26	0.37
	$\lvert F_{\parallel}^{NL,R}\rvert$	0.71	0.55	0.66	0.52	0.35	0.33
	$I \propto \lvert F_{\parallel}^{L,R}\rvert^{2j} \lvert F_{\parallel}^{NL,R}\rvert^{2}$	*0.0050*	*0.0190*	*0.0009*	*0.0165*	*0.0000*	*0.0003*
Ratio	**Melt/Cold Intensity**	***1.76***	***2.61***	***1.92***	***2.42***	***0.06***	***0.08***

It is important to recognize that these calculations depend only on the dielectric constant of the materials and the angle of incidence, and not on the crystalline structure. Comparison of these calculated values with measured harmonic intensities reveal any induced changes in the non-linear susceptibility. Glezer *et. al.* performed this comparison to map out the behavior of $\chi^{(2)}$ for various levels of laser excitation (Glezer, Siegal et al. 1995). However, I believe their exact values to be in question, as it appears they used equations for s-polarized light for the p-polarized experiment. That being said, the same general trends will result from using the correct equation.

6.3.1.2 GaAs

My results show a decrease in SHG and THG (Figure 82) and an increase in reflectivity (Figure 83) for fs laser excited GaAs. Comparison of my GaAs THG data with the values from Table 10 indicate that the non-linear susceptibility of the material is dropping to zero, which indicates a loss of crystalline order due to melting. The reflectivity data confirm this transition to a melted state.

6.3.1.3 Si

My Si data also show a decrease in THG (Figure 84) and an increase in reflectivity (Figure 85) for fs laser excited Si. Comparison of Si data (Figure 84) with the values from Table 10 are somewhat inconclusive. Although the THG decreases upon strong laser excitation of Si, the non-linear Fresnel equations predict that a drop in THG is expected, due to the changing linear index of refraction. Unfortunately, I am unable to determine how far the THG experimentally decreases with enough accuracy to compare with the decrease shown in Table 10. However, the fact that the THG follows the expected drop of intensity suggests that the dielectric constant is changing such that it is

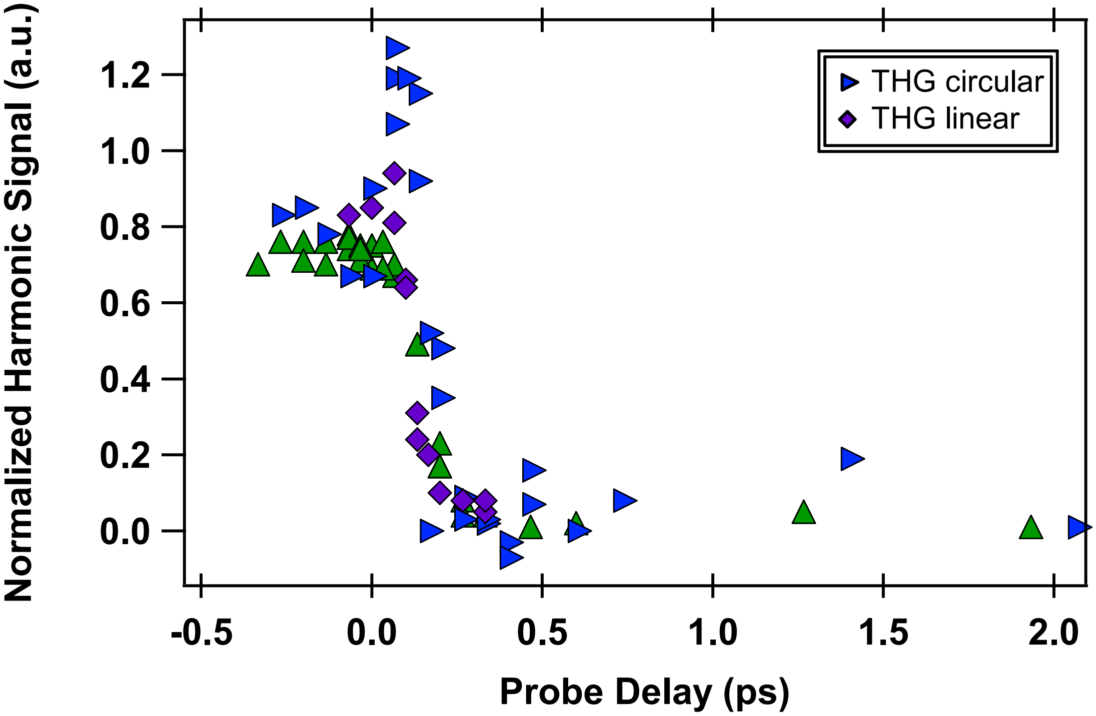

Figure 82. Plot of THG data from laser excited gallium arsenide with a pump fluence of ~ 310 mJ/cm^2. The data was taken using (100) GaAs. The THG using circularly polarized light (blue) shows a coherent artifact near t_o. This is due to temporal overlap of the s-polarized pump with the circularly polarized probe. The artifact does not occur with a p-polarized probe (purple). The SHG and THG data show a 90%-10% fall time of ~ 150 fs.

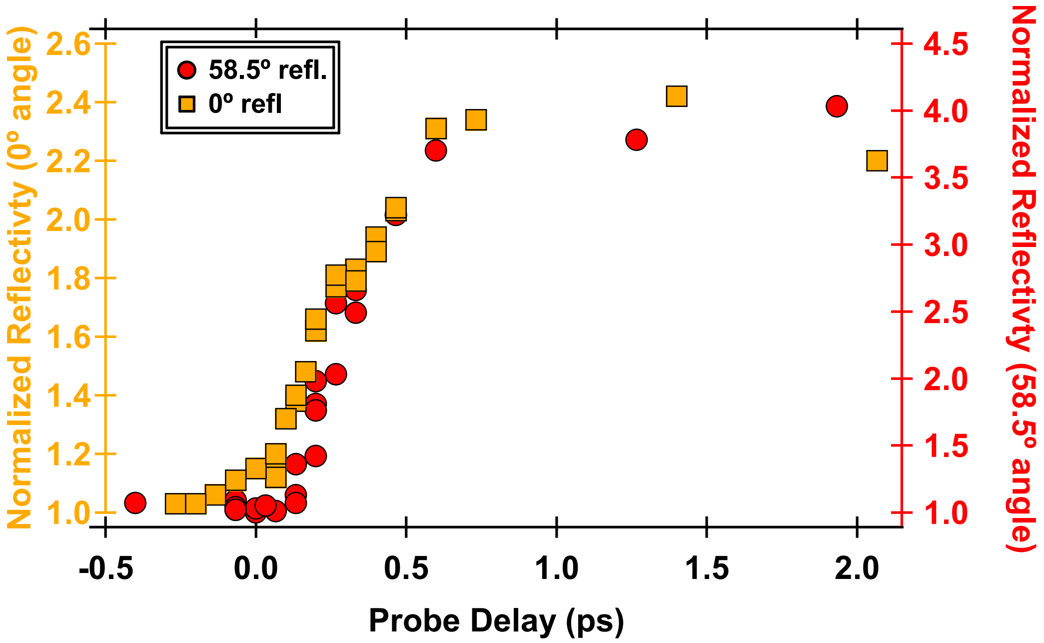

Figure 83. Plot of reflectivity data from laser excited gallium arsenide with a pump fluence of ~ 310 mJ/cm^2. The data was taken using (100) Si. The reflectivity data show a 10%-90% rise time of ~ 500 fs at normal incidence and ~ 350 fs at 58.5°.

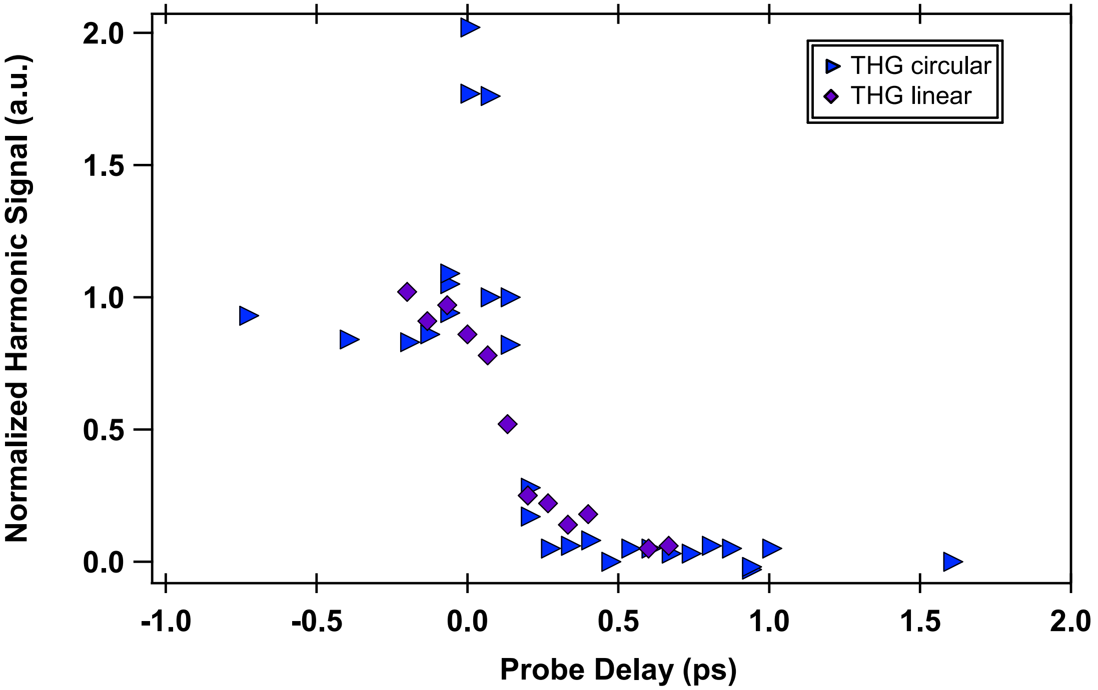

Figure 84. Plot of THG data from laser excited silicon with a pump fluence of ~ 310 mJ/cm^2. The data was taken using (100) Si. The THG using circularly polarized light (blue) shows a coherent artifact near t_o. This is due to temporal overlap of the s-polarized pump with the circularly polarized probe. The artifact does not occur with a p-polarized probe (purple). The THG data show a 90%-10% fall time of ~ 350 fs.

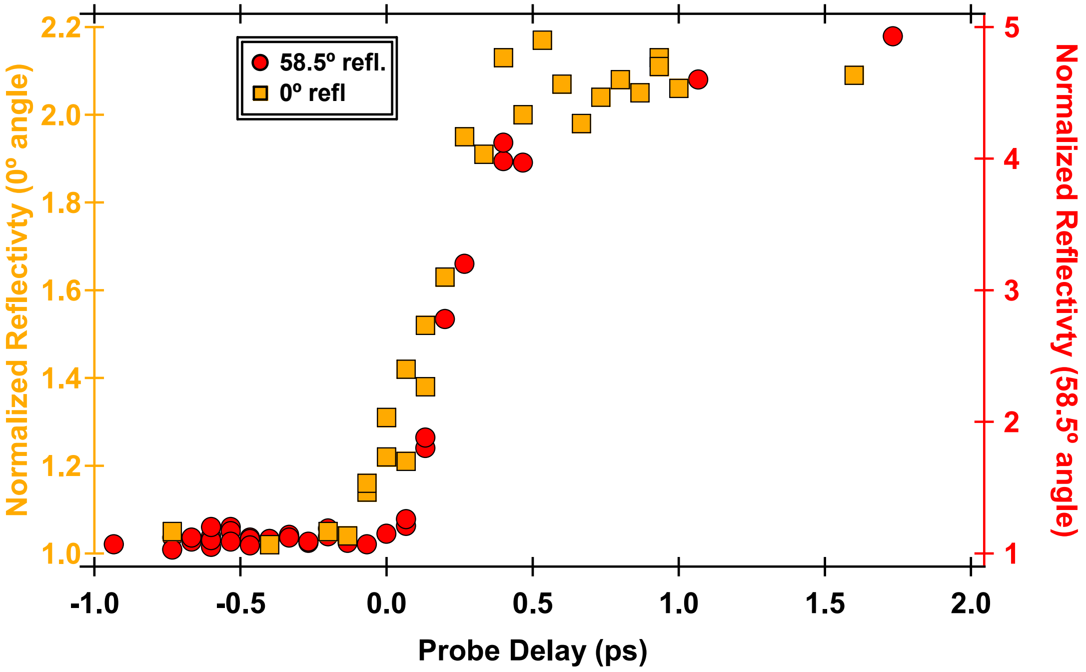

Figure 85. Plot of reflectivity data from laser excited silicon with a pump fluence of ~ 310 mJ/cm^2. The data was taken using (100) Si. The reflectivity data show a 10%-90% rise time of ~ 430 fs both at normal incidence and 58.5°. well modeled by a Drude model. This suggestion is confirmed by the observed increase in the linear reflectivity.

Although I cannot claim to detect the disappearance of the non-linear susceptibility of Si with THG upon melting, I can confirm that the dielectric constant changes to be representative of a melted state. In contrast, both the THG and reflectivity diagnostics indicate a transition to a disordered and melted state upon excitation in these experiments.

6.3.2 THG PROBING OF SHOCK-COMPRESSED SILICON

Once I developed and tested the THG diagnostic, I migrated it over to shocked silicon studies. Unfortunately, much, if not all, of the early THG data from shocked silicon could not be extracted from the PMT signal due to overwhelming noise in the signal. The noise sources that plagued the experiment included electromagnetic interference resulting from ground loop issues and a lack of shielding around the target chamber. There was also an abundance of 266 nm light scattered from the plasma at the front surface, as well as target self-emission (black-body type) from the rear-surface. It was only through careful electrical isolation, common grounding, and BNC cable shielding that I could minimize the EMI to a reasonable level (< 10 mV). I was able to minimize the scattered plasma light by shrouding the inside of the target chamber with black foil, and placing diffuse black baffles in judicious locations near the target. Once I contained these spurious noise sources, I was left with the target self-emission. This is a problem that I have not yet found a solution to, other than to shoot at lower laser intensities and use thicker targets to attenuate the material temperature.

Having said that, I was able to acquire THG data on three shocked Si experiments. I succeeded in probing 95 μm silicon targets out to an expansion of 3.4 μm. This third harmonic data was partially compromised by the inclusion of some scattered self-emission or plasma light. This fact leads to an uncertainty in the actual THG signal, as I was unable to distinguish the THG signal from the random background. Either the PMT signal at the probe time was due only the THG, or the PMT signal contained an average background with the THG signal being what remains after background subtraction. Because of the random nature of the background signal, it was impossible to distinguish, in most cases, which part of the signal was background, and which part was THG. Due to this, I plotted both assumptions as a green dash in the graph, and connected

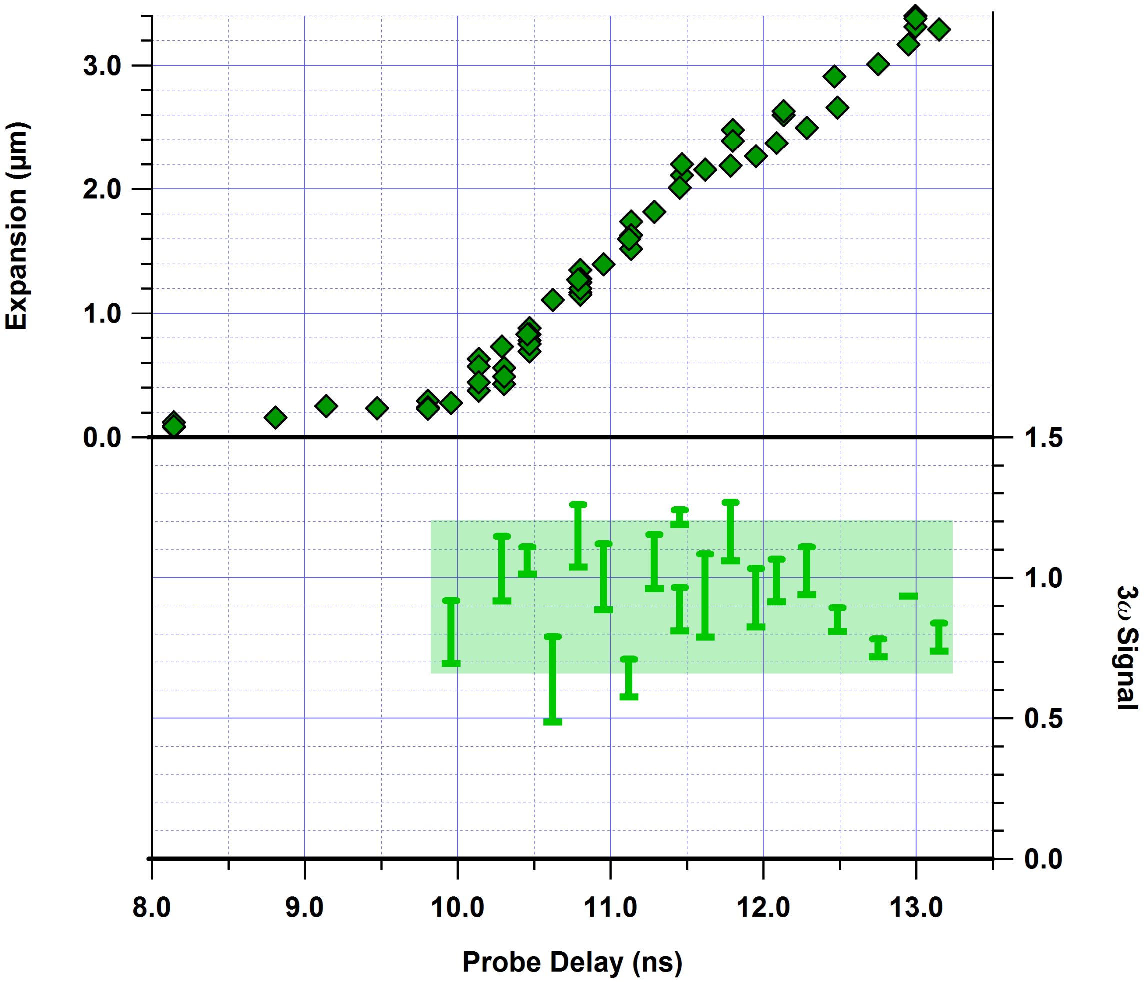

Figure 86. The top plot is of rear surface expansion of 95 µm silicon as a function of probe delay. The bottom plot is normalized THG vs. probe delay. The THG signal remains fairly constant throughout the probed expansion of 3 µm. The green bars between points are uncertainty bars, which are discussed in the text. The broad green line is only to guide the eye.

the dashes with a vertical line to indicate the actual measured signal lies somewhere in between the two end points (Figure 86)

The data indicate that the THG signal remains fairly constant throughout most of the measurements. From this, we can state that the material is remaining crystalline during the shock breakout for at least the first 3 µm of expansion. The crystalline

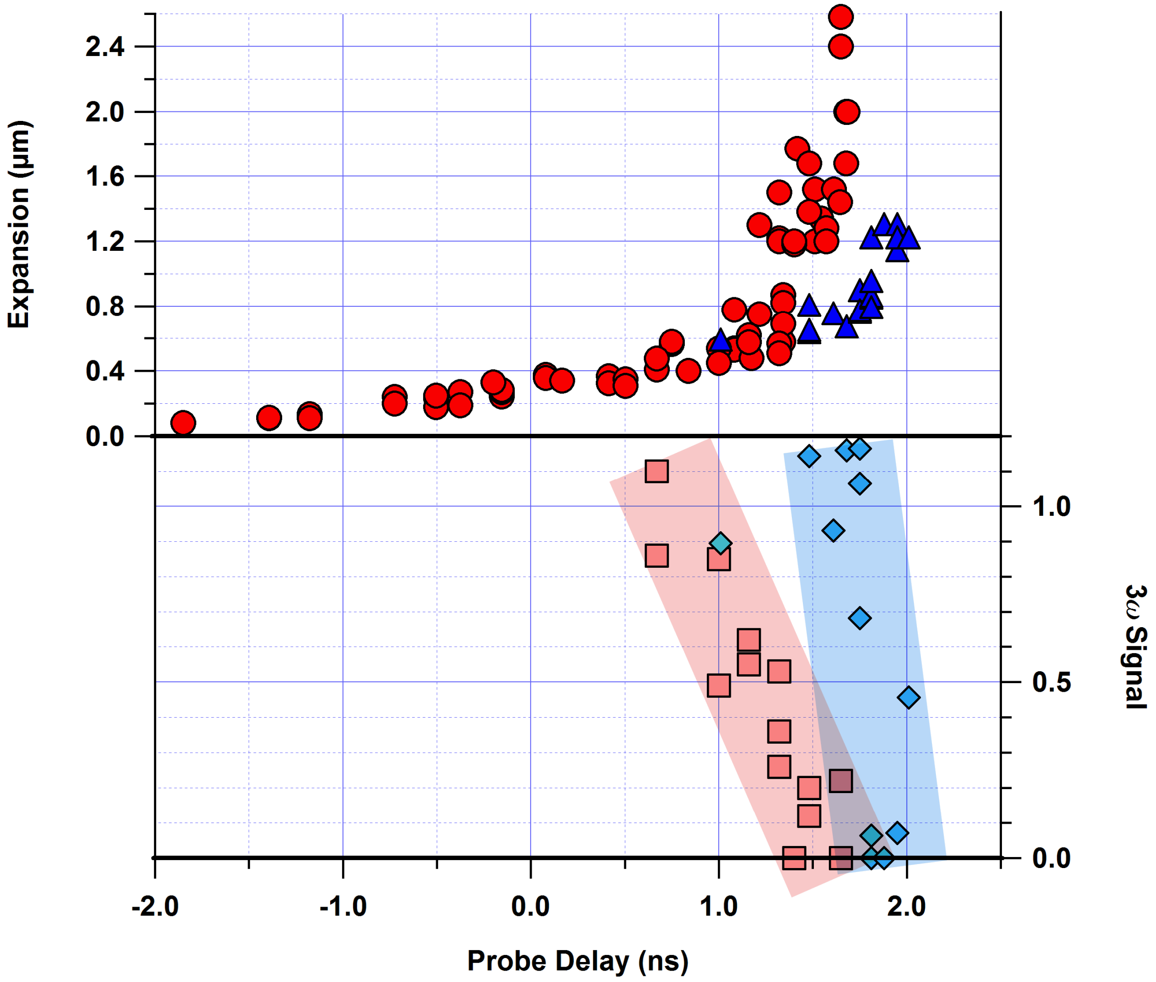

Figure 87. The top plot is of rear surface expansion of 20 µm (red) and 30 µm (blue) silicon as a function of probe delay. The bottom plot is normalized THG vs. probe delay. The THG signal decreases for both target thicknesses. Possible explanations for this are discussed in the text. The broad light red and light blue lines are only to guide the eye.

structure is expected for an elastic shock break-out, but the data actually validates this hypothesis.

In contrast, the 20 and 30 µm data both show a decrease in THG signal (Figure 87). In fact, the 20 µm data seem to indicate the THG begins to decrease just before the shock wave reaches the rear surface. This is quite unexpected, and implies that the drop

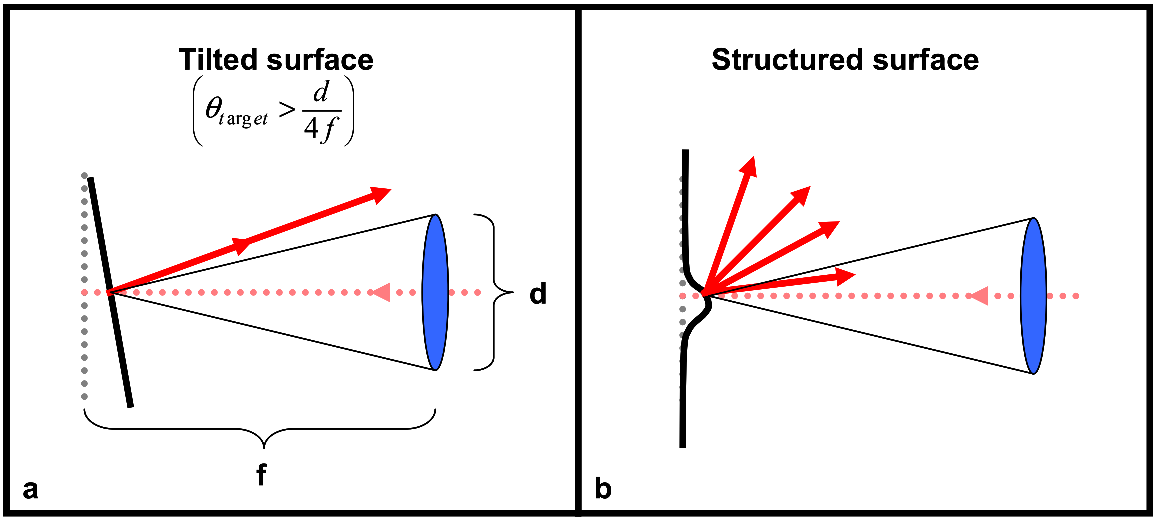

Figure 88. Diagram of target surface tilt in relation to the collection optics and the collected light. (a) target slope reflects light outside of the collection cone. (b) target slope scatters light in several directions

could be due to heating or target break-up from the pre-expansion. It would be nice to say that the drop in THG is due to a structural change, but we must first rule out other possible causes for the drop.

Our first concern is that spatial size of the shock expansion is approximately the same as the probe laser spot size (~20 µm). This small spot size create a shock breakout that is highly non-uniform, which means that the target under the peak intensity will begin expanding sooner and faster than the target under the lower intensity regions of the beam. This creates a sloped target surface, as seen in Figure 88, that can deflect light outside of the collection cone of the optics.

To determine the slope of the target, I took a lineout through the phase expansion data and converted it into expansion distance as a function of target position. Next, I took the derivative of the lineout to produce a plot of the slope of the target as a function of position. To determine if the probe light would be collected by the optics of the

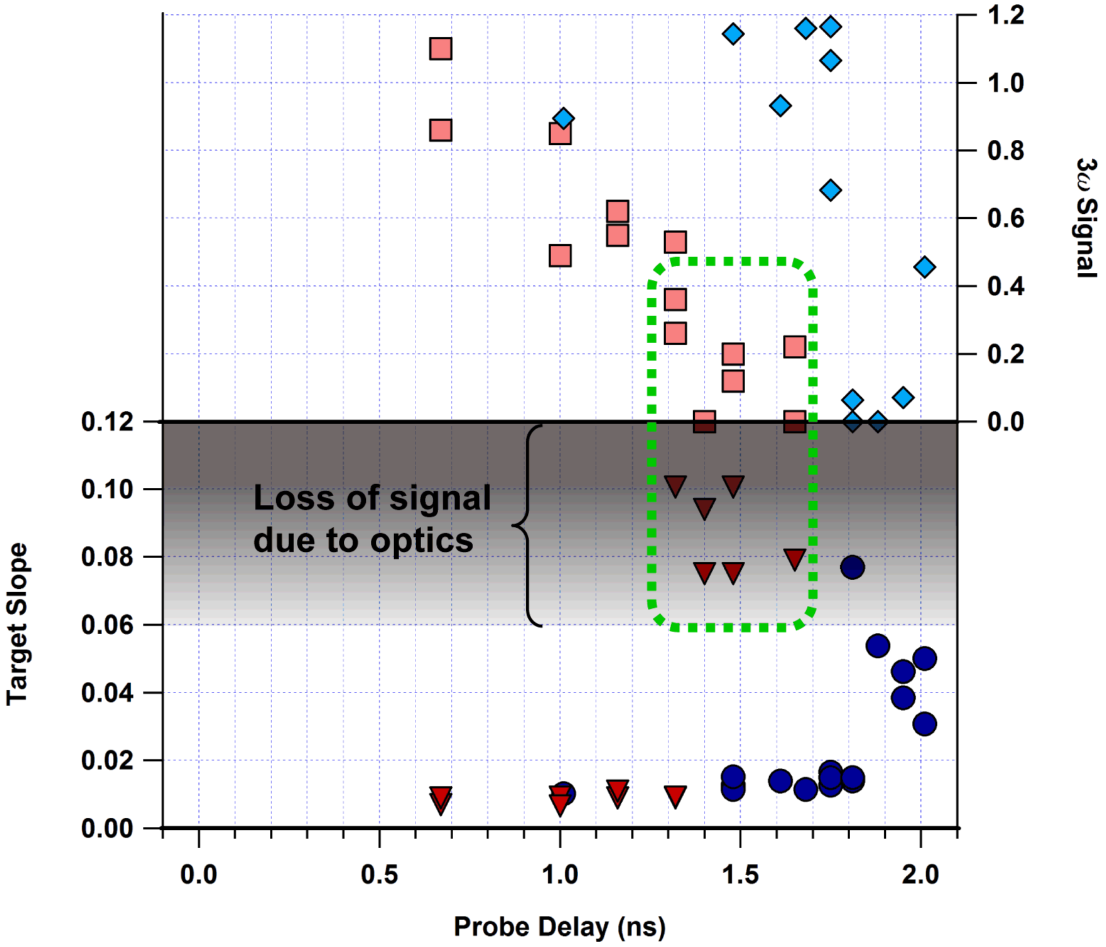

Figure 89. The top graph plots the THG signal for 20 μm (light red) and 30 μm (blue) silicon as a function of probe delay. The bottom graph plots peak target slope as calculated from the interferometric data as a function of probe delay. The gray shaded region indicates the range of target slopes that reflect some light outside of the collection optics. The dark gray region above 0.1 slope indicates the expected region of complete loss of collected light. The green bounding box encompasses data that can possibly be explained by the loss of light from the collection optics.

experiment, I assumed a worst case scenario and compared the peak slope of the target with the *f-number* of the diagnostics. The *f/#=f/d*, where *f* is the lens focal length, and *d* is the lens diameter. If the target slope is greater than *1/(4*f/#)*, then the probe will be reflected outside of the optic's collection cone, and the signal will decrease due to a strictly geometric reasoning (**Figure 88**).

The peak target slope from the expansion data is plotted in Figure 89. Upon comparison of the slope data with the THG data, it is clear that the target slope can explain some of the decrease in the THG signal for the region bounded by a green box in the bottom of Figure 89. However, it does not explain all of the drop, which leaves the door open to further mechanisms.

A further complication of the target slope problem is that the angle of incidence of the 800 nm probe that generates the third harmonic changes as the target slope changes. This change in angle affects the harmonic generation through the linear and non-linear Fresnel equations contained within Equations (3.53) and (3.55). Upon plotting these equations as a function of angle, I found that the third harmonic intensity changes less than 2% for angles less than 5°, which corresponds to target slopes less than 0.09.

The next complication that I was concerned with is the issue of target break-up. The rear surface of the target is expanding at high velocity into vacuum, and at some point the crystalline solid will begin to disintegrate into small particles (Werdiger, Arad et al. 1996; Sorenson, Minich et al. 2002; Rességuier, Signor et al. 2007). In hind sight, I would have liked to have tested for this by comparing the normal incidence reflectivity with the THG to see if the drop in signal could be attributed to scattered light. Unfortunately, I was not able to perform this experiment. The problem with comparing the reflectivity from the interferometer with the THG is in the large differences in the collection optics. The interferometer system has an f/8 collection optic, while the THG has an ~f/3 optic. The target slope easily deflects light outside of the f/8 optic while the f/3 optic continues to collect light.

If the target remains solid over the probe duration and does not break-up, then we are left with the most interesting conclusion. Namely, that the THG decrease is due to a changing nonlinear susceptibility. If the silicon were to melt and become amorphous, then the susceptibility would fall to zero, and THG would be forbidden. However, as mentioned in section 2.2.2, these experiments were performed below the melting threshold, so I do not expect the nonlinear susceptibility to vanish. It is my belief that future research will shed light on this intriguing behavior.

CHAPTER 7. CONCLUSIONS

7.1 Summary

The goal of this work was to study shock induced melting using novel ultra-fast optical techniques. To achieve this goal, two simultaneous experimental programs were studied. The first program, characterization of laser-driven shock waves using THOR, took the majority of time since this research area was new to our group. The second program, development and implementation of optical probes, sometimes took a different direction from the shock wave studies. In the end, these programs were united in the observation of high-pressure shock loaded silicon targets.

Before beginning these studies, the THOR laser lab had to be designed and constructed from the ground up. THOR is a Ti:sapphire, CPA laser operating at 800 nm that produces ~ 1 J of energy in a 600 ps pulse, or up to ~ 0.6 J in a 40 fs pulse. The pulse can be split into two parts such that both a long pulse and a short pulse are produced. This is the configuration that I used in driving and probing the shock waves in my experiments. Since both pulses arise from the same pulse, there is no timing jitter between pulses, which leads to a very high time resolution pump-probe system.

To characterize the shock waves, I implemented a 2D Mach-Zehnder interferometer using the 40 fs laser pulse. This displacement interferometer provided information on the target rear surface expansion as a function of delay time. The slope of this expansion is related to the particle velocity, while the time of shock breakout is related to the shock velocity. These velocities were obtained from different target configurations with Sn foils, and the resulting data agree well with published Hugoniot data. Additionally, the data acquired from Sn/LiF targets matches up very well with HYADES simulations of the experiment.

I attempted to diagnose the melting transition in Sn foils by monitoring the reflectivity of the shocked samples. Unfortunately, all of the data had spurious artifacts in the reflectivity images that swamped the expected decrease reflectivity signal. A variety of behaviors could possibly explain the observed behavior, but attempts to narrow down the cause were unsuccessful.

In addition to reflectivity, I also utilized a third harmonic generation technique to monitor the melt transition in solids. This THG technique uses a circularly polarized input and is sensitive to the crystalline symmetry of the target. I was unable to detect sufficient THG signal from Sn, but I did find success using Si and GaAs targets. To develop this diagnostic, I observed femtosecond laser excitation of Si and GaAs. past the melt transition. These studies revealed an ultra-fast melting transition that occurred in less than 500 fs.

After this success, I implemented the THG diagnostic on laser-shocked Si targets, which produced results showing two distinct behaviors. The THG signal remains mostly constant before and after the breakout of a ~ 100 kbar shock, indicating the target remains crystalline up through an expansion of at least 3 μm. However, probing a ~ 300 kbar shock breakout in Si causes the THG signal to decrease. At this point, I am unable to say with certainty whether or not this decrease in THG is due to a change in the non-linear susceptibility of the material, or if it is due to the break-up and fragmentation of the rear surface. It is my hope that further experiments will help pinpoint the exact cause for the observed decrease in THG at high pressures.

7.2 Future Work

It is important to determine the exact reason for the decrease of the THG signal at higher pressures. Further experimentation with the addition of a normal incidence reflectivity diagnostics should distinguish between target breakup and changes in the non-linear susceptibility of the target. One fairly easy way to implement this is to use the discarded 800 nm light from the 3ω probe. The reflected 800 nm light from the target travels back through the λ/4 waveplate to produce vertically polarized light. This light transmits through the DBS and will be reflected off of the polarizer. A lens could be placed downstream of this reflection to image the target to a detector, such as a photodiode. This diagnostic would give a direct measurement of the reflectivity at the same point as the THG. Because both wavelengths are collected with the same fast optics, it would be beneficial to compare the two results to determine if they decrease at the same rate, which would indicate a geometrical loss of light from the collection optics. If the THG decreases, while the linear reflectivity remains constant, then it would indicate something interesting happening with the THG.

It would also be enlightening to shock GaAs targets. As discussed in this dissertation, harmonic generation from GaAs is less affected by changes in the linear index of refraction than Si, at a fundamental probe wavelength of 800 nm. After resolving the cause for the observed THG decrease, additional pressures should be studied to map the variation of THG from the elastic limit to above the melt transition. Upon successful completion of this experimental campaign, the continued success of the dynamic THG diagnostic depends on its ability to observe a change in different target materials of interest to the shock community.

An experimenter using the setup and techniques discussed in this dissertation will quickly realize the large amount of time and data necessary to achieve these goals. To ease the load, a few upgrades to the experimental setup could be implemented. First off, an encoded x, y, z, θ-stage would speed up the target re-positioning for each shot. Eventual automation using a Labview program would be ideal, as data acquisition from the oscilloscope and various CCD cameras could be included as well. Although doing this would be nice, I could not justify the time and expense necessary during my development of the experiment. However, I believe that a young graduate student new to the ranks would find this to be an exciting and challenging project.

Additionally, further detailed characterization of the shock pressures created using various laser intensities and targets would be beneficial for producing more repeatable shock driven experiments on THOR. The use of a 2D displacement interferometer, as discussed in this dissertation, gives high time resolution, but is unable to track fringe motion for expansion further than a few microns. The use of a line imaging VISAR would provide expansion data over much longer periods of time to aid in the comparison of experiments with simulations using HYADES. Alternatively, the displacement interferometer could be modified to operate with high magnification microscope objectives at normal incidence to prove higher spatial resolution for more accurate fringe tracking (Temnov, Sokolowski-Tinten et al. 2006).

APPENDICIES

Appendix A. Experimental Procedures for Probing Shocked Silicon

A.1 INTRODUCTION

In order to perform a successful laser shocked experiment on THOR, there were numerous steps that had to be completed. In this section, I will describe my thoughts and procedures in the setup and operation stages of an experiment.

A.2 LASER ALIGNMENT INTO THE TARGET ROOM

In general, this experiment needs as much energy as possible to drive a strong shockwave into the target for a reasonably sized spot. The experiment was usually run with THOR outputting ~ 1 J after the 5-pass amplification stage. After the beam leaves the laser table, it traverses open space to the compressor table, where it is periscoped up to the compressor height. Before the 1st crosshair on that table, I installed a 90% reflective, 10% transmissive 2" beamsplitter mounted on a magnetic base plate. It was stored in that general vicinity when the air compressor beamsplitter was being used, and I would swap the whole mount with my mount. This beamsplitter is used to direct 90% of the energy into the long pulse beam line into the target room (Figure 90). The remaining 10% is compressed in the vacuum compressor and used for optical probing in the experiment.

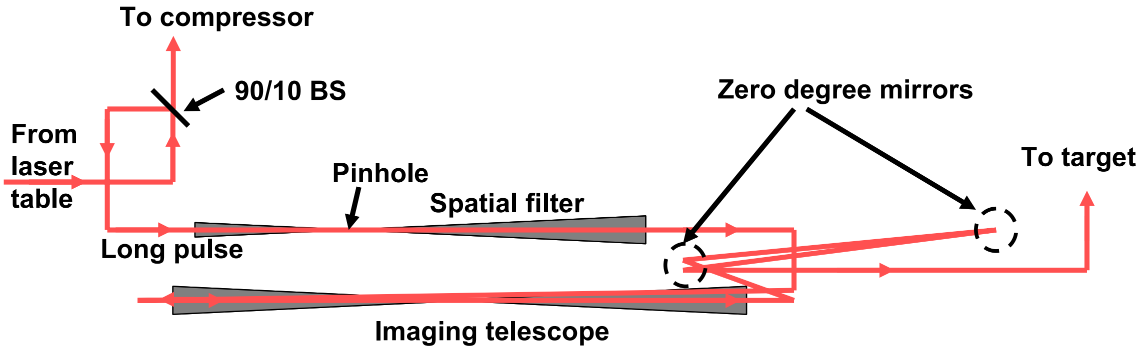

Figure 90. Schematic of the long pulse portion of the laser. Most of the laser energy is diverted into this leg by the 90/10% beamsplitter. The various reflections and beams paths mainly serve to delay the pulse with respect to the compressed pulse so that they are timed up at the target. Note: diagram is not drawn to scale, but the proportions are close to accurate.

After the laser reflects off of the beamsplitter, it hits two turning mirrors and enters my long vacuum spatial filter assembly. The pinhole (~ 1 – 2 mm) for this spatial filter (f/100) does not filter tightly, as I was interested in maintaining the pulse energy, but it does filter some of the higher order structure in the beam. The laser exits the vacuum window in the opening of the wall between the two rooms, and is collimated by a 1.5 m lens located just after the transverse vacuum tube that spans the space between the switchyard and the fusion chamber. Initial alignment through this spatial filter can be difficult, if the beam is not close to the right position and angle. It is crucial to make sure that the beam that is transmitted through the 90% beamsplitter is correctly aligned through the two crosshairs that precede the compressor spatial filter. If that alignment is correct, and the long pulse turning mirror has not been bumped, then the beam should be close to the correct alignment. I could usually get the beam through the telescope by sending a small amount of energy (< ~ 5 - 10 mJ) into the filter, while looking at the beam returning from the target room (above the long vacuum telescope tube) with the IR card, and tweaking the mirror before the spatial filter. If this did not work, I would often resort to using a CCD camera + lens to look at the scatter from a piece of paper located just after the vacuum tube window. The camera is much more sensitive, so I was able to raster the 1st mirror until I could find light being transmitted through the assembly.

In order for the shock and probe pulses to arrive in the chamber at approximately the same time, the long pulse must be delayed the same path length as the beam that traverses the compressor. Due to this extra length, the long pulse must travel back into the laser lab after being turned by two 45° mirrors. The beam barely sneaks by the small interferometer used for the blast wave experiment, so some discussion is usually necessary with that experiment's operator. After passing the interferometer, it travels a path located just above the longest vacuum telescope in the lab, which spans the two rooms. The beam is periscoped down in the laser room, so that the beam can be imaged through the vacuum telescope back into the target room. In order to insure proper alignment through this telescope, I would use the paper scatter imaged with a CCD to observe the shape of the beam. However, once I got the alignment technique for the spatial filter to be repeatable, this telescope did not usually need tweaking.

Once the beam was in the target room, it bounced off of four 0° mirrors to carefully adjust the delay and to avoid obstacles on the table so that the beam can be sent to the far end of the table, opposite of the side from the laser room. At this far end of the table, the beam reflects off of two 45° mirrors, before going through a removable crosshair, and then into the vacuum chamber through a window. Once the beam is centered on the crosshair, this portion of the alignment is done.

A.3 SINGLE SHOT TIMING SETUP

In order to operate the laser in a single-shot configuration, there are a number of changes to the timing control system that have to be made from the standard 10 Hz operation. In this section, I will discuss the correct operation and connection of the cables, control boxes, buttons, and switches. It is important to understand the general operation before we dive into the details, so pay attention.

The operation of the THOR laser is based on the 10 Hz operation of the pump lasers. If we want to operate at a rate slower than this, we must block all of the pulses, except for the ones we want through. In the case of single-shot operation, we want to block all pulses, except for the one pulse that we select. This blocking is done through the use of the Vincent Associates UNIBLITZ shutter that is located between the regen and the 4-pass amplifiers. The shutter control box (located below the SRS delay boxes on the rack in the laser lab) has several inputs, outputs, and switches that we can use to alter and control the operation of the shutter.

I built a small metal box labeled "Will's Big Red Button" that uses a few 555 timer ICs and associated components to output a 5V pulse that lasts ~95 ms. The reason is that we want to AND the signal from this box with one of the pulses from the 10Hz timing of the laser. The output of that AND-ed signal will be synched with the laser pulse, and we are guaranteed to only select one pulse if the button box output duration is less than the timing separation between laser pulses (approximately 10 Hz leads to < ~ 100 ms). The AND operation is performed in another small metal box that is located behind the shutter control box. It takes two inputs and has one output: the shutter button signal, the 10 Hz t_o-30 ns signal, and the output to the UNIBLITZ driver. This AND box actually utilizes a NAND IC, and a 555 chip so that it outputs a square pulse that controls the opening window of the shutter. The opening time is approximately 30 ms, so the shutter will open before the laser pulse arrives, and it will close after the pulse passes through the shutter.

Another key detail involves the stopping of the laser triggering so that data may be acquired using the oscilloscope, camera capture board, or other sources. My system operates in the following manner: all diagnostics are controlled by an SRS delay generator in the target room, and this is triggered at 10 Hz so that testing can be performed up until the actual shot. However, once the shot occurs, we want the trigger to stop so that we may save the data without it being overwritten. To accomplish this, a small trick is played. The target room SRS box is actually triggered by an additional small metal box labeled "Shutter restart box". This box takes two inputs and provided one output: t_o from the laser room, shutter output signal from the UNIBLITZ driver (shutter restart "input"), and "shutter restart output" that is used to trigger the SRS box. This box allows the 10 Hz signal to pass through the box unimpeded until the shutter restart signal from the UNIBLITZ arrives. When this signal arrives, signaling the successful operation of the shutter, the small box blocks any more trigger signals from passing through to the SRS box. This halting of the trigger signal allows data to be saved. After the data is saved, 10 Hz operation can be resumed if the red button is pressed on this box. It essentially "restarts" the normal triggering operation.

Additionally, the switches on the front of the UNIBLITZ need to be positioned such that the shutter is normally closed and is ready for remote operation. If the shutter is switched into remote mode, and the shutter starts going haywire, be sure to check that all of the small metal boxes have correct power supplies plugged in (5-6 V preferable, but should work with 9 V). Also, check that the cables are all connected properly so that the boxes can communicate with the correct devices. Refer to (Figure 91) to see how the cables are routed. Although the boxes all output 5 V signals, they are not able to drive a large current, and all of the inputs and outputs must be connected to HIGH Z connectors. Namely, the SRS boxes need to input and output HIGH Z, not 50 Ohms.

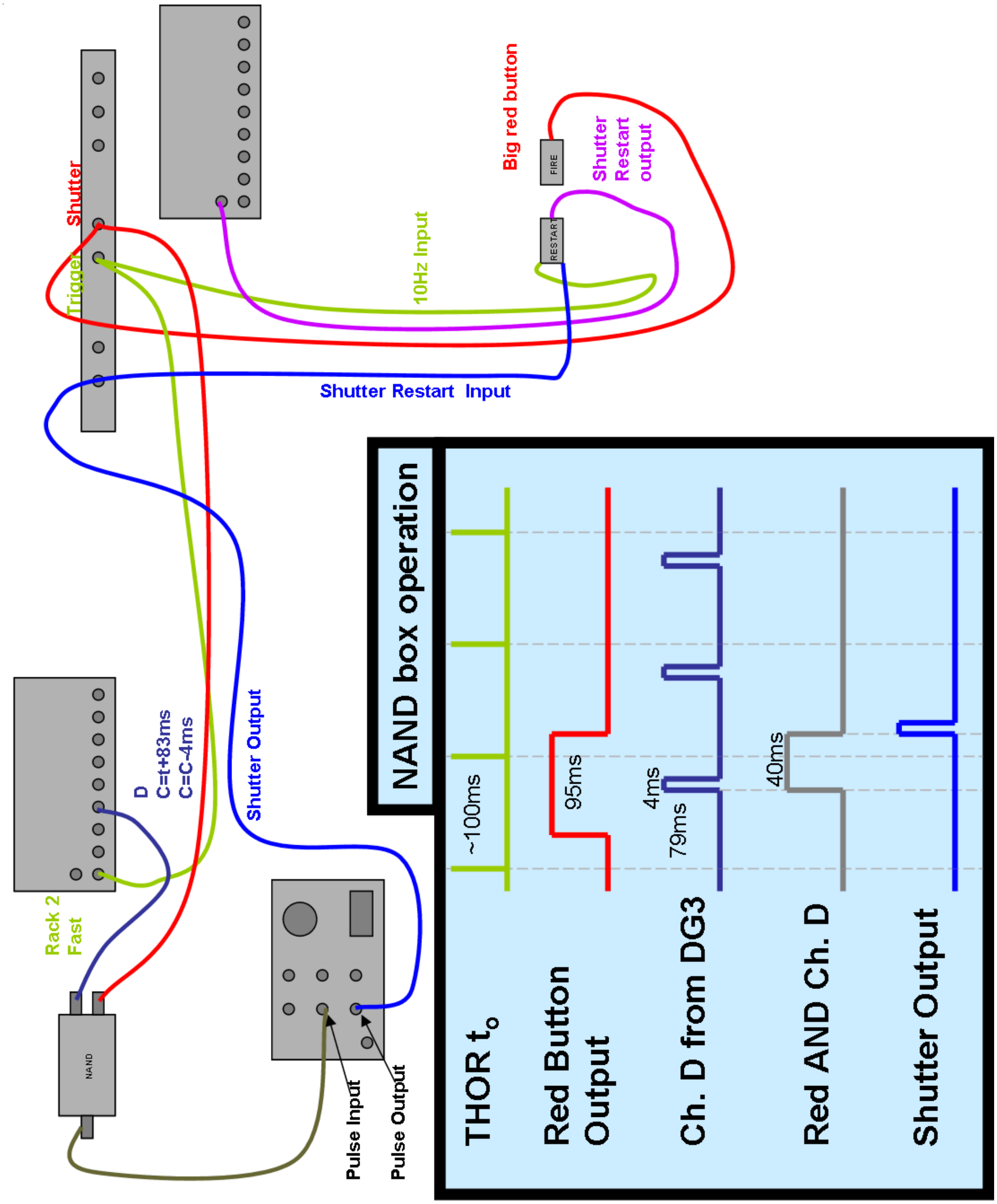

Figure 91. Diagram showing the operation and layout of the wiring for single-shot operation of THOR

In actual operation of the experiment, I found it very beneficial to temporarily switch between 10 Hz operation and single shot mode. In the beginning, I would trek into the laser lab and flip the switch on the shutter driver, but in later times, I built one last metal box. This box has a switch that will either allow the “Big Red Button” signal to pass through, or it will supply a 5 V signal to the shutter AND box. When the 5 V DC signal is used, the shutter will operate at 10 Hz, thus allowing all laser pulses to travel through the system. This mode is indispensable for adjusting the fringes in the interferometer, and for other miscellaneous uses such as measuring the power. When the alignment is complete, flip the switch back to single shot mode and wait a few seconds for the thermal load to stabilize in the 5-pass Ti:sapphire crystal.

A.4 ALIGNING THE SHOCK BEAM TO THE CHAMBER

With the chamber at air pressure, and the top removed, we are ready to align the shock beam to the chamber. It is important to make sure that there is no target in the small magnetic holder, remove the 3” magnetic base plate (either the microscope or the 3ω lens) from the chamber (if installed), and use a piece of paper to block where the beam will go in the 3ω beam line out the back of the chamber, after the first iris. This iris is used as the second alignment aid in conjunction with the giant crosshair before the chamber. Focus a CCD camera with lens onto the piece of paper after the iris. Point and center the shock beam (< ~10 mJ) through the giant crosshair and the small iris after the chamber, using the two, 2”, 45° mirrors before the chamber. It is relatively easy to align to the iris when it is closed down most of the way, and while the crosshair is still in the beam. You should see four lobes of the beam, and just ensure that they are all even in size and intensity. Once this is done, the shock beam is roughly aligned to the correct position.

Perform the same alignment with the HeNe alignment laser. The HeNe beam passes through a negative-positive lens pair before transmitting through the back side of the last steering mirror for the shock beam. The lens pair is adjusted so that the HeNe focuses to the same plane as the 800 nm beam, which eases alignment. Once again, the large crosshair before the chamber, and the crosshairs just after the chamber are used as the alignment aides. It is the HeNe position that we use to define the x-y positioning of the system, so the alignment must be done in a repeatable manner.

A.5 ALIGNING THE PROBE BEAM TO THE CHAMBER

It is very important to take care in aligning the probe beam through the delay rail, through the experiment optics, and to the chamber. This alignment needs to be as repeatable as possible, so care must be taken. Once a repeatable alignment technique is developed, day to day operations will flow more easily.

The 40 fs compressed laser pulse must travel straight through the switchyard after the vacuum compressor. In order for this to happen, the switchyard must be opened, and the kinematic 4” mirror must be moved off to the side. Also, the 6” AR coated window should be installed on the switchyard to allow the beam to exit vacuum, if the compressor is to be pumped down.

After exiting the switchyard, the beam reflects off of a 4” 90° mirror and then transmits through a positive-negative lens pair telescope. This serves to down-collimate the beam so that hard clipping on optics is minimized. Due to the uncoated optics (which cause focused back reflections) and the thickness of the lenses (which cause non-linear self-focusing), the THOR laser should be attenuated before entering the vacuum compressor. I used between 0.6 and 2 orders of neutral density filtering placed just after the 5-pass spatial filter for this purpose. This decreased the intensity of the compressed beam to minimize the aforementioned deleterious effects.

Once the beam is down-collimated, it is down-periscoped using two 4” mirrors so that its height is close to the final beam height of the experiment. It reflects off of two 2” 0° mirrors used for pointing and centering through rail delay line. The first alignment aid is the rotatable crosshair, and the second is the iris located on the rail stage. This 1st crosshair is what determines the alignment fiducial for the rest of the setup. Point and center the beam through the two aids, while being aware of the warped nature of the rail, as you slide the stage back and forth. I find it easiest to focus a CCD + lens onto a piece of paper located in the return path of the rail to visualize the alignment. Use a high magnification, if possible.

To initially align the beam properly thought the delay stage, use the following procedure along with (Figure 92).

1. Center the beam onto iris 1 (I1) at position 1 (P1) by physically moving I1
2. Move the stage to position 2 (P2), and use mirror 1 (M1) to center the beam onto I1
3. Goto step 1 and repeat until finished

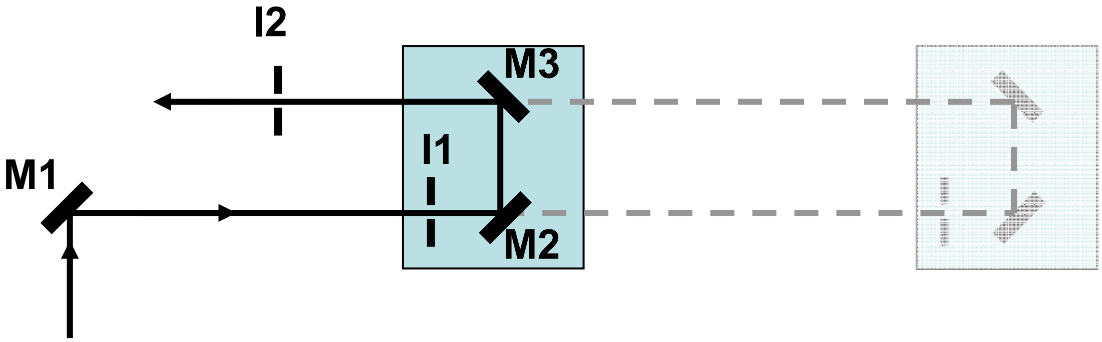

Figure 92. Diagram illustrating the components and positions in the delay leg.

Now, the incoming beam is aligned, so use the following steps to align the outgoing beam:

1. Physically center I2 on the beam at P1
2. Move the stage to P2 and use M3 to steer the beam through I2
3. Goto step 1 and repeat until finished

After aligning this section, move the camera and focus it on a note card placed over the retro mirror of the reference arm of the interferometer setup. Now, use the two 2” mirrors (90° and 0°) to point and center the beam through the next two irises. This is the long straight input path to the diagnostic setup (Figure 49). Use the crosshair as the center fiducial, and center the mark on the pattern from each closed down iris using the camera setup.

Next, we want to adjust the 1” 0° mirror just after the 2nd iris so that the beam is centered on the next iris (located in the reference arm). This also steers the beam into the chamber, so make this a repeatable adjustment. The 1” 90° mirror just before the 3rd iris is then used to align to the 4th iris, located just before the retro mirrors where the camera is focused.

At this point the interferometer beams should be mostly aligned. You can check the reference arm by unblocking the path, and allowing the beam to propagate to the interferometer CCD on the opposite side of the setup. Don’t worry about precisely positioning this beam, as it will be adjusted later.

Before the third iris, there is a 1” beamsplitter which reflects ~66% of the light into the shock probing (chamber) arm of the interferometer. This beamsplitter and the following 2” gold mirror can be used to point and center through the next two irises located just outside the window, and just inside the chamber. Once the correct alignment had been performed, I found it rare for these to need adjusting.

A.6 ADJUSTING THE TIME DELAY BETWEEN PUMP AND PROBE

The precise placement of the four 0° mirrors changes for each experimental run, depending on the obstacles on the table, but also depending on the target thickness and the desired time delay between pump and probe. For example, if I were to change from a 10 μm target to a 110 μm target, and the shock velocity was 10 μm/ns, then I would need the shock driving beam to arrive 10 ns earlier so that I could probe during the shock breakout.

The other variable to consider is that the small one meter rail, located near the switchyard and used for precise delay adjustment, is not straight and or flat. It appears to be warped in the region of ~420 mm to ~550 mm, with a few more distortions at the higher numbers. The smoothest region is from 0 to ~420 mm, so it is best to only use this region. That being said, the other sections of the rail can be used, but expect the probe to walk around slightly, and corrections to the pointing will need to be performed for each location. I have operated in this manner several times, but it will slow the experiment down slightly. However, it is still faster than changing the position of the 0° mirrors in the middle of a shot run.

Once the pump and probe beams are roughly aligned into the chamber (do not be precise yet), it is a good idea to measure the timing delay. I used the small gray Newport photodiode with a ~50 ps rise time for this measurement. I placed the photodiode in a repeatable position near the target position in the chamber, and it detected the scattered light from a piece of paper placed at the target position. The shock beam must be attenuated by several orders of magnitude in order for it to produce the same signal level as that generated from the probe. It is important that the energies of each beam be adjusted so that they produce equivalent voltage levels on the oscilloscope.

When both signals were on the photodiode trace, I used the Tektronix oscilloscope to zoom in on the pulses and I used the cursors to measure the time delay between the pulses. Be sure to block the beam that you are not measuring so that the ringing from its signal is not affecting the signal you are measuring. Perform this measurement at a variety of positions on the probe delay rail, and fit a line through the data. The slope from the line fit should be related to the speed of light, but it will invariably be slightly off. For the real data analysis later on, I used the speed of light as the slope, and fit a line only using the offset as a parameter. This analysis allows you to determine where the "t_o" is located for the two laser pulses, which I used in my data and plots. The delay where these two pulse peaks overlap is correlated to the actual laser signals by the response time of the photodiode and the oscilloscope with the actual laser pulse widths. If these two response factors and the pulse widths are known, then the actual temporal delay between the two pulses should be extractable from the data. However, these factors are not accurately known to me, so I did not correct for this in my data analysis.

Now, the target thickness and estimated shock velocity need to be taken into account so that the probe will arrive at the rear surface at the appropriate timing delay after the shock drive. If the photodiode measurements indicate that the timing will be wrong, then the 0° mirrors need to be adjusted to bring the pulses into correct temporal alignment.

I found that this temporal measurement needed to be done for each day, as slight adjustments in the position of mirrors from day to day tend to slightly adjust the time separation. Typically, there was no need for any physical adjustments, but the later data analysis will benefit from knowing the correct delay.

A.7 SETTING THE TARGET ZERO POSITION

Each day, the home position of the target needs to be set using the broken USAF test pattern target. Be sure to block all 800 nm beams so as not to damage the alignment optics or components. Mount the USAF pattern into one of the magnetic target holders so that it is easily swapped in and out with the other targets. Once in place, insert the magnetic base plate containing the 5x microscope objective, the right angle mirror, and the CCD camera (the “5x spot microscope”). It is this mounted objective plus camera that is used to define the “home” position. Although the objective arm can move slightly when roughly handled, I believe it is still the most reproducible way to define the z-position of my target.

The HeNe beam that is correctly aligned through the chamber is now used to check the rotation of the objective “arm”. If the HeNe travels through the center of the lens, and is positioned in the middle of the CCD, then assume things did not get bumped.

If things did get bumped, be careful not to adjust the “z” of the 5x spot microscope. If the “z” gets changed, then this re-defines the target position, and all spot measurements and positions will need to be re-measured and checked.

If the HeNe is centered on the lens, but not the CCD, make small tweaks to the folding mirror to center it. If the lens centering is off, then continue below.

Unscrew the objective from the mount so that the beam travels into the vertically mounted CCD. Slightly adjust, if necessary, the fold mirror, or the CCD so that the HeNe spot is more or less centered on the camera. Be sure not to rotate the CCD so much that it is non-normal to the beam path. Now, screw in the objective into the mount on the arm. Carefully rotate the arm until the beam is centered on the camera, and continue.

Once the 5x spot microscope is aligned with the correctly aligned HeNe, the xyz target manipulator is adjusted to bring the small features of the USAF target into view and into focus. Make sure the target is aligned so that the chrome coating is located on the “probe” side of the setup and not on the “shock” side. This is so the probe beams do not have to refract into the glass before reflecting off of the chrome pattern. Align the pattern on the CCD so that a unique section of the pattern is visible in the center of the screen and notice *exactly* where the HeNe beam intersects it. It is this exact center that you will need to identify in the measurement arm of the interferometer. Now, unblock the probe portion of the 800 nm beam so that the interferometer beam will travel into the chamber, and reflect off of the USAF pattern. From here, the beam will travel through a 0.5” diameter, 7.5 mm focal length lens that images the target to the interferometer CCD.

After exiting the chamber, the beam reflects off of a 2” mirror that steers it to a 50% beamsplitter that combines the measurement arm with the reference arm of the interferometer. These combined beams travel trough a cube polarizer used to select p-polarization and into the filtered CCD camera. Use the various mirrors, if necessary, to center the unique feature of the USAF target on the interferometer CCD, and adjust the micrometer stage of the 7.5 mm f.l. lens to bring the feature into as sharp a focus as possible. There seems to be a slight astigmatism to the imaging system, but do the best possible.

Use a small piece of tape, or the “grid” software, to mark the exact “center” of the target that was found in the previous part using the 5x spot microscope. The purpose of these actions is to define exactly where on the interferometer camera the shock will be. Once this is done, do not touch the target, or the interferometer, as their precise alignment is necessary to continue the alignment.

A.8 MEASURING SPOT SIZES

Before measuring the shock drive spot size, we need to switch to a higher magnification microscope. Carefully remove the 5x microscope assembly on the magnetic base plate and set it aside. Install the 1” aluminum mirror just outside the 3ω window, and steer the HeNe beam onto the face of a CCD camera that you place in the nearby holder. Install ~ 0.6 or 1 neutral density (ND) filters onto the CCD to attenuate scattered light. Install the 10x objective so that the HeNe beam returns to the same location on the CCD. Now that the beam travels straight and centered through the objective, adjust the “z” of the CCD so that the USAF target is in good focus, and then center the USAF fiducial on the CCD screen. Mark the spot on the screen, and remove the USAF target. Place a paper beam block in front of the objective.

Attenuate the THOR laser by adjusting the delay of the PRO Q-switches. In the target room, install a 2” 0° mirror in the shock driver beam line between the last and next-to-last mirrors before the chamber. This serves to attenuate the beam before sending it into the microscope objective and CCD. If the energy is too high (you can see the beam on an IR card), it will burn the objective. Setup an ND filter holder, and install a few ND filters in the beam to attenuate the laser below the level where you can see the focused spot on an IR card in the dark. If the energy level is safe, remove the paper beam block, and let the laser enter the objective. After blocking the HeNe, carefully steer the shock driving laser onto the center of the marked location.

At this point it is important to mention that any changes in the thermal load in the 5-pass crystal will change the focal spot size. In particular, the exact conditions necessary for a shot must be reproduced in order to correctly measure the spot size. Ensure that the reflected beam from the 0° mirror is properly blocked. Add a few more orders of ND filters to the stack behind the mirror to attenuate the beam so that it is not visible on the CCD. Change the timing system and shutter controller so that the laser will run in single shot mode. Adjust the PRO timing such that the laser is running at full power.

Now, in single shot mode at full energy, we can measure the spot size of the shock driving laser using the 10x objective and CCD. Once the correct beam size is set, correct any steering problems so that the beam is centered on the aforementioned spot that was marked on the monitor. Block the 800 nm beam, and replace the USAF target. Use the xyz manipulator to return the identifiable portion of the target to the center of the marked location. Now, the target is aligned with the shock driving laser.

Once again, let the probe beam travel into the chamber and reflect off of the correctly positioned target. Adjust the mirrors after the chamber to center this spot on the interferometer camera, and confirm the mark on the monitor. At this point, let the reference arm travel to the CCD and overlap the beams. Adjust the reference arm delay micrometer a small amount until the fringes appear in the interferometer. Don't worry about straightening the fringes yet, as the target tilt is most likely different between the USAF target and the silicon wafer target.

A.9 3ω ALIGNMENT

Now that the shock driving laser spot has been measured, we need to focus on the 3ω beam alignment and spot size. Replace the USAF target with a paper target mounted in a target holder. I found that smooth card stock, such as from certain postcards or magazines, offers the best resolution. Carefully adjust the z position of the target manipulator to bring the rear surface of the paper target into focus. Sometimes side illumination with a flashlight allowed the paper grain to be seen clearly on the 10x and used as a focus diagnostic. Once this is done, replace the 10x objective mounted on a magnetic base with the magnetic base containing the 3ω lens.

The 3ω beam line is split from the incoming probe by a 2” beamsplitter between the first and second iris in the probe setup. From here, the beam is delayed using a pair of mirrors on a micrometer stage to retro-reflect the beam, offset to the side. After the delay, the beam reflects off of a 90° mirror and turns straight toward the vacuum chamber. It passes through an iris, a half waveplate, a rotating calcite polarizer, a dichroic beamsplitter that reflects 3ω, a quarter waveplate, another iris, enters the vacuum chamber through a fused silica window, passes through a 0.5” diameter, 2 cm f.l. fused silica lens, and finally passes through a quartz microscope slide before striking the target (Figure 93). The half-wave is plate in combination with the calcite polarizer to variably attenuate the beam. The quarter-wave plate is rotated such that the probe beam is circularly polarized, which can be set by using a mirror to reflect the probe back through the quarter-wave plate and polarizer and adjusting the wave plate until the light transmitted through the polarizer was minimized. When this happens, the net rotation of the light is 90°, and the quarter-wave plate adds 45° rotation on each pass.

This section of the beam line is aligned by using the two irises in combination with the earlier rotatable crosshair. Use a CCD with lens to image the beam spot scattered from a piece of paper to ensure proper alignment. Use the half-wave plate to attenuate the beam so it does not damage the paper. The beam should be visible on the interferometer camera if the filters are removed and/or the gain is increased. Center the 3ω spot on the marked spot on the monitor so that the 3ω spot overlaps the center of the shock spot.

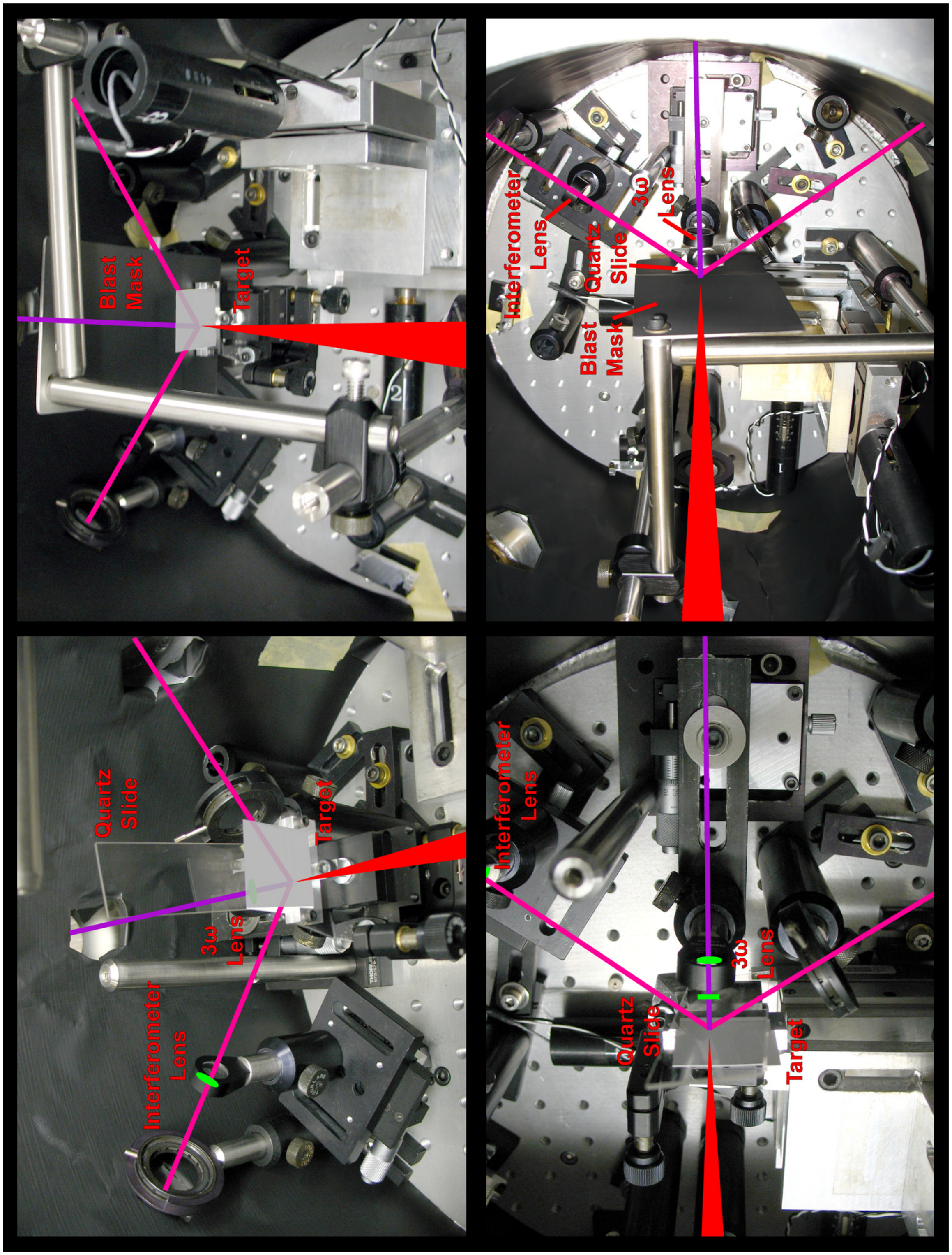

Figure 93. Multiple views of the setup inside the vacuum chamber

At this point, the interferometer camera can be used to image the spot size of the 3ω spot. Be sure to attenuate the beam so that it is not saturated. The spot size might change slightly when the laser changes from 10 Hz to single shot, so in general always take measurements in single shot operation. The spot size can be adjusted by turning the micrometer on the lens translation stage. The stage has some irregularities and hysteresis in its motion, so steering is usually necessary after changing the z position. After this is completed, all of the cameras should be looking at the same section of the target, and the monitors have marks to indicate exactly where the beams are.

The previous alignment was done with a paper target and cameras looking at scatter. Once we install the actual Si wafer target, things will have to be slightly tweaked. Get started by removing the paper target, and installing a Si target. It is quite useful to have a hole in the target that can be seen from both the front and rear of the target. By placing this hole at the center position, we are able to check the alignment of the probe beam line and the interferometer.

First, adjust the z of the target manipulator to bring fringes into the field of the interferometer camera. This can be more accurate than looking at the focus of the target with the 10x objective, depending on if the hole is flush with the rear surface, or if it is eroded at the edges.

Now, the tilt of the target holder needs to be checked so that it is normal to the 3ω beam line and will reflect the third harmonic straight back upstream to the dichroic beamsplitter and then to the PMT. The PMT is positioned by using the IR-viewer to observe the small amount of reflected 800 nm light from the dichroic. Be sure that the 3ω beam will focus on an unimportant section of the Si wafer. This can be checked by looking where the aligned HeNe intersects the front of the wafer.

To check the tilt, I found it best to orient the λ/4 waveplate so that it will generate linear polarization so that the maximum amount of 800 nm light travels upstream. Focus a camera with lens on the rear (target facing) surface of the second iris in the 3ω line from the chamber. It is possible to adjust the target tilt for normal orientation by monitoring the faint scatter of the returned beam on the edge of the closed iris. However, the target manipulator is not a gimbaled mount, so each adjustment will move the z and possibly x, y positions of the target. Use the various cameras to watch the target reflection as you reposition the xyz stage back to the correct position.

A.10 OVERLAPPING THE SPOTS

Once the tilt and the z are set, it is necessary to correlate the obscuration of the HeNe beam transmitted through the hole with the view of the probe beam reflected off of the target. To do this, we need to adjust the x-y view of the target and/or camera. This is much easier to do when the hole is straight through the target, rather than eroded down to the box on the silicon-on-insulator (SOI) wafer (Figure 94). However, an eroded hole can be used if it is first examined under a microscope to determine the amount of erosion. Move the target left and right, and up and down to locate the edges of the hole as seen by the HeNe, and mark those on the monitor showing the interferometer image. This allows you to find where the shock will arrive on the interferometer image.

Move the center of the hole to the shock position. Now focus and adjust the Questar imaging telescope so that the etched silicon target section is in focus. It is necessary, most of the time to block the 800 nm beams so the Questar and CCD do not get damaged. I found it useful to draw lines on the monitor where the corners of the etched Si are to aid in target positioning on future shots. It was also helpful to note the pattern of scattered HeNe light from the target (the HeNe often needed to be attenuated

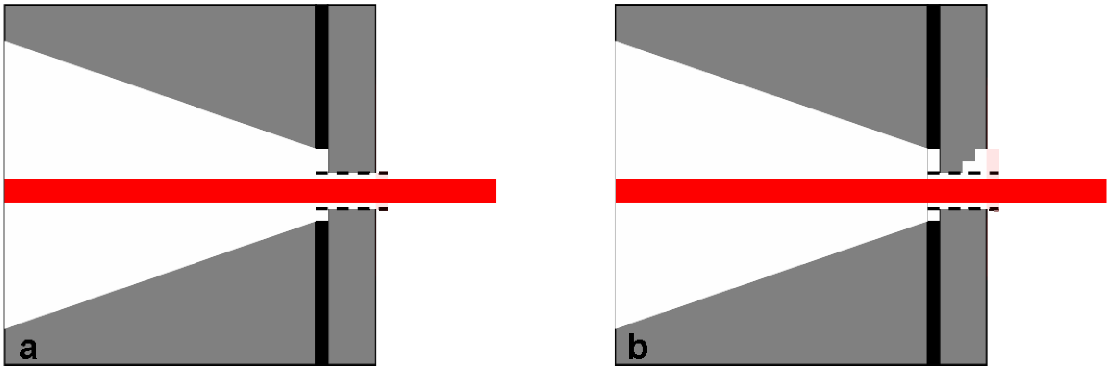

Figure 94. Diagram showing a HeNe beam passing through a hole in the target while the interferometric probe reflects off of the rear surface of the target. (a) a "clean" hole through the target allows easy correlation of the target position with both probes. (b) a "dirty" hole makes correlation difficult between the probes.

so as to not saturate the CCD). It is important to be able to find your way around the target by only watching the Questar view, since only the Questar is useful in positioning a new target location at the center of the shock drive/probe region.

Once the Questar is focused on the interaction region, we can now move on to fine tuning the position of the 3ω beam. Move the target so that a clean section of silicon is in view. Ensure that the correct 3” magnetic base is installed for the 3ω. After attenuating the beam with the λ/2 waveplate, unblock the beam and allow it to hit the target. If the previous alignment was performed correctly, the 3ω beam should be in view of the camera. It might be necessary to increase the gain on the interferometer CCD and/or remove ND filters to see the scattered light on the camera. Once you are able to see it, tweak the last turning mirror in the 3ω line to position the spot at the laser interaction region. Alternatively, it is possible to use the interferometer beam to view the target, while watching for a small dark spot to appear due to damage from the 3ω beam. I found that using the small damage spot worked well for identifying the position of the 3ω spot, but I also found it useful for fine tweaking of the imaging lens in the interferometer.

Before vacuum pump-down, it is important to carefully adjust the position of the 7.5 mm f.l. imaging lens in the interferometer arm. Use the 3ω beam to produce a series of small damage spots in a horizontal row across the screen. At moderate fluences, this can be accomplished by shooting the laser 5-10 times in the same spot before moving to the next spot with the target manipulator. Once there are several damage spots across the screen you can watch them come into and out of focus as you slowly adjust the imaging lens position. Because the target plane is tilted with respect to the imaging plane, the focus of the imaging plane is swept across the view of the interferometer camera due to the limited depth of field. I found that it was necessary to slightly detune the focus from the center of the screen in order to compensate for the change in imaging that occurs upon pump down of the vacuum chamber. The direction of detuning is such that the damage spot becomes a smaller point, rather than a larger donut shape.

A.11 SETTING THE CORRECT PROBE INTENSITIES

The probe intensities are adjusted by multiple mechanisms. The roughest adjustment is the insertion of ND filters in the beam path after the 5-pass spatial filter. I typically used approximate filtering of 0.6 to 1 ND, but the exact amount is determined by a balance between lowering the intensity as much as possible, and keeping enough energy to obtain saturated fringes in the interferometer. This serves to decrease the intensity before the pulse is compressed, thus lowering the non-linear effects that occur at high intensity.

For fine adjustment of the probe beams, there are λ/2 waveplate plus polarizer combinations located in the 3ω line and in the probe line of the interferometer. The fine adjustment is helpful in the interferometer arm for carefully adjusting the brightness of the interference fringes. The higher pressure shock waves tend to cause a loss of reflectivity in the breakout region, so it is necessary to saturate the fringes so that some signal from the breakout is recorded. As more reflectivity is lost, the brightness of the probe arm must be adjusted brighter to be able to obtain any signal.

The reference arm of the interferometer does not have a waveplate-polarizer combination, but it does have an ND filter holder. The problem with this form of adjustment is that as the filters are changed, the delay of the reference arm must be adjusted. However, once the filtering was adjusted correctly, I found it was not necessary to change it.

The variable attenuator in the 3ω arm is used in combination with the iris size to set the probe intensity. I kept the iris closed down to ~ 2 – 3 mm so that the focal spot on target would be more Gaussian shaped. The attenuator was adjusted so that the probe would not damage the target on the first shot. This was checked by probing the same position three or more times. If the second probe signal was not the same as the first, then the intensity was decreased slightly. Because the THG process is relatively weak, the intensity needs to be set as high as possible, within the limit of not damaging the target. This is a sensitive balance that is sometimes difficult to achieve.

A.12 SETUP CHECKLIST

The following list summarizes the main points of the experimental procedures described above.

1. Turn on the laser and let it warm up.
2. Set up single shot timing operation.
3. Set the target zero position and align the HeNe to it (use the 5x microscope).

4. Align beams through spatial filters and the compressor
5. Roughly align the long pulse beam to the chamber
6. Align the probe beam to the target
7. Measure/adjust the rough pump/probe delay with the long pulse 0° mirrors
8. Align the attenuated, full energy long-pulse beam to the target position (use the 10x microscope)
9. Set/measure the shock spot size
10. Align and set/measure the 3ω spot size
11. Align the Questar
12. Confirm that the interferometer camera is viewing the overlapped shock and 3ω beams
13. Set the correct probe intensities

A.13 TAKING DATA

Once the setup has been completed for the day, data acquisition is relatively straightforward. The general procedure is the following:

1. move the target close to a new shot position.
2. adjust the target z-position to bring fringes to the center of the interferometer screen.
3. take several probe-only shots to determine if the position will correctly overlap the peak of the shock breakout, and if the intensity is set correctly.
4. save a reference shot for 3ω.
5. move the target slightly to a fresh position, and save a reference shot for the interferometer, while blocking the 3ω.
6. unblock the shock beam, take a full shot, and save the data.

7. reposition the probe delay rail, if necessary.
8. Check, and re-align the probe beam through the 1st and 2nd irises.
9. Check and re-position the 3ω spot.
10. Go back to step 1 and repeat.

Appendix B. Various useful quantities

$$\omega = 2\pi\nu \tag{B.1}$$

$$\omega = \frac{2\pi e}{h} * [eV] \tag{B.2}$$

$$k = \frac{2\pi n}{\lambda} = \frac{n\omega}{c} \tag{B.3}$$

$$\lambda = \frac{c}{\nu} = \frac{2\pi c}{\omega} = \frac{2\pi n}{k} \tag{B.4}$$

$$\phi = kx = \frac{2\pi nx}{\lambda} \tag{B.5}$$

$$I_{Gaussian}[t] = e^{-\left(4Ln[2]\frac{(t-t_o)^2}{\tau_{FWHM}{}^2}\right)} \tag{B.6}$$

$$\lambda[\mu m] = \frac{1.2398}{[eV]} \tag{B.7}$$

$$T[K] = \frac{e}{k_B} = 11604 \times [eV] \tag{B.8}$$

$$k_B = 1.3807 \times 10^{-23}\,\frac{J}{K} \tag{B.9}$$

$$e = 1.6022 \times 10^{-19}\,C \tag{B.10}$$

$$m_e = 9.1094 \times 10^{-31}\,kg \tag{B.11}$$

$$m_p = 1.6726 \times 10^{-27}\,kg \tag{B.12}$$

$$c = 2.9979 \times 10^{8}\,\frac{m}{s} \tag{B.13}$$

$$h = 6.6261 \times 10^{-34}\,J \cdot s \tag{B.14}$$

$$\hbar = 1.0546 \times 10^{-34}\,J \cdot s \tag{B.15}$$

$$\varepsilon_o = 8.8542 \times 10^{-12}\,\frac{F}{m} \tag{B.16}$$

$$\mu_o = 1.2566 \times 10^{-6}\,\frac{H}{m} \tag{B.17}$$

Table 11. Gaussian pulse widths and relationships for various Gaussian definitions

	$e^{-\frac{x^2}{\omega^2}}$	$e^{-\frac{x^2}{2\cdot\omega^2}}$	$e^{-\frac{2\cdot x^2}{\omega^2}}$	$e^{-\frac{4\cdot Ln(2)\cdot x^2}{\omega^2}}$
$\frac{1}{e}$ radius	ω	$\omega\cdot\sqrt{2}$ =1.414 ω	$\frac{\omega}{\sqrt{2}}$ 0.707 ω	$\frac{\omega}{\sqrt{4Ln(2)}}$ =0.600 ω
$\frac{1}{e^2}$ radius	$\frac{\omega}{\sqrt{2}}$ =0.707 ω	ω	$\frac{\omega}{2}$	$\frac{\omega}{\sqrt{8Ln(2)}}$ =0.425 ω
HM	$\omega\cdot\sqrt{Ln(2)}$ =0.833 ω	$\omega\cdot\sqrt{2Ln(2)}$ =1.177 ω	$\omega\cdot\sqrt{\frac{Ln(2)}{2}}$ =0.589	$\frac{\omega}{2}$
FWHM	$\omega\cdot\sqrt{4Ln(2)}$ =1.665 ω	$\omega\cdot\sqrt{8Ln(2)}$ =2.355 ω	$\omega\cdot\sqrt{2Ln(2)}$ =1.177	ω

Appendix C. Gaussian Beam Profile

Let's define a 2D Gaussian beam intensity profile whose $\frac{1}{e^2}$ radius is *w*. (Note the "2" in the exponent). This definition is based on defining the electric field as a Gaussian without the squared exponent.

$$Fluence(r) = Energy \cdot \frac{2}{\pi w^2} \cdot e^{\left(\frac{-2r^2}{w^2}\right)} \tag{C.1}$$

We can give this beam profile a Gaussian time dependence.

$$Intensity(r,t) = Fluence(r) \cdot \sqrt{\frac{2}{\pi}} \cdot \frac{1}{T} \cdot e^{\left(\frac{-2t^2}{T^2}\right)} \tag{C.2}$$

We can set the area under the 2D spatial profile equal to the area of an equivalent top-hat beam profile whose diameter is *d*. See Figure 95 for a graphical representation.

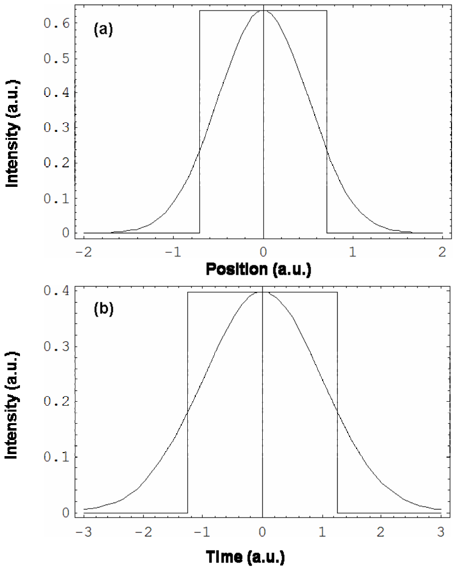

Figure 95. A Gaussian profile is shown with the corresponding top-hat profile whose peak is the same as the Gaussian, and whose area or time integrates to 1 for a 2D spatial profile (a) or a temporal profile (b).

$$\frac{\pi w^2}{2} = \pi\left(\frac{d}{2}\right)^2 \qquad (C.3)$$
$$d = \sqrt{2}w$$

The ${}^{1}\!/_{e^2}$ radius, *w*, can be related to the full width at half maximum (FWHM) by

$$w = \frac{r_{FWHM}}{\sqrt{2Ln(2)}} \qquad (C.4)$$

The peak fluence of the Gaussian beam is equal to the height of the equivalent flat-top beam (see Figure 95). This normalizes both profiles to the pulse energy.

$$Fluence_{Peak} = \frac{Energy}{\pi\left(\frac{d}{2}\right)^2} \qquad (C.5)$$

We can now plug (C.4) into (C.5) to get the peak fluence in terms of the FWHM.

$$\begin{aligned} Fluence_{Peak} &= \frac{Energy}{\pi\frac{\left(\frac{r_{FWHM}}{\sqrt{Ln(2)}}\right)^2}{2^2}} \\ &= Ln(2)\cdot\frac{Energy}{\pi\left(\frac{r_{FWHM}}{2}\right)^2} \qquad (C.6) \\ &\approx 0.69\cdot\frac{Energy}{\pi\left(\frac{r_{FWHM}}{2}\right)^2} \end{aligned}$$

For the 1D Gaussian temporal profile, we can perform a similar calculation. The area under the 1D profile can be set equal to an equivalent top-hat, where T is the ${}^{1}\!/_{e^2}$ radius, and d is the full width of the flat-top.

$$T\sqrt{\frac{\pi}{2}} = d\cdot 1 \qquad (C.7)$$

This full width can be related to the FWHM of the Gaussian by

$$T = \frac{t_{FWHM}}{\sqrt{2Ln(2)}} \tag{C.8}$$

We rearrange this to get the relationship between the FWHM and full width

$$\begin{aligned} d &= \sqrt{\frac{\pi}{2}} \cdot \frac{t_{FWHM}}{\sqrt{2Ln(2)}} \\ &= \sqrt{\frac{\pi}{Ln(2)}} \cdot \frac{t_{FWHM}}{2} \end{aligned} \tag{C.9}$$

We now plug this in to find the peak intensity of a Gaussian pulse.

$$\begin{aligned} Intensity_{peak} &= \frac{Fluence_{peak}}{d} \\ &= \frac{Fluence_{peak}}{t_{FWHM}} \cdot 2 \cdot \sqrt{\frac{Ln(2)}{\pi}} \\ &\approx 0.94 \cdot \frac{Fluence_{peak}}{t_{FWHM}} \end{aligned} \tag{C.10}$$

We can combine the spatial and temporal calibrations to get a single equation for the peak intensity of a Gaussian laser pulse.

$$\begin{aligned} Intensity_{peak} &= Ln(2)^{3/2} \cdot \frac{2}{\sqrt{\pi}} \cdot \frac{Energy}{t_{FWHM} \cdot \pi \left(\frac{r_{FHWM}}{2} \right)^2} \\ &\approx 0.65 \cdot \frac{Energy}{t_{FWHM} \cdot \pi \left(\frac{r_{FHWM}}{2} \right)^2} \end{aligned} \tag{C.11}$$

Appendix D. Depth of Field

For a Gaussian beam, the beam radius ω is given by

$$\omega^2(z) = \omega_0^{\ 2}\left[1+\left(\frac{\lambda z}{\pi\omega_0^{\ 2}}\right)\right] \tag{D.1}$$

where the beam waist ω_0 is

$$\begin{aligned}\omega_0 &= \left(\frac{2\lambda}{\pi}\right)(f/\#)\\ &\approx \frac{1}{2}(f/\#)[\mu m]\quad (\sim 800\text{nm})\end{aligned} \tag{D.2}$$

Here, the photographic f-number is defined as

$$f/\# = \frac{\text{focal length of the lens}}{\text{beam diameter illuminating the lens}} \tag{D.3}$$

For imaging applications, it is important to know the range over which your subject will remain in focus. We can define this depth of field or depth of focus (DOF) as the region surrounding best focus such that $\omega < \sqrt{2}\omega_0$.

$$\begin{aligned}DOF &= \left(\frac{8\lambda}{\pi}\right)(f/\#)^2\\ &= \frac{2\pi\omega_0^{\ 2}}{\lambda}\\ &\approx 2(f/\#)^2[\mu m]\quad (\sim 800\text{nm})\end{aligned} \tag{D.4}$$

This choice of $\omega < \sqrt{2}\omega_0$ is somewhat arbitrary, but this definition is fairly common. The depth of field as defined can also be related to the Rayleigh range z_R as follows:

$$DOF = 2z_R = 2\left(\frac{\pi\omega_0^{\ 2}}{\lambda}\right) \tag{D.5}$$

For example, a 1 cm 800 nm beam focused by an f=10 cm lens has an f-number of 10. For Ti:sapphire wavelengths, the beam waist in μm is approximately equal to half of the f-number. Similarly, the minimum beam diameter is equal to the f-number. Thus an f/10 lens will have a 5µm beam waist or 10 µm diameter. The depth of field for this setup is twice the f-number squared, or 0.2 mm.

Appendix E. Phase to Expansion Conversion

It is important to account for the angle of incidence and the existence of material, such as glass or LiF, at the rear surface in my interferometer fringe calibration. Because the incoming probe beam is at an angle θ_1 with the target normal, it will refract inside the substrate as in Figure 96 For example, using Snell's Law,

$$n_1 \cdot Sin(\theta_1) = n_2 \cdot Sin(\theta_2) \tag{E.1}$$

with $\theta_1 = 10°$, n_1(vacuum) = 1, n_2(LiF,800 nm) = 1.3889, I find that θ_2=7.18°. Using this new angle, I must find the amount of fringe motion due to a rear surface expansion of

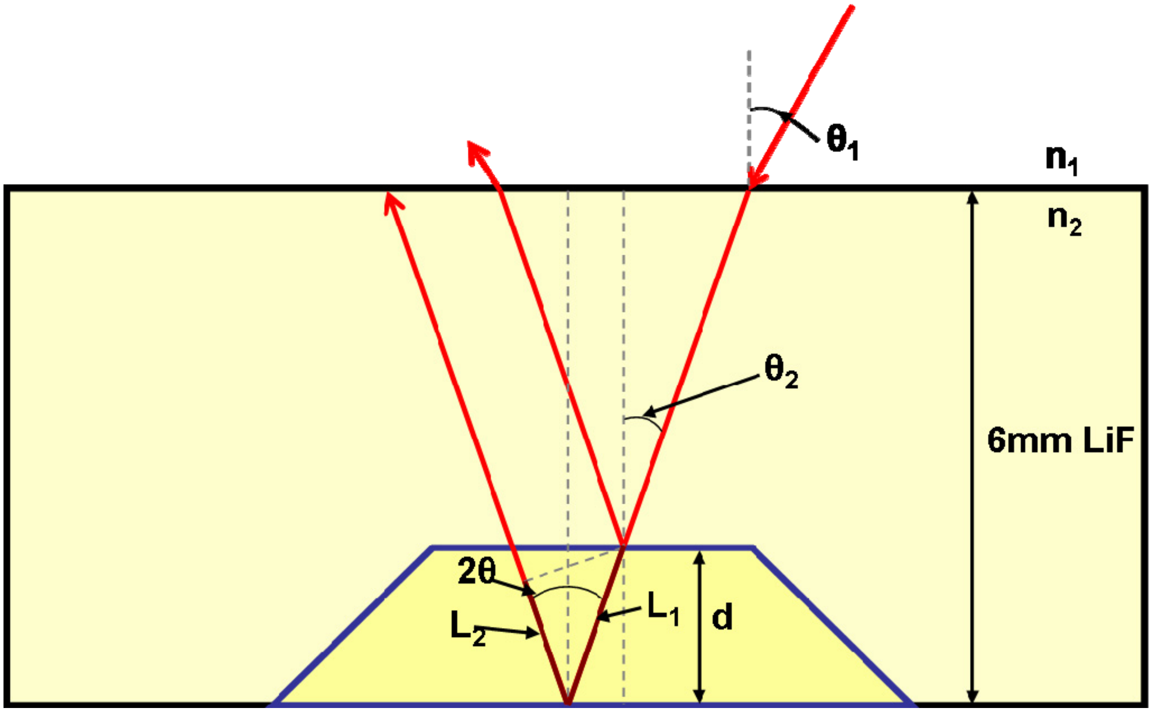

Figure 96. Schematic showing the rays and angles necessary to derive the calibration factor for the interferometer

distance *d*. In the interferometer, the phase of the light is what determines the fringe shift.

$$\phi(x) = \frac{2\pi n_2 x}{\lambda} \tag{E.2}$$

where x is the additional physical path length that the light has traveled.

$$x = L_1 + L_2 \tag{E.3}$$

Utilizing the fact that *L1* is the hypotenuse of a right triangle and *L2* is the adjacent side of a right triangle, we find

$$L_1 = \frac{d}{Cos(\theta_2)} \tag{E.4}$$

$$L_2 = L_1 \cdot Cos(2\theta_2) \tag{E.5}$$

Simplifying x and then plugging into ϕ gives

$$\begin{aligned} x &= L_1 \cdot \left(1 + Cos(2\theta_2)\right) \\ &= \frac{d}{Cos(\theta_2)} \cdot \left(1 + Cos(2\theta_2)\right) \\ &= 2d \cdot Cos(\theta_2) \end{aligned} \tag{E.6}$$

$$\begin{aligned} \phi(x) &= \frac{2\pi n_2 \cdot 2d \cdot Cos(\theta_2)}{\lambda} \\ &= \frac{4\pi n_2 d \cdot Cos(\theta_2)}{\lambda} \end{aligned} \tag{E.7}$$

Rearranging (E.7) gives the calibration for displacement in terms of the phase shift.

$$d = \frac{\lambda \cdot \phi(x)}{4\pi n_2 \cdot Cos(\theta_2)} \tag{E.8}$$

From Snell's Law, we can solve for θ_2 and plug it into (E.8).

$$d = \frac{\lambda \cdot \phi(x)}{4\pi n_2 \cdot Cos\left(Sin^{-1}\left(\frac{n_1}{n_2} Sin(\theta_1)\right)\right)} \tag{E.9}$$

For a LiF window and an angle of incidence of 10°, this reduces to

$$d = 0.0462\mu m \cdot \phi(x) \tag{E.10}$$

As an example, if after analyzing an interferometer image, I find that the peak phase shift is 2π, then that translates into a rear surface motion of $d = 0.29\mu m$. Of course, some of my experiments were performed at different angles, or with different materials at the rear surface, so the calibrations for these situations are different.

Appendix F. HYADES Source file "AlSi08.inf"

```
Laser shock of Silicon block

geometry 1 1

c Aluminum
mesh   1 10 .0    .00003 1.05
region 1 9 1 2.70 2.70e-5
material 1 13 26.98 1.
c eos 44 1
c QEOS 1 7.6e11 2.70
c eos 900 1
c activate Thomas-Fermi ionization model
  ioniz 1 3 2.e-5

c *******************Al
c Aluminum 1100-0  -- This is nearly pure aluminum
c region start end 1 2.70 2.5e-5
c material 1 13 26.98 1.
c eos 43 1
c Aluminum input melt curve
data tmelt 1 1.05e-4 1.5 1.97
c strength   1 2 3 0
c strength   1 2 1 0
c strength   1 2 0 0
c data shear 1 2.76e11 6.5 6.2e-4
c data yield 1 0.4e9 125. 0. 0.10 0.8e9
c data yield 1 0.4e9

c ************************


c Silicon
mesh   10 75 .00003 .0300 1.05
region 10 74 2 2.33 2.70e-5
material 2 14 28.08 1.
eos 391 2

c activate average atom ionization model
  ioniz 2 4 2.e-5
```

```
c Silicon approx input melt curve
 data tmelt 2 .145e-3 1.7 2.1

c 211*.93J pulse averaged over 1mm^2 spot size applied in
3.0ns = 6.5e12 W/cm2
source laser 0.532 1
gauss 0.8e-9 15e19 0.46e-9


parm editdt 1.e-10
parm nstop 200000
parm tstop 10.0e-9
parm itmcyc 100
parm postdt 1.e-10
parm flxlem 0.05
parm temin 2.5e-5
parm timin 2.5e-5
parm trmin 2.5e-5
c
pparray r rcm rho pres u te ti tmelt qtot sd1 flostr zbar
```

Appendix G. HYADES Source file “SnLif9.inf”

```
Laser shock of Tin block
c
c Planar geometry laser shock pulse on left side
c
geometry 1 1
c
c region 1 will be ablated completely away

c *******************Tin***************************


mesh 1 90 .0 .0002 1.05
mesh 90 150 .0002 .0004 0.95
region 1 149 1 7.29 2.5691e-5
material 1 50 118.69 1.
eos 901 1

c eos 402 1
c qeos 1 0.58e12 7.31

c activate Thomas-Fermi ionization model
ioniz 1 3 2.e-5

c Tin input melt curve
data tmelt 1 5.66e-5 1.7 2.27

c Tin Region, Steinberg Shear Model, Von-Mises Yield Model,
no spall model
strength 1 2 3 0
data shear 1 1.79e11 8.66 2.12e-4
c added steinberg model
data yield 1 1.6e9 120 0 0.1 4e9

c *******************Tin***************************
c *******************LiF
mesh 150 250 .0004 .0025 1.05
region 150 249 2 2.638 2.56e-5

material 2 6 12.969 1.
eos  903 2
```

```
c activate Thomas-Fermi ionization model
ioniz 2 3 2.e-5
c LiF input melt curve
data tmelt 2 1.276e-4 1.4 1.69
strength 2 2 3 0
data shear 2 4.90e11 5.0 6.18e-4
data yield 2 3.6e9 0.0 0.0 0.0 3.6e9
c ************************

c .9J pulse averaged over 400 micron diam spot size applied
in 0.6 ns = 1.2e12 W/cm2
source laser 0.8 1
c gauss 1.1e-9 8.0e19 0.6e-9
gauss 1.1e-9 0.80e19 0.6e-9

parm editdt 1.e-10
parm nstop 100000
parm tstop 8.0e-9
parm itmcyc 100
parm postdt 1.e-10
parm flxlem 0.05
parm temin 2.5e-5
parm timin 2.5e-5
parm trmin 2.5e-5

pparray r rcm rho pres u te ti tmelt qtot
```

REFERENCES

Ahrens, T. J. (1975). "Equations of state of the earth." Reviews of Geophysics and Space Physics **13**: 335-372.

Ahrens, T. J. (1980). Shock wave data and the composition of the earth's core. 7th Int'l AIRAPT- High Pressure Conference, Pergamon Press.

Asay, J. R. and M. Shahinpoor, Eds. (1993). High-Pressure Shock Compression of Solids. New York, Springer-Verlag.

Backus, S., C. G. Durfee, et al. (1998). "High power ultrafast lasers." Review Of Scientific Instruments **69**(3): 1207-1223.

Bancroft, D., E. L. Peterson, et al. (1956). "Polymorphism of Iron at High Pressure." Journal Of Applied Physics **27**(3): 291.

Banks, P. S., M. D. Perry, et al. (2000). "Novel all-reflective stretcher for chirped-pulse amplification of ultrashort pulses." IEEE Journal Of Quantum Electronics **36**(3): 268-274.

Batani, D., H. Stabile, et al. (2003). "Ablation pressure scaling at short laser wavelength." Physical Review E **68**(6): 4.

Bloembergen, N. and P. S. Pershan (1962). "Light waves at the boundary of nonlinear media." Physical Review **128**(2): 606.

Bone, D. J. (1991). "Fouriier fringe analysis: the two-dimensional phase unwrapping problem." Applied Optics **30**: 3627-3632.

Braginskii, S. I. (1958). Soviet Physics JETP **6**: 358.

Burns, W. K. (1971). Third Harmonic Generation by Picosecond Laser Pulses. Cambridge, Harvard University. **PhD Thesis**.

Burns, W. K. and N. Bloembergen (1971). "Third-harmonic generation in absorbing media of cubic or isotropic symmetry." Physical Review B (Solid State) **4**(10): 3437.

Bushman, A. V., I. V. Lomonosov, et al. (2003). "Shock Wave Database." from http://teos.ficp.ac.ru/rusbank/index.php?text=1.

C. R. Phipps, J., T. P. Turner, et al. (1988). "Impulse coupling to targets in vacuum by KrF, HF, and CO2 single-pulse lasers." Journal of Applied Physics **64**(3): 1083.

Celliers, P., A. Ng, et al. (1992). "Thermal equilibration in a shock wave." Physical Review Letters **68**(15): 2305.

Chhabildas, L. C., L. M. Barker, et al. (1992). Launch Capabilities to over 10 km/s. Shock Waves in Condensed Matter - 1991. S. C. Schmidt, J. Forbes and R. Dick. New York, Elsevier Science.

Dendy, R. (1993). Plasma Physics: An Introductory Course. Cambridge, Cambridge University Press.

Duvall, G. E. and R. A. Graham (1977). "Phase transitions under shock-wave loading." Reviews of Modern Physics **49**(3): 523.

Eliezer, S., Y. Gazit, et al. (1990). "Shock wave decay and spall strength in laser-mater interaction." Journal Of Applied Physics **68**(1): 356.

Fairand, B. P. and A. H. Clauer (1979). "Laser generation of high-amplitude stress waves in materials." Journal Of Applied Physics **50**(3): 1497.

Fairand, B. P., B. A. Wilcox, et al. (1972). "Laser shock-induced microstructural and mechanical property changes in 7075 aluminum." Journal Of Applied Physics **43**(9): 3893.

Fittinghoff, D. N., B. C. Walker, et al. (1998). "Dispersion considerations in ultrafast CPA systems." IEEE Journal Of Selected Topics In Quantum Electronics **4**(2): 430-440.

Flynn, T. J. (1997). "Two-dimensional phase unwrapping with minimum weighted discontinuity." Journal of the Optical Society of America A **14**(10): 2692.

Ghiglia, D. C. and M. D. Pritt (2001). Two-Dimensional Phase Unwrapping: Theory, Algorithms, and Software, Wiley-Interscience.

Glezer, E. N., Y. Siegal, et al. (1995). "Behavior Of Chi((2)) During A Laser-Induced Phase-Transition In Gaas." Physical Review B **51**(15): 9589-9596.

Goldstein, R. M., H. A. Zebker, et al. (1988). "Satellite radar interferometry: two-dimensional phase unwrapping." Radio Science **23**: 713-720.

Goto, T., T. Sato, et al. (1982). "Reduction of Shear-Strength and Phase-Transition in Shock-Loaded Silicon." Japanese Journal of Applied Physics Part 2-Letters **21**(6): L369-L371.

Gundrum, B. C., R. S. Averback, et al. (2007). "Time resolved measurements of melting and solidification in Si using third harmonic generation of light." Applied Physics Letters **91**: 011906.

Henis, Z. and S. Eliezer (1993). "Melting Phenomenon in Laser-Induced Shock-Waves." Physical Review E **48**(3): 2094-2097.

Huang, L., J. P. Callan, et al. (1998). "GaAs under intense ultrafast excitation: Response of the dielectric function." Physical Review Letters **80**(1): 185-188.

Huba, J. D. (2007). NRL Plasma Formulary. Washington DC, Naval Research Laboratory.

Ishida, Y., T. Yajima, et al. (1985). "A simple monitoring system for single subpicosecond laser pulses using an SH spatial autocorrelation method and a CCD image sensor." Optics Communications **56**: 57-60.

Jankowski, A., J. Ferreira, et al. (2005). "Activation energies of grain growth mechanisms in aluminum coatings." Thin Solid Films **491**(1-2): 61-65.

Kadau, K., T. C. Germann, et al. (2007). "Shock waves in polycrystalline iron." Physical Review Letters **98**(13).

Kalantar, D. H., G. W. Collins, et al. (2006). "In situ diffraction measurements of lattice response due to shock loading, including direct observation of the alpha-epsilon phase transition in iron." International Journal of Impact Engineering **33**(1-12): 343-352.

Kandyla, M., T. Shih, et al. (2007). " Femtosecond dynamics of the laser-induced solid-to-liquid phase transition in aluminum." Physical Review B **75**: 214107.

Kaushik, T. C. and B. K. Godwal (1987). "Laser-driven shock pressure enhancement in plane-layered CH2-Pt targets." Physical Review A **36**(10): 5095.

Kim, A. M.-T. (2001). Ultrafast Carrier and Lattice Dynamics in Highly Photo-Excited Solids, Harvard.

Knudsen, M. (2005). "Shock Waves." HEDP Summer School.

Kruer, W. L. (1988). The physics of laser plasma interaction. Redwood City, CA, Addison-Wesley Publishing Company, Inc.

Kruer, W. L. (2005). "Laser Plasma Interaction - Part 1." HEDP Summer School.

Larsen, J. T. and S. M. Lane (1994). "Hyades - a Plasma Hydrodynamics Code for Dense-Plasma Studies." Journal of Quantitative Spectroscopy & Radiative Transfer **51**(1-2): 179-186.

Lemoff, B. E. and C. P. J. Barty (1993). "Quintic-Phase-Limited, Spatially Uniform Expansion And Recompression Of Ultrashort Optical Pulses." Optics Letters **18**(19): 1651-1653.

Li, K. D. and P. M. Fauchet (1987). "Drude Parameters of Liquid Silicon at the Melting Temperature." Applied Physics Letters **51**(21): 1747-1749.

Lindl, J. (1995). "Development of the Indirect-Drive Approach to Inertial Confinement Fusion and the Target Physics Basis for Ignition and Gain." Physics of Plasmas **2**(11): 3933-4024.

LLNL. "ASC at Livermore." 2007, from http://www.llnl.gov/asc/.

Loveridge-Smith, A., A. Allen, et al. (2001). "Anomalous elastic response of silicon to uniaxial shock compression on nanosecond time scales." Physical Review Letters **86**(11): 2349-2352.

Löwer, T., V. N. Kondrashov, et al. (1998). "Reflectivity and Optical Brightness of Laser-Induced Shocks in Silicon." Physical Review Letters **80**(18): 4000.

Luo, S.-N. and T. J. Ahrens (2004). "Shock-induced superheating and melting curves of geophysically important minerals." Physics of The Earth and Planetary Interiors **143-144**: 369-386.

Lyon, S. P. and J. D. Johnson (1992). "Sesame: Los Alamos National Laboratory Equation of State Database." Los Alamos report **LA-UR-92-3407**.

Maiman, T. H. (1960). "Stimulated Optical Radiation in Ruby." Nature **187** (4736): 493-494.

Malone, R. C., R. L. McCrory, et al. (1975). "Indications of Strongly Flux-Limited Electron Thermal Conduction in Laser-Target Experiments." Physical Review Letters **34**(12): 721.

Marsh, S. P., Ed. (1980). LASL Shock Hugoniot Data. Berkeley, University of California Press.

Martinez, O. E. (1987). "Design of High-Power Ultrashort Pulse-Amplifiers by Expansion and Recompression." IEEE Journal of Quantum Electronics **23**(8): 1385-1387.

Max, C. E., J. D. Lindl, et al. (1983). "Effect of Symmetry Requirements on the Wavelength Scaling of Directly Driven Laser Fusion Implosions." Nuclear Fusion **23**(2): 131-145.

McQueen, R. G. and S. P. Marsh (1960). "Equation of State for Nineteen Metallic Elements from Shock-Wave Measurements to Two Megabars." Journal Of Applied Physics **31**(1253).

Meyers, M. A. (1994). Dynamic Behavior of Materials. New York, John Wiley & Sons, Inc.

Montross, C. S., T. Wei, et al. (2002). "Laser shock processing and its effects on microstructure and properties of metal alloys: a review." International Journal of Fatigue **24**(10): 1021-1036.

Mora, P. (1982). "Theoretical-Model of Absorption of Laser-Light by a Plasma." Physics of Fluids **25**(6): 1051-1056.

More, R. M., K. H. Warren, et al. (1988). "A new quotidian equation of state (QEOS) for hot dense matter." Physics of Fluids **31**(10): 3059.

Moulton, P. F. (1986). "Spectroscopic and laser characteristics of Ti:Al2O3." Journal Of The Optical Society Of America B-Optical Physics **3**(1): 125.

Ng, A. and T. Ao (2003). "Nonequilibrium and Non-Steady-State Evolution of a Shock State." Physical Review Letters **91**(3): 035002.

Ng, A., P. Celliers, et al. (1995). "Electron-Ion Equilibration in a Strongly Coupled Plasma." Physical Review E **52**(4): 4299-4310.

Ng, A., D. Parfeniuk, et al. (1985). "Hugoniot Measurements for Laser-Generated Shock Waves in Aluminum." Physical Review Letters **54**(24): 2604.

Ng, A., D. Parfeniuk, et al. (1985). "Measurement of shock heating in laser-irradiated solids." Optics Communications **53**(6): 389-393.

Nguyen, J. H. and N. C. Holmes (2004). "Melting of iron at the physical conditions of the Earth's core." Nature **427**(6972): 339-342.

Obenschain, S. P., R. R. Whitlock, et al. (1983). "Uniform Ablative Acceleration of Targets by Laser Irradiation at 10^{14} W/cm^{2}." Physical Review Letters **50**(1): 44.

Optica (1995). Optica v1.3. Champaign, IL, Wolfram Research, Inc.

Paisley, D. L. (1990). Laser-driven miniature flyer plates for shock initiation of secondary explosives. Shock Compression of Condensed Matter -- 1989. S. C. Schmidt, J. N. Johnson and L. W. Davison. New York, Elsevier Science.

Palik, E. D. (1985). Handbook of Optical Constants of Solids. New York, Academic Press Inc.

Pessot, M., P. Maine, et al. (1987). "1000 Times Expansion Compression Of Optical Pulses For Chirped Pulse Amplification." Optics Communications **62**(6): 419-421.

Potter, R. F. (1969). Optical Properties of Solids. New York, Plenum

Rashleigh, S. C. and R. A. Marshall (1978). "Electromagnetic acceleration of macroparticles to high velocities." Journal Of Applied Physics **49**(4): 2540.

Regan, S. P., R. Epstein, et al. (2007). "Laser absorption, mass ablation rate, and shock heating in direct-drive inertial confinement fusion." Physics of Plasmas **14**: 056305.

Rességuier, T. d., L. Signor, et al. (2007). "Experimental investigation of liquid spall in laser shock-loaded tin." Journal Of Applied Physics **101**: 013506.

Rice, M. H., R. G. McQueen, et al. (1958). Compression of Solids by Strong Shock Waves. Solid State Physics, Vol VI. F. Seitz and D. Turnbull. New York, Academic Press**:** 1-63.

Saeta, P., J. K. Wang, et al. (1991). "Ultrafast Electronic Disordering During Femtosecond Laser Melting Of Gaas." Physical Review Letters **67**(8): 1023-1026.

Shay, H. D., R. A. Haas, et al. (1978). "Interaction of 1.06 um laser radiation with variable Z targets." Physics of Fluids **21**(9): 1634.

Simon, H. J. and N. Bloembergen (1968). "Second-Harmonic Light Generation in Crystals with Natural Optical Activity." Physical Review **171**(3): 1104.

Sokolowski-Tinten, K. and D. von der Linde (2000). "Generation of dense electron-hole plasmas in silicon." Physical Review B **61**(4): 2643-2650.

Sorenson, D. S., R. W. Minich, et al. (2002). "Ejecta particle size distributions for shock loaded Sn and Al metals." Journal of Applied Physics **92**(10): 5830-5836.

Spitzer, L., Jr. (1962). Physics of Fully Ionized Gases. New York, Interscience.

Steinberg, D. J. (1991). "Equation of State and Strength Properites of Selected Materials." LLNL **UCRL-MA-106439**: February 1996.

Strickland, D. and G. Mourou (1985). "Compression Of Amplified Chirped Optical Pulses." Optics Communications **55**(6): 447-449.

Swift, D. C., T. E. Tierney, et al. (2004). "Shock pressures induced in condensed matter by laser ablation." Physical Review E **69**: 036406.

Swift, D. C., T. E. Tierney, et al. (2005). "Dynamic response of materials on subnanosecond time scales, and beryllium properties for inertial confinement fusion." **12**(5).

Takeda, M., H. Ina, et al. (1982). "Fourier-Transform Method Of Fringe-Pattern Analysis For Computer-Based Topography And Interferometry." Journal Of The Optical Society Of America **72**(1): 156-160.

Temnov, V. V., K. Sokolowski-Tinten, et al. (2006). "Ultrafast imaging interferometry at femtosecond-laser-excited surfaces." Journal Of The Optical Society Of America B-Optical Physics **23**(9): 1954-1964.

Tom, H. W. K., G. D. Aumiller, et al. (1988). "Time-resolved study of laser-induced disorder of Si surfaces." Physical Review Letters **60**(14): 1438.

Trainor, R. J., J. W. Shaner, et al. (1979). "Ultrahigh-Pressure Laser-Driven Shock-Wave Experiments In Aluminum." Physical Review Letters **42**(17): 1154-1157.

Treacy, E. B. (1969). " Optical Pulse Compression with Diffraction Gratings." IEEE Journal Of Quantum Electronics **QE-5**(9): 454-458.

Trunin, R. F., Ed. (2001). Experimental Data on Shock Compression and Adiabatic Expansion of Condensed Matter. SAROV, RFNC-VNIIEF.

Voronin, G. A., C. Pantea, et al. (2003). "In situ x-ray diffraction study of silicon at pressures up to 15.5 GPa and temperatures up to 1073 K." Physical Review B **68**(2).

Walsh, J. M. (1954). Bulletin of the American Physical Society **29**: 28.

Wang, C. C., J. Bomback, et al. (1986). "Optical Third-Harmonic Generation in Reflection from Crystalline and Amorphous Samples of Silicon." Physical Review Letters **57**(13): 1647.

Wavemetrics IGOR Pro. Lake Oswego, OR.

Werdiger, M., B. Arad, et al. (1996). "Asymptotic measurements of free surface instabilities in laser-induced shock waves." Laser and Particle Beams **14**(2): 133-147.

Werdiger, M., S. Eliezer, et al. (1999). "Detecting of melting by changes of rear surface reflectivity in shocked compressed metals using an interferometric diagnostic method." Laser and Particle Beams **17**(3): 547-556.

Yakovlev, V. V. and S. V. Govorkov (2001). "Diagnostics of surface layer disordering using optical third harmonic generation of a circular polarized light." Applied Physics Letters **79**(25): 4136-4138.

Zel'dovich, Y. B. and Y. P. Raizer (1966). Physics of Shock Waves and High-Temperature Hydrodynamic Phenomena. Mineola, NY, Dover Publications.

VITA

Will Robert Grigsby was born on October 31, 1978 in Bryan, TX, the son of Dr. and Mrs. Robert and Paula Grigsby. After completing his work at Westwood High School in Austin, TX in 1996, he attended Texas A&M University in College Station, TX, where he earned a B.S. in Physics in December 1999. In the Fall of 2000, Will began his graduate program in the physics department at The University of Texas at Austin, were he worked for Dr. Todd Ditmire in the Texas Center for High-Intensity Laser Science.

Permanent address: 11917 Lansdowne Rd., Austin, TX 78754

This dissertation was typed by the author.